Theoretische Physik

DARK MATTER, NEUTRINO MASSES AND LEPTON FLAVOR VIOLATION IN RADIATIVE SEE-SAW MODELS

Inaugural-Dissertation zur Erlangung des Doktorgrades
der Naturwissenschaften im Fachbereich Physik
der Mathematisch-Naturwissenschaftlichen Fakultät
der Westfälischen Wilhelms-Universität Münster

vorgelegt von
SONJA ESCH
aus Bonn
-2018-

DEKAN:	Prof. Dr. Michael Klasen
ERSTER GUTACHTER:	Prof. Dr. Michael Klasen
ZWEITER GUTACHTER:	Prof. Dr. Christian Weinheimer
TAG DER MÜNDLICHEN PRÜFUNG:	
TAG DER PROMOTIONON:	

ABSTRACT

The Standard Model of particle physics is a widely successful theory, allowing for very precise predictions. It combines the three elementary forces in one common theory. Sometimes, especially in the light of the discovery of a Higgs-like boson, the Standard Model is presented as complete, yet it has its weaknesses. It does not provide a description of gravity nor does it provide a solution for the hierarchy problem of the Higgs mass. Moreover, it does not provide an explanation for neutrino masses or a dark matter candidate.

In this work minimal extensions of the Standard Model are studied which allow for neutrino masses and dark matter at the same time. First, evidence for dark matter on several scales is summarized. Based on cosmological observations, baryonic matter cannot make up for most of the matter content in the Universe, there has to be an additional matter type, called dark matter, to make up for the difference. Weakly interacting massive particles (WIMPs) provide a good dark matter candidate. WIMPs can appear in extensions of the Standard Model symmetry like Supersymmetry or in minimal models, which only add a few new fields and symmetries.

The next part reviews several dark matter searches. It concentrates on direct searches, indirect searches and collider experiments. Direct searches look for dark matter nucleus interactions in Earth-based experiments, testing the presence of dark matter in the solar system. Indirect searches, on the other hand, try to detect dark matter annihilations in the galactic center or in other parts of our Universe where the dark matter density is significant. In collider experiments the approach is to produce dark matter particles in collisions of Standard Model particles. Overall, the dark matter searches place rather stringent limits on the parameters space of new models.

In the following chapter, the focus is on neutrino oscillations. The observation of oscillations of atmospheric, solar and reactor neutrinos clearly proves that neutrinos cannot be massless. In order to be consistent with the experimental limits at least two of the Standard Model neutrinos have to be massive. The see-saw mechanisms of type I and II can in principle explain neutrino masses but they demand an extension of the Standard Model.

In this work, the focus is on radiative models. They give rise to neutrino masses at one-loop level and can feature dark matter. In addition to neutrino masses, radiative models give rise to lepton flavor violation, which has to be contrasted with current experimental constraints.

As an introductory example the scotogenic model is presented. It is

followed by a detailed analysis of the model T12A. The model T12A can be seen as a fusion of the singlet-doublet scalar and fermion models. First dark matter, neutrino masses and lepton flavor violation are analyzed separately, before performing two random scans. A special emphasis is on the calculation of dark matter to lepton pairs as well as branching ratios for lepton flavor violations.
The two scans are conducted by imposing relic density, Higgs and neutrino mass constraints. Both focus on scalar dark matter. The first scan explores the whole parameter region whereas the second scan is concentrated on mostly singlet-like scalar dark mater in the coannihilation region for fermions and scalars. For the first scan, most regions are either excluded by direct detection or lepton flavor limits and most remaining points will be probed by XENONnT. The second scan direct detection cross sections are too small and quite a large part of the points will be probed by future lepton flavor experiments. In addition to the random scans, LHC constraints are discussed and an outlook on one-loop Higgs masses within the model is given.
Next the model T13A, which is also a radiative see-saw model, is presented. For this work mostly calculations for dark matter annihilation into Standard Model leptons are important. So a special focus is on the exact calculations. All technical details of the calculations in this thesis are collected in several appendices at the end.

ZUSAMMENFASSUNG

Das Standardmodell der Teilchenphysik ist eine erfolgreiche Theorie, die es erlaubt sehr präzise Vorhersagen zu machen. Es beinhaltet die drei fundamentalen Wechselwirkungen, abgesehen von der Gravitation, in einer gemeinsamen Theorie. Manchmal, vor allem im Licht der Entdeckung eines Standardmodell-ähnlichen Higgs-Bosons, wird das Standardmodell als vollständig angesehen, jedoch hat es einige Schwachstellen. Es enthält weder eine Beschreibung der Gravitation noch liefert es eine Erklärung für das Hierarchieproblem der Higgs Masse. Des Weiteren verfügt das Standardmodell nicht über Neutrinomassen oder einen passenden Kandidaten für dunkle Materie.
In dieser Arbeit werden minimale Erweiterungen des Standardmodells untersucht, welche Neutrinomassen und dunkle Materie gleichzeitig beschreiben. Zuerst werden die Evidenzen auf verschiedenen Skalen für dunkle Materie aufgeführt. Basierend auf kosmologischen Beobachtungen kann baryonische Materie nicht den gesamten Materieinhalt des Universums darstellen. Ein Großteil des Materieinhalts muss aus nicht-baryonischer, so genannter dunkler Materie bestehen. Schwach wechselwirkende massive Teilchen (WIMPs) liefern einen guten Kandidaten für dunkle Materie. WIMPs können sowohl in Erweiterungen der Symmetrien des Standardmodells wie Supersymmetrie, als auch in minimalen Erweiterungen, welche nur einige neue Felder benötigen, vorhanden sein.
Der nächste Abschnitt der Arbeit gibt einen Überblick über verschiedene Suchen nach dunkler Materie. Dabei liegt der Fokus auf direkten Suchen, indirekten Suchen und Collider-Experimenten. In direkten Suchen wird, durch Wechselwirkungen von dunkler Materie und Atomkernen in erdgebundenen Experimenten, das Vorhandensein dunkler Materie im Sonnensystem untersucht. Dem gegenüber stehen indirekte Dektektionsexperimente, die versuchen Annihilation von dunkler Materie im galaktischen Zentrum oder anderen Regionen mit hoher dunkler Materiedichte nachzuweisen. In Collider-Experimenten werden Kollisionen von Standardmodell Teilchen auf die Produktion von dunkler Materie hin untersucht. Insgesamt ergeben sich aus den Experimenten für dunkle Materie starke Einschränkungen bezüglich neuer Modelle.
Als nächstes liegt der Fokus auf Neutrinooszillationen. Die Messung von Oszillationen von atmosphärischen, solaren und Reaktor-Neutri -nos, induziert eindeutig, dass Neutrinos nicht masselos sein können. Es sind mindestens zwei massive Neutrinos notwendig, um die Beobachtungen zu erklären. Die See-saw Mechanismen von Typ I und II können prinzipiell Neutrinomassen erklären, benötigen aber auch

eine Erweiterung des Standardmodells.
In dieser Arbeit liegt das Augenmerk auf radiativen Modellen. Sie erzeugen Neutrinomassen auf Einschleifenniveau und können zusätzlich dunkle Materie enthalten. Zusätzlich zu Neutrinomassen beinhalten diese Modelle Prozesse, die Leptonen-Flavor verletzen. Diese Prozesse werden durch aktuelle Experimente beschränkt.
Als einführendes Beispiel wird das skotogene Modell gezeigt. Im Anschluss befindet sich eine detaillierte Analyse des Modells T12A. Das Modell T12A kann als eine Verschmelzung der skalaren und fermionischen Singulett-Dublett Modelle gesehen werden. Zuerst wird der dunkle Materie Sektor des Modells untersucht, dann Neutrinomassen und die Verletzung von Leptonen-Flavor. Danach werden zwei Zufallsscans des Parameterraums durchgeführt, wobei hauptsächlich skalare dunkler Materie gesucht wird. Speziell wird auf die Berechnung von Annihilationsquerschnitten für dunkle Materie in Leptonenpaare und Verzweigungsverhältnisse von Prozessen, die Leptonen-Flavor verletzen, eingegangen.
Die beiden Scans werden durchgeführt, in dem die korrekte Reliktdichte, Higgs-Parameter und Neutrinomassen gefordert werden. Im erste Scan wird der gesamten Parameterraum abgedeckt. Der zweite Scan ist auf die Region mit Singulett-ähnlicher skalarer dunkler Materie konzentriert, in der es zu Ko-Annihilation zwischen Fermionen und Skalaren kommen kann. Bezüglich des ersten Scans zeigt sich, dass große Teile entweder durch direkte Detektion oder durch Grenzen auf Leptonen-Flavor verletzende Prozesse ausgeschlossen werden können. Die meisten verbleibenden Punkte können durch XENONnT geprüft werden. Für den zweiten Scan sind die meisten direkten Detektionsquerschnitte und Verzweigungsverhältnisse zu klein. Jedoch wird ein beachtlicher Anteil durch zukünftige Leptonenexperimente überprüft werden.
Zusätzlich zu den Scans werden Einschränkungen durch den Large Hadron Collider diskutiert, sowie ein Ausblick auf Korrekturen zur Higgs-Masse auf Einschleifenniveau gegeben.

Im weiteren wird das Modell T13A präsentiert, welches ebenfalls zur Gruppe der radiativen See-saw Modelle gehört. Der Schwerpunkt in dieser Arbeit liegt auf der Berechnung von Annihilationsquerschnitten von dunkler Materie in leptonische Endzustände. Technische Details zu den Rechnungen werden in den Anhängen zusammengefasst.

PUBLICATIONS

This work has contributed to the following publications:

SE, M. KLASEN, D. R. LAMPREA, C. E. YAGUNA:
Lepton flavor violation and scalar dark matter in
a radiative model of neutrino masses
In: Eur. Phys. J.C78 (2018)

SE, M. KLASEN, C. E. YAGUNA:
A singlet doublet dark matter model with
radiative neutrino masses
In: arXiv:1804.0338, currently under review for JHEP (2018)

CONTENTS

I INTRODUCTION 1

1 THE STANDARD MODEL AND ITS SHORTCOMINGS 3

II THEORETICAL AND EXPERIMENTAL FRAMEWORK 5

2 DARK MATTER 7
- 2.1 Evidence . . . 7
  - 2.1.1 First evidence . . . 7
  - 2.1.2 Rotation curves . . . 9
  - 2.1.3 Gravitational lensing and the bullet cluster . . . 10
  - 2.1.4 Cosmic microwave background . . . 11
  - 2.1.5 Structure formation and N-body simulations . . . 15
- 2.2 Candidates . . . 16
- 2.3 Experimental searches . . . 18
  - 2.3.1 Direct detection . . . 19
  - 2.3.2 Indirect detection . . . 28
  - 2.3.3 Collider searches . . . 34
- 2.4 Calculations . . . 36
  - 2.4.1 Boltzmann equation and dark matter relic density 36
  - 2.4.2 Direct detection cross section . . . 41
  - 2.4.3 Generic calculations for direct detection processes 44

3 NEUTRINOS AND NEUTRINO MASSES 51
- 3.1 Neutrino sources and detection mechanisms . . . 51
  - 3.1.1 Neutrino sources . . . 51
  - 3.1.2 Neutrino detection processes . . . 52
- 3.2 Neutrino oscillation . . . 52
  - 3.2.1 Neutrino vacuum oscillations . . . 53
  - 3.2.2 Matter enhanced neutrino oscillation: MSW-effect 54
- 3.3 Neutrino oscillation experiments . . . 56
- 3.4 Mechanisms for neutrino mass generation . . . 58
  - 3.4.1 See-saw type I . . . 59
  - 3.4.2 See-saw type II and beyond . . . 60
- 3.5 Neutrino mass measurements . . . 61
  - 3.5.1 Cosmology . . . 62
  - 3.5.2 Neutrinoless double-β decay . . . 62
  - 3.5.3 Supernovae . . . 63
  - 3.5.4 β-decay . . . 64

4 LEPTON FLAVOR VIOLATION 67
- 4.1 Experiments . . . 67
- 4.2 Theory . . . 71

III MAIN PART 73

5 RADIATIVE MODELS FOR NEUTRINO MASSES 75

5.1 The scotogenic model . . . 77
5.1.1 Model description . . . 77
5.1.2 Neutrino masses . . . 78
5.1.3 Lepton flavor violation . . . 80
5.2 Model T12A . . . 86
5.2.1 Model description . . . 86
5.2.2 Dark matter relic density . . . 93
5.2.3 Neutrino masses . . . 105
5.2.4 Lepton flavor violation . . . 117
5.2.5 Numerical results . . . 120
5.2.6 LHC constraints . . . 133
5.2.7 One-loop mass corrections and outlook . . . 135
5.3 Model T13A . . . 136
5.3.1 Model description . . . 137
5.3.2 Neutrino masses . . . 137
5.3.3 Lepton flavor violation . . . 138
5.3.4 Dark matter annihilation into lepton final states 139
5.3.5 Summary of recent results . . . 144

IV CONCLUSION 145

6 CONCLUSION 147

V APPENDIX 151

A CONVENTIONS, γ MATRICES AND TRACE THEOREMS 153
A.1 Conventions . . . 153
A.2 γ matrices . . . 153
A.3 Chirality projectors . . . 153
A.4 Trace theorems . . . 154

B APPENDIX - KINEMATICS 155
B.1 Kinematics for $1 \to 2$ processes . . . 155
B.1.1 Special case: one vanishing mass in the final state 155
B.2 Kinematics for $1 \to 3$ processes . . . 156
B.2.1 Special case: two vanishing masses in the final state . . . 157
B.3 Kinematics for $2 \to 2$ processes . . . 159

C DECAY WIDTH 163

D CROSS SECTION - ANNIHILATION 165
D.1 Direct detection cross section . . . 165
D.2 $\cos\theta$ integration . . . 166

E COUPLINGS AND PROPAGATORS 171
E.1 Generic expressions . . . 171
E.2 Standard Model fermions with Higgs and Z bosons . . . 173
E.3 Expressions in T12A . . . 173

F DARK MATTER ANNIHILATION 175
F.1 Scalar dark matter . . . 175
F.1.1 Fermion final states . . . 175

F.1.2 Vector final states . . . 182
F.1.3 Scalar final states . . . 183
F.2 Fermion dark matter . . . 183
F.2.1 Fermion final states . . . 184
F.2.2 Scalar final states . . . 196
F.2.3 Vector final states . . . 196
F.3 Coannihilation between fermion and scalar . . . 196
F.3.1 Fermion scalar final state . . . 197
F.3.2 Vector boson fermion final state . . . 197
G DIRECT DETECTION DIAGRAMS 205
G.1 Scalar dark matter . . . 205
G.1.1 Generic diagrams . . . 205
G.1.2 Diagrams within T12A . . . 206
G.2 Fermion dark matter . . . 207
G.2.1 Generic diagrams . . . 208
G.2.2 Diagrams within T12A . . . 208
H DIRECT DETECTION CROSS SECTION 211
H.1 Generic direct detection cross section calculation . . . 211
H.2 Direct detection cross section within T12A . . . 213
I LOOP FUNCTIONS AND DIAGRAMS FOR LEPTON FLAVOR VIOLATION 215
I.1 Dimensional regularization . . . 215
I.2 Tensor reduction and Passarino-Veltman integrals . . . 216
I.3 Feynman parametrization and generic loop integrals in D-dimensions . . . 218
I.4 Definition of loop integrals and approximation for heavy masses . . . 219
I.5 Loop topologies for LFV within T12A and similar models 229
I.6 $e_1 \to e_2\gamma$ in T12A and similar models . . . 233
I.7 Process $e_1 \to e_2\gamma\gamma$ . . . 235
I.8 Process: $e_1 \to e_2e_2e_3$ . . . 237
I.9 $\mu \to e\gamma$ example calculation in the scotogenic model . 238
I.10 Loops in the scotogenic model for $\mu \to e\gamma\gamma$ . . . 241
J APPROXIMATION FOR NEUTRINO MASSES 255
J.0.1 $A = 0$ and $m_\lambda = 0$ . . . 255
J.0.2 $\lambda_S = \lambda_D = \lambda'_D = \lambda''_D = 0$ and $A, m_\lambda \ll 1$ . . . 256
J.0.3 $A = 0$ and $m_\lambda \ll 1$ . . . 257
J.0.4 $A \ll 1$ and $m_\lambda = 0$ . . . 258
J.0.5 $A \ll 1$ and $m_\lambda \ll 1$ . . . 259

BIBLIOGRAPHY 261

LIST OF FIGURES

Figure 2.1 Rotation curves of spiral galaxies. 8

Figure 2.2 Observation of Abell S1063 by the Hubble space telescope [8] (ESA/Hubble). The image shows ring fragments from gravitational lensing. Source http://www.spacetelescope.org/images/heic1615a/ 9

Figure 2.3 Picture with spectrum taken by Magellan and Hubble space telescope [12]. Pink overlay shows the x-ray emission taken by Chandra telescope [13]. Blue overlays are according to mass distribution as recorded by gravitational lensing [14]. Image taken from http://chandra.harvard.edu/photo/2006/1e0657/more.html 10

Figure 2.4 Anisotropies in the cosmic microwave background as seen by COBE [21], Planck [1] and WMAP [22, 23] over the years. Credit: NASA/-COBE/DMR; NASA/WMAP science team, ESA and the Planck collaboration 12

Figure 2.5 The figure shows the angular power spectrum of the CMB anisotropies together with the best fit in the ΛCDM model. Figure taken from [1]. 14

Figure 2.6 Simulation of structure formation with dark matter done by the VIRGO collaboration [36]. The figures are public at https://wwwmpa.mpa-garching.mpg.de/galform/virgo/millennium/index.shtml 15

Figure 2.7 Data taken by the 2dF Galaxy Redshift Survey to investigate the larges scale structures in the Universe. Figure is taken from http://www.2dfgrs.net/ 16

Figure 2.8 Schematic view of dark matter interactions. Taken from [75] 18

Figure 2.9 Sketch of Earth passing through the dark matter halo of our galaxy. Image taken from https://www.hep.shef.ac.uk/research/dm/intro.php. 20

Figure 2.10 Sketch of the three possible signals from dark matter,heat, ionization and scintillation. Figure taken from [80]. 21

Figure 2.11 A simple sketch of a CDMS detector element. Image taken from https://physics.aps.org/articles/v2/2, Illustrator Alan Stonebraker. . 22

Figure 2.12 Picture of a CRESST calorimeter element. Image taken from http://www.cresst.de/cresst.php . . . 23
Figure 2.13 Schematic view of a dark matter event inside a dual phase liquid noble gas detector. Image taken from https://en.wikipedia.org/wiki/File:LUXEvent.pdf . . . 24
Figure 2.14 Simplified image of signal (blue) and background (red) regions within different dark matter direct detection experiments. The left panel shows the regions for cryogenic bolometers. Middle panel is the schematic view for liquid noble gas TPCs. The right panel shows the expected signal and background shapes for a liquid single phase Argon TPC. The figures are from [79]. . . . 25
Figure 2.15 Annual modulation measured by DAMA and DAMA/LIBRA. Figure taken from [82] 25
Figure 2.16 Current limits on spin-independent dark matter direct detection cross sections. The left figure is for high WIMP masses whereas the right panel shows curves for lower WIMP masses. Figures taken from [79] . . . 26
Figure 2.17 Most recent exclusion plots on spin-independent direct detection cross sections .Figure taken from [104] . . . 27
Figure 2.18 Current experimental limits for spin-dependent dark matter nucleon interactions. The left panel shows the plot for dark matter and proton interaction. The right image is for WIMP neutron interactions. Figures taken from [79] . . . 28
Figure 2.19 Current constraints on dark matter annihilation cross section from different experiments. Figure taken from [113] . . . 29
Figure 2.20 Limits on indirect detection of dark matter including neutrino signals. Figure taken from [113] . . . 31
Figure 2.21 Current limits on dark matter nucleon cross sections including IceCube observations of neutrino signals from the Sun. Both figures taken from [149]. The color bar indicates the main annihilation channel of dark matter. The hard spectrum mostly consist of τ lepton and similar final states. . . . 33

Figure 2.22 Spin-independent dark matter nucleon cross section limits from CMS under the assumption of scalar (blue) or fermionic (red) dark matter being linked to the Standard Model by the Higgs boson in comparison to recent direct detection results. Figure taken from [75] 35
Figure 2.23 Evolution of dark matter abundance as a parameter of $x = \frac{m_{DM}}{T}$ for different annihilation cross section. Figure taken from [161] 40
Figure 2.24 Rotation curves of spiral galaxies. 41
Figure 2.25 Scalar dark matter interacting with quarks. . . 43
Figure 2.26 Fermion dark matter interacting with quarks showing t- and u-channel contributions. 45
Figure 2.27 Fermion dark matter interacting with quarks, s-channel contributions. 46
Figure 3.28 Neutrino composition for reactor neutrinos at 4 MeV as a function of the distance. There are some regions where it is more likely to observe $\nu_{\mu,\tau}$ than ν_e. The figure is taken from [178]. . 55
Figure 3.29 The figure shows behavior of neutrino mass states within matter allowing for a point of maximal mixing for a specific electron density. The figure is taken from [181]. 56
Figure 3.30 Diagram for neutrinoless double-β decay. As a Majorana particle the neutrino takes part in both decays. Figure taken from [198] 63
Figure 3.31 The β-decay spectrum is shown with a zoom on the theoretical endpoint for massless neutrinos (blue) or neutrinos with masses of 1 eV (red). Figure taken from [208] 65
Figure 4.32 Schematic overview over the MEG detector. It shows the way of the μ beam onto a thin target. The positrons are detected in a drift chamber, the γs are detected by a liquid xenon scintillator. Image from [213] 68
Figure 4.33 Evolution of LFV sensitivities over time. Starting from first measurements in the 1940s reaching the current status. Image from [213] 71
Figure 5.34 Neutrino mass generation at one-loop level. . 75
Figure 5.35 An overview of loop-topology classification. Figure drawn according to the reference in [230]. 76
Figure 5.36 Schematic diagrams for neutrinos coupling to Higgs at one-loop level before electro-weak symmetry breaking. Plots redone from [229]. . . . 77

Figure 5.37 Neutrino mass generation for the Majorana neutrino part. 79
Figure 5.38 Dirac neutrino mass contribution at one-loop level 80
Figure 5.39 Feynman diagrams for $\mu \to e\gamma$. 81
Figure 5.40 Feynman diagrams for $\mu \to e\gamma\gamma$ in the scotogenic model 83
Figure 5.41 New vertices that link the Z_2-odd sector to the Standard Model. 94
Figure 5.42 Original figure 12a from [243] (a) and reproduction (b) illustrating the relic density and direct detection regions for the scalar mass parameters in the setting $\lambda = 0$ and $A = 10$ GeV. 95
Figure 5.43 The original figure 12 b from [243] (a) and a remake (b) for comparison. The dashed blue (solid black) curve indicates the relic density matches the observation.Contour lines for spin-independent direct detection cross section in zb are also shown. 96
Figure 5.44 Original figure 2 from [242] (a) and a reproduction (b) illustrating the suppression in direct detection cross section and the relic density for singlet-doublet fermion dark matter for $y_1 = 0.36$, $M_{F,S} = 200$ GeV and $M_{F,D} = 300$ GeV. 98
Figure 5.45 Figure 6c from [**Chenug2013**] (a) and a reproduction 8 (b). Both showing the plane of singlet and doublet fermion mass parameters with color overlays for relic density and direct detection lines.[**Chenug2013**] 99
Figure 5.46 (Co-)annihilation processes of fermion (left) and scalar (right) dark matter particles to SM leptons.100
Figure 5.47 Influence of the scalar-fermion couplings g_{ij} on the singlet scalar dark matter relic density as a function of its mass parameter $M_{S,S}$. . . . 101
Figure 5.48 Relic density for fermionic dark matter as function of the fermion mass parameter $M_{F,S}$. . . 102
Figure 5.49 Influence of the scalar-fermion couplings g_{ij} on the singlet fermion dark matter relic density as function of the doublet scalar mass parameter $M_{S,D}$. 103
Figure 5.50 Viable and excluded values of the scalar dark matter relic density in the mass plane $M_{S,D}$–$M_{S,S}$ in the presence of similarly light singlet or doublet fermions with couplings $g_{ij} = 0.75$. 105

Figure 5.51 Neutrino mass generation at one-loop in model T12A after electro-weak symmetry breaking. . 106
Figure 5.52 Influence of the scalar-fermion couplings g_{ij} on the sum of neutrino masses as a function of the singlet scalar mass parameter $M_{S,S}$. 110
Figure 5.53 Influence of the scalar-fermion couplings g_{ij} on the sum of neutrino masses as a function of the singlet fermion mass parameter $M_{F,S}$. . . . 111
Figure 5.54 Plot showing the dependence of neutrino mass on y_2 for different fermionic singlet masses. . 114
Figure 5.55 Color plot showing $\sum m_\nu$ as a function of the fermion Yukawa couplings y_1 and y_2 for different singlet fermion masses. 115
Figure 5.56 Influence on the ratio of the singlet scalar mass $M_{S,S} = 1$ TeV over the singlet fermion mass $M_{F,S}$ on the sum of neutrino masses in the plane of Yukawa couplings y_1–y_2. The doublet scalar and singlet fermion have been decoupled via $M_{S,S}/M_{S,D} = 0.6$ and $M_{S,S}/M_{F,S} = 0.3$. 116
Figure 5.57 Color plot showing $\sum m_\nu$ as a function of the fermion Yukawa couplings y_1 and y_2 larger than 10^{-4} and for different singlet fermion masses. 117
Figure 5.58 Radiative one-loop processes $e_k^- \to e_m^- \gamma$ violating lepton flavor. 118
Figure 5.59 Loop diagrams contributing to the leptonic decays $e_k^- \to e_m^- e_n^+ e_o^-$ 119
Figure 5.60 One-loop diagrams for the process $e_k^- \to e_m^- \gamma\gamma$ 121
Figure 5.61 Influence of the scalar-fermion couplings g_{ij} on the branching ratio $BR(\mu \to e\gamma)$ as a function of the singlet scalar mass parameter $M_{S,S}$. 122
Figure 5.62 Direct detection cross section of scalar singlet dark matter as a function of its mass without (blue) and with (red) coupling of the scalar to the fermion sector. 122
Figure 5.63 Direct detection cross section of scalar singlet dark matter as a function of its mass and its correlation with the lepton-flavor violating branching ratio $BR(\mu \to e\gamma)$ (colors). 124
Figure 5.64 Direct detection cross section plotted against singlet scalar coupling λ_S. 125
Figure 5.65 Correlation between y_1 and g_{11}. 125
Figure 5.66 Ratio of $M_{F,S}$ and $M_{S,S}$ as a function of dark matter mass M_{DM} for all viable points in the coannihilation region. 126
Figure 5.67 Viable scalar-fermion couplings in the plane $|g_{11}|$–$|g_{12}|$ (color code for $|g_{13}|$). 128

Figure 5.68 All points projected onto the plane of the singlet scalar mass parameter $M_{S,S}$ and the singlet scalar-fermion coupling g_{13}. 128
Figure 5.69 Correlation between the scalar doublet mass splitting λ''_D and the scalar doublet-fermion neutrino coupling g_{21}. 129
Figure 5.70 Correlation between the Casas-Ibarra angle θ_R and the fermion-scalar coupling g_{11}. 130
Figure 5.71 Viable Yukawa couplings in the plane $|y_1|$–$|y_2|$ (color code for the mass ratio $M_{F,S}/M_{S,S}$). . . . 131
Figure 5.72 Spin independent direct detection cross section σ_{SI} as a function of λ_S for scalar dark matter. . 131
Figure 5.73 Predicted branching ratios for the most sensitive lepton-flavor violating processes BR($\mu \to e\gamma$), BR($\tau \to e\gamma$) and BR($\mu \to 3e$) (color) with current (full black lines) and future (dashed black lines) exclusion limits. 132
Figure 5.74 Typical diagrams for the production of heavy scalars (top) and fermions (bottom) decaying into two- or multi-lepton final states and missing transverse energy, carried away by scalar dark matter X_1 and neutrinos. 134
Figure 5.75 Influence of the scalar and fermion mass parameters $M_{F,D}$ and $M_{S,S}$ on the one-loop Higgs mass (dashed line) in comparison to the tree-level result (solid line). 136
Figure 5.76 Neutrino-mass generation at one-loop in the model T13A after electro-weak symmetry breaking. 138
Figure 5.77 Radiative one-loop processes $e_k^- \to e_m^-\gamma$ violating lepton flavor in T13A. 139
Figure 5.78 (Annihilation processes of scalar dark matter particles ϕ_{S_1} to SM leptons 140
Figure 5.79 (Dark matter fermions χ_i annihilating to neutrinos. 143
Figure B.80 Momenta for a $1 \to 2$ process. 155
Figure B.81 Kinematics for a $1 \to 3$ process. 156
Figure B.82 Kinematics for a $2 \to 2$ process. 159
Figure F.83 Annihilation of fermion dark matter to two fermions175
Figure F.84 Scalar dark matter annihilation to fermions: s-channel diagrams. 176
Figure F.85 t-channel diagrams for scalar to fermion processes. 176
Figure F.86 s-channel diagram for scalar dark matter annihilating to charged leptons in T12A. 179

Figure F.87 t-channel diagram within T12A for scalar dark matter going to charged leptons. 179
Figure F.88 Process for dark mater annihilating to neutrinos. 181
Figure F.89 Scalar to vector boson processes. 182
Figure F.90 Direct interaction between scalars and vector bosons. 182
Figure F.91 s-channel contributions for scalar dark matter to vector bosons. 183
Figure F.92 Scalar to vector boson processes in t-channel diagrams. 183
Figure F.93 Scalar to scalar processes. 184
Figure F.94 Four fermion interaction. 184
Figure F.95 s-channel diagram for a two scalar to two scalar process. 184
Figure F.96 t-channel contributions for scalar to scalar annihilation. 185
Figure F.97 Schematic sketch for fermion to fermion annihilation. 185
Figure F.98 Fermion dark matter annihilation to fermions: s-channel diagrams. 186
Figure F.99 t-channel diagrams for fermion to fermion processes mediated by a scalar. 186
Figure F.100 t-channel diagrams for fermion to fermion processes mediated by a vector boson. 187
Figure F.101 s-channel diagram for fermion dark matter annihilating to charged leptons. 193
Figure F.102 s-channel diagram for fermion dark matter annihilating to charged leptons. 193
Figure F.103 Diagrams for χ_i annihilation to charged leptons within T12A. 194
Figure F.104 Neutrino final state for fermion dark matter annihilation in T12A. 198
Figure F.105 t-channel diagram for neutrino final states within T12A. 198
Figure F.106 Fermion dark matter annihilation to scalars: s-channel diagrams. 198
Figure F.107 t-channel diagrams for fermion to scalar processes. 199
Figure F.108 s-channel diagrams for vector boson final sates. 199
Figure F.109 Diagrams for dark matter fermions annihilating to vector bosons. 200
Figure F.110 Coannihilation between fermion and scalar dark matter to fermion scalar final states. 200
Figure F.111 t-channel diagrams for fermion to vector final sates. 201

Figure F.112 Diagrams for χ_i and X_j co-annihilation within T12A. 201
Figure F.113 s-channel diagram for fermion scalar coannihilation to a fermion and a vector boson. 202
Figure F.114 t-channel contributions for fermion and vector boson final states. 202
Figure F.115 Diagrams for χ_i and X_j co-annihilation within T12A. 203
Figure F.116 s-channel diagram for χ_i and X_j coannihilation within T12A. 203
Figure G.117 Generic process of scalar - fermion scattering. 205
Figure G.118 s-channel diagrams 205
Figure G.119 t-channel diagrams 206
Figure G.120 s-channel diagrams for X_i and quark scattering within T12A. 206
Figure G.121 s-channel diagram for X_i and e^- scattering within T12A. 207
Figure G.122 t-channel diagrams for X_i and e^- scattering within T12A. 207
Figure G.123 Generic process of fermion - fermion scattering. 207
Figure G.124 s-channel diagrams for fermion - fermion scattering in the context of dark matter direct detection. 208
Figure G.125 t-channel diagrams for direct detection processes of fermion dark matter. 208
Figure G.126 Diagrams for χ_i and q interactions within T12A. 209
Figure G.127 s-channel diagram for χ_i and e^- scattering within T12A. 209
Figure G.128 Diagrams for χ_i and e^- interactions within T12A. 210
Figure I.129 Loop for I_A. 229
Figure I.130 Diagram for I_B. 230
Figure I.131 Topology for integral I_C 230
Figure I.132 Diagrams for I_D 231
Figure I.133 Diagram for loop integral I_E. 231
Figure I.134 Diagram with three final state fermions. 232
Figure I.135 Loop with Higgs. 233
Figure I.136 Loop with Higgs. 233
Figure I.137 Diagrams for $\mu \to e\gamma$. 234
Figure I.138 Diagrams for $\mu \to e\gamma\gamma$. 253
Figure I.139 Diagrams for $e_1 \to e_2 e_3 e_4$. 254

Table 4.1	Current and future limits on lepton-flavor violating processes.	72
Table 5.2	Free parameters in model T12A.	93
Table 5.3	Parameters used in Fig. 5.47	101
Table 5.4	Parameters used in Fig. 5.48	102
Table 5.5	Parameters used in Fig. 5.49	104
Table 5.6	parameters used in Fig. 5.55, Fig. 5.56, Fig. 5.57 andFig. 5.54	113
Table 5.7	Parameters used for the first random scan	123
Table 5.8	Parameters used for the coannihilation region random scan	126
Table 5.9	Parameters used for Fig. 5.75	135
Table F.10	Vertex relations for scalar dark matter annihilation to fermion final states	177
Table F.11	Fermion to fermion annihilation overview	188
Table I.12	Arguments for C^0 integral.	222
Table I.13	Arguments and functions for I_{C^1}	222
Table I.14	Overview for I_{C^2}	223
Table I.15	Results for I_{C^3}.	223
Table I.16	Coefficients for I_{D^0}	225
Table I.17	Coefficients for I_{D^1}	226
Table I.18	Coefficients for I_{D^3} in the approximation.	227
Table I.19	Overview for I_{D^4}	228
Table I.20	Arguments for Fig. I.129	229
Table I.21	Loop arguments for I_B	230
Table I.22	Table for I_C	230
Table I.23	Arguments for loop functions in I_D from Fig. I.132	231
Table I.24	Loop function arguments for I_E.	232
Table I.25	Argument set for I_F.	232
Table I.26	Arguments for I_G.	233
Table I.27	Loop function arguments for Fig. I.136.	233
Table I.28	Arguments for $e_1 \to e_2\gamma$	234
Table I.29	Arguments for loop functions in $e_1 \to e_2\gamma\gamma$	235
Table I.30	Arguments for the loop integrals	237

Part I

INTRODUCTION

1

THE STANDARD MODEL AND ITS SHORTCOMINGS

The Standard Model (SM) of particle physics describes the fundamental particles and interactions. It is a widely used, very successful theory which allows to make predictions with high precision, yet it has some missing pieces. This chapter briefly describes the Standard Model and its shortcomings.

The appeal of the Standard Model is the common description of all forces (except gravity) within one mathematical formalism. Particles and forces observed in nature are described by a common Lagrangian, combining the electro-weak theory and the theory of strong interactions. The Standard Model Lagrangian is symmetric under $SU(3)_c \times SU(2)_L \times U(1)_Y$ symmetry groups. It contains three generations of quarks and leptons and one Higgs doublet. The Yukawa interactions for up- and down-type quarks are different, which leads to flavor violation in the quark sector. For charged leptons there is no mixing like this, so observation of lepton flavor violation would be a clear indication for physics beyond the Standard Model. Chapter 4 sums up some or the experimental efforts.

In addition to the particles, three fundamental forces, strong, weak and electro-magnetic force, are described by the Standard Model, yet gravity, which is much weaker, is not. The forces are mediated by gauge particles, which are γs, Z- and W bosons. Up to now, there is no description of gravity in a renormalizable quantum field theory framework. Furthermore, the Lagrangian does not contain a CP violating term for the strong interactions. But there is no symmetry prohibiting it.

When electro-weak symmetry breaks, and the Higgs doublet acquires a vacuum expectation value, leptons, quarks and gauge bosons obtain masses. Due to the absence of a right-handed neutrino, the neutrinos remain massless. This is in contrast to neutrino oscillations observed in experiment. They give a clear indication for at least two massive neutrinos. So, an extension of the Standard Model is needed to explain the neutrino masses. In Chapter 3 experiments for neutrino oscillation and mass measurements along with mass generation mechanisms are presented.

Furthermore the Standard Model contains many free parameters, which are not fixed by symmetries. For example, there is no explanation why there are three generations of leptons and quarks with quite different mass scales. The difference in interaction strength for the four fundamental forces is also not explained in the Standard Model.

Considering the Higgs mass, there are in principle large radiative

corrections which exceed the observed Higgs mass by many orders of magnitudes. An exact cancellation is needed to obtain the correct mass. In some extensions, like Supersymmetry, this appears naturally by the introduction of new fermionic and bosonic degrees of freedom. Based on cosmological observations, some are summarized in Chapter 2, the Universe does not only consist of baryonic matter, which is described by the Standard Model. Yet there is strong evidence for the existence of a new type of matter, named dark matter. The Standard Model itself does not contain a suitable candidate to reproduce all observations. In order to fit them, an extension is needed. There are many different approaches, which explain dark matter. In Chapter 5 few models for a minimal extension of the Standard Model are portrayed. In addition to dark matter, they also contain radiative neutrino masses. This makes them quite interesting, as two open issues can be explained simultaneously. The investigation of two models regarding dark matter, neutrino masses and lepton flavor violation is the focus of this work.

Part II

THEORETICAL AND EXPERIMENTAL FRAMEWORK

2 DARK MATTER

This chapter is organized as follows: first, evidence for dark matter is presented in Section 2.1, starting with the first hints, followed by observations of galactic rotation curves and gravitational lensing. Then, the results from the cosmic microwave background, structure formation and N-body simulations are shown.
Next comes a short overview of potential dark matter candidates in Section 2.2. Experimental searches for dark matter are presented in Section 2.3, starting with direct detection experiments, followed by indirect searches and collider searches. Finally, calculations regarding relic density and detection cross sections are shown in Section 2.4.

2.1 EVIDENCE

One of the missing pieces to understand our Universe is dark matter. There is plenty of evidence for its existence. However, it has not been directly detected, yet. Over the past years, cosmological surveys [1, 2] have revealed that only around 5% of our Universe is made of ordinary baryonic matter. Up to 25 % of our Universe consists of dark matter, a non-baryonic kind of matter, which remains invisible up to now. The rest of the Universe's energy content, called dark energy, is even more mysterious. Only little is known about dark energy.
As dark matter seems not to emit light in any form, all evidence is based on its gravitational interaction. Hints for the existence of dark matter can be found on very different scales throughout the Universe.

2.1.1 *First evidence*

First glimpses of dark matter occurred in the early 1930s. Both J.H. Oort [5] and F. Zwicky [6] made observations based on gravitational interactions hinting towards the existence of dark matter. Oort used mass-to-luminosity ratios to estimate the mass within the Milky Way. Redshift measurements of stars close to the Galactic Center led to a velocity larger than the escape velocity of the galaxy. Hence, Oort deduced there had to be an additional matter component, which was non-luminous, in order to make up for the discrepancy. A year later, Zwicky made observations in the Coma cluster. The Coma cluster is a cluster of over one thousand galaxies which is roughly 99 Mpc away from our Earth [7]. Zwicky assumed that the members of the cluster

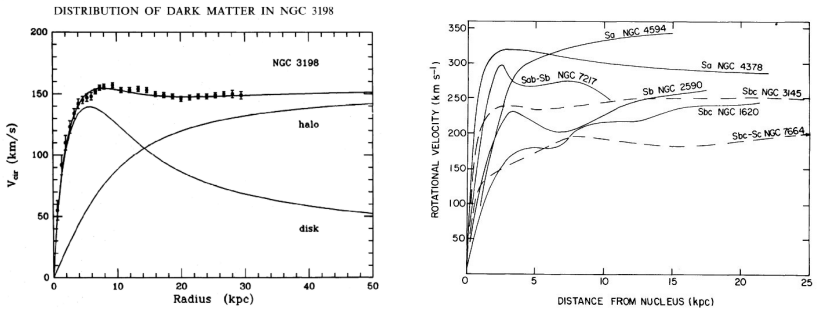

(a) Rotation curve of NGC 3198 taken from [3].

(b) Rotation curve of several galaxies taken from [4].

Figure 2.1: Rotation curves of spiral galaxies.

have reached equilibrium and are gravitationally bound. Therefore, the virial theorem

$$\overline{T} = \frac{k}{2}\overline{V}, \tag{2.1}$$

should apply, where the time averaged kinetic energy $\overline{T}$ is balanced by the averaged potential energy $\overline{V}$. The factor k is equal to -1 for a spherical mass distribution with only gravitational interaction. According to Kepler's third law, the potential energy in a distance R is given by

$$\overline{V} = \frac{-3GM^2}{5R}, \tag{2.2}$$

where M is the total mass of the system and G is Newton's gravitational constant. Further, the kinetic energy in the system can be expressed as

$$\overline{T} = \frac{1}{2}M\overline{v}^2, \tag{2.3}$$

with an average velocity $\overline{v}$. If one assumes that there is no distinguished direction of velocity, it is sufficient to take one specific velocity v and apply

$$\overline{v}^2 = 3v^2. \tag{2.4}$$

According to Eq. 2.1, v can be estimated as

$$v = \sqrt{\frac{GM}{5R}}. \tag{2.5}$$

Zwicky was able to estimate the total cluster mass M by using the mass-to-luminosity ratio $R \approx 0.3\text{Mpc}$. He compared his estimated velocity with redshift measurements of several galaxies in the cluster. The galaxies displayed a too large velocity dispersion to be bound within the cluster. He concluded that there must be more than the estimated luminous mass. A non-luminous matter component was needed in order to stabilize the system.

Figure 2.2: Observation of Abell S1063 by the Hubble space telescope [8] (ESA/Hubble). The image shows ring fragments from gravitational lensing. Source `http://www.spacetelescope.org/images/heic1615a/`

2.1.2 *Rotation curves*

In the 1960s and 1970s V. Rubin and K. Ford Jr. investigated rotation curves of spiral galaxies [4, 9], providing a very strong evidence towards the existence of dark matter. They measured rotation curves and redshifts of stars and H1 regions using the 21-cm hydrogen lines and spectroscopy. Following the lead of Rubin and Kent, a lot of spiral galaxies have been measured. Some results are shown in the right panel of Fig. 2.1. For example in 1985 T. van Albada et al investigated the rotation curve of NGC 3198 [10], which is shown on the left panel of the figure.
According to the Newtonian mechanics, the velocity v of a star on a circular orbit inside a galaxy is given by

$$v(r) = \sqrt{\frac{GM(r)}{r}}, \tag{2.6}$$

The gravitational force acts as the centripetal force. G is the gravitational constant, r is the distance of the star to the center of galaxy and $M(r)$ is the mass enclosed in a sphere of radius r. For the luminous mass one can assume a spherical mass distribution $\rho(r)$, which allows to obtain the mass $M(r)$ by integration

$$M(r) = 4\pi \int_0^r x^2 \rho(x) dx. \tag{2.7}$$

On the outskirts of the galaxy, where almost all mass is enclosed within r, one would assume $M(r)$ to be nearly constant. The rotation velocity is then expected to display a $\frac{1}{\sqrt{r}}$ behavior. The results of Rubin, Kent and many others did not meet this expectation. The left panel of Fig. 2.1 shows the measured rotation curve of NGC 3198. At around 6 Mpc most of the luminous mass lies within the sphere of this radius, yet the velocity does not decrease, but stays at a constant value. From previous considerations, one would expect the velocity

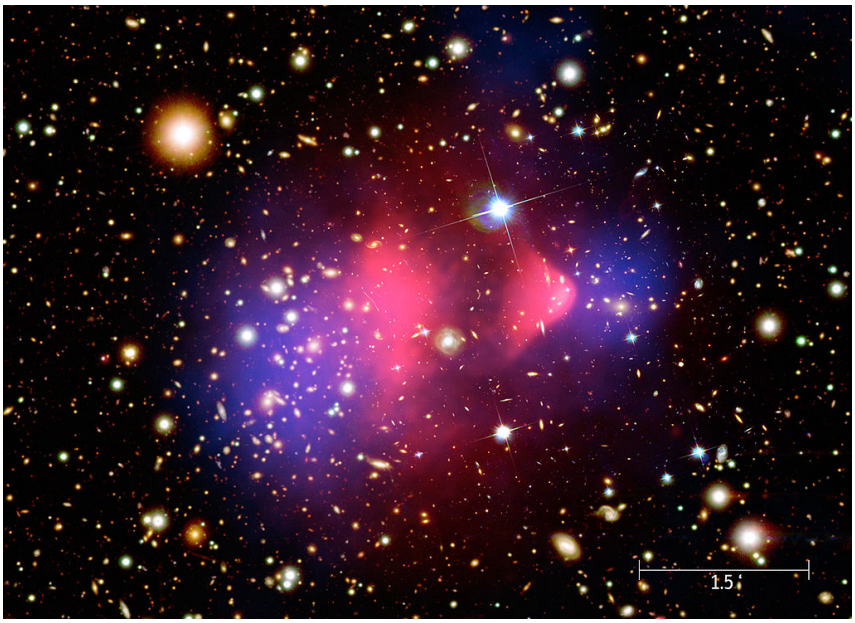

Figure 2.3: Picture with spectrum taken by Magellan and Hubble space telescope [12]. Pink overlay shows the x-ray emission taken by Chandra telescope [13]. Blue overlays are according to mass distribution as recorded by gravitational lensing [14]. Image taken from `http://chandra.harvard.edu/photo/2006/1e0657/more.html`

to behave like the curve labeled disk. One solution to this mismatch is modified Newtonian dynamics (MOND) [11], which proposes a different version of Eq. 2.6 in order to have $v(r)$ constant for large distances. Another option is the existence of additional distribution of non-luminous matter gathered in a halo around the luminous disk. $M(r)$ would not be constant in the exterior regions of the galaxy, but proportional to r when assuming a nearly spherical halo. This depicted by the line labeled halo in Fig. 2.1. As this new matter component could not be luminous, due to its non-observations, one is not able to measure the outer edge of the halo distribution. The observation of constant rotational speed was made for several different galaxies and is not unique to NGC 3198.

2.1.3 *Gravitational lensing and the bullet cluster*

Most hints of dark matter stem from its gravitational interaction. As it does not interact electro-magnetically, this is the only way to infer its existence. As known from general relativity, light gets deflected by massive objects. The more massive an object is, the more the path of light gets altered. It is possible to obtain distorted or enhanced images of light sources beyond heavy matter accumulations along the line of sight. This effect is called gravitational lensing [15, 16]. Gravitational lensing can be used to look for non-luminous matter distributions.

Fig. 2.2 shows an image of Abell S1063 taken by the Hubble space telescope [**Abell2016**]. One can see circular shaped fragments of Einstein rings from background galaxies. The light of these galaxies has been bent by massive foreground objects.
A first idea was to look for massive astrophysical compact halo objects (MACHOs) [17, 18], large, dark jupiter-like objects made from baryonic matter. These MACHOs were thought to be an explanation for dark matter. The MACHO surveys using gravitational lensing did not yield enough objects to explain all dark matter evidence. The MACHO abundance is way too small to account for all observations. Also it would not explain evidence from structure formation or the cosmic microwave background.
The most recent evidence of dark matter comes from the investigation of the ongoing cluster merger 1E 0657-558, which is also called the bullet cluster [14]. The bullet cluster is located around four billion light years from our solar system. Recently, about 100 million years ago, a smaller cluster started to cross a larger cluster forming the now observed structure. Fig. 2.3 shows an image of the cluster. The visible spectrum is taken by the Magellan and Hubble telescopes [12]. Pink overlays are from X-ray emission as recorded by the Chandra satellite [13]. Blue regions correspond to matter distribution as determined by gravitational lensing [14]. The visible spectrum shows the galaxies and stars being mostly concentrated in the two former cluster centers. As these objects are rather sparse within a cluster, they simply passed through each other without interacting. The interstellar gas clouds are visible in the X-ray spectrum. They were stripped of the former centers, when the crossing started. The dense gas clouds interacted with each other and slowed down. In this process the smaller cluster on the left formed a shock front shaped like a bullet which gave the merger its name. Naively one would expect, that a marginal part of the mass is centered around the gas clouds in between the galaxy accumulations. Yet, the gravitational lensing survey reveals, that most of the matter is found around the galaxies. MOND theories could not explain this observation, therefore this is a very strong evidence in favor of dark matter. It also indicates that the self-interaction of dark matter must be very limited in order to let the dark matter halos pass each other unaffected. Similar observations have been made in other cluster mergers e.g. [19, 20].

2.1.4 *Cosmic microwave background*

One of the most compelling indirect pieces of evidence for dark matter is found in the measurement of the cosmic microwave background (CMB). It is a nearly uniform background of photons at a temperature of around T = 2.725 K as measured by FIRAS on the COBE satellite [24–26]. The CMB originated at the time of recombination when the

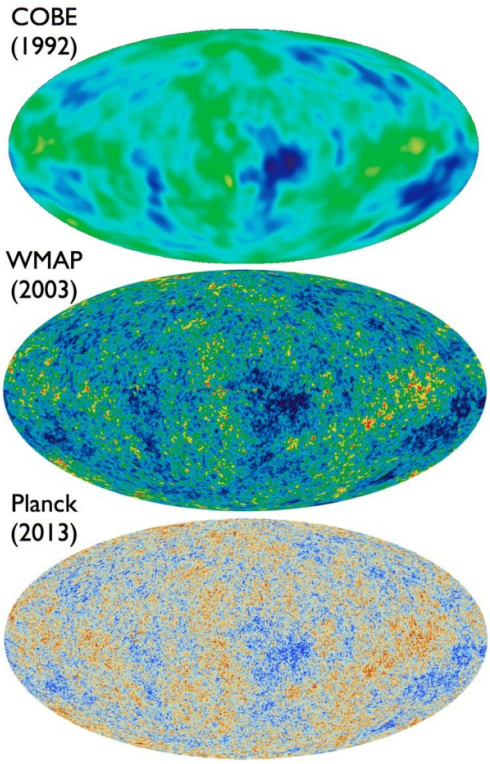

Figure 2.4: Anisotropies in the cosmic microwave background as seen by COBE [21], Planck [1] and WMAP [22, 23] over the years. Credit: NASA/COBE/DMR; NASA/WMAP science team, ESA and the Planck collaboration

Universe was around 3.8×10^5 years old. The CMB was released as photons decoupled from thermal equilibrium with matter. The ongoing expansion of the Universe shifted the photon wavelength after the surface of last scattering, such that it is nowadays in the microwave region. The CMB carries an imprint of primordial density fluctuations by means of the non-integrated Sachs-Wolfe effect [27]. At the time of decoupling over- and under dense regions shifted the wavelength of the photons. The existence of the background radiation was predicted by Gamov [28] and Dicke [29] in the 1940s. After its first measurement by Penzias and Wilson [30] many more observations were made. For example the Cosmic Background Explorer (COBE) [21] the Wilkinson Microwave Anisotropy Probe (WMAP) [22, 23] and the Planck satellite [1] refined its measurement over several decades. Their results on the temperature fluctuations of the CMB are shown in Fig. 2.4. In order to look only at the background radiation, it is necessary to subtract all kinds of foregrounds [31]. One also has to take into account the integrated Sachs-Wolfe effect [32]. The effect describes how the photon wavelength is altered in a time dependent gravitational potential. Entering a potential well shifts the wavelength of a photon. When the photon leaves the well, due to the spatial expansion, the gravitational potential has flattened, though, the initial shift is

not fully compensated. After treating all possible effects, the CMB is a highly uniform background radiation. The fluctuations are on the scale of 30 μK. This smoothness of the CMB leads to theories of inflation in the early Universe. Otherwise there is no chance that distant regions of the Universe could have been in causal contact in order to smooth the density and thus temperature fluctuations. An era of inflation is capable to explain the smallness of the temperature fluctuations. Starting with a map of these fluctuations, as shown in Fig. 2.4, following the considerations in [32–34], one can define

$$\Theta(\hat{n}) = \frac{T(\hat{n}) - \langle T \rangle}{\langle T \rangle} \tag{2.8}$$

which describes the deviation from the average temperature $\langle T \rangle$ along a certain direction $\hat{n}$. $\Theta(\hat{n})$ is defined to be a dimensionless quantity. One can expand this quantity in surface spherical harmonics

$$Y_{lm} = \sqrt{\frac{2l+1(l-m)!}{4\pi(l+m)!}} P_l^m(\cos\theta) e^{im\phi}, \tag{2.9}$$

which form an orthonormal set with P_l^m being the Legendre polynomials. The fluctuations from Eq. 2.8 can then be expressed as

$$\Theta(\hat{n}) = \sum_{l=0}^{\infty} \sum_{m=-l}^{l} a_{lm} Y_{lm}(\hat{n}). \tag{2.10}$$

Where the coefficients, also known as multipole moments, can be obtained by

$$a_{lm} = \int \Theta(\hat{n}) Y^*_{lm}(\hat{n}) d\hat{n}. \tag{2.11}$$

One can average over all modes m from $-l$ to l, to obtain the power spectrum

$$C_l = \frac{1}{2l+1} \sum_{m=-l}^{l} \left\langle |a_{lm}|^2 \right\rangle. \tag{2.12}$$

The power spectrum is shown in Fig. 2.5 as a function of multipole moment l. The multipole l corresponds to a specific angular size in 2d surface plots. One can then use cosmological models to fit the power spectrum. The specific shape of the power spectrum is due to baryon acoustic oscillations, which where oscillations moving at the speed of sound in the early Universe's baryon-photon plasma. Before the time of recombination, radiation and baryonic matter have been in thermal equilibrium. Over dense regions in the diffuse plasma have a larger gravitational potential. They start to attract more matter which accumulates into an even deeper potential. The radiation pressure from photons acts as a restoring force, counteracting the gravitational

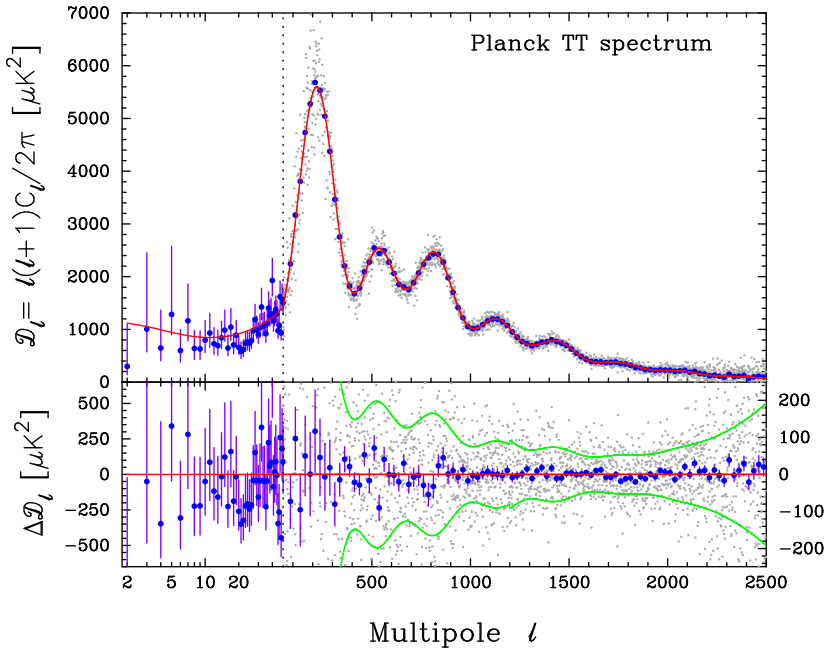

Figure 2.5: The figure shows the angular power spectrum of the CMB anisotropies together with the best fit in the ΛCDM model. Figure taken from [1].

collapse. The restoring force is strong enough to drive smaller structures apart. This is called Silk dampening [35] and it is observed for larger multipoles in Fig. 2.5. After a big initial peak, followed by two smaller ones, the rest of the power spectrum only shows small features. The interaction of gravitational forces and radiation pressure leads to oscillating matter clouds. After the decoupling of photons, the oscillation stops and the density fluctuation is transfered to the photon wavelength by the non-integrated Sachs-Wolfe effect [27]. The largest peak in the power spectrum at around $l = 200$ corresponds to the largest matter cloud which could oscillate once. One can conclude, that the Universe is flat from the position of this first peak as open or closed geometries would have changed the angle under which it appears. Furthermore, the power spectrum reveals the amount of gravitationally interacting matter as opposed to matter experiencing the radiation pressure from photons. One can use a ΛCDM model, a cosmological model containing cold dark matter and dark energy (Λ), to fit the power spectrum. This allows to conclude, that the baryonic matter density is about $\Omega_B h^2 = 0.02229 \pm 0.00017$, whereas there must be a huge amount of non-baryonic but gravitationally interacting dark matter with an abundance of $\Omega_{DM} h^2 = 0.1199 \pm 0.0022$.

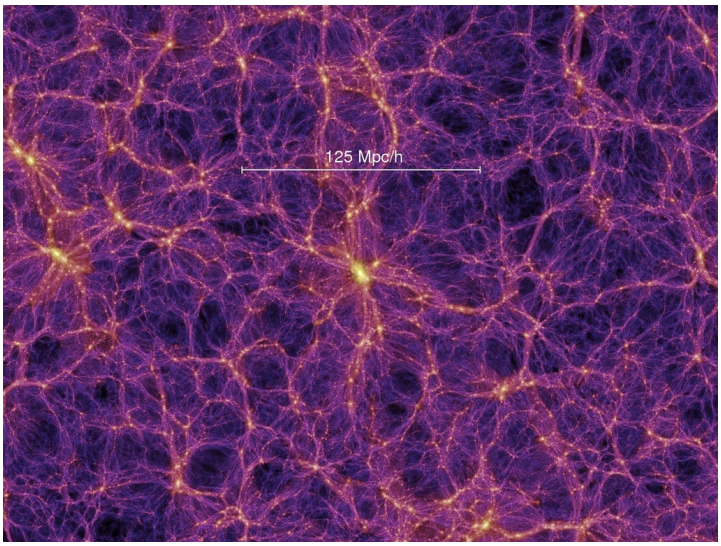

Figure 2.6: Simulation of structure formation with dark matter done by the VIRGO collaboration [36]. The figures are public at `https://wwwmpa.mpa-garching.mpg.de/galform/virgo/millennium/index.shtml` (14/Mai/2018)

2.1.5 *Structure formation and N-body simulations*

The formation of baryon acoustic oscillation within the early Universe indicates that dark matter has a strong impact on structure formation, due to its gravitational interaction. The density perturbations of matter, which are imprinted into the CMB, can act as a starting point for structure formation. One approach is to assume dark matter clumped first, forming gravitational wells in which baryonic matter could be trapped afterwards. The density fluctuations could grow over time to form the structures observed today.
Redshift surveys like the 2dF Galaxy Redshift Survey [37, 38] investigate the structure in the Universe. They observe a highly anisotropic and rather coarse distribution as shown in Fig. 2.7. With modern computers the process of structure formation is simulated, as for example in the Virgo collaboration [36] conducting the Millennium simulation [39]. It turns out, that cold dark matter is a necessary ingredient in order to reproduce the observations. An example is shown in Fig. 2.6. Cold in this sense means, that the dark matter is non-relativistic at the time of structure formation. As it has a short free streaming length, the dark matter clumps easily, forming spherical halos around galaxies. This supports the idea of dark matter halos being responsible for the observed galactic rotation curves. However, the N-body simulations yield much more small scale structures like dwarf galaxies than observed in nature. This is called the missing satellite problem [40, 41]. It could be alleviated by adding hot or warm dark matter, which is not non-relativistic at the time of structure formation. Yet,

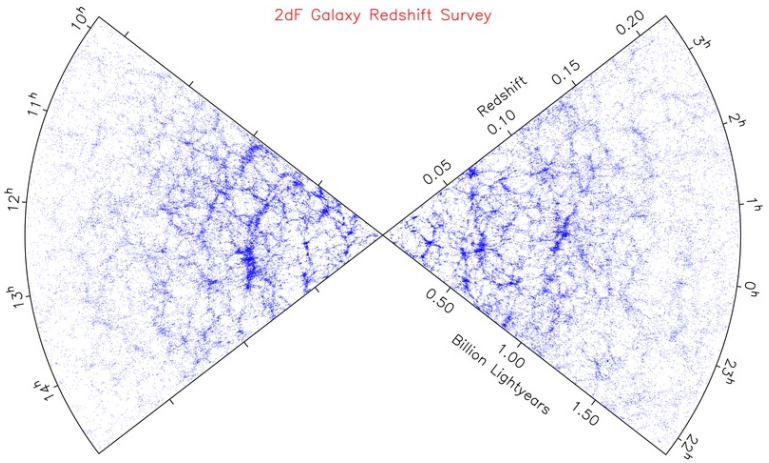

Figure 2.7: Data taken by the 2dF Galaxy Redshift Survey to investigate the larges scale structures in the Universe. Figure is taken from `http://www.2dfgrs.net/`

this would be in contrast with the ΛCDM model used to fit the CMB power spectrum.

This catalog of dark matter evidence is by no means complete, yet it shows that hints towards dark matter can be found on very different scales and time periods throughout the Universe. Up to now one is in need for an explanation of this new kind of matter. There are several candidates and theories which try to explain the observations. Many experiments are looking for the direct or indirect detection of dark matter.

2.2 CANDIDATES

There have been several ideas to explain the observations summarized in the previous sections. This includes theories for massive objects like MACHOs [42] or modified gravitational dynamics like MOND [43]. Here, we are mostly interested in particle dark matter. Which properties should a dark matter candidate have? First, it should be dark, which means non-luminous. If it has an interaction with photons, it has to be suppressed. The dark matter particle is an electrically neutral color singlet as no bound states with dark matter are expected. Furthermore, it should be non-baryonic as required by the CMB observations. Dark matter should be stable or at least have a lifetime which is much larger than the age of the Universe. Structure formation mostly supports cold non-relativistic dark matter, even though ideas for warm dark matter were presented, for example in [44–46]. A very appealing candidate for dark matter is a so called **w**eakly **i**nteracting **m**assive **p**article (WIMP). Particles with

weak scale cross sections like WIMPs yield relic densities which are in good agreement with WMAP and Planck measurements [47] as

$$\Omega_{DM} h^2 \propto \frac{3 \times 10^{-27} cm^3/s}{\langle \sigma v \rangle} \propto \mathcal{O}(0.1), \tag{2.13}$$

arrives at the correct relic density for masses around 100 GeV. There is no WIMP in the Standard Model. The only neutral SM particle, which fulfills most dark matter requirements, is the neutrino. However, neutrinos are way too light, hence not cold and not compatible with the structure formation requirements. Neutrinos are also not abundant enough to account for the entire dark matter relic density. Despite WIMP dark matter, there are also other theories like universal extra dimensions [48] in which dark matter is associated with for example the lightest Kaluza-Klein particle. Other non-WIMP dark matter candidates are axions. Axions are hypothetical particles introduced to solve the strong CP problem [49, 50], since no magnetic dipole moment of the neutron has been observed up to now. Axion searches are conducted with the Primakoff effect on virtual photons in strong magnetic fields. One specific experiment is the light through the wall experiment [51].

WIMP dark matter models offer a broad variety of realizations. For example WIMP dark matter can be featured as the lightest neutralino in supersymmetric models (see e.g. [52]). Supersymmetry (SUSY) is a space time symmetry connecting fermions and bosons. Each Standard Model particle is associated with a supersymmetric partner. Bosons obtain fermionic and fermions obtain bosonic partners. Both degrees of freedom are linked by at least one SUSY generator. A minimal realization of supersymmetry is the MSSM, the minimal supersymmetric Standard Model [53–55]. It contains the Standard Model as a low energy limit. Furthermore, the MSSM allows for unification of gauge couplings at high scales. This is appealing since it allows the description of all interactions in the same fashion with one coupling.

The first supersymmetric Lagrangian was formulated by J. Wess and B. Zummino [56]. SUSY naturally contains a dark matter candidate (WIMP): the neutralino, which is a mixture of the wino, bino and higgsino, the superpartners of the gauge bosons and Higgs bosons. In MSSM models, which feature R-parity conservation, the neutralino is stable. R-parity is originally introduced to prohibit proton decay. R-parity is a $\mathbb{Z}_2$ symmetry under which all SM particles are even and all SUSY particles are odd. The entire MSSM features a lot of free parameters. It is convenient to reduce the number of free parameters. A lot of investigations have been done regarding dark matter in supersymmetric frame works either theoretical as for example [57, 58] or experimental at LHC etc. [59–62]. As no SUSY particles have been observed yet, SUSY has to be spontaneously broken. Otherwise, the superpartners would have the same mass as their SM partners and would have been found.

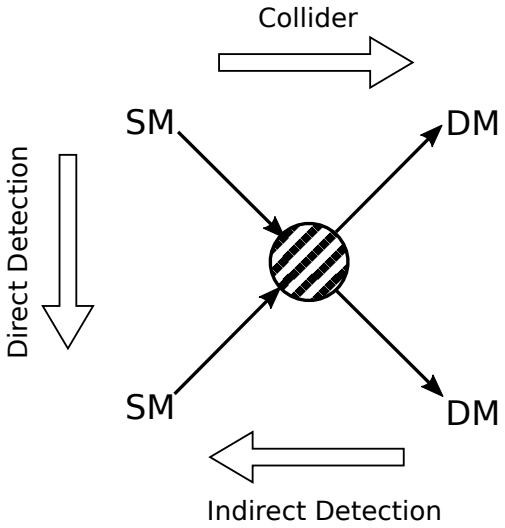

Figure 2.8: Schematic view of dark matter interactions. Taken from [75]

Despite looking at rather large frameworks like SUSY, it is possible to make a minimal extension of the SM in order to provide a dark matter candidate. These minimal models only add few new fields and symmetries e.g. extra U(1) [63], $\mathbb{Z}_2$ or $\mathbb{Z}_n$ [64] to the SM in order to achieve either one ore several stable dark matter candidates. It is easier to analyze the impact of new symmetries and particles in the minimal approach than in complex theories like SUSY.
A broad range of minimal models has already been investigated. One extensively studied model is for example the inert Higgs models [65, 66], which extends the SM by one or more scalar doublets along with an extra $\mathbb{Z}_2$ symmetry. The new doublets are odd under this symmetry. Thus, these models feature scalar dark matter. Other minimal models extend the SM by a singlet fermion dark matter particle – see [67, 68] or a scalar allowing for singlet dark matter [69]. There are also plenty of models featuring doublet fermion or doublet scalar dark matter [70]. In addition there are models with fermionic and scalar dark matter, as well as mixed dark matter [71]. A lot of minimal models are so called Higgs portal models [72–74] in which only the Higgs boson links the dark matter to the Standard Model. In this work minimal models containing additional scalars and fermions as well as radiative neutrino masses are analyzed. The models are introduced in Chapter 5.

2.3 EXPERIMENTAL SEARCHES

In the following sections different searches for dark matter will be presented. The focus is on WIMPs under the assumption that they interact with Standard Model particles in a specific way beyond pure gravitational interactions. The experimental searches can be divided in three categories: Direct detection, indirect detection and collider

searches. All three types of searches exploit the interaction of dark matter and Standard Model particles as shown schematically in Fig. 2.8. Direct detection experiments look for signals from dark matter nucleus interactions (DM SM $\rightarrow$ DM SM) where dark matter scatters off of some target material. Indirect detection experiments search for signatures from dark matter annihilations in the Universe, mostly in the center of the galaxy or around other massive objects. Colliders try in Standard Model particle collisions to produce dark matter. The creation of dark matter particles might lead to specific signatures.

2.3.1 *Direct detection*

A flux of dark matter can be explained, when assuming our galaxy is embedded into a dark matter halo, similarly to the considerations from rotational curves. This would imply, that Earth is passing through the local dark matter halo, experiencing some kind of WIMP wind, when it orbits the Sun. In this WIMP wind it is possible to look for dark matter interactions with nuclei from target materials. The interaction can lead to a nuclear recoil, resulting in a measurable signal. A possible signature is a direct signal, since any interaction induced by the dark matter flux through the detector would give an immediate signal. Another option is to look for annual modulated signals.

The solar system together with Earth is moving at about 220 km/s with respect to the Galactic Center [76] see Fig. 2.9. The local dark matter density ρ_{DM} surrounds the complete solar system, resulting in a flux of dark matter particles passing through it. Under the assumption of ρ_{DM} being approximately 0.3 GeV/cm^3 [77], the expected WIMP flux is around $10^5 \frac{100GeV}{m_{DM}} s^{-1} cm^{-2}$ [78]. Hence, uncertainties on ρ_{DM} translate to uncertainties within any measurements. Therefore, it is necessary to work within a specific framework, which should be as model independent as possible to yield comparable results. Annual modulations are related to Earth's movements. As Earth orbits the Sun at an angle of around 60° with respect to the galactic plane, the WIMP flux is either maximally enhanced, as the velocities of Earth and Sun align, or the flux is decreased, when both velocity vectors are anti-parallel. This results in the annual modulation of the flux being maximal in December and minimal around June. As Earth itself is rotating, it is also possible to investigate the directionality of the signal.

Dark matter particles scattering off of target nuclei can produce signals in three different channels as summarized in Fig. 2.10. The three main channels are heat, ionization and scintillation. Within a solid target, phonons could arise from the recoil or in general, the deposited energy can translate to thermal energy. Dark matter nucleus interaction deposits energy within the target. Suitable materials can pro-

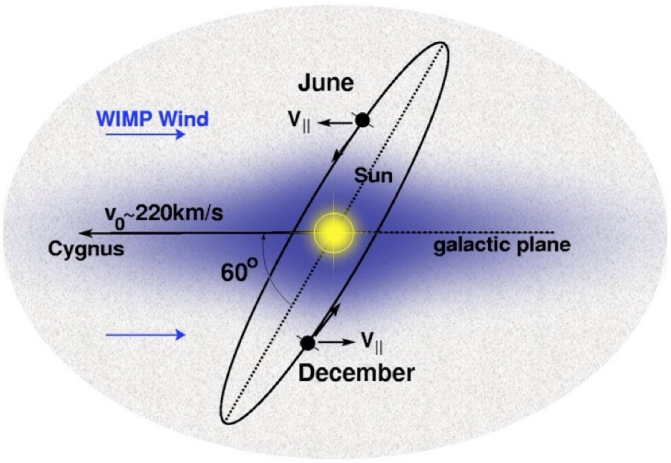

Figure 2.9: Sketch of Earth passing through the dark matter halo of our galaxy. Image taken from `https://www.hep.shef.ac.uk/research/dm/intro.php`.

duce ionization. For example in semiconductors, the charge creation might only need a few eV of energy. De-excitations of the material and charge recombination can lead to scintillation. There are many different direct detection experiments looking in one or two of these channels for dark matter. Some of them are presented in this section, focusing on the different detector techniques. The overview is by no means exhaustive.

In general, dark matter experiments need to have low energy thresholds and low background to be able to detected the small nuclear recoil caused by dark matter interactions. A large target mass is desirable in order to enhance the exposure and probe smaller interaction cross sections. Most of the experiments are based underground and shielded heavily to reduce background from cosmic rays and other sources. Their materials are screened and selected carefully to minimize intrinsic backgrounds as much as possible. The most efficient experiments feature dual channel searches, because it allows for better background rejection. If it is possible to distinguish between electron and nuclear recoil, which differ in ionization density and efficiency, WIMP interactions (nuclear) can be separated from background events (electron).

The next paragraphs, based on [79], introduce some experiments utilizing one channel searches and later dual channel searches are presented.

SCINTILLATION

Experiments like SABRE [81], DAMA/LIBRA [82, 83] and its predecessor DAMA [82, 84] look for scintillation signals. DAMA/LIBRA uses Sodium Iodine (NaI) crystals at room temperature which are ultra low in radioactivity as a target. SABRE also uses NaI crystals sur-

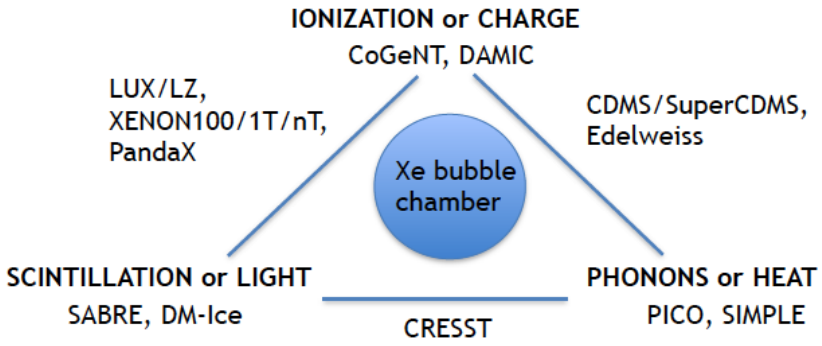

Figure 2.10: Sketch of the three possible signals from dark matter,heat, ionization and scintillation. Figure taken from [80].

rounded by an active scintillation veto. The crystals are doped with impurities to enhance the light yield and shift the scintillation wavelength, making the crystals more transparent for the signal. Larger target masses can be achieved by stacking several crystals. The advantage is the simplicity of the detector, but as only one channel is considered, there is no background rejection from electron recoils possible. Therfore, these experiments look for an annually modulated signal which matches the expected frequency from the WIMP flux.
Another detector type focusing on scintillation signals from dark matter, are single phase liquid noble detectors like DEAP [85], CLEAN [86] and XMASS [87]. They utilize spherical containers filled with liquid noble gas, which is monitored by photo sensitive detectors, mostly photo multiplier tubes (PMTs). The advantage of noble gases is the rather large atomic number and the possibility for larger target masses. The spherical set up of the detectors yields a good coverage. Although, the single channel read out leads to larger issues with intrinsic backgrounds and fiducialization than dual phase detectors.

IONIZATION

CoGent [88] is a cryogenic detector at Soudan Underground Laboratories which uses single Germanium crystals cooled with liquid nitrogen. The used Germanium allows for high radio purity, but the scalability is limited, as the noise grows with crystal volume. When a WIMP hits the detector, the deposited energy translates to ionization. The rise time of the signal allows to reject events which happened close to the detector surface and are much likely due to background interactions.

PHONONS/HEAT

Bubble chambers or droplet detectors like PICO at the SNOLAB underground laboratory in Sudbury [89] or SIMPLE [90] at LSSB look for dark matter signals in the heat channel. The detectors contain superheated liquid or superheated liquid droplets embedded in a gel

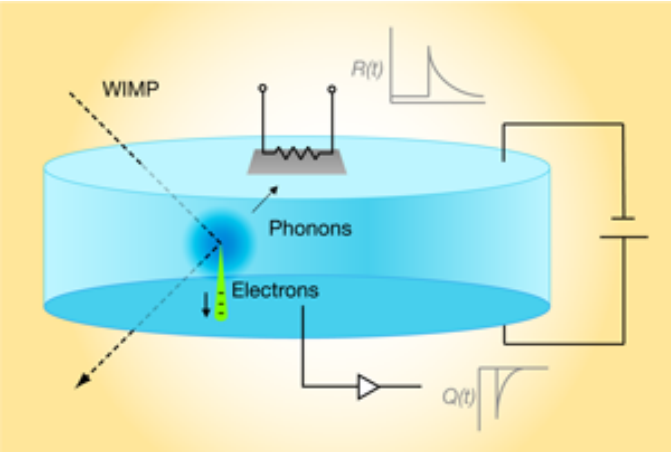

Figure 2.11: A simple sketch of a CDMS detector element. Image taken from `https://physics.aps.org/articles/v2/2`, Illustrator Alan Stonebraker.

matrix. A WIMP depositing energy causes the superheated fluid to undergo a phase transition ,hence gas bubbles emerge. The resulting signal is either acoustically or optically monitored. For temperatures close to the phase transition, background is low and the energy threshold is adjustable by detector temperature.
The following paragraphs will describe some dual channel experiments in more detail adding schematic sketches of the detector functionality.

IONIZATION AND PHONONS

Cryo bolometer like CDMS and SuperCDMS [91–93] or EDELWEISS [94, 95] are capable of detecting both ionization and heat signals from nuclear recoils. CDMS and SupderCDMS are located at the Soudan mine, EDELWEISS is at the Modane Underground Laboratory.
Both SuperCDMS and EDELWEISS use similar detector layouts consisting of an array of semi-conductors cooled down to mK temperature. The semi-conductors are Germanium and silicon crystals. A schematic view of a CDMS detector element is shown in Fig. 2.11. The low temperatures are necessary to reduce the thermal noise, otherwise dark matter signals could be shadowed. In order to achieve larger target masses, several crystals have to be stacked together, as the crystals themselves are size limited. The crystals are semi-conductors, so nuclear recoils can create electron-hole pairs and phonons. The phonons are detected by transition edge sensors (TES) [96]. The TES is a super-conductor, which is close to the phase transition between its normal and its superconducting state. Temperature changes allow for the phase transition to happen. Resistance changes immediately, which can be related to the deposited energy. The ionization signal is enhanced by an amplifier. The amplifier is an interleaved electrode at the top of the crystals. This electrode layout allows for identification

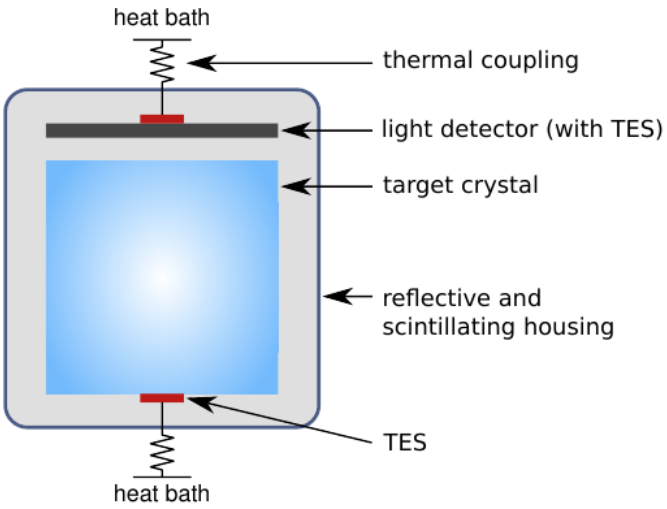

Figure 2.12: Picture of a CRESST calorimeter element. Image taken from http://www.cresst.de/cresst.php

of surfaces events. Surface events are rejected in order to reduce background. The rise time of the charge and the pulse shape of the heat signal allow for further background reduction.

SCINTILLATION AND PHONONS

Similarly to SuperCDMS and EDELWEISS, the CRESST [97–99] experiment is a cryogenic calorimeter. However, instead of ionization the scintillation signal is used. The detector, as shown in Fig. 2.12, consists of scintillating Calcium Tungstate crystals ($CaWo_4$), which are cooled down to mK temperatures, and silicon detectors. Most of the deposited energy translates to phonons. Again, TES are used to detect this signal. The rest of the energy causes scintillation light, which is absorbed by silicon detectors. Comparing a scintillation and phonon signal allows for electron recoil identification. Further, the detector is surrounded by heavy shielding and an active muon veto.

SCINTILLATION AND IONIZATION

A huge and successful class of direct detection experiments uses scintillation and ionization signals in dual phase time projections chambers (TPCs) with liquid and gaseous noble gas. For example there is LUX [100] at the Homestake mine, PandaX [101, 102] at China Jinping Underground Laboratory (CJPL) and XENON [103, 104] at Laboratori Nazionali del Gran Sasso (LNGS). All three use Xenon as the target material. The dual phase TPCs consist of a cryostat filled with liquid Xenon, topped by a gaseous layer as shown in Fig. 2.13. The cryostat is surrounded by heavy shielding, which could include a water Cherenkov detector to reject muons from cosmic rays.
Dark matter interactions cause nuclear recoils and deposit energy within the liquid Xenon. The recoil causes scintillation and ioniza-

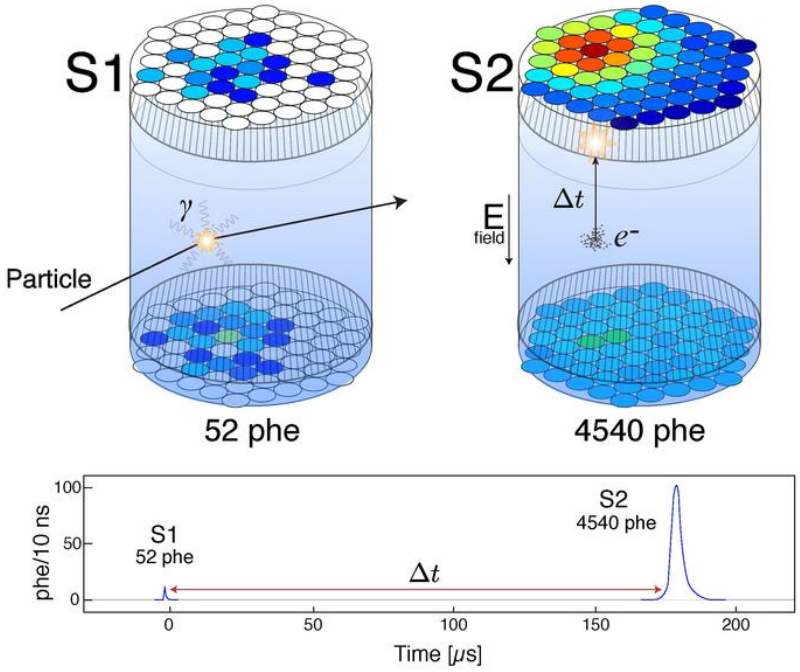

Figure 2.13: Schematic view of a dark matter event inside a dual phase liquid noble gas detector. Image taken from `https://en.wikipedia.org/wiki/File:LUXEvent.pdf`

tion. The charges are drifted by electric fields towards the gas phase. A stronger electric field within the gaseous phase acts as an amplifier for the ionization signal. The scintillation light, which is in the UV range, is collected by photo multiplier (PMT) arrays at the top and bottom of the cryostat. The drift time of the ionization allows for z-position reconstruction. The hit pattern of the PMTs determines the x-y-position of the event. This full 3D-position reconstruction can be used to define a fiducial volume, rejecting all events close to the detector surface. Nuclear recoils have a high ionization density, but are not very efficient in ionizing. A lot of charge is recombined to scintillation, whereas electron recoils can cause spatially wide ionization tracks and little scintillation. Hence, the comparison between the prompt scintillation signal (S1) and the ionization signal (S2) allows to discriminate between electron and nuclear recoils. Another appeal of dual phase TPCs is the large target mass and the scalability. This allows to translate the detector technology to larger targets. In order to have as little intrinsic background as possible, the Xenon needs to be pure.

Fig. 2.14 shows schematically the different background (red) and signal (blue) regions for various detectors. In the left panel the regions are shown for a cryogenic bolometer, e.g. with Germanium crystals. The bands are narrow and there is also little overlap, hence good discrimination is possible. In the middle panel the regions for dual

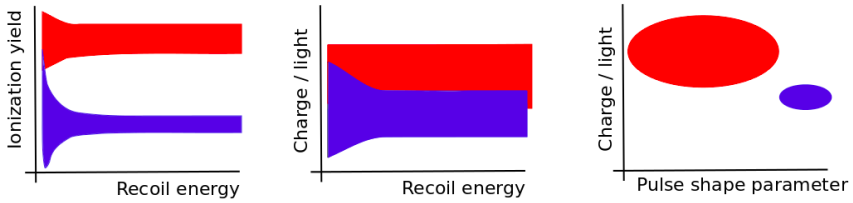

Figure 2.14: Simplified image of signal (blue) and background (red) regions within different dark matter direct detection experiments. The left panel shows the regions for cryogenic bolometers. Middle panel is the schematic view for liquid noble gas TPCs. The right panel shows the expected signal and background shapes for a liquid single phase Argon TPC. The figures are from [79].

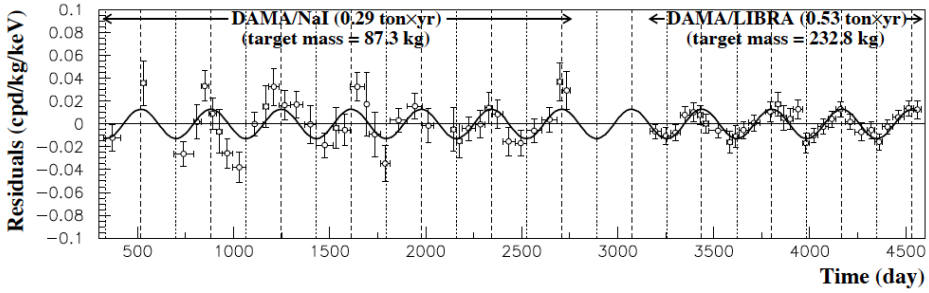

Figure 2.15: Annual modulation measured by DAMA and DAMA/LIBRA. Figure taken from [82]

phase liquid noble gas detectors are shown. The broader bands lead to better acceptance, but they also demand more severe cuts for background rejection. The right panel is for a single phase liquid Argon TPC. It exhibits very good separation, but a very small signal region compared to a large background.
Detector calibration allows to determine the two regions before starting the data analysis. Similarly important is energy calibration, which could be done with neutron sources. Neutrons can induce small nuclear recoils similar to the expected dark matter signals. The different experiments are all very dedicated and operate in a highly competitive field with high demands on background rejection. The experiments DAMA/LIBRA and DAMA observed an annual modulated signal in 1.33 ton year^{-1} exposure [82] as shown in Fig. 2.15. The signal is in the 2 to 6 keV range and its minima and maxima are compatible with the expected flux from Earth's movement through the dark matter halo [105]. The observed signal would either suggest a WIMP mass around 10 to 15 GeV or 60 to 100 GeV [106]. However, all other experiments did not observe a positive signal. There is a strong tension between the results. Since there is no discrimination between nuclear or electron recoil in the DAMA experiment, background rejection is not as easy as in dual channel experiments. Also CoGeNT and others did not find a significant annual modulation signal [107]. Var-

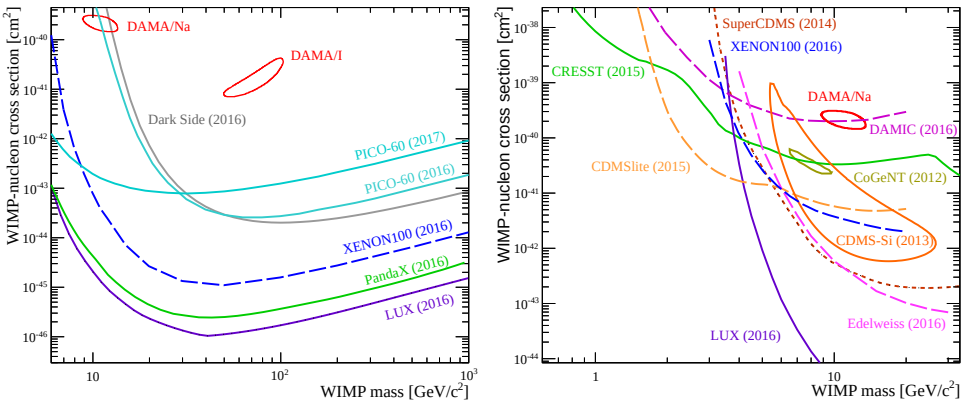

(a) (b)

Figure 2.16: Current limits on spin-independent dark matter direct detection cross sections. The left figure is for high WIMP masses whereas the right panel shows curves for lower WIMP masses. Figures taken from [79]

ious experiments aim at detecting dark matter nucleon interactions with different techniques, which are sensitive for different parameter regions. Fig. 2.16 shows limits on WIMP cross section. The low WIMP mass range is presented in the right panel, the left panel features higher masses. This differentiation is due to different analysis techniques regarding the two mass ranges. Not all experiments show the same sensitivity over all ranges. Different experiments specialize on one of the regions. It might even be necessary to analyze data in different ways, starting from different WIMP masses.
Closed contours shows signal indications, as for example DAMA/LIBRA shown in red, as well as some old results from CDMS (orange) and CoGeNT (green). The latter were not stable against more recent measurements and analysis with different background assumptions. CDMS and CoGeNT tried to reproduce the annual modulation signal, but mostly background effects accounted for the effects. Specifically, they did not confirm the annual modulations observed by DAMA see Fig. 2.15. Some ideas how to resolve this tension are presented in [108–110].

The non-closed exclusion lines give upper limits on the cross section, excluding the parameter region above. Starting with low WIMP (see Fig. 2.16 (b)) CRESST (green) is the most sensitive for lowest masses. CDMSLite (dashed orange) takes over at around 2 GeV and LUX is the most constraining for masses larger than 6 GeV. From the figure one can see, that cryogenic bolometers are efficient at low WIMP masses. Detection at low masses is always difficult due to energy thresholds. The limits go down to 10^{-44} cm^2 in cross section, showing the tension between the signal regions found by DAMA and the exclusion curves from other experiments like LUX, XENON

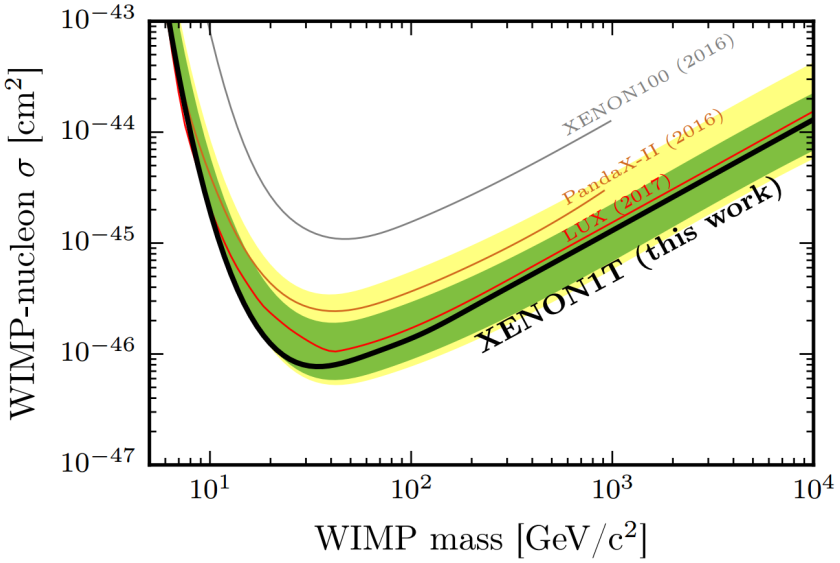

Figure 2.17: Most recent exclusion plots on spin-independent direct detection cross sections .Figure taken from [104]

and EDELWEISS. The larger WIMP mass regions up to 10^3 GeV are dominated by dual phase liquid Xenon TPCs like LUX (violet), PandaX (green) and XENON (dashed blue) detectors. They work best for larger WIMP masses as the target sizes are large and easy scalable for improved sensitivity.

More recent results are in Fig. 2.17, which shows a slight improvement. XENON reaches down to 10^{-46} cm^2 cross sections for WIMP masses around 30 GeV, just below the LUX exclusion line. Older exclusion curves show a huge improvement on sensitivity over time. There is for example over one order of magnitude improvement between the XENON100 results from 2016 and the recent XENON1T limits. The closeness and diversity of experiments shows it is a highly competitive field with quick developments. There are even more measurements coming up and most of the experiments are still taking data.

The presence of different isotopes with unpaired nucleons in target materials offers the opportunity to investigate spin-dependent WIMP nucleon couplings as well (compare Section 2.4.2). Fig. 2.18 shows a larger WIMP mass range under the assumption that dark matter interacts only with protons (left panel) or solely with neutrons (right panel) in the target material. PandaX (green) is most constraining for the neutron case going down to 10^{-40} cm^2 due to a long exposure time. Overall the constraints on neutron WIMP cross sections are dominated by liquid Xenon TPCs. CDMS is up to 4 orders of magnitude worse compared to the TPC results. This is due to some isotopes which naturally occur in Xenon, that are very well suited for spin-dependent WIMP interactions. On the contrary, the proton spin-dependent cross section is dominated by PICO (cyan), a bubble

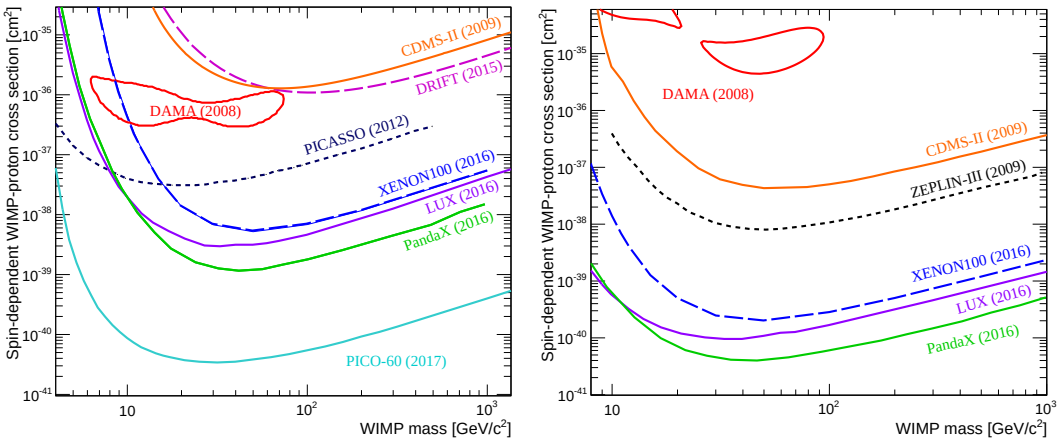

(a) (b)

Figure 2.18: Current experimental limits for spin-dependent dark matter nucleon interactions. The left panel shows the plot for dark matter and proton interaction. The right image is for WIMP neutron interactions. Figures taken from [79]

chamber detector, which excludes cross sections down to 10^{-40} cm^2. The second best results from PandaX are at least 2 orders of magnitude worse.
If any signal is detected, a confirmation within another detector is needed (see DAMA). Hence, it is good to have a rich field with various detection techniques. Even after a discovery is made, different experiments could be used to determine WIMP properties like the precise cross section, mass etc. Future plans for large, ton scale detectors such as LZ [111], XENONnT [112] are already in preparation.

2.3.2 *Indirect detection*

Indirect dark matter searches look for signals from dark matter annihilation. Comparing Fig. 2.8, one can see that indirect searches are complementary to direct searches. Indirect dark matter experiments depend on the thermally averaged annihilation cross section. The cross section includes processes, which also are responsible for the dark matter relic density. Today the dark matter relic density is fairly constant, usually dark matter particles do not meet and annihilate. Therefore, one has to look for places with enhanced dark matter densities in order to obtain measurable signals. Regions with high gravitational potential should accumulate dark matter over time, such that the density is increased. Such regions are for example the Sun, the galactic center and halo as well as dwarf galaxies and galaxy clusters. The dark matter density inside gravitational wells is determined by the dark matter elastic scattering cross section and annihilation rate.

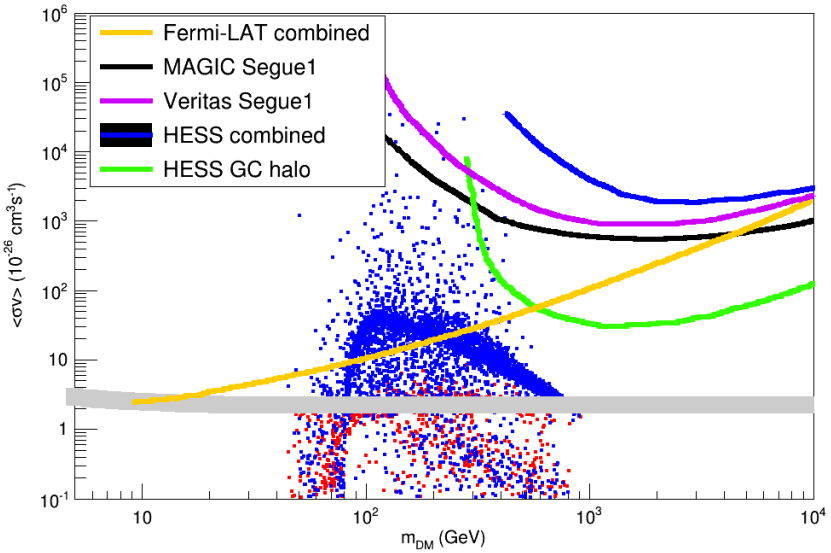

Figure 2.19: Current constraints on dark matter annihilation cross section from different experiments. Figure taken from [113]

Annihilation signals can for example feature γ rays, charged particles or neutrinos. The considerations and data in this section are based on [113].

γ RAYS

γ rays, that are being searched for, cannot come from photons radiated directly by dark matter as its coupling to photons is usually very suppressed. On the other hand, annihilation products like quarks or gauge bosons yield a continuous γ spectrum. Sharp γ lines can be found for direct photon production or from internal bremsstrahlung from virtual particles. These sharp lines give a very clear signal with little background. Typically, backgrounds come from other astrophysical objects like pulsars or diffuse galactic emission. Furthermore, matter affects the γ propagation in the medium.
There are several regions, for example the Sun or the galactic center, which are investigated for γ rays from dark matter annihilation. The galactic center is not easy to observe, as Earth is within the Milky Way. It is best to look at it in the infrared and radio wavelength. The nuclear star cluster at the center seems to consist of visible stars and dust only [114]. However, the presence of a super massive black hole [115, 116] causes a deep gravitational potential. This potential allows for dark matter accumulation. As the dark matter annihilation signal is proportional to the square of the dark matter density, a large density is favored. Yet, there is a huge uncertainty on the inner region of dark matter profiles. It is not resolved if profiles should be cored or cusped. Still, the expected fluxes are high but the galactic center has also a rich astrophysical background.
An option with less background are dwarf galaxies. They are sup-

posed to be dominated by dark matter and one can determine their halo by measuring radial velocities. Besides little background, the expected fluxes are also small.
If the dark matter distribution is known, the observation of galactic diffuse emission can contain annihilation signals. Moreover, there are large uncertainties regarding dark matter distributions within galaxies.
Currently, different types of experiments look for γ rays from dark matter annihilation, for example ground based Cherenkov telescope arrays like VERITAS [117, 118], HESS [119, 120] and MAGIC [121, 122]. The array structure allows for a large target area but brings a small field of view. Hence, they are best suited to search for dark matter with mass above 100 GeV, even if the arrays were not exclusively designed for dark matter searches.
To complement the ground based experiments, there are satellite based experiments looking for dark matter signatures like Fermi-LAT [123]. Satellite experiments have a much smaller effective area than ground based telescopes, but a higher field of view. Fermi-LAT is most sensitive for dark matter masses in a large region between 100 MeV up to 100 GeV. It conducted dark matter searches and found no evidence [124, 125].
The X-ray region of γ rays is probed by satellite experiments like Chandra [126] or XMM-Newton [127]. They detected a 3.5 keV line feature. Even though, other explanations for this line were found [128, 129], it still could be an annihilation product of dark matter as explained in [130–132].
An overview of current constraints on dark matter annihilation cross sections from γ ray searches is shown in Fig. 2.19. It spans from WIMP masses of 10 GeV to 10^4 GeV. The red points are viable regions within the SSM-7 which are consistent with the currently measured relic density. Blue points are associated with relic densities below the observed one. The results from MAGIC (black) [133], VERITAS (violet) [134] and HESS (blue) [135] are from dwarf galaxy observations. They reach down to $10^3 \times 10^{-26} \mathrm{cm}^3 \mathrm{s}^{-1}$. For small dark matter masses, the strongest limits come from Fermi-LAT dwarf galaxy observations (yellow) [136]. In the high mass region above 10^3 GeV the best sensitivity is obtained by HESS [137] observing the galactic halo center.

CHARGED PARTICLE SIGNALS

A promising channel for dark matter annihilation is the production of charged particles. Experiments search for example anti-proton, proton, electron and positron fluxes. In the case of anti-particles the background is low. There are nearly no secondary processes, making this a promising channel. Possible signals show up as excesses in anti-particle fluxes. Currently, PAMELA [138, 139] based on a satellite and

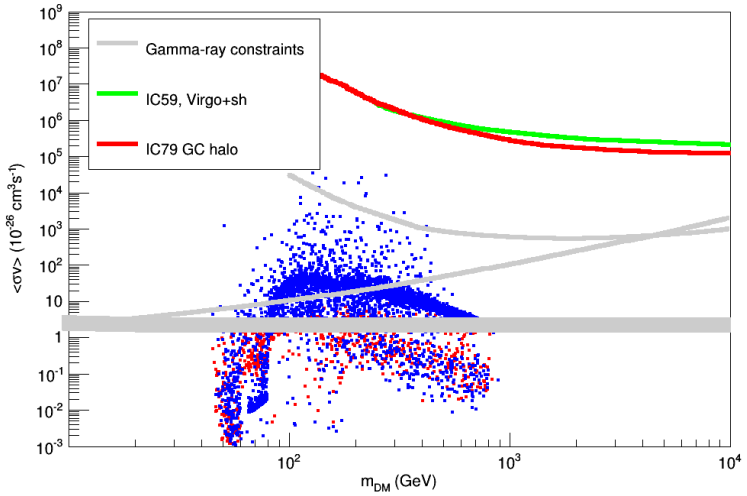

(a) Quark annihilation channel

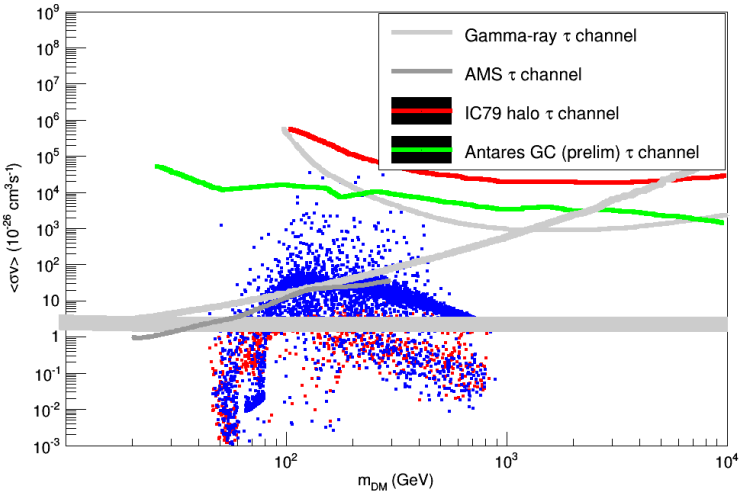

(b) τ annihilation channel

Figure 2.20: Limits on indirect detection of dark matter including neutrino signals. Figure taken from [113]

AMS-02 [140, 141] on the international space station look for charged particle signals. In 2008 PAMELA measured an excess in positron flux, which has been confirmed by AMS in 2013. If the excess is due to dark matter it, would favor dark matter masses in the TeV regions which is quite heavy. However, there are also different explanation for the excess like pulsars or super nova remnants.

NEUTRINOS

In contrast to γ rays and charged particles, neutrinos can travel to the Earth unaffected. Therefore, dark matter annihilating to neutrinos is a promising channel. This paragraph is based on [113, 142].
Similarly to γ rays and charged particle signals, experiments search for signals from regions with enhanced dark matter density like the

Sun. The Sun is rich in hydrogen, enhancing spin-dependent dark matter interactions. The interactions lead to dark matter capture. The capture is due to interactions with nuclei slowing down dark matter until its velocity is below the escape velocity of the gravitational potential. Inside the potential the velocity distribution can be assumed to be Maxwellian up to the escape velocity as dark matter can thermalize by scattering. Consequently, the entire process is determined by the nucleon scattering cross section which is the same as the cross section probed by direct detection experiments.
In the following some short calculations for the dark matter number density within the Sun $n_{DM}^{\odot}$ are described like in [142]. The evolution of the number density $n_{DM}^{\odot}$ is expressed as

$$\frac{d}{dt}n_{DM}^{\odot} = C_{\odot} - A_{\odot}n_{DM}^{\odot 2} - E_{\odot}n_{DM}^{\odot}, \tag{2.14}$$

with the capture rate $C_{\odot}$, the evaporation rate $E_{\odot}$ and the annihilation rate $A_{\odot}$. $A_{\odot}$ scales with the squared number density as two dark matter particles annihilate with each other. The dark matter density can be decreased by evaporation. Scattering within the medium might increase dark matter velocity above the escape velocity. The accumulation and evaporation rate counteract each other. Under the assumption that this process has reached equilibrium, one looks for a stable solution to Eq. 2.14 with a constant dark matter density in the Sun.
The expected neutrino signal is proportional to the given dark matter annihilation rate

$$\Gamma_{\nu\odot} = A_{\odot}\frac{n_{DM}^{\odot 2}}{2}. \tag{2.15}$$

In the case of equilibrium and negligible evaporation compared to the accumulated amount of dark matter, the neutrino production rate becomes

$$\Gamma_{\nu\odot} = \frac{C_{\odot}}{2}. \tag{2.16}$$

This rate only depends on the capture rate C which directly translates to the dark matter nucleon cross section. If evaporation is not negligible, the production rate is suppressed by the evaporation rate.
Currently, IceCube [143, 144] at the South Pole and Antares [145] in Mediterranean sea are looking for ν signals in general and in the context of dark matter annihilation. IceCube uses the antarctic ice as a target, looking for Cherenkov light induced by ν interactions. It has several photo sensors deployed in the ice. Antares similarly uses water as target material, which is observed by optical modules. Fig. 2.20 shows limits on indirect detection including neutrino signals as well as γ ray and antiparticles searches. IceCube [146] and ANTARES [147] observed the galactic halo, and IceCube also investigated signals from

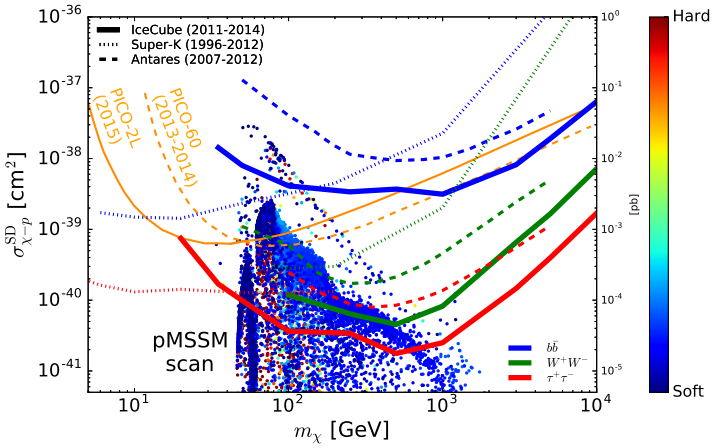

(a) Spin-dependent interaction

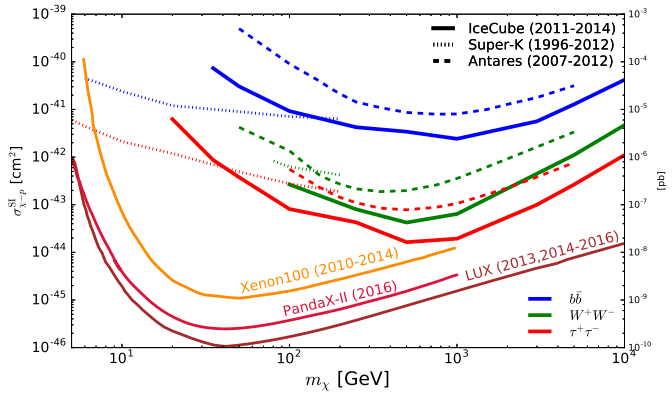

(b) Spin-independent interaction

Figure 2.21: Current limits on dark matter nucleon cross sections including IceCube observations of neutrino signals from the Sun. Both figures taken from [149]. The color bar indicates the main annihilation channel of dark matter. The hard spectrum mostly consist of τ lepton and similar final states.

dwarf galaxies [148]. The top panel displays limits for dark matter annihilation into quarks. In this region the results from IceCube (red, green) are about two orders of magnitude worse than the limits from γ-ray searches (thin gray). On the bottom panel results for dominant annihilation to τ leptons are shown. In this region IceCube is compatible or in some places puts even more stringent bounds for lower dark matter masses than searches focusing on γ-rays. The best sensitivity is achieved for dark matter signals from the Sun, constraining mostly the spin-dependent dark matter cross section.

Fig. 2.21 shows limits on spin-dependent (top) and spin-independent (bottom) dark matter interaction cross sections comparing different types of experiments. The blue points in the top panel correspond to predictions from the phenomenological MSSM described in [149]. The IceCube results are differentiated by color (solid red, green, blue) ac-

cording to the main annihilation channel. As before, IceCube places the most stringent bounds on spin-dependent interactions for dark matter masses above 40 GeV in the τ channel (red). This is due to the fact, that the neutrino production rate depends on the capture rate which is determined by elastic scattering of hydrogen in the Sun. These results are several orders of magnitudes better than the PICO results. Looking to the bottom-panel for spin-independent interactions the neutrino experiments are not competitive with direct detection searches. There is at least one order of magnitude difference.

2.3.3 *Collider searches*

To complement direct and indirect searches, collider searches look for dark matter signatures in collision experiments. This section uses [75] as reference. Particle collisions can produce either dark matter directly or heavier particles subsequently decaying to dark matter. Typical signatures include mono-jets, mono-photons and charged lepton pairs, accompanied by missing transverse energy $\not{E}_T$. When the particles collide, momenta in the transverse plane should cancel, but some collision products can escape undetected, such as dark matter, leading to $\not{E}_T$. Mono-jets or mono-photons can be produced by initial state radiation. The final state can contain several charged leptons.
In principle, experiments collide protons or heavy ions to search for new particles. As a part of the investigation, the data can be analyzed for dark matter signatures. Hadron colliders like Tevatron [150] and LHC [151] use effective field theories (EFT) [152, 153] to conduct dark matter analyses, assuming the experiment probes low energy approximations of some theories. Similar methods can be found in direct detection experiments. Within the effective theories it is assumed that mediator particles are integrated out. Interactions can be described by effective operators. This makes the effective theory only valid up to a certain scale. As collider experiments feature large energies not all EFT approaches are applicable. Besides EFT one can use the so called simplified models [154, 155]. Simplified models allow for model independent comparisons. Within the simplified models the mediators are not integrated out and only renormalizable interactions are considered. Analogous to minimal dark matter models, only few particles and symmetries are introduced to the SM in order to obtain a certain collider signature. For example Higgs portal models (see Section 2.2) are suitable simplified models. Here dark matter interactions are solely mediated by Higgs bosons. If the mediator is not a SM particle, one can also search for signatures of the mediator in collisions. The approach of simplified models is more flexible in producing the different channels and signals for collisions than EFTs.
The large hadron collider LHC [151] collides protons at center of mass

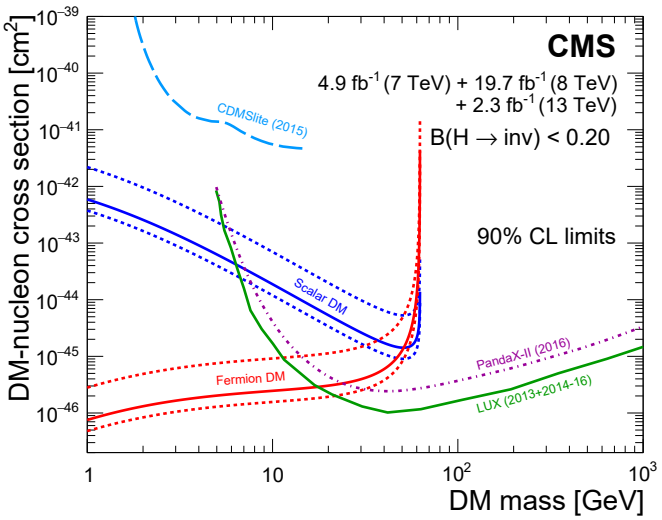

Figure 2.22: Spin-independent dark matter nucleon cross section limits from CMS under the assumption of scalar (blue) or fermionic (red) dark matter being linked to the Standard Model by the Higgs boson in comparison to recent direct detection results. Figure taken from [75]

energy of 7 TeV (2011), 8 TeV (2012) or 13 TeV (since 2015). It has four main experiments investigating the collisions. Two of them, CMS [156] and ATLAS [157], are dedicated to searches for particles, which come from physics beyond the Standard Model (BSM) including dark matter. Up to now, there is no evidence for BSM particles within the LHC data. Everything is in agreement with Standard Model expectations, see for example [62, 158]. Some of the signatures CMS and ATLAS look into are mono-jets or mono-photons occurring with high energy accompanied by back-to-back missing E_T. The main background is from neutrino production due to Z decay together with a jet or a photon. Also leptonic W decays accompanied by a mono-jet or mono-photon, where the charged lepton escapes detector, contribute to the background. If the dark matter mass is high enough, mono-jets can be produced by hadronic decays of associated gauge bosons. Also, the decay of a Higgs boson into dark matter could result in mono-jets and $\not{E}_T$. Such invisible Higgs decays can place severe bounds on BSM physics including dark matter. Another promising channel is the production of heavy quarks like $b\bar{b}$ or $t\bar{t}$, which depends on the mediator particle. This process has a large QCD background but can be discriminated by identifying the quark-antiquark pair. The di-jet signature also is a good handle on BSM physics. It has reduced background at higher transverse momenta p_T. It allows to constrain the mediator and dark matter masses depending on the model.

Fig. 2.22 from [75] shows spin-independent elastic scattering cross sections for dark matter and nucleons within a simplified Higgs por-

tal model for different experiments. Such a model can feature invisible Higgs decays as well as other signatures. Collider experiments place stringent limits by looking for invisible Higgs decays. The red line is the limit obtained by CMS for fermion dark matter, the blue line is for scalar dark matter. In comparison, LUX results from 2016 [159] are shown in green. CMS excludes cross sections down to 10^{-46} cm^2 for fermionic dark matter and places overall the most stringent constraints for dark matter masses below 20 GeV. This low mass region is not so easily accessed by direct detection experiments, so the searches are complementary.
It is also possible to perform a similar analysis in the framework of the MSSM and not only simplified models. In this approach the search for dark matter is accompanied by searches for other SUSY particles. It allows to obtain bounds on SUSY masses. As of now, there have been no observations of supersymmetric particles and the LHC provides stringent bounds on SUSY models [160]. Since there are no observations of supersymmetric partners at the same mass as Standard Model particles, it follows that SUSY must be a broken symmetry. The symmetry breaking explains the mass difference.

2.4 CALCULATIONS

2.4.1 *Boltzmann equation and dark matter relic density*

The evolution of dark matter number density n_{DM} is described by the Boltzmann equation. Integrating this equation allows for the determination of the dark matter relic density Ω_{DM}, which is constrained by the CMB measurements. This section follows [161, 162] in calculating the relic density starting from the time evolution equation for n_{DM}

$$\frac{dn_{DM}}{dt} = -3Hn_{DM} - \langle\sigma v\rangle \left(n_{DM}^2 - \overline{n}_{DM}^2\right). \tag{2.17}$$

In Eq. 2.17 the first term describes the dilution of particles due to expansion of the Universe and the second term takes into account the annihilation and creation of dark matter. $\overline{n}$ is the equilibrium number density, which is defined by

$$\overline{n} = g \int \frac{d^3p}{2\pi^3} \overline{f}(p, T), \tag{2.18}$$

at which g are the internal degrees of freedom and f can be assumed to have a Maxwell-Boltzmann distribution, following

$$\overline{f} \approx e^{-E/T}, \tag{2.19}$$

where T is the photon temperature yielding a Boltzmann suppression factor. Putting this into Eq. 2.18, allows us to simplify

$$\overline{n}_{DM} = \frac{g m_{DM}^2 T}{2\pi^2} K_2 \left(\frac{m_{DM}}{T}\right). \tag{2.20}$$

Here, m_{DM} is the dark matter mass and K_2 is the modified Bessel function of second kind of order 2. In general for modified Bessel functions of the second kind of order i in the limit $x >> 1$, we have

$$K_i(x) \approx \sqrt{\frac{\pi}{2x}} e^{-x}. \tag{2.21}$$

The quantity $\langle \sigma v \rangle$ is the thermally averaged annihilation cross section multiplied by the velocity and is given by

$$\langle \sigma v \rangle = \frac{\int \sigma v e^{-E_i/T} e^{-E_j/T} d^3p_i d^3p_j}{\int e^{-E_i/T} e^{-E_j/T} d^3p_i d^3p_j}, \tag{2.22}$$

for incoming particles ϕ_i and ϕ_j with momenta p_i and p_j and energies E_i and E_j. Performing the integration and using simplifications in the non-relativistic limit, one obtains

$$\langle \sigma v \rangle = \frac{1}{8 m_{DM}^4 T} K_2^2 \left(\frac{m_{DM}}{T} \right) \int_{4m_{DM}^2}^{\infty} \sigma(s - 4m_{DM}^2) \sqrt{s} K_1 \left(\frac{s}{T} \right) ds. \tag{2.23}$$

Here s is the Mandelstam variable – compare Appendix B.
Let's assume the evolution of the Universe proceeds according to the ΛCDM model with Friedmann-Robertson-Walker (FRW) metric. Which means the evolution of the scale factor R is related to the Hubble parameter H as

$$H = \frac{\dot{R}}{R}. \tag{2.24}$$

Today the Hubble parameter is

$$H_0 = \frac{100 km}{s \cdot Mpc} h = 67.74 \pm 0.46 \frac{km}{s \cdot Mpc}. \tag{2.25}$$

as measured by the Planck satellite [1]. From the FRW-metric one can deduce that

$$\begin{aligned} \dot{H} + H^2 &= \frac{1}{6 M_{Planck}} (\rho + 3p) \\ H^2 + \frac{\kappa^2}{R^2} &= \frac{\rho}{3 M_{Planck}}, \end{aligned} \tag{2.26}$$

with the Planck scale M_{Planck}, the total averaged energy density and pressure ρ and p and the curvature κ – where $\kappa = -1$ is for an open, $\kappa = 0$ for a flat and $\kappa = +1$ for a closed Universe. From CMB measurements it is known, that the Universe is flat. Hence, it is reasonable to express all quantities with respect to the critical density ρ_C at which $\kappa = 0$ holds. In general, ρ is given by

$$\rho = \frac{\pi^2}{30} g_{eff}(T) T^4, \tag{2.27}$$

with g_{eff} being the effective number of relativistic degrees of freedom.
In order to solve the Boltzmann equation, one needs a link between the entropy density s and the evolution of the Universe, which is given by entropy conservation as

$$\frac{ds}{dt} = -3Hs. \tag{2.28}$$

Further, it is known that

$$s = \frac{2\pi^2}{45} h_{eff}(T) T^3, \tag{2.29}$$

with the effective number of degrees of freedom for entropy h_{eff}.
In order to simplify Eq. 2.17 even more, one can define the abundance Y

$$Y := \frac{m_{DM}}{s} \qquad \text{and} \qquad x = \frac{m_{DM}}{T}., \tag{2.30}$$

and transform the equation using the abundance to obtain

$$\frac{dY}{dx} = \frac{1}{3H}\frac{ds}{dx} - \langle \sigma v \rangle . \tag{2.31}$$

Plugging in Eq. 2.26 and Eq. 2.29, this simplifies to

$$\frac{dY}{dx} = -\frac{45}{\pi M_{Planck}} \frac{\sqrt{g^*} m_{DM}}{x^2} \langle \sigma v \rangle , \tag{2.32}$$

where

$$\sqrt{g*} = \frac{h_{eff}}{\sqrt{g_{eff}}} \left(1 + \frac{1}{3}\frac{T}{h_{eff}}\frac{dh_{eff}}{dT} \right). \tag{2.33}$$

The evolution of Y becomes more elaborate in the case of multiple particle species. There, one obtains coupled Boltzmann equations that have to be solved. Let's assume there is a lightest stable dark matter particle ϕ_0 and other heavier particles ϕ_i for i from 1 to N. The heavier particles can decay subsequently into ϕ_0. This would modify the number density equation for ϕ_i to

$$\begin{aligned} \frac{n_i}{dt} = &-3Hn_i - \sum_j \left\langle \sigma_{ij} v_{ij} (n_i n_j - \overline{n}_i \overline{n}_j \right\rangle \\ &- \sum_{j \neq i} \left(\left\langle \sigma^X_{ij} v_{ij} \right\rangle (n_i n_X - \overline{n}_i \overline{n}_x) - \left\langle \sigma^X_{ji} v_{ij} \right\rangle (n_j n_X - \overline{n}_j \overline{n}_x) \right) \\ &- \sum_{j \neq i} \left(\Gamma_{ij} (n_i - \overline{n}_) - \Gamma_{ji} (n_j - \overline{n}_j) \right), \end{aligned} \tag{2.34}$$

with the label i regarding ϕ_i. The first term describes the expansion of the Universe. The second term takes into account particle creation and (co-) annihilation such as $\phi_i \phi_j \leftrightarrow X$ where X is some SM final state. Since there are multiple species, one needs to sum over all

contributions $\sigma_{ij} = \sum_X \sigma_{\phi_i\phi_j\to X}$. The third term is dedicated to conversion $\phi_i X \leftrightarrow \phi_j \tilde{X}$, where a particle of species i is transferred into another species j and vice versa. Again, one needs to sum all different combinations, which could appear as $\sigma_{ij}^X = \sum_{X,\tilde{X}} \sigma_{\phi_i X\to\phi_j\tilde{X}}$. The following term includes decays of ϕ_j producing ϕ_i. If all ϕ_i heavier than ϕ_0 are not stable, one is left with only the lightest state as dark matter. Otherwise, one would have multiple active dark matter species for which coupled equations have to be solved. In the case of only one dark matter species, it is sufficient to look at the total density of all ϕ_i $n_{DM} = \sum_i n_i$ as the n_i for heavier particles transforms to n_0. Thus, one can rewrite the evolution equation as

$$\frac{d_{DM}}{dt} = -3Hn_{DM} - \langle\sigma v\rangle \left(n_{DM}^2 - \overline{n}_{DM}^2\right), \tag{2.35}$$

with

$$\langle\sigma v\rangle = \sum_{i,j} \left\langle\sigma_{ij} v_{ij}\right\rangle \frac{\overline{n}_i \overline{n}_j}{\overline{n}_{DM}\overline{n}_{DM}}. \tag{2.36}$$

This equation is of similar form as Eq. 2.17. Again, this can be transformed into an equation for Y like Eq. 2.32.
In order to obtain the dark matter relic density Ω_{DM}, the Boltzmann Eq. 2.35 has to be solved. There is a link between abundance Y and relic density given by

$$\begin{aligned}\Omega_{DM} =& \frac{\rho_{DM}^0}{\rho_C} = \frac{m_{DM} s_0 Y_0}{GeV} \\ =& 2.75 \times 10^8 \frac{m_{DM}}{GeV} Y_0.\end{aligned} \tag{2.37}$$

A subscript 0 denotes the quantity today, so ρ^0 stands for the energy density today. For numerical results, the photon temperature of CMB is used and one finds that the relic density displays a behavior proportional to the inverse of the thermally averaged annihilation cross section times velocity $\frac{1}{\langle\sigma v\rangle}$. As mentioned before and as it will be important for later parts of this work, several particle species can play a role contributing to conversion and co-annihilation processes. Co-annihilation is enhanced for small mass difference $\Delta m = m_{\phi_1} - m_{\phi_0}$. The suppression for larger mass differences could in principle be weakened for large cross-sections, but in general, co-annihilation is only important in regions with small mass differences. Let's assume only two particle species play a role, such that they are of nearly equal mass $m_{\phi_0} \approx m_{phi_1}$ and all other particles are much heavier. Thus, only terms regarding ϕ_0 and ϕ_1 in Eq. 2.34 have to be considered. In the non-relativistic limit of $T << m_{\phi_i}$ one finds

$$\overline{n}_0 \overline{n}_1 \propto \left(\frac{m_{\phi_1}}{m_{\phi_0}}\right)^{3/2} \exp\left(-\frac{x_{FO}}{T}\frac{\Delta m}{m_{\phi_0}}\right). \tag{2.38}$$

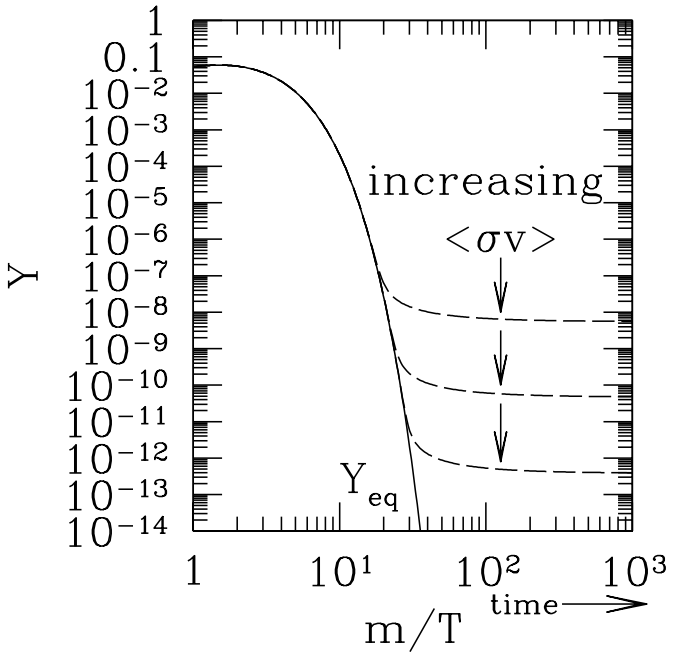

Figure 2.23: Evolution of dark matter abundance as a parameter of $x = \frac{m_{DM}}{T}$ for different annihilation cross section. Figure taken from [161]

Fig. 2.23 shows the evolution of abundance Y according to the Boltzmann Eq. 2.32 for different values of $\langle\sigma v\rangle$. In the early Universe annihilation and creation of dark matter are in thermal equilibrium for temperatures much larger than particle mass. The processes between dark matter and SM particles work equally in both directions. Once DM production becomes kinematically suppressed, due to temperature decreasing (x grows, it is anti-proportional to T), the annihilations starts to dilute the number density. Only the high energy end of the distribution can still produce dark matter particles. The distribution follows the decreasing equilibrium distribution, which is suppressed by the Boltzmann factor. If the expansion of the Universe proceeds, the mean free path of dark matter particles becomes larger than the size of Universe. This implies, there are basically no annihilations any more. The co-moving number density becomes constant. This is called freeze-out. It happens at x_{FO} corresponding to a freeze-out temperature T_{FO} by Eq. 2.30. The exact position of the freeze-out depends on cosmological quantities like the evolution of cosmos and on particle physics parameters like the annihilation cross section $\langle\sigma v\rangle$. As seen in Fig. 2.23, the larger the cross section the longer the particles stay in equilibrium. Larger cross sections mean more efficient annihilation, hence there is larger Boltzmann suppression. The smaller the resulting abundance, the better the annihilation works.
The above approach assumes that dark matter has been in thermal equilibrium, this demands a sufficiently large cross section. If the

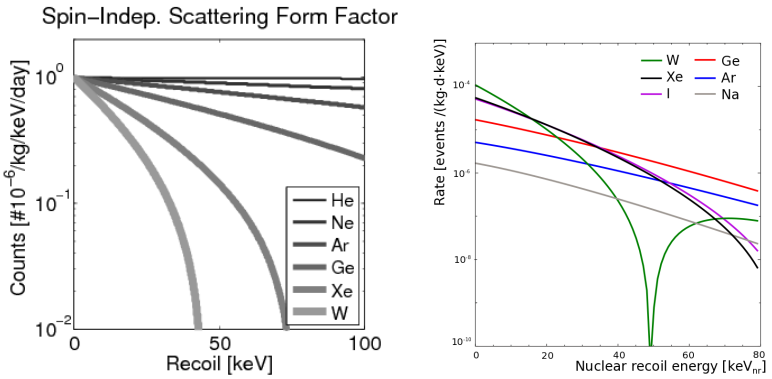

(a) Dependence of the spin-independent scattering form factor. Image taken from [165].

(b) Differential event rate for various target nuclei. Figure taken from [79].

Figure 2.24: Rotation curves of spiral galaxies.

cross section is too small, such that at no time thermal equilibrium is achieved, one speaks of **F**eebly **I**nteracting **M**assive **P**articles (FIMPs). FIMP relic densities are produced in a freeze-in scenario rather than freeze-out (see [163]). The number density is still described by a Boltzmann equation like Eq. 2.17, but instead of the annihilation cross section term, one only considers dark matter production from heavier particles like $\phi_j \rightarrow \phi_i \phi_0$ with ϕ_0 being the DM particle. The DM itself is decoupled from the thermal bath and assumed to have a vanishing small abundance in the early Universe. Once the temperature falls below the FIMP mass, particles from the thermal bath stop producing the FIMP via decay if they are lighter. The abundance from the decays freezes in. The larger the production cross section, the larger is the resulting relic density. Another option is the non-thermal production of dark matter either from the decay of heavier particles or from phase transitions see e.g. [164].

2.4.2 *Direct detection cross section*

As mentioned before, there are plenty of direct detection experiments looking for dark matter. The experiments do not measure the interaction cross section directly, but the differential recoil spectrum. This section about the link between the cross section and the recoil spectrum is based on [166]. The differential recoil spectrum $\frac{dR}{dE}$ depends on the recoil energy E and is given by

$$\frac{dR}{dE}(E,t) = \frac{\rho_{DM}}{m_{DM} m_N} \int v f(v,t) \frac{d\sigma}{dE} d^3v. \tag{2.39}$$

m_{DM} is the dark matter mass and m_N the target nucleus mass. The dark matter velocity v in the detector system follows the velocity distribution $f(v,t)$ due to the movement of the Earth through a dark

matter halo. For the resulting velocity one can assume a Maxwell distribution

$$f(v,t) = \frac{1}{\sqrt{2\pi\sigma}} exp\left(\frac{-|v|^2}{2\sigma^2}\right). \tag{2.40}$$

The dispersion relation σ is correlated to the circular velocity of 220 km/s and is cut off at the escape velocity v_{max} above which dark matter is no longer bound in the galaxy [76]. The local dark matter density ρ_{DM} is assumed to be around 0.3 GeV/cm^3 [77]. Both the density and velocity distributions contain astrophysical uncertainties for dark matter detection. The rest is determined by particle physics. In the non-relativistic limit, one can link the recoil energy to the momentum transfer Q by

$$Q = \sqrt{2m_N E}, \tag{2.41}$$

which allows to obtain the approximation

$$\frac{dR}{dQ} = \frac{\sigma_0 \rho_{DM}}{\sqrt{\pi} v m_{DM} \mu_N^2} F^2(Q) T(Q). \tag{2.42}$$

F is the nuclear form factor. The integral over the velocity distribution is contained in $T(Q)$ and σ_0 is the cross section at zero momentum transfer. μ_N is the reduced WIMP nucleus mass defined by

$$\mu_N = \frac{m_{DM} \cdot m_N}{m_{DM} + m_N}. \tag{2.43}$$

Limits on the energy E or on the momentum transfer Q can be obtained from the velocity limits. There is a minimal velocity v_{min}, in order to produce a recoil energy E big enough to reach the threshold of the detector

$$v_{min} = \sqrt{\frac{m_N E_{min}}{2\mu_N^2}}. \tag{2.44}$$

The maximal value of v is given by the escape velocity, as dark matter needs to be gravitationally bound within the galaxy to be part of the WIMP wind and it needs to be detectable. For our galaxy this is $v_{max} \approx 544$ km/s .

Considering the interaction cross section σ_0, there is in general a spin-independent (SI) and a spin-dependent (SD) part. The SI part can be expressed as

$$\sigma_0^{SI} = \sigma_p \frac{\mu_N^2}{\mu_p^2} \left(Z f^p + (A - Z) f^n\right)^2, \tag{2.45}$$

with σ_p being the elastic scattering cross section between nucleon and dark matter. μ_p is the reduced mass of dark matter and the proton,

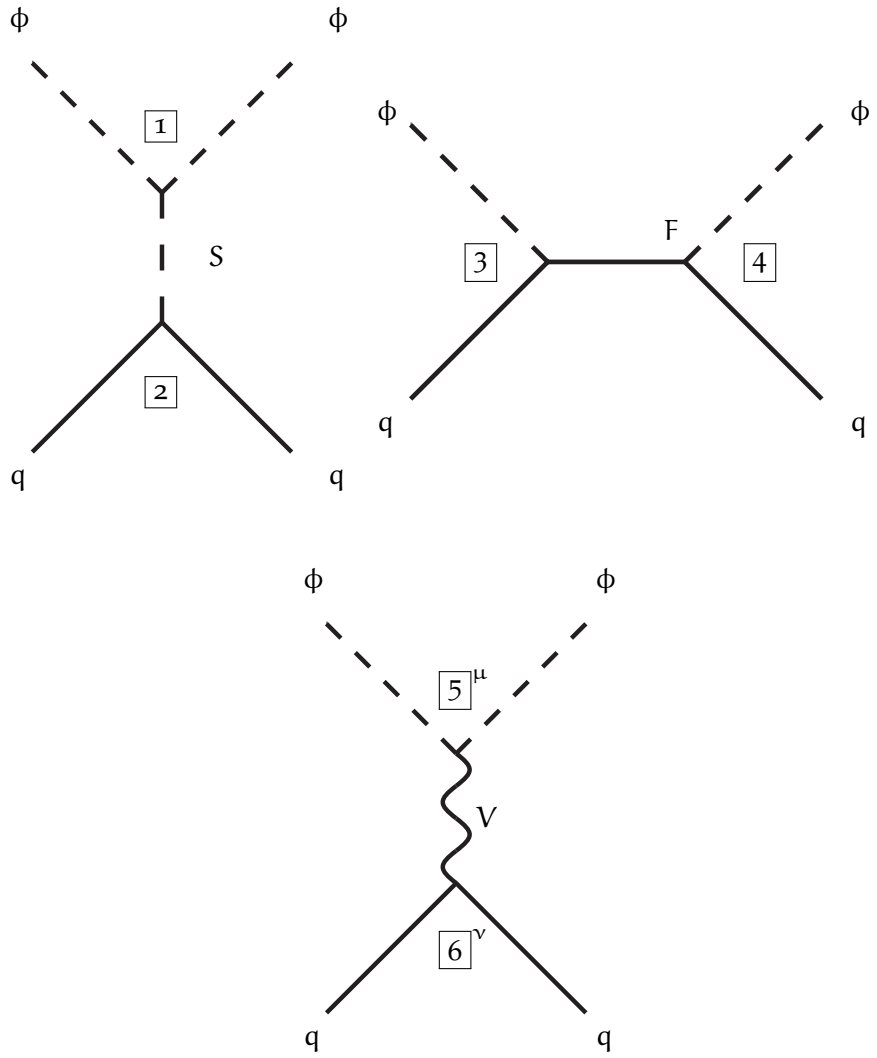

Figure 2.25: Scalar dark matter interacting with quarks.

Z the atomic number of target nucleus, and A is the mass number of target nucleus. N gives the number of neutrons within the nucleus. f^p and f^n are the spin-dependent coupling strength of protons and neutrons to dark matter. Usually, one assumes dark matter couples in the same fashion to protons and neutrons, but there are models where this is not the case. As $\sigma_0^{SI} \propto A^2$ has a quadratic dependence on mass number, heavier elements are favorable as target materials.
For the SD part of the cross section, we have

$$\sigma_0^{SD} = \frac{32}{\pi}\mu_N^2 G_F^2 \left(a_p \langle S^p \rangle + a_n \langle S^n \rangle\right)^2 \frac{J+1}{J}. \tag{2.46}$$

G_F is the Fermi's constant, a_p and a_n describe effective couplings to the proton and neutron. With $\langle S_{p,n} \rangle$ the expectation value of the spin content within nucleus comes into account. In order to be sensitive to

spin-dependent interactions, targets need unpaired neutrons or protons. For example in Xenon, naturally isotopes with odd numbers of protons or neutrons appear, thus Xenon based experiments are sensitive to spin-dependent as well as spin-independent dark matter interactions.
Low momentum transfers allow for coherently summing contributions from all nucleons inside the nucleus. At larger momentum transfer, the de Broglie wavelength of dark matter becomes smaller than the radius of the nucleus, the form factors decrease with increasing momentum transfer Q as seen in Fig. 2.24. Hence, there is an upper bound on momentum transfer for which coherent processes take place. At higher energies the A^2 dependence of spin-independent dark matter interaction is suppressed. Thus, better sensitivity for heavier targets is only true for lower energy regions. Fig. 2.24 shows the elastic scattering form factor (left) and differential event rate (right) under the assumption of a WIMP mass of 100 GeV and a cross section of 10^{-45} cm^2. There is a clear decrease in form factor for larger Q. For heavy elements like Xenon (black) or Wolfram (green) in the low Q region, the event rates are high, in the larger Q regions, there is a stronger suppression compared to light elements like Germanium (red).

2.4.3 *Generic calculations for direct detection processes*

In the previous section, the correlation between differential recoil and interaction cross section is pointed out. This section contains some generic calculations for scalar and fermionic dark matter interactions with quarks, which might result in sizable direct detection cross sections.

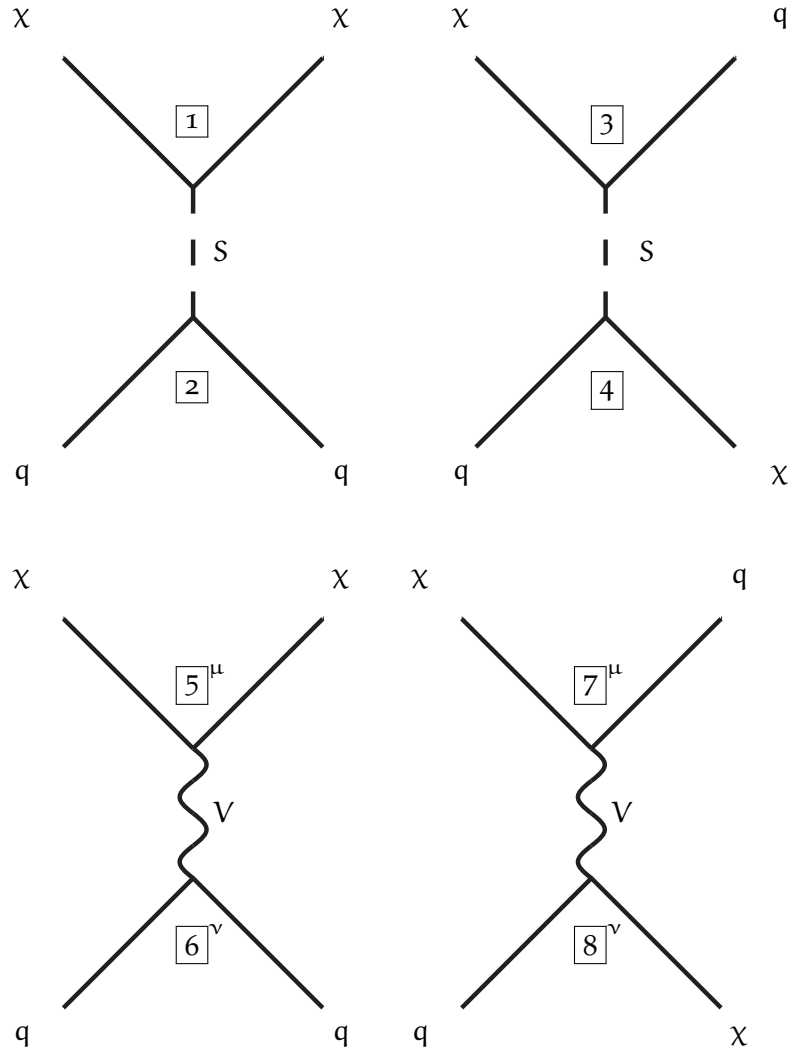

Figure 2.26: Fermion dark matter interacting with quarks showing t- and u-channel contributions.

Starting with an incoming (outgoing) dark matter particle at four momentum p_1 (p_3) and quark at p_2 (p_4), kinematics and Mandelstam variables can be expressed as

$$\begin{aligned} p_1 + p_2 &= p_3 + p_4, \\ s &= (p_1 + p_2)^2, \\ t &= (p_1 - p_3)^2, \\ u &= (p_1 - p_4)^2. \end{aligned} \tag{2.47}$$

Which simplifies for zero momentum transfer to

$$\begin{aligned} p_1^2 &= p_3^2 = m_{DM}^2, \\ p_2^2 &= p_4^2 = m_q^2. \end{aligned} \tag{2.48}$$

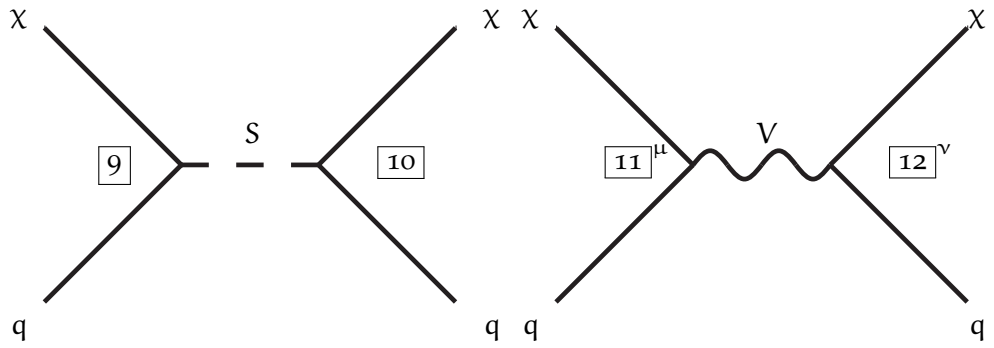

Figure 2.27: Fermion dark matter interacting with quarks, s-channel contributions.

The generic expressions for different vertices and propagators can be found in Appendix E. For scalar dark matter ϕ scattering off of quarks, there are three different options as shown in Fig. 2.25. The scattering can be mediated by a scalar S in the t-channel, a fermion F in the s-channel or a vector boson V in the t-channel. For fermion dark matter interacting with quarks, six different diagrams can contribute. They are shown in Fig. 2.26 and Fig. 2.27. The exact realization depends on the model and not all vertices might be present, limiting the number of diagrams. The general amplitudes for the diagrams in Fig. 2.25 are

$$\begin{aligned}
M_{S,a} =& i\boxed{1}\frac{i}{t-m_S^2}\bar{u}_4 i\boxed{2}u_2,\\
M_{S,b} =& \bar{u}_4 i\boxed{4}i\frac{\not{p}_1+\not{p}_1+m_F}{s-m_F^2}i\boxed{3}u_2,\\
M_{S,c} =& i\boxed{5}^{\mu}i\frac{1}{t-m_V^2}\\
&\left(-g_{\mu\nu}+\frac{(p_1-p_3)_\mu(p_1-p_3)_\nu}{m_V^2}\right)\bar{u}_4 i\boxed{6}^{\nu}u_2,
\end{aligned} \tag{2.49}$$

where the labels and vertices are according to the figure. Spinor and mass indices are chosen to match the index at particle momentum. Similarly, for fermion dark matter the amplitudes corresponding to Fig. 2.26 and Fig. 2.27 are

$$\begin{aligned}
M_{F,a} =& \bar{u}_3 i\boxed{1}u_1 i\frac{1}{t-m_S^2}\bar{u}_4 i\boxed{2}u_2,\\
M_{F,b} =& \bar{u}_4 i\boxed{3}u_1 i\frac{1}{u-m_S^2}\bar{u}_3 i\boxed{4}u_2,
\end{aligned}$$

$$
\begin{aligned}
M_{F,c} =& \bar{u}_3 i\boxed{5}^{\mu} u_1 i \frac{1}{t - m_V^2} \\
& \left(-g_{\mu\nu} + \frac{(p_1 - p_3)_\mu (p_1 - p_3)_\nu}{m_V^2}\right) \bar{u}_4 i\boxed{6}^{\nu} u_2, \\
M_{F,d} =& \bar{u}_4 i\boxed{7}^{\mu} u_1 i \frac{1}{u - m_V^2} \\
& \left(-g_{\mu\nu} + \frac{(p_1 - p_4)_\mu (p_1 - p_4)_\nu}{m_V^2}\right) \bar{u}_3 i\boxed{8}^{\nu} u_2, \\
M_{F,e} =& \bar{v}_1 i\boxed{9} u_2 i \frac{1}{s - m_S^2} \bar{u}_4 i\boxed{10} v_3, \\
M_{F,f} =& \bar{v}_1 i\boxed{11}^{\mu} u_2 i \frac{1}{s - m_V^2} \\
& \left(-g_{\mu\nu} + \frac{(p_1 + p_2)_\mu (p_1 + p_2)_\nu}{m_V^2}\right) \bar{u}_4 i\boxed{12}^{\nu} v_3.
\end{aligned} \tag{2.50}
$$

Starting from these expressions, one can calculate spin averaged squared amplitudes. It is possible to make simplifications if left- and right-couplings are the same $g_{iL} = g_{iR}$, as well as only real couplings contribute $\boxed{i}^* = \boxed{i}$.
Within the non relativistic limit and zero momentum transfer

$$
\begin{aligned}
s =& (m_{DM} + m_q)^2, \\
u =& (m_{DM} - m_q)^2, \\
t =& 0
\end{aligned} \tag{2.51}
$$

allows to obtain results in this limit as

$$
\begin{aligned}
|\overline{M_{S,aa}}|^2 =& \frac{8 g_1^2 g_2^2 m_q^2}{m_S^4}, \\
|\overline{M_{S,ab}}|^2 =& -\frac{8 g_1 g_2 g_3 g_4 m_q^2}{(m_{DM} - m_F + m_q) m_S^2}, \\
|\overline{M_{S,ac}}|^2 =& -\frac{4 g_1 g_2 g_5 g_6 m_{DM} m_q (m_{DM} + 3 m_q)}{m_S^2 m_V^2}, \\
|\overline{M_{S,bb}}|^2 =& \frac{8 g_3^2 g_4^2 m_q^2}{(m_{DM} - m_F + m_q)^2}, \\
|\overline{M_{S,bc}}|^2 =& \frac{4 g_3 g_4 g_5 g_6 m_{DM} m_q (m_{DM} + 3 m_q)}{(m_{DM} - m_F + m_q) m_V^2}, \\
|\overline{M_{S,cc}}|^2 =& \frac{16 g_5^2 g_6^2 m_{DM}^2 m_q (m_{DM} + m_q)}{m_V^4}.
\end{aligned} \tag{2.52}
$$

where indices label the diagrams which have been multiplied and evaluated within the approximation. The full results for scalars without simplifications can be found in appendix Section H.1. The results for fermions are too long to be usefully displayed there. For

the fermion amplitudes, the couplings are even more simplified by using $\boxed{3} = \boxed{4}$, $\boxed{7} = \boxed{8}$, $\boxed{9} = \boxed{10}$, $\boxed{11} = \boxed{12}$ to obtain

$$
\begin{aligned}
|\overline{M_{F,aa}}|^2 =& \left(64 g_1^2 g_2^2 m_{DM}^2 m_q^2\right) \times \frac{1}{m_S^4}, \\
|\overline{M_{F,ab}}|^2 =& -\left(32 g_1 g_2 g_3^2 m_{DM}^2 m_q^2\right) \\
& \times \frac{1}{m_S^2\left(m_{DM}^2 - 2 m_q m_{DM} + m_q^2 - m_S^2\right)}, \\
|\overline{M_{F,ac}}|^2 =& -\left(4 g_1 g_2 g_{5Lc}(g_{6L} + g_{6R}) m_{DM}^2 m_q (m_{DM} + 3 m_q)\right) \\
& \times \frac{1}{m_S^2 m_V^2}, \\
|\overline{M_{F,ad}}|^2 =& -\left(8 g_1 g_2 g_7^2 m_{DM}^2 m_q \left(2 m_q^3 + 2 m_{DM}^2 m_q\right.\right. \\
& \left.\left. -5 m_V^2 m_q + m_{DM}\left(m_V^2 - 4 m_q^2\right)\right)\right) \\
& \times \frac{1}{m_S^2 m_V^2\left(m_{DM}^2 - 2 m_q m_{DM} + m_q^2 - m_V^2\right)}, \\
|\overline{M_{F,ae}}|^2 =& 0 \\
|\overline{M_{F,af}}|^2 =& \left(2 g_1 g_{11Lc} g_2 m_{DM}^2 m_q \left(g_{12L}\left(-m_{DM}^3 + 3 m_q m_{DM}^2\right.\right.\right. \\
& \left. + 9 m_q^2 m_{DM} + 2 m_V^2 m_{DM} + 5 m_q^3 + 6 m_q m_V^2\right) \\
& + g_{12R}\left(m_{DM}^3 - 3 m_q m_{DM}^2 - 9 m_q^2 m_{DM} - 5 m_q^3\right. \\
& \left.\left.\left. + 16 m_q m_V^2\right)\right)\right) \\
& \times \frac{1}{m_S^2 m_V^2\left(m_{DM}^2 + 2 m_q m_{DM} + m_q^2 - m_V^2\right)}, \\
|\overline{M_{F,bb}}|^2 =& \left(64 g_3^4 m_{DM}^2 m_q^2\right) \\
& \times \frac{1}{\left(m_{DM}^2 - 2 m_q m_{DM} + m_q^2 - m_S^2\right)^2}, \\
|\overline{M_{F,bc}}|^2 =& -\left(4 g_3^2 g_{5Lc} m_{DM}^2 m_q (g_{6L}(m_{DM} + 3 m_q) - 8 g_{6R} m_q)\right) \\
& \times \frac{1}{\left(m_{DM}^2 - 2 m_q m_{DM} + m_q^2 - m_S^2\right) m_V^2}, \\
|\overline{M_{F,bd}}|^2 =& \left(16 g_3^2 g_7^2 m_{DM}^2 m_q \left(2 m_q^3 + 2 m_{DM}^2 m_q\right.\right. \\
& \left.\left. -3 m_V^2 m_q - m_{DM}\left(4 m_q^2 + m_V^2\right)\right)\right) \\
& \times \frac{1}{m_V^2\left(m_{DM}^2 - 2 m_q m_{DM} + m_q^2 - m_V^2\right)} \\
& \times \frac{1}{\left(m_{DM}^2 - 2 m_q m_{DM} + m_q^2 - m_S^2\right)}, \\
|\overline{M_{F,be}}|^2 =& 0, \\
|\overline{M_{F,bf}}|^2 =& -\left(2 g_{11Lc} g_3^2 m_{DM}^2 m_q \left(g_{12L}\left(-m_{DM}^3\right.\right.\right. \\
& \left. + 3 m_q m_{DM}^2 + 9 m_q^2 m_{DM}\right. \\
& \left. + 2 m_V^2 m_{DM} + 5 m_q^3 + 6 m_q m_V^2\right) \\
& + g_{12R}\left(m_{DM}^3 - 3 m_q m_{DM}^2 - 9 m_q^2 m_{DM}\right. \\
& \left.\left.\left. - 5 m_q^3 + 16 m_q m_V^2\right)\right)\right)
\end{aligned}
$$

$$
\begin{aligned}
&\times \frac{1}{\left(m_{DM}^2 - 2m_q m_{DM} + m_q^2 - m_S^2\right) m_V^2} \\
&\times \frac{1}{\left(m_{DM}^2 + 2m_q m_{DM} + m_q^2 - m_V^2\right)},\\
|\overline{M_{F,cc}}|^2 =& \left(16 g_{5L} g_{5Lc} m_{DM}^2 m_q \right.\\
&\times \left.\left(m_{DM} g_{6L}^2 - g_{6R} m_q g_{6L} + g_{6R}^2 m_q\right)\right)\\
&\times \frac{1}{m_V^4},\\
|\overline{M_{F,cd}}|^2 =& \left(4 g_{5L} g_7^2 m_{DM}^2 m_q \left(2 g_{6R}\right.\right.\\
&\left(-2m_q^3 - 2m_{DM}^2 m_q + 3m_V^2 m_q\right.\\
&\left.+m_{DM}\left(4m_q^2 + m_V^2\right)\right)\\
&+g_{6L}\left(m_{DM}^3 - m_q m_{DM}^2\right.\\
&\left.\left.\left.-\left(m_q^2 + 4m_V^2\right) m_{DM} + m_q^3\right)\right)\right)\\
&\times \frac{1}{m_V^4\left(-m_{DM}^2 + 2m_q m_{DM} - m_q^2 + m_V^2\right)},\\
|\overline{M_{F,ce}}|^2 =& 0,\\
|\overline{M_{F,cf}}|^2 =& \left(4 g_{11Lc} g_{5L} m_{DM}^2 m_q \left(g_{12R} m_q \left(g_{6L}\right.\right.\right.\\
&\times \left(m_{DM}^2 + 2m_q m_{DM} + m_q^2 + 2m_V^2\right)\\
&\left.-2g_{6R}\left(m_{DM}^2 + 2m_q m_{DM} + m_q^2 - m_V^2\right)\right)\\
&+g_{12L}\left(2g_{6R} m_q\right.\\
&\left(m_{DM}^2 + 2m_q m_{DM} + m_q^2 - m_V^2\right)\\
&\left.\left.+g_{6L}\left(m_{DM}^3 - 3m_q^2 m_{DM} - 2m_q^3 + 4m_q m_V^2\right)\right)\right)\right)\\
&\times \frac{1}{m_V^4\left(m_{DM}^2 + 2m_q m_{DM} + m_q^2 - m_V^2\right)},\\
|\overline{M_{F,dd}}|^2 =& -\left(16 g_7^3 (g_7 + g_8) m_{DM}^2 m_q (m_{DM} + m_q)\right)\\
&\times \frac{1}{m_V^2\left(m_{DM}^2 - 2m_q m_{DM} + m_q^2 - m_V^2\right)},\\
|\overline{M_{F,de}}|^2 =& 0,\\
|\overline{M_{F,df}}|^2 =& -\left(2 g_{11Lc} g_7 m_{DM}^2 m_q \left(g_{12R}\left(2g_7 m_q\right.\right.\right.\\
&\times \left(m_{DM}^4 - \left(2m_q^2 + 5m_V^2\right) m_{DM}^2\right.\\
&\left.+6m_q m_V^2 m_{DM} + m_q^4 + 4m_V^4 - 5m_q^2 m_V^2\right)\\
&-g_8(m_{DM} + m_q)\left(m_{DM}^4 - 2m_q m_{DM}^3 + 2m_V^2 m_{DM}^2\right.\\
&\left.+2m_q\left(m_q^2 + m_V^2\right) m_{DM} - m_q^4 - 4m_V^4\right)\\
&+g_{12L}\left(g_7\left(m_{DM}^5 - m_q m_{DM}^4 - 2m_q^2 m_{DM}^3\right.\right.\\
&+2\left(m_q^3 + 5m_V^2 m_q\right) m_{DM}^2\\
&\left.+\left(m_q^4 - 4m_q^2 m_V^2\right) m_{DM} - m_q^5 + 4m_q m_V^4 + 2m_q^3 m_V^2\right)\\
&-2g_8 m_q\left(m_{DM}^4 + \left(m_V^2 - 2m_q^2\right) m_{DM}^2\right.\\
&\left.\left.\left.\left.-6m_q m_V^2 m_{DM} + m_q^4 - 2m_V^4 + m_q^2 m_V^2\right)\right)\right)\right)
\end{aligned}
$$

$$
\begin{aligned}
&\times \frac{1}{m_V^4\left(m_{DM}^2-2m_q m_{DM}+m_q^2-m_V^2\right)}\\
&\times \frac{1}{\left(m_{DM}^2+2m_q m_{DM}+m_q^2-m_V^2\right)},\\
|\overline{M_{F,ee}}|^2 =&0,\\
|\overline{M_{F,ef}}|^2 =&0,\\
|\overline{M_{F,ff}}|^2 =&-\left(4g_{11L}g_{11Lc}m_{DM}^2 m_q\right.\\
&\times\left(\left(m_{DM}^5+2m_q m_{DM}^4-2\left(m_q^2+m_V^2\right)m_{DM}^3\right.\right.\\
&-8m_q^3 m_{DM}^2+\left(6m_q^2 m_V^2-7m_q^4\right)m_{DM}\\
&\left.-2m_q\left(m_q^4-2m_V^2 m_q^2+2m_V^4\right)\right)g_{12L}^2\\
&+2g_{12R}m_q\left(m_{DM}^4+4m_q m_{DM}^3+\left(6m_q^2-2m_V^2\right)m_{DM}^2\right.\\
&+4\left(m_q^3-m_q m_V^2\right)m_{DM}\\
&\left.+m_q^4-2m_V^4-2m_q^2 m_V^2\right)g_{12L}\\
&+g_{12R}^2\left(m_{DM}^5+2m_q m_{DM}^4-2\left(m_q^2+m_V^2\right)m_{DM}^3\right.\\
&-8m_q^3 m_{DM}^2+\left(6m_q^2 m_V^2-7m_q^4\right)m_{DM}\\
&\left.\left.-2m_q\left(m_q^4-2m_V^2 m_q^2+2m_V^4\right)\right)\right)\\
&\times\frac{1}{m_V^4\left(m_{DM}^2+2m_q m_{DM}+m_q^2-m_V^2\right)^2}. \qquad (2.53)
\end{aligned}
$$

The matrix elements then can be used to obtain the direct detection cross section – see Section D.1. The formula for the spin-independent scattering cross section is

$$\sigma_{n,p}^{SI}=\frac{|\overline{M}|^2}{32\pi}\frac{f_{n,p}^2}{(m_{DM}+m_{n,p})^2}, \qquad (2.54)$$

where $m_{n,p}$ is the neutron (proton) mass and $f_{n,p}$ are the form factors for the quark distribution within the nucleon.

3

NEUTRINOS AND NEUTRINO MASSES

3.1 NEUTRINO SOURCES AND DETECTION MECHANISMS

After Pauli's first idea of neutrinos around 1930 emerged [167], a lot has been discovered about these particles. Pauli proposed the neutrino in oder to explain the continuous nature of β-decay spectra. The neutrino is a neutral and massless particle within the Standard Model. It only takes part in weak interactions. Further, it is found that weak processes violate parity maximally. One of the first experiments on parity violation was conducted by Wu [168]. In the investigation of β decay of polarized ^{60}, it was found that parity was violated. In 1957 Goldhaber et.al. [169] measured the helicity of neutrinos by observing electron capture of ^{152}Eu by resonance absorption of the emitted photons. It was found that neutrinos have negative helicity. As one can see from the Standard Model Lagrangian, only left-handed fields contribute to weak processes. Such weak interactions are associated with small cross sections, due to the massiveness of the mediator bosons. Despite the small cross sections, R. Davis et.al. [170] were able to observe solar neutrinos by means of a radio chemical method using ^{37}Cl proposed by Pontecorvo [171]. Only one third of the expected solar neutrino flux was observed. This discrepancy can be explained by neutrino oscillations as described in Section 3.2. In 2015 a Nobel prize was awarded to Kajita and McDonald for the discovery of neutrino oscillations. Neutrino oscillations are possible, as the flavor states are a linear superposition of mass eigenstates conveyed by the PMNS matrix see Section 3.2.
The next section shortly describes sources for neutrinos. Next, in Section 3.2, neutrino oscillation vacuum and matter is shown. Section 3.3 summarizes some oscillation experiments followed by mass generation mechanisms in Section 3.4 and neutrino mass measurements in Section 3.5.

3.1.1 *Neutrino sources*

When looking for neutrinos, one has to consider the different neutrino sources. This section gives a short non-exhaustive overview, based on [172, 173].
Neutrinos, for example, can be produced in the Sun. There are three different production mechanisms contributing to this. Proton-proton interactions ($p + p \rightarrow d + e^+ + \nu_e$) yield neutrino energies below 0.42 MeV. The vast majority of solar neutrinos is produced by this mecha-

nism with an expected flux around
$6 \times 10^{10} s^{-1} cm^{-2}$. This reaction also allows to build heavier elements like ^7Be, which in turn can produce neutrinos by electron capture. The reaction $^7Be + e^- \rightarrow ^7 Li + \nu_e$ is associated with an energy of 0.86 MeV. The ^7Be could also interact with protons forming Boron (^8B). Boron is not stable and undergoes β decay $^8B \rightarrow ^8 Be + e^+ + \nu_e$ yielding neutrino energies around 15 MeV. All solar processes feature electron neutrinos ν_e, none of the other flavors are produced.
Another source for neutrinos are cosmic rays. Cosmic rays can interact with the outer atmosphere producing pions and kaons which subsequently produce neutrinos by decaying.

$$\pi^+(\pi^-) \rightarrow \mu^+(\mu^-) + \nu_\mu(\overline{\nu}_\mu),$$
$$\mu^+(\mu^-) \rightarrow e^+(e^-) + \nu_e(\overline{\nu_e}) + \overline{\nu}_\mu(\nu_\mu).$$

From these reaction one expects at least twice as many ν_μ as ν_e.
Supernova explosions can lead to short but intense neutrino emission, when protons undergo β decay in the high density region of the supernova – see Section 3.5.3. Similar to the CMB there are cosmic background neutrinos present from early stages of the Universe – see Section 3.5.1. Also nuclear reactors and particle accelerators can be used as artificial neutrino sources.

3.1.2 *Neutrino detection processes*

Neutrinos can interact by quasi-elastic or deep inelastic scattering off of n or p within target nuclei.

$$^{(}\overline{\nu}_l^{)} + p(n) \rightarrow l^{-(+)} + n(p),$$
$$^{(}\overline{\nu}_l^{)} + p(n) \rightarrow l^{-(+)} + X.$$

These reactions produce charged leptons and potentially hadronic showers. Here ν_l is either a neutrino ν or an anti-neutrino $\overline{\nu}$ according to the processes. l in stands for e, ν or τ, differentiating between lepton flavor.

3.2 NEUTRINO OSCILLATION

Since the observation of neutrino oscillation [174–176], it is clear that neutrinos cannot be massless but have to have a small, non-negligible mass. The following sections contain a short overview on neutrino oscillations in vacuum and in matter, followed by an overview of neutrino oscillation experiment. The sections follow [173, 177].

3.2.1 *Neutrino vacuum oscillations*

Neutrinos have interaction eigenstates ν_l, which are a linear combination of mass eigenstates ν_i. The interaction states occur in weak processes as partners of charged leptons l (e, μ, τ). Similarly to the quarks sector, the neutrino mixing is described by a 3×3 unitary mixing matrix U_ν, the PMNS matrix.

$$\nu_l = \sum_{i=1}^{3} U_{\nu,li}\nu_i \tag{3.55}$$

From experiments it is known, that at least two of the masses m_i cannot vanish. For simplicity, one can look at two flavor mixing, which is characterized by a single angle α. Consider two flavor neutrinos ν_f with f either a or b and two mass eigenstates ν_1 and ν_2.

$$\begin{pmatrix}\nu_a\\ \nu_b\end{pmatrix} = \begin{pmatrix}\cos\alpha & \sin\alpha\\ -\sin\alpha & \cos\alpha\end{pmatrix}\begin{pmatrix}\nu_1\\ \nu_2\end{pmatrix}. \tag{3.56}$$

In a charged current interaction only flavor states ν_f take part. Usually, neutrinos are create in charged current interactions as

$$|\nu_f> = |\nu_i> U^{\dagger}_{\nu,fi}. \tag{3.57}$$

The propagation in vacuum, though, is described by the propagation of mass eigenstates ν_i. If the mass eigenstates have different masses and therefore energies E_i, the propagation leads to different phase factors between the different states. The propagation in vacuum can be expressed as

$$\begin{aligned}
|\nu_f>_t &= e^{-iHt}|\nu_i> U^{*}_{\nu,fi},\\
|\nu_f>_t &= |\nu_i> e^{-iE_it}U^{\dagger}_{\nu,fi},\\
|\nu_f>_t &= \sum_{f'} |\nu_{f'}> U_{\nu,f'i}|\nu_i> e^{-iE_it}U^{*}_{\nu,fi}.
\end{aligned} \tag{3.58}$$

Neutrino detection again, happens via charged current interactions, thus it acts on flavor. As the phase factors have changed, a different flavor than at creation time $t = 0$ might be detected. One needs to transform back to the flavor states like in the last step of Eq. 3.58. The probability of changing flavor from a to b is then given as

$$P(\nu_a \to \nu_b) = |<\nu_b|U_{\nu,f'i}e^{-iE_it}U_{\nu,fi} * |\nu_a>|^2. \tag{3.59}$$

The probability of obtaining the same flavor neutrino as created is

$$P(\nu_a \to \nu_a) = 1 - P(\nu_a \to \nu_b). \tag{3.60}$$

Plugging in the mixing matrix from Eq. 3.56 and using $|\nu_a> = \begin{pmatrix} 1 \\ 0 \end{pmatrix}$ and $< \nu_b| = \begin{pmatrix} 0 & 1 \end{pmatrix}$ in Eq. 3.59, gives

$$P(\nu_a \to \nu_b) = \left| \begin{pmatrix} -\sin\alpha \\ \cos\alpha \end{pmatrix} \begin{pmatrix} 1 & 0 \\ 0 & e^{-i(E_2-E_1)t} \end{pmatrix} \begin{pmatrix} \cos\alpha \\ \sin\alpha \end{pmatrix} \right|^2 . \quad (3.61)$$

Furthermore, one can use the relativistic energy momentum relation as

$$E_2 - E_1 = \frac{m_2^2 - m_1^2}{2p} =: \frac{\Delta m^2}{2p}, \quad (3.62)$$

where p is the ν momentum. Inserting this to Eq. 3.61 and using trigonometric relations, one arrives at

$$\begin{aligned} P(\nu_a \to \nu_b) &= \sin^2(2\alpha)\,\frac{1}{2}\left(1 - \cos\left(\frac{\Delta m^2}{2p}t\right)\right) \\ &= \sin^2(2\alpha)\,\frac{1}{2}\left(1 - \cos\left(\frac{\Delta m^2 L}{2E}\right)\right) \\ &= \sin^2(2\alpha)\sin^2\left(\frac{\Delta m^2 L}{4E}\right), \end{aligned} \quad (3.63)$$

where the relations for ultra relativistic particles $E \approx pc$ and $ct \approx L$ were used. From Eq. 3.63 it is visible, that the oscillation of neutrino flavor depends periodically on the ratio of energy E and distance L. In the case of three flavors, Eq. 3.59 still holds, just the mixing matrix is different than in Eq. 3.61. Fig. 3.28 illustrates the oscillation of ν_e created in a reactor to other neutrino flavors as a function of the distance L. The figure shows a fast oscillation seen as a modulation on top of of slow oscillation. This fact can be used to disentangle the two dynamics depending on the involved length scales. Hence, different scaled experiments have access to different squared mass differences and mixing angles.

3.2.2 *Matter enhanced neutrino oscillation: MSW-effect*

The above section describes neutrino oscillations in vacuum. However, when neutrinos travel through a medium, they do interact with the matter. Matter mostly contains electrons but not μ or τ-leptons. Hence, ν_e can interact via Z exchange (NC) or W exchange (CC) with the electrons, where the other neutrino flavors only take part in Z mediated interactions. The different scattering cross sections for the different flavors have an impact on the propagation. This effect is called MSW effect, which is short for Mikheev-Smirnov-Wolfenstein effect [179, 180].

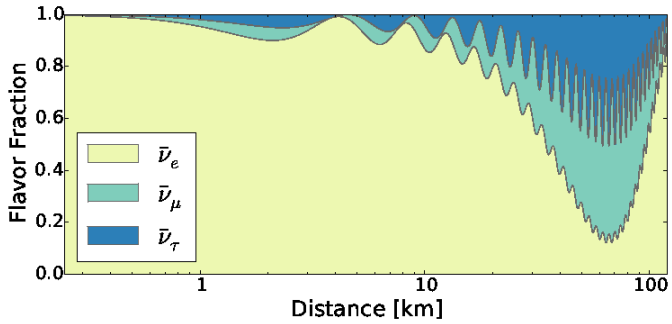

Figure 3.28: Neutrino composition for reactor neutrinos at 4 MeV as a function of the distance. There are some regions where it is more likely to observe $\nu_{\mu,\tau}$ than ν_e. The figure is taken from [178].

In order to describe the propagation in a medium, one can add a Hamiltonian for neutrino interactions in matter

$$\mathcal{H}_{\text{matter}} = \frac{2}{G_F} n_e, \tag{3.64}$$

to the Hamiltonian for the free fields. Here G_F is the Fermi constant and n_e the electron density. This is in flavor basis, it has to be transformed to the mass basis using the ν mixing matrix. This leads to off diagonal terms in the mass eigenbasis Hamiltonian, that are not there for the vacuum case. ν_i are no longer eigenstates within matter. A mixing between ν_i occurs. Therefore, it is useful to determine a matter mass basis $\nu_{i,\text{matter}}$. This allows for oscillations between the vacuum mass eigenstates.
In the simplification of two neutrino flavors, this would lead to one mass, which is proportional to the electron density, and one constant mass, without flavor mixing. Depending on the hierarchy of the vacuum mass eigenstates, the matter state masses $m_{i\text{matter}}$ could cross. If m_2 is smaller than m_1 no crossing is observed. Considering flavor mixing as well, there is no longer a crossing but a resonance point, where the difference between $m_{i\text{matter}}$ becomes minimal. The minimum depends on Δm^2 and n_e as illustrated in Fig. 3.29. The dashed lines show the crossing, whereas the solid lines follow the matter eigenstates. There is one density, for which the distance between the two masses is minimal. A resonance occurs, this is associated with a point of maximal mixing. If the matter distribution varies spatially, it is possible that the resonance condition is met and oscillation is enhanced.
Following [173], the oscillation probability is given by

$$P(\nu_a \to \nu_b) = \sin^2(\alpha_m) \sin^2\left(\frac{\Delta m^2_m L}{4E}\right), \tag{3.65}$$

with the matter mixing angle α_m defined by

$$\tan(2\alpha_m) = \frac{\sin(2\alpha)}{\cos(2\alpha) - \frac{A}{\Delta m^2}}. \tag{3.66}$$

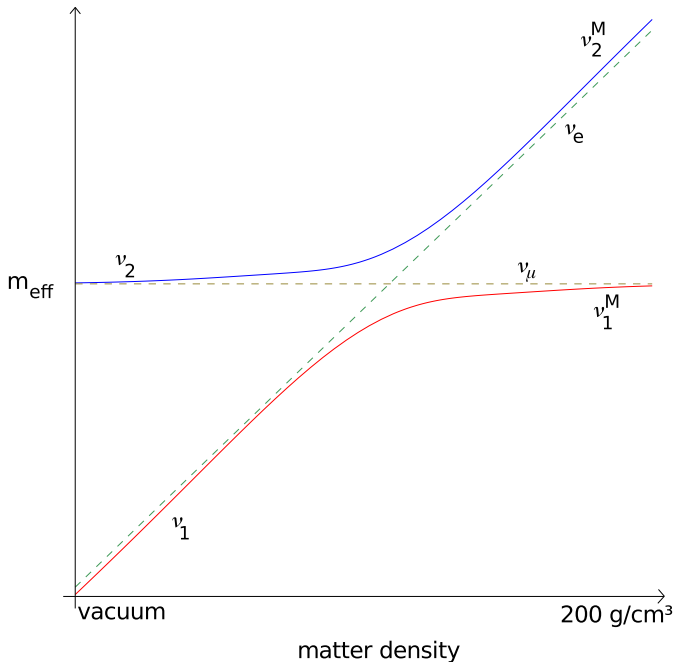

Figure 3.29: The figure shows behavior of neutrino mass states within matter allowing for a point of maximal mixing for a specific electron density. The figure is taken from [181].

α is the mixing angle in vacuum as in Eq. 3.61. The abbreviation $A := 2p\sqrt[2]{G_F}n_e$ is also introduced.
The application of the matter enhanced oscillation effects on the expected neutrino flux from the Sun provides a good explanation of the observations made by several experiments of the disappearance of solar ν_e. Additionally with help of the MSW effect the sign of Δm^2_{12} can be determined. For Δm^2_{23} this is not possible.

3.3 NEUTRINO OSCILLATION EXPERIMENTS

The previous section contains a a short introduction to neutrino oscillation, this section gives a summary of experiments investigating the oscillations. It is based on the same review [177].
Depending on the energy and length scale of the fast and slow oscillations – see Fig. 3.28 — one can disentangle the dynamics and reduce to only two flavors being involved. This allows for experiments to probe different mixing angles and mass differences for various neutrino sources.

SNO

The Sudbury Neutrino Experiment (SNO) [182] is a solar neutrino experiment, which utilizes heavy water as a target. It consists of around 1000t D_2O in an acrylic vessel monitored by PMTs. Due to its energy threshold, it is only sensitive for neutrinos from the B^8 process in the

Sun(Section 3.1.1). There are three ν interaction channels, which can lead to a signal in SNO: Charged current interactions (CC) $\nu_e + d \rightarrow e^- + p + p$, neutral current processes (NC) $\nu_x + d \rightarrow \nu_x + p + n$ and elastic neutrino-electron scattering $\nu_x + e^- \rightarrow \nu_x + e^-$. NC processes are open for all flavors whereas CC and ES reactions only happen for ν_e. Hence, one can compare the total neutrino flux to the electron neutrino flux. It is found that ν_e only have a third of the expected flux, but the entire flux for all flavors is consistent with the expectation. This is a clear sign, that the ν_e produced in the Sun oscillated, when passing through the solar medium and traveling to the Earth, such that they are no longer detected as ν_e. On the other hand, this also allows to strongly restrict the probability for ν_e to oscillate to sterile neutrinos, which would not interact in the detector.

KAMLAND

The KamLAND experiment [183] investigates reactor neutrinos from 55 reactors in around 140 km to 205 km distance. It consists of a liquid scintillator monitored by PMTs, surrounded by a water Cherenkov veto. The average ν energy is around 3.6 MeV. The combination of energy and length scale makes the oscillation be dominated by Δm^2_{12} and the corresponding mixing angle θ_{12}. The main detection channel is $\bar{\nu}_e + p \rightarrow e^+ + n$. Subsequently, the e^+ annihilate with electrons emitting two γs with an energy of around 0.51 each. The neutron gets captured as well releasing a γ. KamLAND is looking for a coincidence measurement between these two events. The observed spectrum is compared to the expected spectrum from the processes in the reactors. The distortion allows to determine

$$\begin{aligned} \Delta m^2_{12} &= (7.66\,^{+0.20}_{-0.22}) \times 10^{-5} eV^2, \\ \tan^2 2\theta_{12} &= 0.52\,^{+0.16}_{-0.10}\,. \end{aligned}$$

SUPER-KAMIOKANDE

Super-Kamiokande [184] is a huge cylindrical water Cherenkov detector with 50 kt of water and over 10 000 PMTs. It consists of an inner detector and an outer detector in order to reject interactions from cosmic ray muons. The detector looks for atmospheric neutrinos via the process $\nu_l + N \rightarrow l + X$ with $l = e, \mu$. The charged leptons can be distinguished by the hit pattern on the PMTs. μs leave a sharp ring whereas e lead to a more diffuse appearance. The detector also allows for energy and direction reconstruction of the ν event. Thus, one can measure the zenith-angle θ dependence of ν fluxes. The zenith-angle is defined such that for $\theta = 0$ the event goes straight down, originating from the atmosphere the distance is around 20 km. For $\theta = \pi$, events come straight up. Hence, the neutrinos have to travel through the Earth for around 1300 km to reach the detector. Comparing the up- and downward neutrino fluxes, Super-Kamiokande finds a dis-

appearance of ν_μ, which are due to neutrino oscillations. Mostly due to ν_μ to ν_τ oscillations, as τ interactions are rarely observed in the detector, due to the large production threshold.

MINOS AND T2K

Both MINOS [185] and T2K [186] are so called long baseline experiments. MINOS consists of two detectors, observing neutrinos produced at Fermilab. K2K receives neutrinos from the KEK accelerator with a distance of 250 km to the far detector. For MINOS, the near detector is around 1 km from the Fermilab target, the far detector is within a distance of 735 km. Both detectors work with the same principle, looking for the interaction $\nu_\mu + Fe \rightarrow \mu^- + X$, where the total ν energy is obtained by summing up the μ and hadronic shower X energies. The near detector measures the initial spectrum, to which the distorted spectrum recorded by the far detector is compared. The oscillation process is dominated by Δm^2_{23} and θ_{23} and the results are for MINOS

$$\Delta m^2_{23} = (2.32 \, ^{+0.12}_{-0.08}) \times 10^{-3} eV^2,$$
$$\sin^2 2\theta_{23} > 0.90.$$

DAYA BAY AND RENO

Daya Bay [187], similarly to Reno [188], is another long baseline experiment. It uses six scintillation detectors to observe six reactors. Three detectors act as near detectors with a distance of 470-570 m to the reactors and three are considered far with around 1648 m distance. It probes the θ_{13} region by the detection mechanism $\overline{\nu}_e + p \rightarrow e^+ + n$ and comparing the number of events in the near and far detectors. This corresponds to the $\overline{\nu}_e$ survival probability. In the analysis it was found that

$$\sin^2 2\theta_{13} = 0.113 + 0.013 + 0.019.$$

3.4 MECHANISMS FOR NEUTRINO MASS GENERATION

After the discovery of neutrino oscillation it is clear, that neutrinos cannot be massless. This section aims at explaining some mechanisms for neutrino mass generation. In general, in the Standard Model fermion masses are generated in the electro-weak symmetry breaking (EWSB) via the mass mechanism. Therefore, it is needed to couple two fermions to a scalar, the Higgs, which obtains a vacuum expectation value. The fermion mass matrices arising from EWSB are not diagonal, but can be diagonalized by 3×3 unitary mixing matrices. Yukawa interactions link left-handed fermion doublets and right-handed singlets. A typical Dirac fermion mass term combines left and right components, such as $M\overline{\psi}_R\psi_L$. Yet, as there is no right-handed neutrino within the Standard Model, neutrinos cannot obtain mass by this mechanism.

There has to be an extension to the SM to explain neutrino masses. Furthermore, cosmology puts limits on the sum of ν masses. They must be below 1 eV. This implies, neutrino masses are many orders of magnitudes below charged lepton masses. From oscillation experiments the squared mass differences are known, but the absolute neutrino mass scale is not revealed yet. The sign of the mass differences is not known for Δm^2_{23}. Hence, one can have normal hierarchy m^2_1, $m^2_2 < m^2_3$ or inverted hierarchy m^2_1,m^2_2>m^2_3 regarding the mass state masses m_i. The following sections are based on [173, 177].

3.4.1 *See-saw type I*

The simplest idea for neutrino masses is to introduce a mass term like the one for charged leptons. This needs the addition of right-handed neutrinos ν_R to the Standard Model. ν_R allow tow write a term for Dirac neutrino masses as

$$\mathcal{L}_{D_\nu} = -Y_{\nu,ij}\nu_R\tilde{H}^\dagger l_{L,j}. \tag{3.67}$$

Here i and j are family indices, Y_ν Yukawa couplings, l_i is the lepton doublet and H the Higgs doublet. Spontaneous symmetry breaking leads to $H \to \begin{pmatrix} 0 \\ \frac{1}{\sqrt{2}}(h+v) \end{pmatrix}$ with $v = 246$ GeV. The above mass term would translate to a Dirac mass for neutrinos m_{LR}. Yukawa couplings for charged leptons are of order 1 MeV for all flavors. Since the neutrino masses are at least six orders of magnitude below the charged lepton masses, their Yukawa couplings had to be comparably small. This is not a very satisfying explanation on why neutrino masses are so small.
The mass terms includes a chirality flip. There is one incoming particle with one chirality one outgoing particle with the other. In case of Majorana fermions, the chirality flipped particles can be the same. Particle and antiparticle are not distinguishable. Since neutrinos are neutral, it is possible to have Majorana neutrinos. In this case one can also define mass terms like

$$\begin{aligned} \mathcal{L}_{M_\nu} = &-\frac{1}{2}M_{LL}\overline{\nu}^C_L\nu_L && (3.68)\\ &-\frac{1}{2}M_{RR}\overline{\nu}^C_R\nu_R && (3.69)\\ &+ \text{h.c.} \end{aligned}$$

which violates lepton flavor number by two units. In addition to creating a neutrino mass term, Majorana neutrinos also allow for new processes like neutrinoless double-β decay – see Section 3.5.2. Putting all

the mass terms together, one can read of the non-diagonal neutrino mass matrix

$$M_\nu = \begin{pmatrix} M_{LL} & M_{LR} \\ M_{LR} & M_{RR} \end{pmatrix}. \tag{3.70}$$

M_ν has the mass eigenvalues

$$m_{1,2} = \frac{1}{2}\left((M_{LL} + M_{RR}) \pm \sqrt{(M_{LL} - M_{RR})^2 + 4M_{LR}^2} \right). \tag{3.71}$$

The presence of the M_{LL} term Eq. 3.68 violates weak isospin, as ν_L is in the doublet with e_L. Hence, it is not allowed easily when extending the SM without loosing renormalizability. All other terms can be formulated, when adding ν_R to the SM. When taking $M_{LL} = 0$ and assuming $M_{LR} \ll M_{RR}$, such that the right-handed neutrinos are very heavy, Eq. 3.71 can be approximated by

$$\begin{aligned} m_1 &\approx M_{RR}, \\ m_2 &\approx \frac{M_{LR}^2}{M_{RR}}. \end{aligned} \tag{3.72}$$

The smaller eigenvalue m_2 gets lighter for larger M_{RR}. Therefore, this is sometimes called see-saw mechanism.
For just one neutrino and lepton family, it is sufficient to have M_{RR} around the Planck scale to yield reasonably small neutrino masses of about 10^{-3} eV. The large mass of ν_R can be associated with a scale at which unification of forces might take place in grand unified theories (GUT). Also, the existence of very heavy ν_R might explain the matter-antimatter asymmetry, if they preferably decayed to leptons instead of anti-leptons in the early Universe, enhancing the asymmetry by leptogenesis e.g. see [189].
When integrating out the heavy ν_R, an effective dimension five operator is obtained. It should be sufficient to describe neutrino masses by such an effective operator. In 1979 Weinberg [190] showed that there is essentially one operator for this

$$\frac{g_{ij}}{\Lambda}\left(\bar{l}_{Li}^{C}\sigma_2 H\right)\left(H^T\sigma_2 l_{Lj}\right). \tag{3.73}$$

with the second Pauli matrix σ_2. The scale Λ corresponds to the mass scale of the particles which have been integrated out.

3.4.2 *See-saw type II and beyond*

Other than adding a heavy right-handed Majorana neutrino, this operator could also be achieved by introducing either a scalar triplet (see See-saw type II) or a heavy fermion triplet. This is shortly depicted in this subsection. which is also based on [177, 191, 192].

When looking for new terms to add to the SM Lagrangian, they have to be renormalizable and fulfill all requirements for Lagrangian terms. As neutrino masses should be generated, the terms should involve two fermionic parts such as a fermion singlet S, fermion doublet D or a fermion triplet T depending on the extension of the SM. In addition, scalar terms are needed. They can either involve a scalar singlet φ, a scalar doublet ϕ, which could be the SM Higgs doublet, or a scalar triplet Σ. Different allowed combinations are shown below

$$\begin{aligned} S\ S &: \varphi S S \\ S\ D &: \overline{D}\tilde{\phi} S \\ S\ T &: \mathrm{Tr}[\overline{T}\Sigma S] \\ D\ D &: \overline{D} D^C \varphi \text{ or } \overline{D}\Delta D^C \\ D\ T &: \tilde{\phi}^\dagger \overline{T} D \\ T\ T &: \mathrm{Tr}\left[\varphi \overline{T}^C T\right] \end{aligned} \tag{3.74}$$

For example, adding an extra Higgs triplet Σ to the SM allows to produce the M_{LL} which was forbidden by symmetries before. This is sometimes called see-saw type II. It is one of the UV completions of the SM which gives neutrino masses at tree-level.
Neutrino masses might not occur at tree-level but at one- or two-loop order, when they do not couple directly to scalars, which acquire a vacuum expectation value. Some realizations are found in plenty of radiative see-saw models see Chapter 5. These radiative models need Majorana neutrinos and thus violate lepton flavor conservation. Lepton flavor violation leads to flavor changing processes which can be constraint by other experiments than neutrino experiments.

3.5 NEUTRINO MASS MEASUREMENTS

From oscillation experiments the squared mass differences for neutrinos are known, but not the absolute mass scale. The current constraints are consistent with either two or three non-zero neutrino masses. After describing some mechanisms for neutrino mass generation, this section is dedicated to experimental searches and constraints on neutrino masses. It is based on [193].
There are different options to determine or constrain neutrino masses, the limits might depend on the neutrino mass hierarchy. Related to what experiments are probing, they are sensitive to different mass parameters. Obtaining the mass of one flavor allows to reconstruct all other masses either for flavor or mass eigenstates using the oscillation data on mass differences and mixing angles.

3.5.1 *Cosmology*

Similarly to other dark matter particles, neutrinos are involved in structure formation. As they are light and relativistic at the time of structure formation, they can dilute small scale structures. Due to this, they are not good cold dark matter candidates.
In the same fashion as CMB photons, at some point the neutrinos decoupled from thermal equilibrium. Hence, there is a background of cosmic neutrinos of around 330 cm^{-3} with a temperature, which can be inferred from the CMB photon temperature. Before the freeze-out, neutrinos have been in thermal equilibrium with the other particles by Z, W and γ mediated interactions. They decoupled when their interaction rate fell below the Hubble expansion – compare the freeze-out mechanism in Eq. 2.35. Yet, the free electrons and positrons still annihilate to neutrinos increasing their temperature. Taking into account this reheating and the expansion of the Universe, the neutrino temperature today can be calculated to be around 1.95 K, assuming vanishing neutrino masses.
Cosmological studies are sensitive to the sum of neutrino masses $\sum_i mi$. An upper bound of order 0.1 eV can be derived from Planck data [194], as there is a link between CMB and neutrino background. A combined analysis of data from Planck [1, 194], 6dFSS [195], SDSS [196] BOSSLOWZ and CMASSDRII [197] deducted in [193] yields limits for normal hierarchy (NH) and inverted hierarchy (IH)

$$\sum_i m_i \geqslant \begin{cases} 0.06\text{eV} & (\text{NH}), \\ 0.10\text{eV} & (\text{IH}). \end{cases}$$

These constrains depend on the model which was used to analyze the data.

3.5.2 *Neutrinoless double-β decay*

Besides cosmological studies, the investigation of particle physics motivated processes is promising. For example, neutrinoless double-β decay ($0\nu\beta\beta$), which is only possible for Majorana neutrinos, see Fig. 3.30. The two Majorana neutrinos cancel each other out, there are only charged leptons in the final state. Normal double-β decay ($2\nu\beta\beta$) is allowed, if the state with lower energy cannot be reached by two subsequent β decays. This process of $2\nu\beta\beta$ leads to two neutrinos along with two charged leptons in the final state. If the final state contains no neutrinos, the spectrum shows a sharp line at the endpoint of the continuous $2\nu\beta\beta$, as all momentum is transferred to the charged leptons which can be detected. $0\nu\beta\beta$ is sensitive to a mass combination including the CP phase $m_{\beta\beta}^2 = \left|\sum_i |U_{ei}|^2 m_i e^{i\delta_i}\right|$. This combination can be seen as an effective Majorana mass. It coherently sums over all neutrino flavors. The decay rate of such a process can

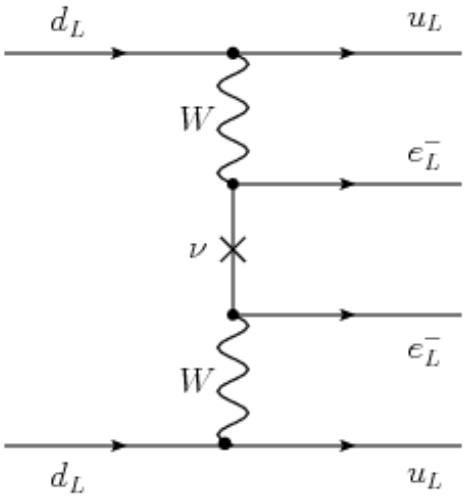

Figure 3.30: Diagram for neutrinoless double-β decay. As a Majorana particle the neutrino takes part in both decays. Figure taken from [198]

be very suppressed by the nuclear matrix element M associated with the decay as the half life is given as

$$T_{1/2}^{-1} = G\,|M|^2\,m_{\beta\beta}. \tag{3.75}$$

where G is the phase space factor.
Until now, there is no observation of $0\nu\beta\beta$. Thus, experiments set lower bounds on the half-life and consequently upper bounds on $0\nu\beta\beta$. In [193] a combined analysis from KamLAND-Zen [199], GERDA [200] and EXO-200 [201] yields a result of

$$m_{\beta\beta} < 0.18\text{eV at } 2\sigma,$$

which does not depend on the mass hierarchy.

3.5.3 *Supernovae*

In addition to the before mentioned sources, this subsection is also based on [202].
When looking for neutrinos, supernovae provide a less model dependent framework. In order to gain information on neutrino masses, the photon and neutrino arrival times from a supernova explosion can be compared. This difference probes the effective ν_e mass $m_{\nu_e}^2 = \sum_i |U_{ei}|^2 m_i^2$ which is an incoherent sum. Since neutrinos are not massless, the delay depends on kinematical considerations.
When a star turns into a supernova, it collapses and matter falls towards its center due to gravity. The pressure increases until the short ranged nuclear forces become repellent. Energy loss is then conveyed by de-leptonization $p + e^- \to n + \nu_e$, which produces a lot of electron neutrinos. Most of the energy is transported by neutrinos. Only

about 1 % is emitted as light and yet a supernova is very bright. Due to their small cross section, neutrinos can travel through the medium. This cycle of collapsing and energy release continues until the maximal density is reached. Within the explosion process, the hull of the star is ejected forming a shock front. One important assumption is, that the neutrinos leave the supernova all at approximately the same time, traveling through the shock. Matter enhanced oscillation can happen in the outer hull regions and vacuum oscillations as the neutrinos travel to Earth. As neutrinos are massive, they cannot arrive at the same time as the photons. The delay in arrival time Δt from a supernova at distance d depends on the neutrino mass m_{ν_e} and on the kinetic energy E_ν as

$$\Delta t = d\frac{m_{\nu_e}^2}{2E_\nu^2}. \tag{3.76}$$

In 1987 a supernova occurred in the large Magellanic cloud around 50 kpc away. This supernova SN1987A was detected by the water cherenkov telescopes IMB [203] and Kamiokande [204]. Kamiokande observed 24 neutrinos within a 13 s interval. The ν energy ranged between 10 MeV and 40 MeV. Only this few events were recorded as the distance was quite large and the ν cross section is small. Still it allowed to put a limit of $m_{\nu_e} < 5.8$ eV [205].
If a supernova burst is observed, it might be possible to detect the neutrino mass hierarchy by the modulation of the shock seen in neutrino telescopes like IceCube [206]. The signal would appear as diffuse correlated noise over all detector modules. The energy deposition of ν from Supernovae can be measured and the MSW effect might occur, if the ν have to travel through Earth in order to be detected. The comparison between IceCube and another efficient neutrino telescope like the planned Hyper-Kamiokande [207] could allow to determine the mass hierarchy.

3.5.4 β-*decay*

The spectrum of a single β-decay, for example in tritium, contains kinematical information about the neutrino masses. It is sensitive to a mass combination for ν_e which is $\sum_i |U_{ei}|^2 m_i^2$. It can be seen as an average ν_e mass. This section contains some β-decay experiments. In addition to the above sources, it is also based on [208, 209].
Single β-decay follows the process

$$(Z.A) \to (Z, A-1) + e^- + \overline{\nu}_e.$$

The exact endpoint of the spectrum depends on the neutrino mass. It is associated with neutrino momentum which can be expressed $p_\nu^2 = (E_{end} - E)^2 - m_\nu^2$ where $E_{end} - E$ is the neutrino energy, when E

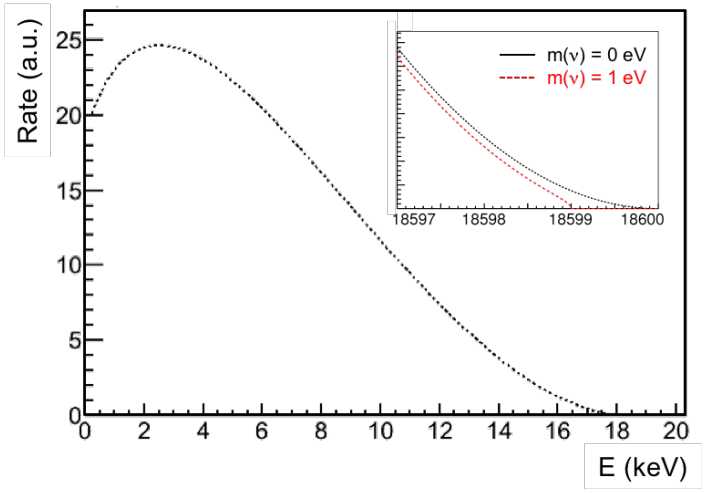

Figure 3.31: The β-decay spectrum is shown with a zoom on the theoretical endpoint for massless neutrinos (blue) or neutrinos with masses of 1 eV (red). Figure taken from [208]

is the measured energy of electrons, while neglecting the nuclear recoil. Theoretically, the endpoint is $E_{end} = Q - E_{rec}$ with the total decay energy Q and the nuclear recoil energy E_{rec} . From the exact determination of the endpoint, the neutrino mass can be calculated. For this the nuclear matrix element describing the processes is needed. Up to the endpoint the spectrum is assumed to be continuous, when distributing kinetic energy between the electron and the neutrino. The endpoint is reached, when the electron gets all kinetic energy and the neutrino is only left with the energy necessary for its non-zero rest mass. The shape around the endpoint gets altered with respect to massless neutrinos see Fig. 3.31.
For single β-decay investigations, either a calorimeter type measurement can be used, where source is embedded in detector, or a spectrometer type measurement, where source and detector are separated. A well suited isotope for this survey is tritium ^3H. It has a short half life of 12.3 yrs and a rather low endpoint energy of 18.6 keV. Even though, the endpoint energy is large enough to be above detector thresholds, the expected flux is very small. This puts high demands on background reduction in experiments.
A very large experiment with low background expectations is KATRIN (**Ka**rlsruhe **tr**itium **n**eutrino experiment) [210]. It observes the tritium decay

$$^3H \rightarrow ^3 He + e^- + \overline{\nu}_e.$$

For this purpose, a high luminous windowless gaseous molecular tritium source was built. Which is connected to a specially designed spectrometer, which uses the so called MAC-E filter technique. Strong magnetic fields are utilized to guide electrons adiabatically without energy loss together with an electrostatic filter. This functions as a

high pass filter on electrons. For background reduction wire electrodes and shielding are used. The detector is designed for around 0.93 eV energy resolution in the vicinity of the β decay endpoint.
Before KATRIN, the Mainz [211] and Troitsk [212] experiment measured the endpoint of tritium putting a strong limit on ν_e to be below 2.05 eV. With KATRIN it is expected to reach limits down to 0.2 eV.

4

LEPTON FLAVOR VIOLATION

Lepton flavor differentiates between the three lepton families within the SM, as they have different Yukawa coupling strength. Decays like $\mu^- \to e^- \overline{\nu}_e \nu_\mu$ seem to indicate lepton flavor conservation. Yet, this is not a symmetry imposed on the SM Lagrangian by any gauge symmetry. Only the absence of right-handed neutrinos ν_R and the presence of only one Higgs doublet prohibits lepton flavor violating decays. When diagonalizing the flavor eigenstates to the matter eigenbasis, this does not affect the interaction terms with Z bosons and photons, hence there is no flavor violation.
In the SM, as mentioned before, neutrinos are massless. The recent observation of neutrino oscillation implies, that they indeed have masses different from zero. Neutrino oscillations violate lepton flavor, as a neutrino of one flavor oscillates to a neutrino of another flavor. It is not possible to keep flavor conservation for massive neutrinos. The mass generation involves new couplings for the lepton doublets. Which give rise to other lepton flavor violating processes as well (see Chapter 3). The same dimension five operator, which provides Majorana neutrino masses, is responsible for LFV at one-loop level. Models with LFV appearing on tree-level need higher dimensional operators. LFV processes are for example μ decays like $\mu \to e\gamma$ and $\mu^- \to e^- e^- e^+$ or μ conversion in nuclei $\mu N \to eN$. Similarly, the presence of an extra Higgs doublet would lead to LFV processes, unless there is an additional $\mathbb{Z}_2$ symmetry like R-parity in supersymmetric models. This chapter, which is based on the review [213] by Calibbi and Signorelli, will give a short introduction and overview over the current experimental status. Recent experiments were able to put stringent bounds on LFV branching ratios, but no direct evidence of such a process has been observed.

4.1 EXPERIMENTS

Most experiments investigating LFV processes are looking for μ decay and conversion. The mass $m_\mu = 105.6583745(24)$ MeV and lifetime $t_{1/2} = 2.1969811(2) \times 10^{-6}$ s of μs are known to a very high precision, reducing possible uncertainties. Further, it is possible nowadays to create μ beams directly. Before, pion beams or μs from cosmic rays have been used. In order to achieve good results, experiments need to have a very low SM background and a high single event detection efficiency. As in many other low background experiments, one has to find a balance between these two. The typical signatures in the rest

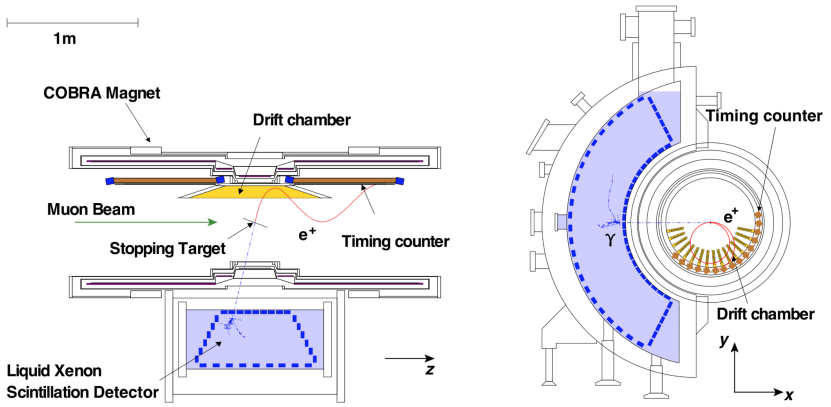

Figure 4.32: Schematic overview over the MEG detector. It shows the way of the μ beam onto a thin target. The positrons are detected in a drift chamber, the γs are detected by a liquid xenon scintillator. Image from [213]

frame of the decaying μ are coincident particles with balanced momenta. The aim is to stop the incoming μ within a thin target, such that the μ is basically at rest. Conversion in nuclei alters the observed spectrum with regard to the decay of μ in vacuum.
The momenta and energy of produced charged leptons can be measured by calorimeters and be tracked in magnetic fields. Mostly, tracking with amplification and collection of ionization needs for a lot of detector modules, which can be relatively slow. Whereas calorimeters need to be efficient at collecting the entire electromagnetic shower induced by an electron. Hence, one does need fast but not too many detectors. If there are photons in the final state, these can either be observed directly by PMTs, which have high detection efficiencies, or by conversion to e^-e^+ pairs in a suited materials, which offers good energy resolution.

PROCESS: $\mu \to e\gamma$

One of the most investigated LFV processes is the decay of a μ^+ into a photon and a positron. The signature of the process $\mu^+ \to e^+\gamma$ consists of a back-to-back photon and positron, which both have the same energy of about half the muon mass. The largest backgrounds come either from radiative μ decays $\mu^+ \to e^+\nu_e\overline{\nu}_\mu\gamma$ with small neutrino momenta and nearly back-to-back emission of γ and e^+. Or it might be an accidental correlation of e^+ from the SM μ decay and a γ, which happens to have the right energy. The extra γ can be produced as Bremsstrahlung or from another μ decay. The latter is most limiting for current experiments. Therefore, good γ energy resolution is needed for background rejection. Best signal-to-noise ratios are achieved with continuous μ beams.
Currently, the most stringent limits come from the MEG detector [214], which is shown schematically in Fig. 4.32. A μ beam hits a

thin stopping target inside the COBRA (**Co**nstant **B**ending **Ra**dius) magnet, which is specially designed for this purpose. The produced γs are detected by a 800 liter liquid xenon tank, which is monitored by around 800 PMTs. The positron momentum is measured within drift chambers and subsequent plastic scintillators. As no signal was observed, MEG places an upper limit on the branching ratio of

$$\mathrm{BR}(\mu \to e\gamma) < 4.2 \times 10^{-13}. \tag{4.77}$$

As the current MEG setup has reached its maximal sensitivity, an upgrade to MEG II [215] is planned. It will reuse the existing MEG setup and expects to reach a sensitivity of

$$\mathrm{BR}(\mu \to e\gamma) = 5 \times 10^{-14}, \tag{4.78}$$

which is around one order of magnitude below the current limit.

PROCESS: $\mu \to 3e$

The signature of the μ^+ decay to $e^+e^-e^+$ is the three charged leptons with their momenta lining up within a plane starting from the same origin. Kinematics in this case limit the maximum momentum to half the muon mass. The entire energy should add up to the whole muon mass. Typical backgrounds are from SM μ decays $\mu^+ \to e^+e^+e^-\nu_e\overline{\nu}_\mu$ with small neutrino momenta or the accidental coincidence between two or three SM μ decays. Yet, these falsely correlated particles will not originate from the same point, so background rejection needs for good position reconstruction and tracking. As the final state momenta can vary over a broad range, it is necessary to have a low energy threshold, as well as good resolution over the whole range.

The strongest limit on the branching ratio for this decay is from the SINDRUM experiment [216]. Within a magnetic solenoid field a μ beam is stopped within a thin target. The target is surrounded by concentric proportional counting wire chambers and enclosed by a layer of plastic scintillators. The measurements constrain

$$\mathrm{BR}(\mu \to 3e) < 1.0 \times 10^{-12}. \tag{4.79}$$

For the future the Mu3E experiment [217] is planned with an expected sensitivity around 10^{-16}. It will use the same μ beam as the MEG and MEG II experiment, stopping the μ within a thin Mylar target inside a solenoid magnetic field. The tracking is done by silicon pixel detectors and a fiber detector will time the detections. The overall resolution for the μ decay to three leptons is limited by multiple Coulomb scattering.

PROCESS: $\mu + N \to e + N$

Similar to the μ decay in vacuum, the process can happen to μ in

bound states. As the conversion takes place inside the nucleus, only μ^- can take part. When looking for conversions, which leave the nucleus unexcited, the rate is proportional to the μ capture, as all energy is transferred to the electron. Hence, the signal consists of an monoenergetic e^- with an energy around the μ mass. It is easiest to measure the conversion rate CR ,instead of the branching ratio. Where CR is defined as the ratio of conversion and μ capture width.

$$\mathrm{CR}\,(\mu\mathrm{N} \to e\mathrm{N}) := \frac{\Gamma\,(\mu - e \text{ conversion})}{\Gamma\,(\mu \text{ capture})}. \tag{4.80}$$

This also reduces the model dependent uncertainties from the nuclear matrix elements.
The main background comes from μ decays outside nuclei, producing electrons at the right energy, radiative π capture yielding e^-e^+ pairs and cosmic rays interacting within the detector. The decay of μ which are not bound can be rejected by precisely measuring the electron energy which demands a good energy resolution. The π process is correlated with the incoming beam hence a pulsed beam will allow to reject these events by picking an appropriate time window. Cosmic ray interactions can be vetoed by an outer detector surrounding the actual detection device.
Currently the best limit is from SINDRUM II [218] as

$$\mathrm{CR}\,(\mu\mathrm{N} \to e\mathrm{N}) < 7 \times 10^{-13}. \tag{4.81}$$

There are two future experiment planned looking for this process. On the one hand Mu2e [219] at Fermilab and on the other COMET [220] at J-Parc. The have planned to reach sensitivities around

$$\mathrm{CR}\,(\mu\mathrm{N} \to e\mathrm{N}) \leqslant 7 \times 10^{-17}, \tag{4.82}$$

which is many orders of magnitude better than the SINDRUM II limit. Yet, these are rather big and complicated set ups which take some time. Currently, DeeMe [221] is also under construction at J-Parc is. DeeMe is much simpler than COMET, allowing for earlier data taking. It is expected to reach a sensitivity of 10^{-15} for conversion in silicon carbide SiC, which has a high μ capture rate. The idea is to stop a proton beam inside a SiC target producing πs, which decay to μs that can be captured by nuclei. Again, wire chambers and magnetic spectrometers are used to observe the process.

LFV PROCESSES INVOLVING τ LEPTONS

Instead of LFV process of μ, one can look at τ leptons. The τ decays can happen via similar channels as μ decays, yet the larger mass of the τ lepton allows for hadronic final states as well. The issue is, that the τ lifetime is much shorter and they are not as easy to produce as μ. Currently, the best sources for τs are electron and proton accelerators, as B-factories have a large production efficiency for τ leptons.

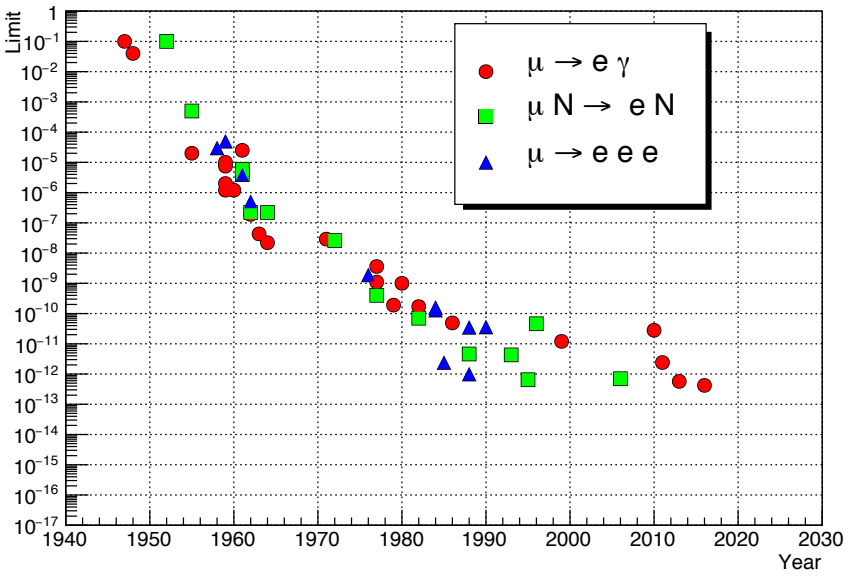

Figure 4.33: Evolution of LFV sensitivities over time. Starting from first measurements in the 1940s reaching the current status. Image from [213]

There are two experiments located at different sites, which look into LFV τ decays. Originally, they are designed to investigate CP violation with B-mesons. There is BarBar [222] at SLAC and Belle [223] at KEKB. The production always features a $\tau^+\tau^-$ pair. Hence, a clear signature is found when identifying both τ leptons by adding up the entire energy of the decay products. Different than SM τ decays LFV processes do not involve neutrinos in the final state. Thus, energy reconstruction allows for good background rejection. Current limits obtained at Belle and BarBar are shown in Tab. 4.1 along with the observations mentioned before. Allover, LFV experiments were able to push the sensitivity on the branching ratios further and further over the past decades, starting with μ from cosmic rays, until using stopped μ beams directly. An overview over the time evolution is shown in Fig. 4.33.

4.2 THEORY

The exact realization of lepton flavor violation depends heavily on the underlying model. In Chapter 5 three radiative models with neutrino masses are presented. All of them feature lepton flavor violating processes at one-loop order. For the three models lepton flavor violation is explained on a theoretical basis. In addition several loop topologies involved in processes like $\mu \rightarrow e\gamma$ for example are summarized in Appendix I.

Table 4.1: Current and future limits on lepton-flavor violating processes.

Process	Current limit		Future expectation	
$\mu \to e\gamma$	5.7×10^{-13}	[214]	6×10^{-14}	[224]
$\tau \to e\gamma$	3.3×10^{-8}	[222]	$\approx 3\times10^{-9}$	[225]
$\tau \to \mu\gamma$	4.4×10^{-8}	[222]	$\approx 3\times10^{-9}$	[225]
$\mu \to 3e$	1.0×10^{-12}	[216]	$\approx 10^{-16}$	[217]
$\tau \to 3\mu$	2.1×10^{-8}	[223]	$\approx 10^{-9}$	[225]
$\tau^- \to e^-\mu^+\mu^-$	2.7×10^{-8}	[223]	$\approx 10^{-9}$	[225]
$\tau^- \to \mu^- e^+ e^-$	1.8×10^{-8}	[223]	$\approx 10^{-9}$	[225]
$\tau \to 3e$	2.7×10^{-8}	[223]	$\approx 10^{-9}$	[225]
μ^- Ti $\to e^-$ Ti	4.3×10^{-12}	[226]	$\approx 10^{-18}$	[227]
μ^- Au $\to e^-$ Au	7.0×10^{-13}	[218]	–	
μ^- Al $\to e^-$ Al	–		$10^{-15} - 10^{-18}$	[228]
μ^- SiC $\to e^-$ SiC	–		10^{-14}	[221]

Part III

MAIN PART

5

RADIATIVE MODELS FOR NEUTRINO MASSES

In (Chapter 3), especially Section 3.4, mass generation mechanisms for neutrinos are presented. This chapter will present some radiative see-saw models in more detail. A special focus is put on the scotogenic model, in Section 5.1, as an introductory example, quickly going over its field content, neutrino masses and lepton flavor violation. Followed by a broad phenomenological investigation of a model called T12A in Section 5.2. It starts with the model description, going to dark matter, followed by neutrino masses and lepton flavor violation. After which two random scans are presented, which analyze the parameter space of the model. The last sections are about LHC constraints and give an outlook on one-loop mass corrections. At last, a short overview on the T13A model is given in Section 5.3.
All of these models do not only contain neutrino masses, but also dark matter candidates, which makes them very appealing. From the overview in Eq. 3.74, it becomes obvious, that neutrino masses demand the introduction of new particles. Given the correct field content, this can allow for neutrino mass generation at one-loop level. In addition, if a suitable neutral field is present, the models can also describe dark matter. Often a $\mathbb{Z}_2$ symmetry is introduced, which in some cases is needed to prevent tree-level neutrino masses and also to stabilize dark matter.
After symmetry breaking, these models feature diagrams for neutrino masses at one-loop level as shown in Fig. 5.34. The loop responsible for the masses contains a fermion and a scalar connecting the outer neutrino lines. Before electro-weak symmetry breaking, there are sev-

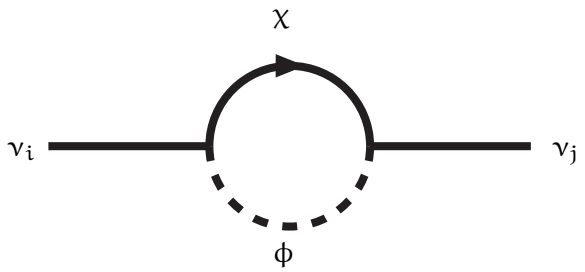

Figure 5.34: Neutrino mass generation at one-loop level.

eral topologies which can lead to neutrino masses and dark matter. The fields allow to couple two Higgs fields to two neutrino fields, causing the neutrino masses due to symmetry breaking. In principle, the SM is extended by new fields, scalar and fermionic – see Eq. 3.74 – arranged as singlet or n-tuplets regarding $SU(2)$. A classification of all different topologies with up to four new fields (not considering

the different generations of same field types) was done in [229]. They followed a work on the dimension five Weinberg operator at one loop in [230] and identified the viable contributions, which also contain dark matter. The notation within this thesis follows their work. The schematic view for one-loop topologies with four legs without field assignment is found in Fig. 5.35.

Therefore, by introducing new scalar ϕ and fermionic fields χ, the

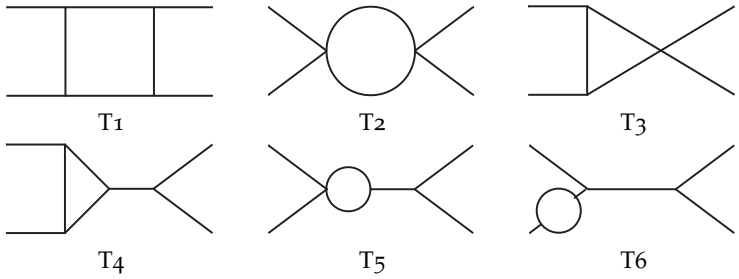

Figure 5.35: An overview of loop-topology classification. Figure drawn according to the reference in [230].

different loop topologies involving the fields, which are shown in Fig. 5.36, can be obtained. Since a dark matter candidate is stable, all particles in the loop have to be odd under the new $\mathbb{Z}_2$ symmetry. Hence, only an even number of odd particles can appear in one vertex. Furthermore, dark matter has to be neutral i.e. a color-singlet. This demands for all particles within the loop to be color-singlets. Its hypercharge $Y = 2(Q - I_3)$ (Q is the charge, I_3 the third component of the weak-isospin) has to be zero. Starting from this, the hypercharges for all other fields can be determined up to a factor α. Thus, starting from one topology, several different Lagrangians can be found which reproduce the diagram.

Diagrams of type T2 do not match by dimensional arguments, whereas topologies like T4, T5 and T6 either have to feature more additional symmetries than $\mathbb{Z}_2$, to restrict dark matter or they do not prevent neutrino masses at tree-level.

The presence of dark matter fields and neutrino masses gives a handle on the parameter space of each model by looking at dark matter and neutrino searches. Also, some models can give rise to exotic charges such as doubly charged scalars or fermions which can be easily constrained by LHC data.

Some of the models have been investigated before. For example, the scotogenic model [66, 231, 232] with a scalar doublet (inert Higgs) and an additional fermion singlet as well as similar models with two scalars and one fermion [233–236] which are all of type T3. A model of type T1-1 with three scalars and one fermion [237] and a model like T1-3 which contains only one scalar and three fermions [238, 239] have been studied before with the restriction of considering mostly

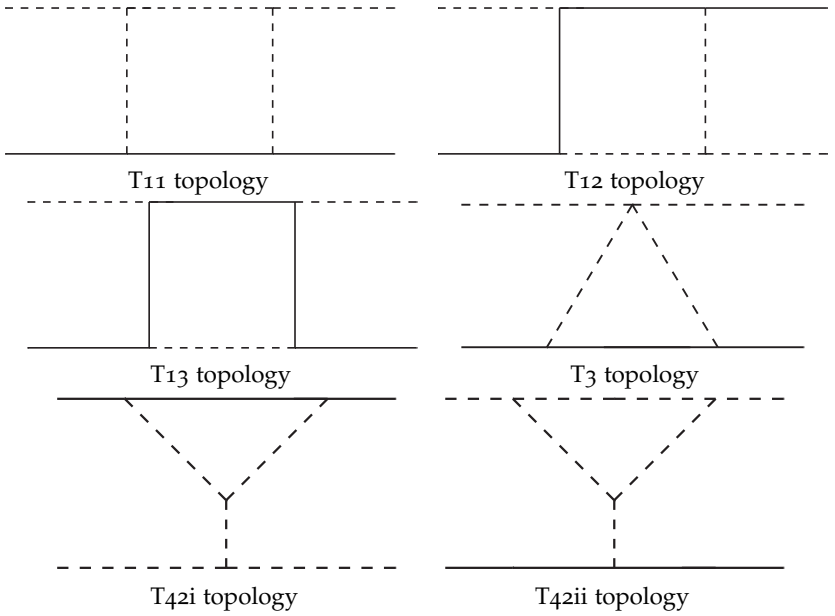

Figure 5.36: Schematic diagrams for neutrinos coupling to Higgs at one-loop level before electro-weak symmetry breaking. Plots redone from [229].

scalar dark matter mostly. A T1-2 type model with doublet and triplet scalars and fermions is presented in [240].

5.1 THE SCOTOGENIC MODEL

The so-called scotogenic model is a model for radiative neutrino masses and dark matter proposed and investigated by Ma [231]. It is very simple, so it is used to familiarize with calculations within such models before going to more complex models like T12A and T13A. The calculations follow mostly the results from the paper [231] except for $\mu \to e\gamma\gamma$ which is performed for this work.

5.1.1 *Model description*

In order to provide the ingredients to construct the Weinberg dimension-five operator, three right-handed Majorana fermion singlets N_i, which are basically right-handed neutrinos, are added to the Standard Model. An extra complex scalar doublet

$$\eta = \begin{pmatrix} \eta^+ \\ \frac{1}{\sqrt{2}}\left(\eta_R^0 + i\eta_I^0\right) \end{pmatrix}, \tag{5.83}$$

is also introduced. In principle, this would allow for a Dirac neutrino mass term – compare Section 3.4. However, for the model not to be excluded by the LHC and other experiments, N_i need to be heavy. An

extra $\mathbb{Z}_2$ is added to render N_i and η stable, which would otherwise decay to lighter particles. All Standard Model particles are even under the new symmetry.
The model allows for the Yukawa interaction

$$L = f_{ij}(H^- \nu_i + \overline{H} l_i) l_j^c + y_{ij}(\overline{\nu}_i \eta^0 - \bar{l}_j \eta^+) P_R N_j^c + \text{H.c.} \tag{5.84}$$

where H is the Standard Model Higgs doublet and l_i denotes any charged lepton, where ν_i is the neutrino. Additionally there are the Majorana mass terms for N_i

$$\frac{1}{2} M_i \overline{N}_i N_i, \tag{5.85}$$

and a quartic scalar term

$$\frac{1}{2} \lambda_5 (H^\dagger \eta)^2 + \text{H.c.}. \tag{5.86}$$

The corresponding Higgs potential before electro-weak symmetry breaking is

$$\begin{aligned} V =& m_1^2 H^\dagger H + m_2^2 \eta^\dagger \eta + \frac{1}{2}\lambda_1 (H^\dagger H)^2 + \frac{1}{2}\lambda_2 (\eta^\dagger \eta)^2 + \lambda_3 (H^\dagger H)(\eta^\dagger \eta) \\ &+ \lambda_4 (H^\dagger \eta)(\eta^\dagger H) + \frac{1}{2}\lambda_5 [(H^\dagger \eta)^2 + \text{h.c.}]. \end{aligned} \tag{5.87}$$

After electro-weak symmetry breaking, where the Higgs acquires the vacuum expectation value $v = 246$ GeV, the resulting masses of physical scalar bosons are according to [231]

$$\begin{aligned} m^2(\eta^\pm) =& m_2^2 + \lambda_3 v^2, \\ m^2(\eta_R) =& m_2^2 + (\lambda_3 + \lambda_4 + \lambda_5) v^2, \\ m^2(\eta_I) =& m_2^2 + (\lambda_3 + \lambda_4 - \lambda_5) v^2. \end{aligned} \tag{5.88}$$

Due to the $\mathbb{Z}_2$ symmetry, η does not obtain a vacuum expectation value and does not mix with the Higgs field.
The lightest neutral odd particle is a dark matter candidate, so it can be either scalar or fermionic. The symmetry also forbids the direct Dirac mass term and makes neutrino masses appear at loop-level as lowest order as in Fig. 5.34 where the Fermion is any N_i and the scalar is η_R^0 or η_I^0, the neutral components of the scalar doublet after EWSB. Before EWSB the model features the T3 topology.

5.1.2 *Neutrino masses*

As mentioned before, the neutrino masses appear at one-loop level. The squared matrix element of Fig. 5.37 is calculated as in [**Ma**]. Starting from the digram in Fig. 5.37, where one explicitly looks at two

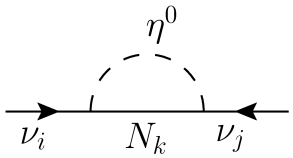

Figure 5.37: Neutrino mass generation for the Majorana neutrino part.

incoming neutrinos while ignoring whether they are Majorana neutrinos or not, the radiative correction by the exchange of η_R is determined as

$$I_R := -i\Sigma^{\nu}_{ij(k)} = -y_{ik}y_{jk}\int \frac{d^4q}{(2\pi)^4} P_R \frac{\not{q} + M_k}{q^2 - M_K^2} \frac{1}{(q-p)^2 - m_R^2}.P_R. \tag{5.89}$$

Where the neutrino ν has momentum p and q is the momentum running in the loop. The sum over all three additional heavy neutrinos N_k is omitted here. A similar expression is obtained for the exchange of η_I. The correction must be valid for any choice of p, so it is possible to take p equal to zero. By applying dimensional regularization and going from 4 to D dimensions and identifying the Passarino-Veltman integrals – see Appendix I – the following result is obtained

$$\begin{aligned} I_R &= y_{ik}y_{jk}M_k \frac{i}{16\pi^2} B_0(p^2 = 0, M_k^2, m_R^2), \\ I_I &= -y_{ik}y_{jk}M_k \frac{i}{16\pi^2} B_0(p^2 = 0, M_k^2, m_I^2). \end{aligned} \tag{5.90}$$

The loop integral B_0 with this argument set is given as

$$\begin{aligned} B_0(0, m_0^2, m_1^2) =& \Delta + 1 \\ & - \frac{1}{m_1^2 - m_0^2}(m_1^2 \log(\frac{m_1^2}{\mu^2}) - m_0^2 \log(\frac{m_0^2}{\mu^2})), \end{aligned} \tag{5.91}$$

with the divergent part summarized in Δ as shown in Section I.1. Adding I_R and I_I leads to a cancellation of the divergent parts. This is what one would expect, as this is the leading order for neutrino masses and hence the result should be finite. The sum yields

$$\begin{aligned} I_R + I_I =& \frac{i y_{ik}y_{jk}M_k}{16\pi^2} \times \\ & \left(-\frac{1}{m_R^2 - M_k^2} \left(m_R^2 \log\left(\frac{m_R^2}{\mu^2}\right) - M_k^2 \log\left(\frac{M_k^2}{\mu^2}\right)\right) \right. \\ & \left. + \frac{1}{m_I^2 - M_k^2} \left(m_I^2 \log\left(\frac{m_I^2}{\mu^2}\right) - M_k^2 \log\left(\frac{M_k^2}{\mu^2}\right)\right)\right). \end{aligned} \tag{5.92}$$

Further simplification leads to an expression for neutrino mass matrix elements

$$(M_\nu)_{ij} = \sum_k \frac{y_{ik}y_{jk}}{16\pi^2} M_k \times$$

$$\left(\frac{m_R^2}{M_k^2 - m_R^2}\log\left(\frac{m_R^2}{M_k^2}\right) - \frac{m_I^2}{M_k^2 - m_I^2}\log\left(\frac{m_I^2}{M_k^2}\right)\right). \tag{5.93}$$

Analogous to Fig. 5.37, a diagram for Dirac neutrino mass terms could naively be constructed as in Fig. 5.38. However, this diagram

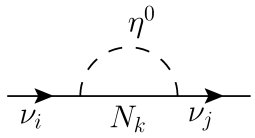

Figure 5.38: Dirac neutrino mass contribution at one-loop level

does not give a contribution to the mass but only contains a correction to the kinematic part. The amplitude without spinors and without summing over all three neutrino flavors is

$$A = \int \frac{d^4q}{(2\pi)^4}\frac{y_{ik}y_{ij}}{2}P_R\left(\frac{\not{q}}{(q^2 - M_k^2)((p-q)^2 - m_r^2)} - \frac{\not{q}}{(q^2 - M_k^2)((p-q)^2 - m_I^2)}\right)P_L, \tag{5.94}$$

where $P_{R(L)}$ is the right-handed (left-handed) projector and q is the momentum inside the loop.
Tensor reduction allows to write A as

$$A = \frac{y_{ik}y_{jk}}{32\pi^2}P_R\not{p}\left(B_1(p^2, M_k^2, m_R^2) - B_1(p^2, M_k^2, m_I^2)\right). \tag{5.95}$$

In general this is proportional to p which is a purely kinematic contribution. One can infer, as expected, that neutrinos within this radiative model are Majorana neutrinos. Usually it is not necessary to distinguish between the two neutrino mass diagrams as one can just use the entire vertex with its left and right part to compute the neutrino masses.

5.1.3 *Lepton flavor violation*

When trying to assign lepton numbers to the new particles it can be seen that this is not possible without violating lepton flavor conservation by two units. Hence in the scotogenic model lepton flavor changing processes like $\mu \to e\gamma$, $\mu \to e3\gamma$ and $\mu \to 3e$ are allowed. In order to determine a branching ratio, the decay width needs to be calculated, for a general overview see Appendix C. Starting with $\mu \to e\gamma$ the contributing diagrams are shown in Fig. 5.39.

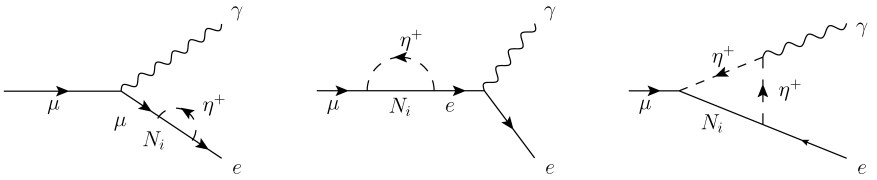

Figure 5.39: Feynman diagrams for $\mu \to e\gamma$.

The corresponding amplitudes are

$$M_a = \frac{-e y^*_{ie} y_{i\mu}}{2} \epsilon^*_\nu \overline{u}(p_e) P_R \gamma_\delta I_a^\delta \frac{\not{p}_e + m_\mu}{-m_\mu^2} u(p_\mu), \tag{5.96}$$

$$M_b = \frac{-e y^*_{ie} y_{i\mu}}{2} \epsilon^*_\nu \overline{u}(p_e) P_R \gamma^\nu \frac{\not{p}_\mu}{m_\mu^2} \gamma_\delta I_b^\delta u(p_\mu), \tag{5.97}$$

$$M_c = \frac{-e y^*_{ie} y_{i\mu}}{2} \epsilon^*_\nu \overline{u}(p_e) P_R \gamma_\delta I_c^{\delta\nu} u(p_\mu), \tag{5.98}$$

where the loop integrals are given by

$$I_a^\delta = \int \frac{q^\delta}{(q^2 - M_i^2)((q-p_e)^2 - m^2_{\eta^+})} \frac{d^4q}{(2\pi)^4}, \tag{5.99}$$

$$I_b^\delta = \int \frac{q^\delta}{(q^2 - M_i^2)((q-p_\mu)^2 - m^2_{\eta^+})} \frac{d^4q}{(2\pi)^4}, \tag{5.100}$$

$$I_c^{\delta\nu} = \int \frac{q^\delta (2q^\nu - 2p_e^\nu)}{(q^2 - M_i^2)((q-p_e)^2 - m^2_{\eta^+})((q-p_\mu)^2 - m^2_{\eta^+})} \times \frac{d^4q}{(2\pi)^4}, \tag{5.101}$$

and p_e and p_μ are the momenta of the electron and the muon, q is the momentum in the loop, m_μ is the mass of the muon. The mass of the electron m_e is assumed to be zero in comparison to m_μ. In order to solve the loop integrals $I_{a,b,c}$ Feynman parametrization is used – see Section I.3. Due to the vanishing electron mass and the approximation of small lepton masses in the loop functions only the triangular diagram with I_c gives a finite result. Its divergence is canceled by the purely divergent I_b whereas I_a is zero as it is proportional to m_e after evaluating the integral. One finds that the finite part I_c can be expressed as

$$I_{c,fin}^{\delta\nu} = \frac{i\pi^2}{(2\pi)^4} \frac{1}{m^2_{\eta^+}} F_2(\zeta_i) (p_\mu)^\delta (p_\mu)^\nu. \tag{5.102}$$

Here

$$\zeta_i := \frac{M_i^2}{m^2_{\eta^+}}, \tag{5.103}$$

and F_2 is a loop function defined as

$$F_2(x) := \frac{1 - 6x + 3x^2 + 2x^3 - 6x^2 \log x}{6(1-x)^4}. \tag{5.104}$$

The spin averaged squared amplitude $|M|^2 = |M_a + M_b + M_c|^2$ for the whole process is

$$|\overline{M}|^2 = K_2^2 \mathrm{Tr}(\not{p}_e P_R (\not{p}_\mu + m_\mu) P_L p_\mu^2). \tag{5.105}$$

which simplifies to

$$|\overline{M}|^2 = K_2^2 \mathrm{Tr}(\not{p}_e P_R \not{p}_\mu m_\mu^2), \tag{5.106}$$

by means of $\{\gamma_5, \gamma_\nu\} = 0$, $P_R P_R = P_R$ and $P_R P_L = 0$. The trace can be evaluated using the trace theorems Appendix A and the final result is

$$|\overline{M}|^2 = K_2^2 2 p_e p_\mu m_\mu^2. \tag{5.107}$$

In order to get familiar with automated calculation of branching ratios and scattering amplitudes with tools like FeynCalc **[Feyncalc]** the branching ratio of $\mu \to e\gamma\gamma$ is computed. All diagrams and their exchange diagrams in Fig. 5.40 contribute to this process. Additionally to the diagrams in the figure, the six exchange diagrams ($k_1 \leftrightarrow k_2$)) also contribute. The amplitudes corresponding to the diagrams in Fig. 5.40 are

$$\begin{aligned}
M_1 &= K \epsilon_{1\mu}^* \epsilon_{2\nu}^* \overline{u}_2 \gamma^\nu \frac{\not{p}_1 - \not{k}_1}{(p_1 - k_1)^2} P_R \gamma_\delta I_1^\delta \frac{\not{p}_1 - \not{k}_1 + m_1}{(p_1 - k_1)^2 - m_1^2} \gamma^\mu u_1, \\
M_2 &= K \epsilon_{1\mu}^* \epsilon_{2\nu}^* \overline{u}_2 P_R \gamma_\delta I_2^{\delta\nu} \frac{\not{p}_1 - \not{k}_1 + m_1}{(p_1 - k_1)^2 - m_1^2} \gamma_\mu u_1, \\
M_3 &= K \epsilon_{1\mu}^* \epsilon_{2\nu}^* \overline{u}_2 \gamma^\nu \frac{\not{p}_1 - \not{k}_1}{(p_1 - k_1)^2} P_R \gamma_\delta I_3^{\delta\mu} u_1, \\
M_4 &= K \epsilon_{1\mu}^* \epsilon_{2\nu}^* \overline{u}_2 P_R \gamma_\delta I_4^\delta \frac{\not{p}_2 + m_1}{-m_1^2} \gamma^\nu \frac{\not{p}_1 - \not{k}_1 + m_1}{(p_1 - k_1)^2 - m_1^2} \gamma^\mu u_1, \\
M_5 &= K \epsilon_{1\mu}^* \epsilon_{2\nu}^* \overline{u}_2 \gamma^\nu \frac{\not{p}_1 - \not{k}_1}{(p_1 - k_1)^2} \gamma^\mu \frac{\not{p}_1}{m_1^2} P_R \gamma_\delta I_5^\delta u_1, \\
M_6 &= K \epsilon_{1\mu}^* \epsilon_{2\nu}^* \overline{u}_2 P_R \gamma_\delta I_6^{\delta\mu\nu} u_1.
\end{aligned} \tag{5.108}$$

Where p_1 is the muon momentum, p_2 is the electron momentum, $k_{1,2}$ are the four-momenta of the photons from left to right which are associated with the index μ and ν. The momenta in the loop are always chosen such that q runs along the fermion line. The amplitudes for the exchange diagrams are obtained when exchanging k_1 with k_2 and the indices ν and μ. u_1 is the spinor corresponding to the muon with mass m_1 and momentum p_1, $\overline{u}_2$ is associated with the electron, which has negligible momentum p_2 and mass, $\epsilon_1 = \epsilon(k_1)$ and $\epsilon_2 = \epsilon(k_2)$.

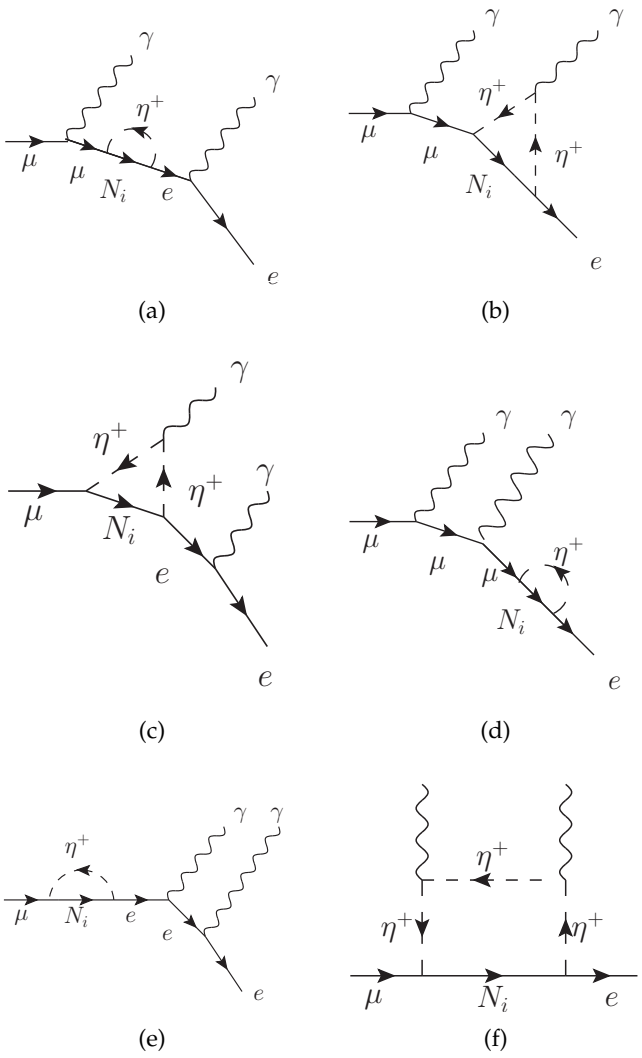

Figure 5.40: Feynman diagrams for $\mu \to e\gamma\gamma$ in the scotogenic model

The loop integrals are given by

$$
\begin{aligned}
I_1^{\delta} &= \int \frac{d^4q}{(2\pi)^4} \frac{q^{\delta}}{(q^2 - M_i^2)((q - p_1 + k_1)^2 - m_{\eta^+}^2)}, \\
I_2^{\delta\nu} &= \int \frac{d^4q}{(2\pi)^4} \frac{2q^{\delta}(q^{\nu} - p_2^{\nu})}{(q^2 - M_i^2)((q - p_1 + k_1)^2 - m_{\eta^+}^2)} \\
&\quad \frac{1}{((q - p_2)^2 - m_{\eta^+}^2)}, \\
I_3^{\delta\mu} &= \int \frac{d^4q}{(2\pi)^4} \frac{2q^{\delta}(q^{\mu} - p_1^{\mu})}{(q^2 - M_i^2)((q - p_1 + k_1)^2 - m_{\eta^+}^2)} \\
&\quad \frac{1}{((q - p_1)^2 - m_{\eta^+}^2)}, \\
I_4^{\delta} &= \int \frac{d^4q}{(2\pi)^4} \frac{q^{\delta}}{(q^2 - M_i^2)((q - p_2)^2 - m_{\eta^+}^2)},
\end{aligned}
$$

$$
\begin{aligned}
I_5^{\delta} &= \int \frac{d^4q}{(2\pi)^4} \frac{q^{\delta}}{(q^2 - M_i^2)((q-p_1)^2 - m_{\eta^+}^2)}, \\
I_6^{\delta\mu\nu} &= \int \frac{d^4q}{(2\pi)^4} \frac{4q^{\delta}(q^{\nu} - p_2^{\nu})(q^{\mu} - p_1^{\mu})}{(q^2 - M_i^2)} \\
&\quad \frac{1}{((q-p_2-k_2)^2 - m_{\eta^+}^2)} \frac{1}{((q-p_2)^2 - m_{\eta^+}^2)} \\
&\quad \frac{1}{((q-p_1)^2 - m_{\eta^+}^2)}.
\end{aligned} \tag{5.109}
$$

The treatment of the amplitudes and the loop integrals is similar to the cases for $\mu \to e\gamma$. It is assumed that the electron mass vanishes and for the loop functions the approximation of $m_{\mu} \ll M_i, M_{\eta^+}$ is made. With the help of the Feynman parametrization the loop integrals are evaluated in dimensional regularization. The calculation of the integrals can be found in Appendix I and especially in Section I.10.

$$
\begin{aligned}
I_1^{\delta} =& \frac{i\pi^2}{(2\pi)^4} \pi^{-2\epsilon} \int_0^1 dx N_1 \left(\Delta - \Gamma(1+\epsilon)\right) \log\left(\frac{A_1}{\mu^2}\right), \\
I_2^{\delta\nu} =& I_{21}^{\delta\nu} + I_{22}^{\delta\nu}, \\
I_{21}^{\delta\nu} =& 2g^{\delta\nu} \frac{i\pi^2}{(2\pi)^4} \pi^{-2\epsilon} (4\pi)^{\epsilon} \left(\frac{1}{2}\Delta \right. \\
& \left. - \int_0^1 \log\left(\frac{A_2}{\mu^2}\right) \delta(x+y+z-1) dx dy dz \right), \\
I_{22}^{\delta\nu} =& \frac{-i\pi^2}{(2\pi)^4} \left(k_1^{\delta} - p_1^{\delta}\right) \left(p_1^{\nu} - k_1^{\nu}\right) \frac{F_2(\zeta_i)}{m_{\eta^+}^2}, \\
I_3^{\delta\mu} =& I_{31}^{\delta\mu} + I_{32}^{\delta\mu}, \\
I_{31}^{\delta\mu} =& 2g^{\mu\delta} \frac{i\pi^2}{(2\pi)^4} \pi^{-2\epsilon} (4\pi)^{\epsilon} \left(\frac{1}{2}\Delta \right. \\
& \left. - \int_0^1 \log\left(\frac{A_2}{\mu^2}\right) \delta(1-x-y-z) dx dy dz \right), \\
I_{32}^{\delta\mu} =& \frac{-i\pi^2}{(2\pi)^4} \left(k_1^{\delta} - 2p_1^{\delta}\right) p_1^{\mu} \frac{F_2(\zeta_i)}{m_{\eta^+}^2}, \\
I_4 =& 0, \\
I_5^{\delta} =& \frac{i\pi^2}{(2\pi)^4} \pi^{-2\epsilon} p_1^{\delta} \int_0^1 dx (1-x) (\Delta - \Gamma(1+\epsilon) \log\left(\frac{A_1}{\mu^2}\right), \\
I_6 =& I_{61} + I_{62} + I_{63} + I_{64}, \\
I_{61} =& \frac{2}{3} \left(k_2^{\delta} + p_1^{\delta}\right) \frac{G_2(\zeta_i)}{m_{\eta^+}^2}, \\
I_{62} =& -2p_1^{\nu} \frac{F2(\zeta_i)}{m_{\eta^+}^2} + k_1^{\nu} \frac{H_1(\zeta_i)}{m_{\eta^+}^2},
\end{aligned}
$$

$$
\begin{aligned}
I_{63} =& \frac{2}{3} p_2^\mu \frac{G_2(\zeta_i)}{m_{\eta^+}^2} - p_1^\mu \frac{H_1(\zeta_i)}{m_{\eta^+}^2}, \\
I_{64} =& k_2^\delta \left(p_1^\mu \left(p_1^\nu H_2(\zeta_i) + p_2^\nu H_3(\zeta_i) \right) \right. \\
& \left. + k_2^\mu \left(p_1^\nu H_4(\zeta_i) + p_2^\nu H_5(\zeta_i) \right) \right) \\
& + k_1^\delta (p_1^\mu (\frac{3}{3} p_1^\nu H_2(\zeta_i) + p_2^\nu H_6(\zeta_i)) \\
& + k_2^\mu (\frac{3}{2} p_1^\nu H_4(\zeta_i) + p_2^\nu H_7(\zeta_i))),
\end{aligned} \tag{5.110}
$$

where $F_2(x)$ is as in Eq. 5.104, ζ_i as in Eq. I.380 and the other loop functions are listed in Section I.10. Using the results for the integrals from before one can identify the divergent and scale dependent parts of the amplitudes:

$$
\begin{aligned}
M_1^D &\propto \bar{u}_2 P_R \gamma^\nu \frac{\not{p}_1 - \not{k}_1}{(p_1 - k_1)^2} (\not{k}_1 - \not{p}_1)(-\frac{1}{2}\Delta + F) \frac{\not{p}_1 - \not{k}_1 + m_1}{(p_1 - k_1)^2 - m_1^2} u_1 \\
&= -\bar{u}_2 P_R \gamma^\nu (-\frac{1}{2}\Delta + F) \frac{\not{p}_1 - \not{k}_1 + m_1}{(p_1 - k_1)^2 - m_1^2} \gamma^\mu u_1, \\
M_2^D &\propto \bar{u}_2 P_R \gamma^\nu \frac{\not{p}_1 - \not{k}_1 + m_1}{(p_1 - k_1)^2 - m_1^2} \gamma^\mu u_1 \\
&\sim -M_1^D, \\
M_3^D &\propto \bar{u}_2 P_R \gamma^\nu \frac{\not{p}_1 - \not{k}_1}{(p_1 - k_1)^2} \gamma^\mu (\frac{1}{2}\Delta - F) u_1, \\
M_5^D &\propto \bar{u}_2 P_R \gamma^\nu \frac{\not{p}_1 - \not{k}_1}{(p_1 - k_1)^2} \gamma^\mu \frac{\not{p}_1^2}{m_1^2} (-\frac{1}{2}\Delta + F) u_1 \\
&\sim -M_3^D.
\end{aligned}
$$

with

$$
F = \int_0^1 (1-x) \log(\frac{A_1}{\mu^2}) dx. \tag{5.111}
$$

Adding up all amplitudes it is found that all the divergent parts cancel. The only finite contributions are obtained from the diagrams (b), (c) and (f) in Fig. 5.40 and their exchange diagrams, i.e. from $I_{2,3,6}$.
In order to obtain the decay width, the phase space integral is evaluated, but it contains infrared divergences, which appear when one of the photons is created with zero momentum. These can either be canceled by the appropriate emission diagrams or by applying an energy cut. The whole process itself is not convergent, as with the infrared divergences this process can be seen as a correction to $\mu \to e\gamma$, so one can only investigate both processes at the same time to obtain a convergent result including $\mu \to e\gamma\gamma$. The squared amplitudes are summarized in Section I.10. Still, it is sufficient to apply energy cuts, since detectors have certain energy limits for the detection of photons.

5.2 MODEL T12A

One of the models classified in [229] is called T12A as it is of the T12 topology. It contains two additional scalar and two additional fermion fields.
In the following, in Section 5.2.1 the model is described. In Section 5.2.2 the dark matter section of the model is evaluated. And in Section 5.2.3 neutrino masses are shown. This is followed by Section 5.2.5, which presents two numerical scans conducted for this work. Finally, Section 5.2.6 about LHC constraints and Section 5.2.7 , which shortly mentions one-loop mass corrections and gives a short outlook, are presented.

5.2.1 *Model description*

To define a T12 type model, the Standard Model is extended by a singlet Majorana Weyl fermion ψ_S. α, a parametrization of the hypercharge for the new fields, is set to zero. A vector-like fermion doublet ψ_D of hypercharge $1+\alpha$, a scalar singlet ϕ_S with hypercharge α and scalar doublet ϕ_D with hypercharge $1+\alpha$ are also introduced. An extra discrete $\mathbb{Z}_2$ is also established, to render dark matter stable. All new particles are odd and all Standard Model particles are even under this symmetry. This discrete symmetry also allows neutrino masses to appear at one-loop level and not at tree-level. α is introduced in order to have a correct quantum number assignment within topology T12. If $\alpha = -2$, a model with different hypercharges than T12A, is obtained. It is called inert Zee model [241], which already has been analyzed. Viable parameter regions within the inert Zee model regarding dark matter, neutrino masses and lepton flavor violation have been found.
Setting hypercharge $\alpha = 0$, fixes the hypercharges of all particles and the model T12A is obtained. The model T12A is equal to the model T12C with $\alpha = -1$, so the results presented here are applicable to T12C as well.
T12A belongs to the few models from the classification in [229], which allow for gauge coupling unification at a scale $\Lambda = \mathcal{O}(10^{13})$. Others are for example T13A with $\alpha = 0$ as well as the scotogenic model.
Regarding the $SU(2)_L \bigotimes U(1)_Y \bigotimes \mathbb{Z}_2$ symmetry group the new particles have the following quantum numbers:

$$\begin{aligned} \phi_S &\propto (1, 0, -), \\ \phi_D = \begin{pmatrix} \phi^+ \\ \phi_R + i\phi_I \end{pmatrix} &\propto (2, \frac{1}{2}, -), \\ \psi_S &\propto (1, 0, -), \end{aligned}$$

$$\psi_{D_1} = \begin{pmatrix} \psi^0_{D_1,L'} \\ \psi^-_{D_1,L} \end{pmatrix} \propto (2, -\frac{1}{2}, -),$$
$$\psi_{D_2} = \begin{pmatrix} -(\psi_{D_2,R})^\dagger, \\ (\psi^0_{D_2,R})^\dagger \end{pmatrix} \propto (2, \frac{1}{2}, -). \tag{5.112}$$

T12A contains the singlet-doublet scalar [242–245] and singlet-doublet fermion dark matter model [242, 243, 246–248] in addition to new terms which arise when linking both models together. The new terms give rise neutrino masses.
The next sections first introduce Lagrangians and mixings for the singlet-doublet models separately, before describing the additional Lagrangian for the lepton sector.

5.2.1.1 *Singlet-doublet scalar dark matter*

The Lagrangian of singlet-doublet scalar model is

$$\begin{aligned} \mathcal{L}_{SDS} = &- \left(\frac{1}{2} M^2_{S,S} \phi_S^2 + M^2_{S,D} |\phi_D|^2 + \frac{1}{2} \lambda_S \phi_S^2 |H|^2 \right. \\ &+ \lambda_D |\phi_D|^2 |H|^2 + \lambda'_D |\phi_D^\dagger H|^2 \\ &\left. + \frac{1}{2} \lambda''_D \left((\phi_D^\dagger H)^2 + \text{h.c.} \right) + A \left(\phi_D^\dagger H \phi_S + \text{h.c.} \right) \right), \end{aligned} \tag{5.113}$$

where H is the Standard Model Higgs doublet. The Higgs acquires a vacuum expectation value $v = 246 GeV$ in the process of electro-weak symmetry breaking. Hence, the term with A introduces a mixing between the real neutral scalars ϕ_S, ϕ_R and ϕ_I. ϕ_R and ϕ_I are the real and imaginary part of the neutral component of ϕ_D. This term is of Yukawa like shape and as the extra $\mathcal{Z}_2$ is unbroken, the new scalars have no quartic potentials and do not obtain vacuum expectation values but have explicit mass terms along with the five new couplings introduced in $\mathcal{L}_{SDS}$.
Extracting the squared mass matrix for real neutral scalars in the basis (ϕ_S,ϕ_R,ϕ_I) gives

$$M^2_S = \begin{pmatrix} \overline{M}^2_S & Av & 0 \\ Av & \overline{M}^2_D & 0 \\ 0 & 0 & M^2_{S,D} + \frac{1}{2} v^2 (\lambda_D + \lambda'_D - \lambda''_D) \end{pmatrix}, \tag{5.114}$$

with

$$\begin{aligned} \overline{M}^2_S &= M^2_{S,S} + \frac{1}{2} v^2 \lambda_S, \\ \overline{M}^2_D &= M^2_{S,D} + \frac{1}{2} v^2 (\lambda_D + \lambda'_D + \lambda''_D). \end{aligned} \tag{5.115}$$

Since there are no CP violating couplings, ϕ_I cannot mix with ϕ_S or ϕ_R. Only the upper left part of M^2_S, which is a 2×2 matrix, results in

a mixing of ϕ_S and ϕ_R. The characteristic equation for this upper left part is

$$(M_X^2 - \overline{M}_S^2)(M_X^2 - \overline{M}_D^2) - v^2 A^2 = 0. \tag{5.116}$$

It gives rise to two eigenvalues

$$M_{X_{1,2}}^2 = \frac{1}{2}\left(\overline{M}_S^2 + \overline{M}_D \pm \sqrt{(\overline{M}_S^2 - \overline{M}_D^2)^2 + 4v^2A^2}\right). \tag{5.117}$$

The third eigenstate X_3 obtains a mass of

$$M_{X_3}^2 = M_{S,D}^2 + \frac{1}{2}v^2\left(\lambda_D + \lambda'_D - \lambda''_D\right). \tag{5.118}$$

λ''_D in general introduces a mass splitting between the CP even and odd neutral doublet components. The corresponding transformation matrix U_S is (for $\overline{M_S} > \overline{M_D}$)

$$U_S = \begin{pmatrix} \cos(\theta_S) & -\sin(\theta_S) & 0 \\ \sin(\theta_S) & \cos(\theta_S) & 0 \\ 0 & 0 & 1 \end{pmatrix}. \tag{5.119}$$

It describes the basis shift from $\begin{pmatrix} S \\ \phi_R \\ \phi_I \end{pmatrix}$ to the mass eigenbasis $\begin{pmatrix} X_1 \\ X_2 \\ X_3 \end{pmatrix}$.
U_S depends on the scalar mixing angle θ_S which is defined by

$$\tan 2\theta_s = \frac{2Av}{\overline{M}_S^2 - \overline{M}_D^2}. \tag{5.120}$$

In addition to the three neutral states X_i, the particle spectrum contains a charged scalar ϕ^- with mass $m_{\phi^-} = M_{S,D}$.

5.2.1.2 *Approximation for small mixing*

For small mixing A, the mass eigenstates Eq. 5.117 and mixing matrix entries Eq. 5.119 can be simplified. The masses in this approximation the matrix elements up to second order in A are

$$\begin{aligned} M_{X_1} =& \frac{1}{2}\sqrt{2\lambda_S v^2 + 4M_{S,S}^2} \\ & - \frac{2A^2v^2}{\sqrt{2\lambda_S v^2 + 4M_{S,S}^2}} \\ & \frac{1}{\left(-\lambda_S v^2 + \lambda_D v^2 + \lambda'_D v^2 + \lambda''_D v^2 + 2M_{S,D}^2 - 2M_{S,S}^2\right)} + O\left(A^3\right), \\ M_{X_2} =& \frac{1}{2}\sqrt{2\lambda_D v^2 + 2\lambda'_D v^2 + 2\lambda''_D v^2 + 4M_{S,D}^2} \end{aligned}$$

$$
\begin{aligned}
&+\frac{2A^2v^2}{\sqrt{2\lambda_D v^2+2\lambda'_D v^2+2\lambda''_D v^2+4M^2_{S,D}}}\\
&\frac{1}{\left(-\lambda_S v^2+\lambda_D v^2+\lambda'_D v^2+\lambda''_D v^2+2M^2_{S,D}-2M^2_{S,S}\right)}\\
&+O\left(A^3\right),\\
M_{X_3} =&\sqrt{\frac{1}{2}v^2(\lambda_D+\lambda'_D-\lambda''_D)+M^2_{S,D}}.
\end{aligned}
\tag{5.121}
$$

For small angles $tan x \approx x$ is true, hence

$$
\begin{aligned}
\theta_S &\approx \frac{Av}{\overline{M}^2_S-\overline{M}^2_D},\\
\sin(\theta_S) &\approx \theta_S,\\
\cos(\theta_S) &\approx 1-\frac{\theta^2_S}{2}.
\end{aligned}
\tag{5.122}
$$

For negligible mixing , $A = 0$, the masses of Eq. 5.121 reduce to

$$
\begin{aligned}
M^2_{X_1} =&\frac{\lambda_S v^2}{2}+M^2_{S,S},\\
M^2_{X_2} =&\frac{1}{2}v^2(\lambda_D+\lambda'_D-\lambda''_D)+M^2_{S,D},\\
M^2_{X_3} =&\frac{1}{2}v^2(\lambda_D+\lambda'_D+\lambda''_D)+M^2_{S,D}
\end{aligned}
\tag{5.123}
$$

and Eq. 5.122 becomes

$$
\begin{aligned}
\cos(\theta_S) =&1\\
\sin(\theta_S) =&0.
\end{aligned}
\tag{5.124}
$$

5.2.1.3 *Singlet-doublet fermion dark matter*

Given only the new fermion fields of Eq. 5.112, the model is known as the singlet-doublet fermion model – see e.g. [242, 243]. ψ_D is decomposed into two chiral components $\psi_{\psi_{D_1}}$ and $\psi_{\psi_{D_2}}$ with opposite hypercharge signs to cancel gauge anomalies. Thus, in a similar fashion to the inert Higgs model with H_u and H_d, this model is anomaly free [65]. The corresponding Lagrangian terms are

$$
\begin{aligned}
\mathcal{L}_{SDF} =&\frac{i}{2}(\overline{\psi}_{D_1}\sigma^\mu D_\mu \psi_{D_1}+\overline{\tilde{D}}_2\sigma^\mu D_\mu\tilde{\psi}_{D_2})-\frac{M_{F,S}}{2}\psi^2_S\\
&-M_{F,D}\psi_{D_1}\psi_{D_2}-y_1\psi_{D_1}H\psi_S-y_2\overline{\psi}_{D_2}H\overline{\psi}_S+h.c.
\end{aligned}
\tag{5.125}
$$

$\mathcal{L}_{SDF}$ contains a Majorana mass term for ψ_S and Dirac mass terms for ψ_{D_1} and ψ_{D_2}. Furthermore, it introduces Yukawa interactions between the fermions and the Higgs. Similar to the scalar case, electro-

weak symmetry breaking leads to mixing for the y_1 and y_2 terms. The mass matrix for neutral fermions is then

$$M_F = \begin{pmatrix} M_{F,S} & m_\lambda \cos(\theta) & m_\lambda \sin(\theta) \\ m_\lambda \cos(\theta) & 0 & M_{F,D} \\ m_\lambda \sin(\theta) & M_{F,D} & 0 \end{pmatrix} \tag{5.126}$$

in the basis $\begin{pmatrix} \psi_S \\ \psi_{D_1} \\ \psi_{D_2} \end{pmatrix}$, with

$$\begin{aligned} y =& \sqrt{y_1^2 + y_2^2}, \\ m_\lambda =& \frac{y v}{\sqrt{2}}, \\ \tan(\theta) =& \frac{y_2}{y_1}, \end{aligned} \tag{5.127}$$

such that $y_1 = \cos(\theta) y$ and $y_2 = \sin(\theta) y$.
In order to obtain the eigenvalues for the mass eigenstates χ_1, χ_2 and χ_3, one has to solve the characteristic polynomial equation for M_χ, which is the cubic equation

$$\begin{aligned} 0 =& M_\chi^3 - M_S M_\chi^2 + (-M_D^2 - m_\lambda^2) M_\chi + M_D^2 M_S \\ & - 2 M_D m_\lambda^2 \cos(\theta) \sin(\theta). \end{aligned} \tag{5.128}$$

Mixing with the Majorana singlet ψ_S results in all χ_i being Majorana particles. The spectrum also contains a charged Dirac fermion $\psi^- = \begin{pmatrix} \psi^-_{D_1,L} \\ \psi^-_{D_2,L} \end{pmatrix}$ with mass $m_{\psi^-} = M_{F,D}$.
In general, cubic equations can be solved by means of Cardano's theorem [249]. Eq. 5.128 corresponds to a case with three real solutions given by

$$\begin{aligned} M_{\chi_1} =& z_2 + \frac{M_{F,S}}{3}, \\ M_{\chi_2} =& z_3 + \frac{M_{F,S}}{3}, \\ M_{\chi_3} =& z_1 + \frac{M_{F,S}}{3}, \end{aligned} \tag{5.129}$$

– compare to [229] — with

$$\begin{aligned} z_1 =& \left(-\frac{q}{2} + \sqrt{\frac{q^2}{4} + \frac{p^3}{27}} \right)^{\frac{1}{3}} + \left(-\frac{q}{2} - \sqrt{\frac{q^2}{4} + \frac{p^3}{27}} \right)^{\frac{1}{3}}, \\ z_2 =& -\frac{z_1}{2} + \sqrt{\frac{z_1^2}{4} + \frac{q}{z_1}}, \end{aligned}$$

$$z_3 = -\frac{z_1}{2} - \sqrt{\frac{z_1^2}{4} + \frac{q}{z_1}}, \tag{5.130}$$

and

$$\begin{aligned} p =& -\frac{1}{3}M_{F,S}^2 - \left(M_{F,D}^2 - m_\lambda^2\right), \\ q =& -\frac{2}{27}M_{F,S}^3 - \frac{1}{3}M_{F,S}(M_{F,D}^2 + m_\lambda^2) \\ &+ \left(M_{F,S}M_{F,D}^2 - m_\lambda^2 \sin^2(\theta) M_{F,D}\right). \end{aligned} \tag{5.131}$$

The unitary transformation matrix U_F is obtained by solving the eigenvector equation $M_F v_i = M_{\chi_i} v_i$ for $i = 1, 2, 3$. With U_F the basis is shifted as

$$U_F^T \begin{pmatrix} \psi_S \\ \psi_{D_1} \\ \psi_{D_2} \end{pmatrix} = \begin{pmatrix} \chi_1 \\ \chi_2 \\ \chi_3 \end{pmatrix} \Leftrightarrow \begin{pmatrix} \psi_S \\ \psi_{D_1} \\ \psi_{D_2} \end{pmatrix} = U_F \begin{pmatrix} \chi_1 \\ \chi_2 \\ \chi_3 \end{pmatrix}. \tag{5.132}$$

5.2.1.4 *Approximation for small mixing*

In the limit of small mixing $y_1, y_2 \ll 1$ respectively $m_\lambda \ll 1$ the mass eigenvalues in Eq. 5.129 simplify to

$$\begin{aligned} M_{\chi_1} =& M_{F,S} + \frac{m_\lambda^2 (M_{F,D}\sin^2(\theta) + M_{F,S})}{M_{F,S}^2 - M_{F,D}^2} + O\left(m_\lambda^3\right), \\ M_{\chi_2} =& M_{F,D} + \frac{m_\lambda^2 (\sin^2(\theta) + 1)}{2M_{F,D} - 2M_{F,S}} + O\left(m_\lambda^3\right), \\ M_{\chi_3} =& -M_{F,D} + \frac{m_\lambda^2 (\sin^2(\theta) - 1)}{2(M_{F,D} + M_{F,S})} + O\left(m_\lambda^3\right). \end{aligned} \tag{5.133}$$

An approximation for the mixing matrix is found as

$$\begin{aligned} U_{F,11} =& 1 - \frac{m_\lambda^2 \left(M_{F,D}^2 + 2M_{F,D}M_{F,S}\sin(2t) + M_{F,S}^2\right)}{2\left(M_{F,D}^2 - M_{F,S}^2\right)^2}, \\ U_{F,12} =& \frac{m_\lambda (\sin(t) + \cos(t))}{\sqrt{2}(M_{F,D} - M_{F,S})}, \\ U_{F,13} =& \frac{m_\lambda (\sin(t) - \cos(t))}{\sqrt{2}(M_{F,D} + M_{F,S})}, \\ U_{F,21} =& \frac{m_\lambda (M_{F,D}\sin(t) + M_{F,S}\cos(t))}{M_{F,D}^2 - M_{F,S}^2}, \\ U_{F,22} =& \frac{1}{\sqrt{2}} \\ & - m_\lambda^2 (\sin(t) + \cos(t)) \\ & \times \frac{((2M_{F,D} - M_{F,S})\sin(t) + M_{F,S}\cos(t))}{4\sqrt{2}M_{F,D}(M_{F,D} - M_{F,S})^2}, \end{aligned}$$

$$
\begin{aligned}
U_{F,23} =& -\frac{1}{\sqrt{2}} \\
& - \frac{m_\lambda^2((M_{F,D}+M_{F,S})\cos(2t)+M_{F,D}(\sin(2t)-1))}{4\sqrt{2}M_{F,D}(M_{F,D}+M_{F,S})^2}, \\
U_{F,31} =& \frac{m_\lambda(M_{F,D}\cos(t)+M_{F,S}\sin(t))}{M_{F,D}^2-M_{F,S}^2}, \\
U_{F,32} =& \frac{1}{\sqrt{2}} \\
& - m_\lambda^2(\sin(t)+\cos(t)) \\
& \times \frac{((2M_{F,D}-M_{F,S})\cos(t)+M_{F,S}\sin(t))}{4\sqrt{2}M_{F,D}(M_{F,D}-M_{F,S})^2}, \\
U_{F,33} =& \frac{1}{\sqrt{2}} \\
& \frac{m_\lambda^2(M_{F,D}(\sin(2t)-1)-(M_{F,D}+M_{F,S})\cos(2t))}{4\sqrt{2}M_{F,D}(M_{F,D}+M_{F,S})^2},
\end{aligned} \tag{5.134}
$$

by using its diagonalization properties and the unitarity relation. The results are handled in the same way and are compatible with similar approximations in [229].
For negligible mixing, $m_\lambda = 0$, Eq. 5.133 simplifies to

$$
\begin{aligned}
M_{\chi_1} =& M_{F,S}, \\
M_{\chi_2} =& M_{F,D}, \\
M_{\chi_3} =& -M_{F,D}
\end{aligned} \tag{5.135}
$$

and the mixing matrix takes the form

$$
U_F = \begin{pmatrix} 1 & 0 & 0 \\ 0 & \frac{1}{\sqrt{2}} & \frac{1}{\sqrt{2}} \\ 0 & \frac{1}{\sqrt{2}} & \frac{-1}{\sqrt{2}}. \end{pmatrix}.
$$

5.2.1.5 *Couplings with Standard Model leptons*

T12A contains the singlet-doublet scalar and fermion Lagrangian from Eq. 5.113 and Eq. 5.125 along with additional terms affecting the Standard Model lepton sector

$$
-\mathcal{L}_{lep} = g_{1i} L_i \phi_S \psi_{D_2} + g_{2i} L_i \phi_D \psi_S + h.c., \tag{5.136}
$$

with the lepton doublets L_i of generation i

$$
L_i = \begin{pmatrix} \nu_{i,L}^0 \\ e_{i,L}^- \end{pmatrix} \propto (2, -\frac{1}{2}, +). \tag{5.137}
$$

The Yukawa couplings g_{ij} give rise to one-loop neutrino masses. There are no tree level contributions, as they are prohibited by the $\mathbb{Z}_2$ symmetry. Altogether, T12A contains several free parameters. Some which

Table 5.2: Free parameters in model T12A.

Sector	Parameters
Scalar sector	$M_{S,S}$, $M_{S,D}$, λ_S, λ_D, λ'_D, λ''_D, A
Fermion sector	$M_{F,S}$, $M_{F,D}$, y_1, y_2
Neutrino sector	g_{11}, g_{12}, g_{13}, g_{21}, g_{22}, g_{23}

only concern the scalar or fermion part and others which connect fermions, scalars and Standard Model leptons. An overview is found in Tab. 5.2.

5.2.2 *Dark matter relic density*

Within the model T12A, the relic density is generated in a thermal freeze-out scenario described by the Boltzmann equation – see Section 2.4. The dark matter annihilation is governed by electro-weak interactions and there are regions where co-annihilation processes can be important. Both singlet-doublet models feature Higgs portal dark matter, for which the Higgs links the visible to the dark sector. In the case of fermion dark matter, there is also the possibility of Z boson mediated interactions due to the doublet nature. Considering co-annihilation, Z boson mediated processes are also possible in the scalar case. Similarly to inert doublet models or the MSSM with extra Higgs doublets, only the pseudoscalar ϕ_I and scalar ϕ_R part of the neutral scalar doublet component are linked by the Z boson and ϕ_I does not mix. Other vertices involve two gauge bosons. In general, Higgs and Z mediated processes determine the relic density in the singlet-doublet models. Thus, the relic density is closely related to the direct detection cross section. The same diagrams contributing to dark matter annihilation can be flipped to obtain dark matter-quark scattering. The presence of fermion-scalar couplings in T12A opens up more final states, especially states with leptons and neutrinos, weakening the correlation between the relic density and direct detection cross section. A small overview of annihilation channels for scalar and fermion dark matter is presented in Appendix F.Appendix E contains a summary of all vertices within T12A which concern dark matter, Fig. 5.41 shows the corresponding vertices.

The entire Lagrangian from Eq. 5.113, Eq. 5.125 and Eq. 5.136 is modeled in LanHep [250] and SARAH as a reference [251]. Sarah also provides input for the spectrum generator SPheno [252]. Dark matter observables are obtained with microMEGAs [253], lepton flavor violating processes are handled by SPheno. The mixings are calculated within a C-code which calls microMEGAs and if needed SPheno. An

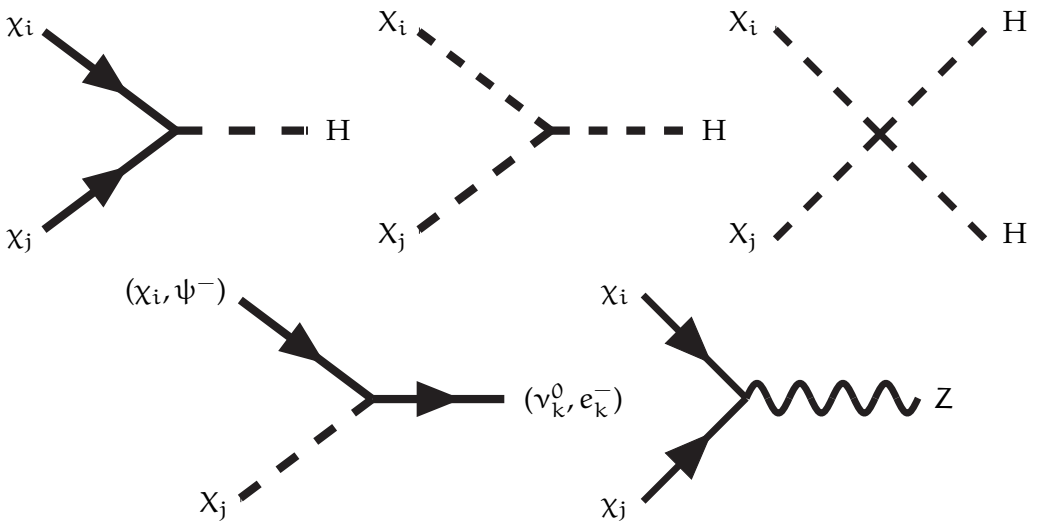

Figure 5.41: New vertices that link the Z_2-odd sector to the Standard Model.

improved version, which allows for simple introduction of different models, is currently under construction. It is established in a basic version but not tested enough to be featured here. When it is complete, it will be made available within the working group.
The next sections contain a recap of the singlet-doublet scenarios regarding dark matter phenomenology, followed by a section highlighting the additional features in T12A.

5.2.2.1 *Singlet-doublet scenarios*

SINGLET-DOUBLET SCALAR DARK MATTER

In order to have a singlet-doublet scalar model, which is a subset of T12A, the fermions are set to a high mass scale and the fermion-scalar couplings g_{ij} are set to zero. This effectively decouples the fermions and prohibits direct interactions with the Standard Model leptons. For example, in [243] the singlet-doublet scalar model is investigated and two plots from this work are reproduced and shown here. For this reason, the simplifications $\lambda_S = \lambda_D = \lambda$ and $\lambda'_D = \lambda''_D = 0$ are used throughout this section.

The first plot, shown Fig. 5.42 (b), is a reproduction of figure 12 in [243] – see Fig. 5.42 (a). It depicts the plane of singlet and doublet scalar mass parameters $M_{S,S}$ and $M_{S,D}$ for intermediate scalar mixing $A = 10$ GeV and negligible other scalar couplings. The masses are varied between 200 GeV and 2 TeV and microMEGAs is used to calculate the corresponding relic density and direct detection cross section. Along the black line (dashed blue in the original) the relic density matches the observations. To the right of the black line (deep violet) it is too large, the left (light violet) region features too small values. In principle, these models are not excluded, but then an additional explanation for the missing relic density is needed. In this scenario

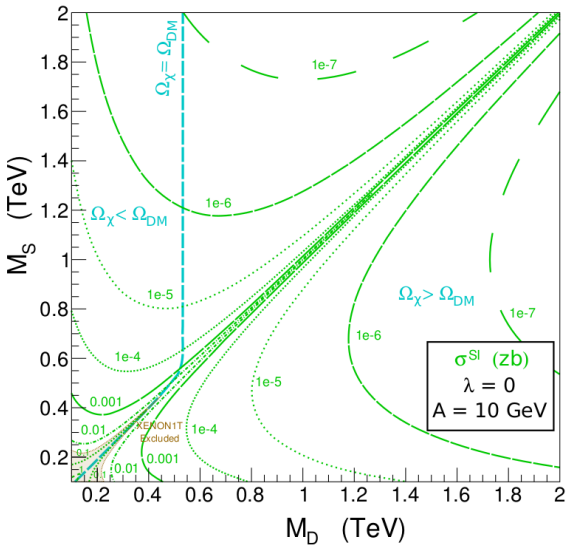

(a)

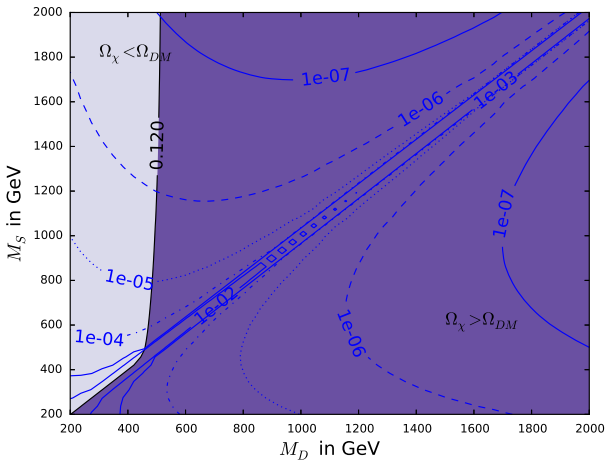

(b)

Figure 5.42: Original figure 12a from [243] (a) and reproduction (b) illustrating the relic density and direct detection regions for the scalar mass parameters in the setting $\lambda = 0$ and $A = 10$ GeV.

the correct relic density is obtained for $M_{S,S} \approx M_{S,D}$ for the doublet mass below 500 GeV. Beyond that value the line increases steeply, such that $M_{S,D}$ cannot exceed notably 500 GeV for the correct relic density whereas the singlet component can take any value as long as the doublet is light enough.
Contour lines for the spin-independent elastic scattering cross section σ_{SI} in zb are shown in blue (dashed green). In the original Fig. 5.42 (a) a shaded region indicates experimental exclusion limits. With the absence of all scalar couplings λ, relic density and direct detection are controlled by the mixing A and the mass parameters. σ_{SI} exhibits a strong increase towards the line of $M_{S,S} \approx M_{S,D}$.

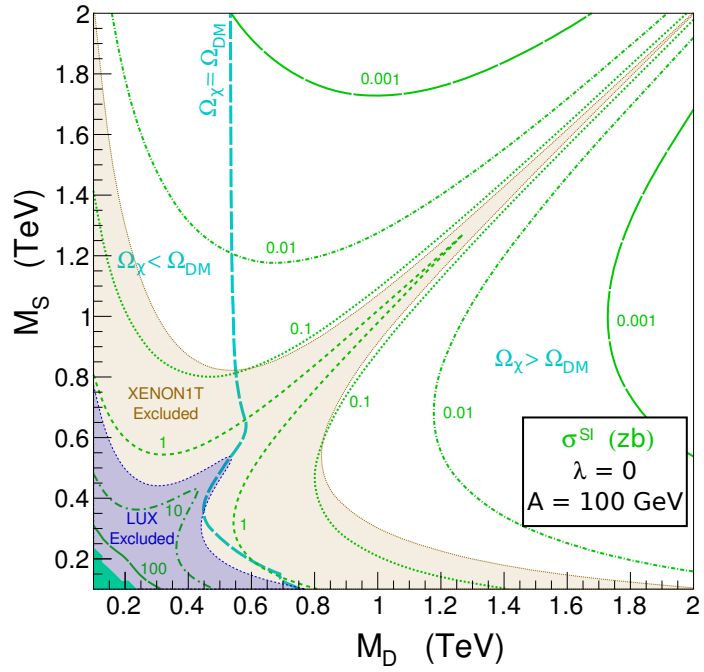

(a)

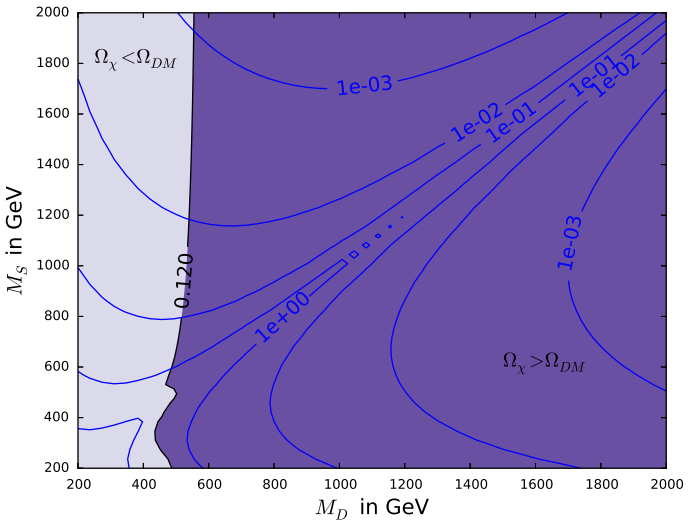

(b)

Figure 5.43: The original figure 12 b from [243] (a) and a remake (b) for comparison. The dashed blue (solid black) curve indicates the relic density matches the observation.Contour lines for spin-independent direct detection cross section in zb are also shown.

Increasing the mixing A from 10 GeV to 100 GeV leads to the results shown in Fig. 5.43 (a) and Fig. 5.43 (b) . The former is figure 12b from [243], the latter is the reproduction. The color set up is the same as in the previous figures. In the lower left corner the turquoise area in the original Fig. 5.43 (a) does not yield a physical spectrum

and is therefore not viable. Looking at the mass eigenstates defined in Eq. 5.117, the square root $\sqrt{(\overline{M}_S^2 - \overline{M}_D^2)^2 + 4v^2A^2}$ cannot become larger than $\overline{M}_S^2 + \overline{M}_D^2$, otherwise the mass square becomes negative. This imposes $\overline{M}_S^2\overline{M}_D^2 > A^2v^2$. Regarding the relic density, the region with viable values still is to the left of the black line. The line now shows a different behavior for small singlet masses as compared to the $A = 10$ GeV case. Again, $M_{S,D}$ cannot be too large, whereas viable points can be found for any $M_{S,S}$ in this $\lambda = 0$ setting.
For $\lambda = 0$, only A determines the coupling of scalar sector to SM as well as mixing. In [243] it is shown that the situation drastically changes for $\lambda \neq 0$. The presence of λ introduces more couplings to the Standard Model besides the mixing parameter A. With additional couplings, annihilation can be enhanced. There are also regions where $M_{S,D}$ is rather large and the relic density is still within reasonable range.
Altogether, some viable points are found in [243], which obey current experimental limits regarding the CMB measurement and direct detection. For $\lambda < 0$, all points are excluded by XENON1T, whereas for $\lambda > 0$ viable regions are found with a fine-tuning of less than 10%. Dark matter masses in this scenario were probed between 100 GeV to a few TeV.

SINGLET-DOUBLET FERMION DARK MATTER

When not decoupling the fermions but the scalars by setting their mass to a much higher scale, the singlet-doublet fermion model is recovered. It has been previously investigated for example in [242, 243]. This section contains reproductions of one figure from each reference, testing our implementation. For singlet-doublet fermion dark matter only the two Yukawa couplings y_1 and y_2 determine mixing as well as interactions with Standard Model particles. As a consequence relic density, spin-dependent and independent direct detection cross sections σ_{SD} and σ_{SI} depend on y_1 and y_2. For figure Fig. 5.44 (b), all parameters except y_2 (called λ' on the plot) are fixed as $y_1 = 0.36$, $M_{F,S} = 200$ GeV and $M_{F,D} = 300$ GeV. It is a replica of figure 2 from [242], which is shown in Fig. 5.44 (a). In both figures the relic density is shown in blue, spin-dependent and spin-independent cross sections in green and red, respectively. Both elastic scattering cross sections feature a strong cancellation for a certain value of y_2. In case of spin-dependent interactions the cancellation happens when the coupling to Z is suppressed. In this scenario this is true for $y_2 = -0.36$. This coincides with an enhanced relic density as for both processes the interactions mediated by the Z bosons are the most important in this region. The relic density stays nearly constant afterwards for different values of y_2 around the expected value from CMB measurements. Cancellation in the Higgs vertex occurs for $y_2 \approx -0.14$, leading to a strong decrease in σ_{SI} whereas Ωh^2 is rather unaffected.

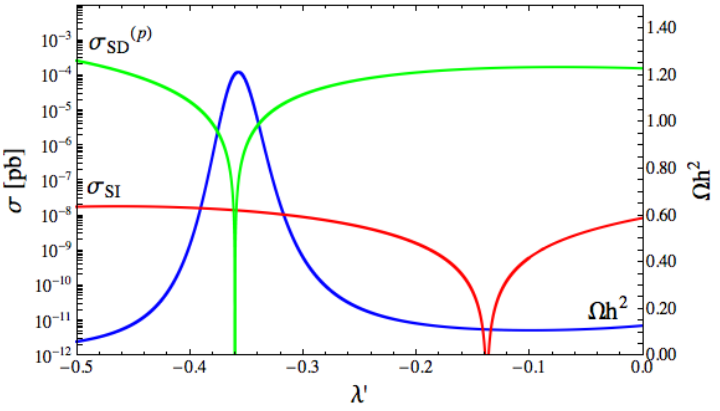

(a)

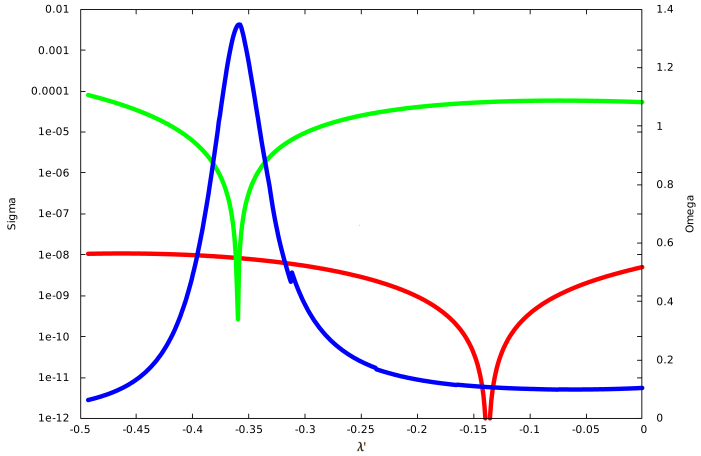

(b)

Figure 5.44: Original figure 2 from [242] (a) and a reproduction (b) illustrating the suppression in direct detection cross section and the relic density for singlet-doublet fermion dark matter for $y_1 = 0.36$, $M_{F,S} = 200$ GeV and $M_{F,D} = 300$ GeV.

Analogous to singlet-doublet scalar dark matter, the fermionic singlet-doublet model is investigated in [243]. Fig. 5.45 (a) shows their figure 6c of which Fig. 5.45 (b) is a remake. The plots show the plane of the fermion singlet and doublet mass parameters $M_{F,S}$ and $M_{F,D}$ for $y = \sqrt{y_1^2 + y_2^2} = 1.5$ and $\tan\theta = 10$. Similarly to the light violet region in Fig. 5.42, in the light violet region the relic density is too small to match the observation. The solid black line separates this from the deep purple area with a too high value. In the original figure the two regions are separated by a dashed blue line. A broad space of viable points is found. For large $M_{F,D}$ the singlet mass $M_{F,S}$ also needs to be large to produce the correct relic density, whereas up to $M_{F,D}$ around 1.2 TeV a nearly constant value of $M_{F,S}$ is needed. Direct detection cross section contour lines in zb are shown in blue respectively in dashed green in the original Fig. 5.45 (a). In this figure the blue shaded region indicates the direct detection exclusion, which

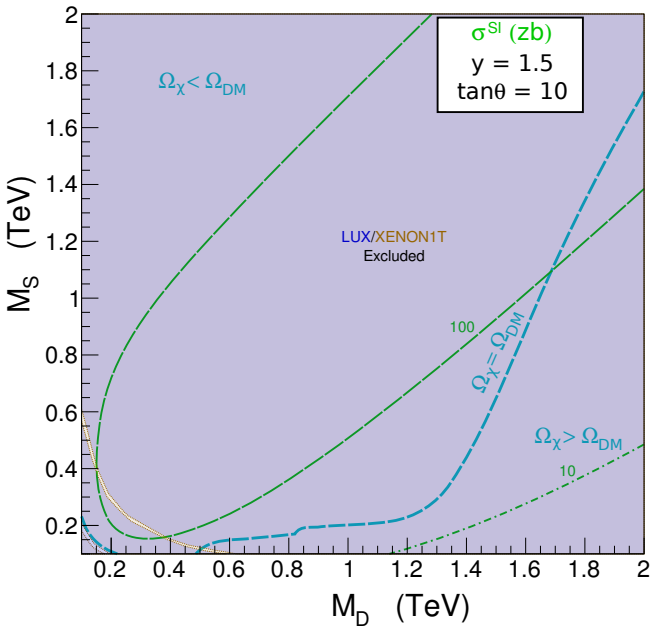

(a)

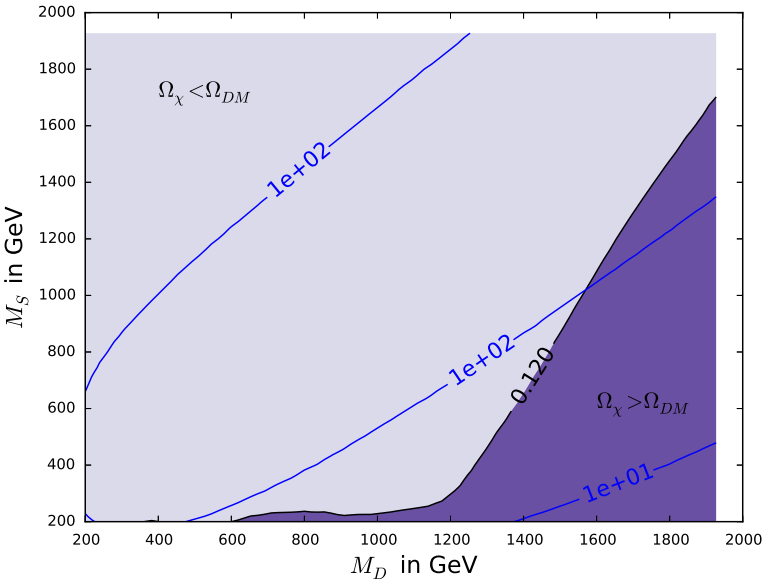

(b)

Figure 5.45: Figure 6c from **[Chenug2013]** (a) and a reproduction 8 (b). Both showing the plane of singlet and doublet fermion mass parameters with color overlays for relic density and direct detection lines.**[Chenug2013]**

covers almost the entire space. Altogether, [243] found viable regions with $y < 0.1$ only, which are fine-tuned to at least 10%.

5.2.2.2 *Leptophilic dark matter and influence of g_{ij} on the relic density*

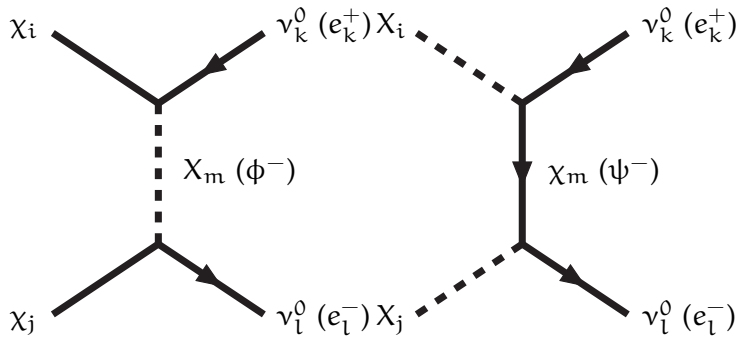

Figure 5.46: (Co-)annihilation processes of fermion (left) and scalar (right) dark matter particles to SM leptons.

In addition to the singlet-doublet models, T12A provides additional couplings between the fermions, scalars and Standard Model leptons. The same vertex associated with g_{ij}, shown in the bottom left diagram in Fig. 5.41, which creates neutrino masses at one-loop, allows for coannihilation between fermions and scalars as well as lepton final states. Coannihilation can be important for small mass differences. Similarly to coannihilation, small mass differences support the conversion ($\chi_i\chi_j \leftrightarrow X_iX_j$) to be more relevant. For a larger mass gap, the heavier particles decouple much earlier. The dynamics are disentangled.
In the case of small couplings to the Higgs and small mixing but sizable coupling to leptons g_{ij}, the neutrino and lepton final states can be largely enhanced providing somewhat leptophilic dark matter. Diagrams for this process are shown in Fig. 5.46, a general overview can be found in Appendix F. These new contributions to dark matter annihilation do not take part in interactions regarding nuclear recoils. The correlation between the annihilation cross section and direct detection observables is therefore diminished. Under the assumption of purely leptophilic dark matter, the annihilation cross sections scale with the relative velocity v of the thermal relic as

$$\begin{aligned} &\sigma v(\chi_i\chi_j \to e_k^+ e_l^-) \propto v^2\,, \qquad &&\sigma v(X_iX_j \to e_k^+ e_l^-) \propto v^4, \\ &\sigma v(\chi_i\chi_j \to \nu_k^0 \nu_l^0) \propto v^0\,, \qquad &&\sigma v(X_iX_j \to \nu_k^0 \nu_l^0) \propto v^2. \end{aligned} \tag{5.138}$$

LEPTON AND NEUTRINO FINAL STATES

In Fig. 5.47 the impact of the new couplings g_{ij} with regard to the singlet-doublet models on dark matter is studied. In the plot the singlet scalar mass parameter $M_{S,S}$ is a common mass scale for all particles. The scaling factors are $M_{F,D} = 2.5M_{S,S}$, $mfs = 3M_{S,S}$ and $M_{S,D} = 3.1M_{S,S}$. Together with small couplings – see Tab. 5.3– mix-

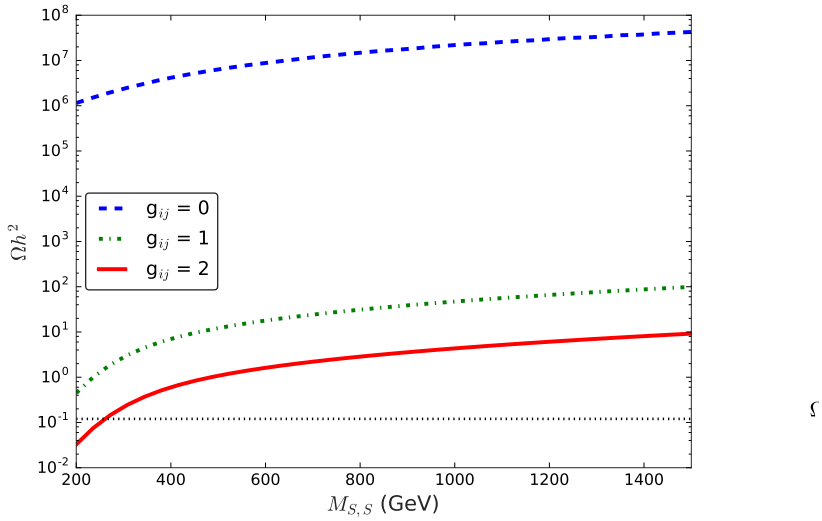

Figure 5.47: Influence of the scalar-fermion couplings g_{ij} on the singlet scalar dark matter relic density as a function of its mass parameter $M_{S,S}$.

Table 5.3: Parameters used in Fig. 5.47

Parameter	Value
λ_S	9.3×10^{-6}
λ_D	-1.2×10^{-6}
λ'_D	3×10^{-6}
λ''_D	2.4×10^{-8}
A (GeV)	3.5×10^{-7}
y_1	3.5×10^{-10}
y_2	0.79
$M_{S,D}$ (GeV)	3 $M_{S,S}$
$M_{F,S}$ (GeV)	3.1 $M_{S,S}$
$M_{F,D}$ (GeV)	2.5 $M_{S,S}$

ing is small and dark matter is mostly scalar singlet-like. For this choice of parameters, conversion and coannihilation are not important. Furthermore, as λ_S, λ_D, λ'_D and λ''_D are small, couplings to the Higgs and Standard Model particles are suppressed and annihilation is not very efficient. Thus, in case of no lepton final states for $g_{ij} = 0$, the relic (dashed blue line) is rather larger. It is around seven orders of magnitude above the limit observed by Planck (dotted black line). With $g_{ij} \neq 0$ the relic density is reduced, as new final leptonic states become available. $g_{ij} = 2$ is sufficient to fulfill the constraint from CMB measurements. A value of $g_{ij} = 1$ is not large enough, yet the

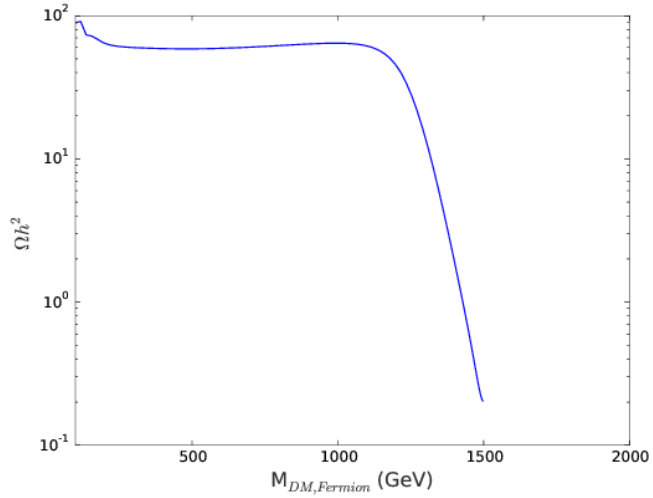

Figure 5.48: Relic density for fermionic dark matter as function of the fermion mass parameter $M_{F,S}$.

relic density is around six orders of magnitude smaller than without lepton channels. The direct detection cross section does not depend on g_{ij} and is unaffected by the change from 0 to 2, such that it is the same for all three options.

Table 5.4: Parameters used in Fig. 5.48

Parameter	Value
λ_S	0.1
λ_D	0.1
λ'_D	0.1
λ''_D	0.1
A (GeV)	0.0
y_1	0.2
y_2	0.01
$M_{S,S}$ (GeV)	2500
$M_{S,D}$ (GeV)	3500
$M_{F,S}$ (GeV)	(500 - 1500)
$M_{F,D}$ (GeV)	1500
g_{ij}	0

COANNIHILATION BETWEEN FERMIONS

For small mass differences, coannihilation can be of large importance for the relic density. Coannihilation processes can occur between fields of the same or different types.

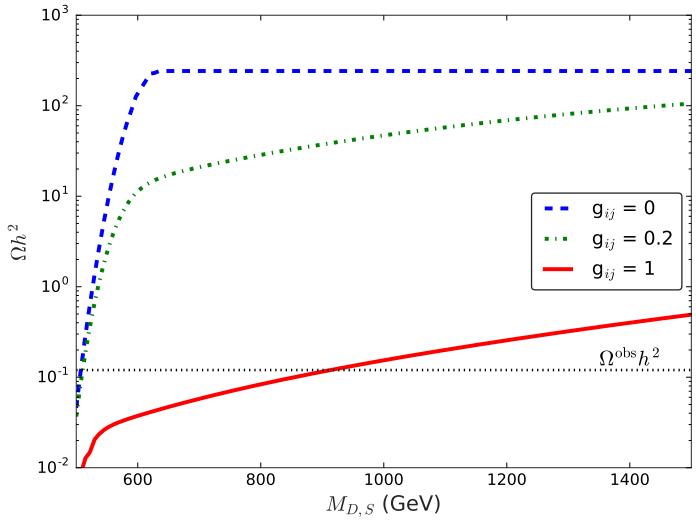

Figure 5.49: Influence of the scalar-fermion couplings g_{ij} on the singlet fermion dark matter relic density as function of the doublet scalar mass parameter $M_{S,D}$.

First, coannihilation among fermions is considered. For this, the lepton and neutrino processes are turned off as $g_{ij} = 0$. The scalars are decoupled as well by their heavy masses $M_{S,S} = M_{S,D} = 3500$ GeV as shown in Tab. 5.4. Regarding the fermions, small to intermediate Yukawa couplings are chosen, $y_1 = 0.2$ and $y_2 = 0.01$. The doublet is fixed ad 1500 GeV and the singlet mass parameter $M_{F,S}$ runs from 500 GeV to 1.5 TeV. The corresponding relic density is shown in Fig. 5.48. The lightest particle in this scenario is then mostly singlet-like. Its relic density is fairly constant for small masses. When approaching $M_{F,D} = 1500$ GeV, the value drops by roughly three orders of magnitude due to coannihilations allowing for a viable relic density. Concerning scalar dark matter, similar scenarios can be found for small mass differences of neutral states X_i and X_j.

COANNIHILATION AND CONVERSION

In the presence of g_{ij}, coannihilation between scalars and fermions are possible. Fig. 5.49 shows the fermion relic density as a function of the doublet scalar mass $M_{S,D}$. In order to look at the effect of g_{ij} on singlet fermion dark matter, the doublet is set to $M_{F,D} = 3000$ GeV. $M_{F,S} = 450$ GeV and y_1 and y_2 are not too large as shown in Tab. 5.5. The scalar singlet is also decoupled with a mass of $M_{S,S} = 2.5$ TeV and a small scalar mixing $A = 0.01$ GeV. In the absence of scalar-fermion couplings (dashed blue line), no coannihilation between the different states takes place. Above $M_{S,D} = 600$ GeV the relic density is constant. Below this mass the difference between the lightest scalars

Table 5.5: Parameters used in Fig. 5.49

Parameter	Value
λ_S	0.003
λ_D	2.4
λ'_D	0.008
λ''_D	1.8
A (GeV)	0.01
y_1	0.06
y_2	0.28
$M_{S,S}$ (GeV)	2500
$M_{F,S}$ (GeV)	450
$M_{F,D}$ (GeV)	3000

X_i and dark matter, the lightest of χ_i, is only a few tens of GeV. This results in conversion $X_i X_j \leftrightarrow \chi_l \chi_k$ to be important. This conversion depletes the relic density to the correct value (dotted black line) for approximately $M_{F,S} \approx M_{S,D}$ by coupled dynamics of X_i and χ_i. In all other regions the neutral scalar states are too heavy and decouple at a much different time scale. Hence, dynamics between fermion and scalar states are disentangled resulting in a constant relic density. Setting g_{ij} to 0.2 (dashed green line) or even 1 (solid red line) provides the opportunity to study the influence of coannihilation. The larger g_{ij}, the more coannihilation is enhanced, decreasing the relic density by up to three orders of magnitude. In the region of $M_{S,D}$ close to $M_{F,S}$ this is expected. For lager masses the relic density still stays below the line for $g_{ij} = 0$ as the couplings open more annihilation channels with neutrinos and charged leptons in the final states. With increasing $M_{S,D}$ this effect becomes smaller due to the propagator suppression. For all three lines direct detection is the same since it is independent of g_{ij}.

As shown in the previous figure, the presence of new couplings alters the available parameter space with regard to singlet-doublet scalar and singlet-doublet fermion models. Especially, coannihilation between different particle species and the presence of new final states gives rise to new compatible regions without altering direct detection limits. Considering scalar dark matter, Fig. 5.50 shows the relic density in the plane $(M_{S,S}, M_{S,D})$ for $\lambda_S = \lambda_D = 10^{-4}$, $\lambda'_D = \lambda''_D = 0$ and $A = 10^{-4}$ GeV. The couplings g_{ij} are set to 0.75. Along the solid black line, labeled „no coann.“, the relic matches the observation in a case with decoupled fermions since $M_{F,S} = M_{F,D} = 5$ TeV. This is compatible with the results found in the singlet-doublet model in [243]. In order to enhance coannihilation, the mass parameters for fermions are chosen such that the difference to the lightest scalar state is only

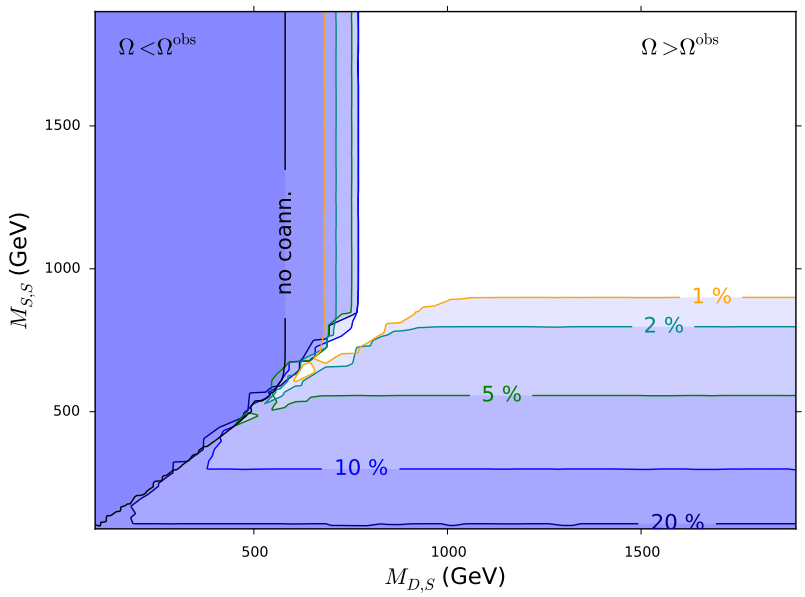

Figure 5.50: Viable and excluded values of the scalar dark matter relic density in the mass plane $M_{S,D}$–$M_{S,S}$ in the presence of similarly light singlet or doublet fermions with couplings $g_{ij} = 0.75$.

few percent as indicated on the label of the colored lines. Since the couplings are small or zero and mixing $A = 10^{-4}$ GeV is also small dark matter is mostly singlet for $M_{S,S} < M_{S,D}$ and mostly doublet for the opposite case of $M_{S,D} < M_{S,S}$. Thus, it is sufficient to leave $M_{F,S}$ at 5 TeV for singlet-like dark matter and adapt only $M_{F,D}$. For doublet like lightest scalars only $M_{F,S}$ is altered while $M_{F,D}$ stays at 5 TeV. In the region where $M_{S,D}$ is lighter, the blue shaded viable regions, limited by the vertical colored lines, extend up to 750 GeV. Without coannihilation, only masses up to 600 GeV are feasible. Regarding singlet-like dark matter, completely new regions open up, bound below by the horizontal lines which restrict $M_{S,D}$ to be not above 250 Gev for a mass splitting of 20% or up to 900 GeV for a mass difference of 1%. Thus, the impact of coannihilation is huge especially for singlet scalar dark matter.

5.2.3 *Neutrino masses*

As T12A is a model for radiative neutrino masses, it contains neutrino mass generation at the one-loop level. After electro-weak symmetry breaking, the fermions and scalars mix. The T12 topology transforms to the diagrams shown in Fig. 5.51. Analogous to the scotogenic model, a neutral fermion and scalar run in the loop. However, within T12A there are more neutral scalars over which one has to sum and the couplings are different. In general, the couplings concerning the

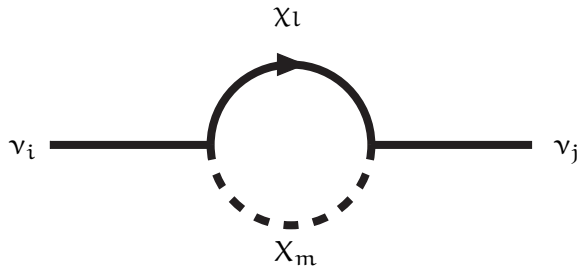

Figure 5.51: Neutrino mass generation at one-loop in model T12A after electro-weak symmetry breaking.

neutrinos are obtained from the Lagrangian in Eq. 5.136 by shifting to the mass basis using the transformation matrices for scalars U_S and fermions U_F. Thus, the coupling C_{ijm} between a neutrino ν_i, a fermion χ_j and a scalar X_m as in the list in the appendix – see Appendix E– is

$$C_{ijm} = g_{1i}U_{F,3j}U_{S,1m} + g_{2i}U_{F,1j}U_{S,2m} + g_{2i}iU_{F,1j}U_{S,3m}. \tag{5.139}$$

This definition allows to obtain an amplitude for the one-loop Majorana mass diagram, omitting the external spinors. The amplitude is

$$F_{ik} \sim \sum_{j,m} P_L \int C_{kjm}C_{ijm} \frac{(\not{q} - \not{p}_1) + M_{\chi_j}}{(q^2 - M^2_{X_m})((q-p_1)^2 - M^2_{\chi_j})} \frac{d^4q}{(2\pi)^4} P_L, \tag{5.140}$$

where q is the momentum running along the fermion line in the loop. The incoming ν momentum is p_1 and the outgoing is p_2. In this calculation the P_L and P_R part of the vertex are considered separately. This is for illustrative purposes to show, that indeed only a Majorana mass contribution exists, whereas the Dirac contribution vanishes. Usually, all parts of the vertex have to be considered since χ and the neutrinos are Majorana particles.
In order to evaluate the expression, dimensional regularization is applied – see Appendix I. After the Passarino-Veltman functions are identified, the amplitude is

$$\begin{aligned} F_{ik} \sim & M_{\chi_j} C_{kjm} C_{ijm} B_0(0, M^2_{X_m}, M^2_{\chi_j}) \\ = & M_{\chi_j} C_{kjm} C_{ijm} \Bigg(\Delta + 1 \\ & - \frac{1}{M^2_{\chi_j} - M^2_{X_m}} (M^2_{\chi_j} \log \frac{M^2_{\chi_j}}{\mu^2} - M^2_{X_m} \log \frac{M^2_{X_m}}{\mu^2}) \Bigg). \end{aligned} \tag{5.141}$$

The sum over j and m is not explicitly shown. The amplitude can be split into an infinite and scale dependent part $F_{ik,div}$ and into a finite part $F_{ik,con}$, which are

$$F_{ik,div} \sim M_{\chi_j} C_{kjm} C_{ijm} \times (\Delta + 1 - \log\mu^2),$$

$$F_{ik,con} \sim M_{\chi_j} C_{kjm} C_{ijm} \times \frac{1}{M^2_{\chi_m} - M^2_{\chi_j}} (M^2_{\chi_j} \log M^2_{\chi_j} - M^2_{\chi_m} \log M^2_{\chi_m}). \quad (5.142)$$

The divergent part $F_{ik,div}$ vanishes, as the following relations apply

$$\begin{aligned}
\sum_{j,m} M_{\chi_j} C_{kjm} C_{ijm} &:= \sum_{j,m} K_{ikjm} \\
&= \sum_{j,m} M_{\chi_j} (g_{1i} g_{1k} U^2_{F,3j} U^2_{S,1m} \\
&\quad + g_{1i} g_{2k} U_{F,1j} U_{F,3j} U_{S,1m} U_{S,2m} \\
&\quad + i g_{1i} g_{2k} U_{F,1j} U_{F,3j} U_{S,1m} U_{S,3m} \\
&\quad + g_{2i} g_{1k} U_{F1j} U_{F,3j} U_{S,1m} U_{S,2m} \\
&\quad + g_{2i} g_{2k} U^2_{F,1j} U^2_{S,2m} \\
&\quad + i g_{2i} g_{2k} U^2_{F,1j} U_{S,2m} U_{S,3m} \\
&\quad + i g_{2i} g_{1k} U_{F,1j} U_{F,3j} U_{S,1m} U_{S,3m} \\
&\quad + i g_{2i} g_{2k} U^3_{F,1j} U_{S,2m} U_{S,3m} \\
&\quad + g_{2i} g_{2k} i^2 U^2_{F,1j} U^2_{S,3m}), \quad (5.143)
\end{aligned}$$

and

$$\begin{aligned}
\sum_m U_{S,am} U_{S,bm} &= \sum_m U_{S,am} \left(U^T\right)_{smb} \\
&= \left(U_S U_S^T\right)_{ab} = \delta_{ab}, \\
\sum_j U_{F,aj} M_{\chi_j} U_{F,bj} &= \sum_j U_{F,aj} M_{\chi_j} \left(U^T\right)_{F,jb} \\
&= \left(U_F F_{diag} U_F^T\right)_{ab} = M_{F,ab}. \quad (5.144)
\end{aligned}$$

The corresponding matrix elements are taken from Eq. 5.114 and Eq. 5.126. Most terms vanish, only

$$\sum_{j,m} K_{ikjm} = g_{2i} g_{2k} m_s + i^2 g_{2i} g_{2k} m_s = 0, \quad (5.145)$$

is left, which simplifies to zero as well. As expected from a process which appears at leading order on one-loop level there should be no scale dependence and divergence. The remaining finite part is

$$\begin{aligned}
F_{ik,con} = \sum_{j,m} \frac{M_{\chi_j}}{16\pi^2} \frac{1}{(M^2_{\chi_m} - M^2_{\chi_j})} &\left(M^2_{\chi_j} \log M^2_{\chi_j} - M^2_{\chi_m} \log {MX_m}^2\right) \\
&(g_{1i} g_{1k} U^2_{F,3j} U^2_{S,1m} \\
&+ g_{1i} g_{2k} \left(U_{F,1j} U_{F,3j} U_{S,1m} U_{S,2m} + i U_{F,1j} U_{F,3j} U_{S,1m} U_{S,3m}\right) \\
&+ g_{2i} g_{2k} \left(U_{F,1j} U_{F,3j} U_{S,1m} U_{S,2m} + i U_{F,1j} U_{F,3j} U_{S,1m} U_{S,3m}\right) \\
&+ g_{2i} g_{2k} \left(U^2_{F,1j} U^2_{S,2m} + 2i U^2_{F,1j} U_{S,2m} U_{S,3m} - U^2_{F1j} U_{S,3m}\right)). \quad (5.146)
\end{aligned}$$

which defines the neutrino mass matrix elements as $M_{\nu,ij} = F_{ij,con}$. Overall M_ν can be expressed as

$$\begin{aligned} M_\nu =& g^T M g \\ =& \begin{pmatrix} g_{11} & g_{12} & g_{13} \\ g_{21} & g_{22} & g_{23} \end{pmatrix}^T \begin{pmatrix} M_{11} & M_{12} \\ M_{21} & M_{22} \end{pmatrix} \begin{pmatrix} g_{11} & g_{12} & g_{13} \\ g_{21} & g_{22} & g_{23} \end{pmatrix}. \end{aligned} \tag{5.147}$$

The elements of the symmetric matrix M are defined by the following equations:

$$\begin{aligned} M_{11} &= \sum_{l,m} m_{lm} U_{F,3l}^3 U_{S,1m}^2, \\ M_{12} &= \sum_{l,m} m_{lm} U_{F,1l} U_{F,3l} U_{S,1m} U_{S,2m} = M_{21}, \\ M_{22} &= \sum_{l,m} m_{lm} U_{F,1l}^2 \left(U_{S,2m}^2 - U_{S,3m}^2 \right). \end{aligned} \tag{5.148}$$

The mass function m_{lm} is given by

$$m_{lm} = \frac{1}{16\pi^2} \frac{M_{\chi_l}}{M_{\chi_m}^2 - M_{\chi_l}^2} \left(M_{\chi_l^2} \ln M_{\chi_l}^2 - M_{\chi_m}^2 \ln M_{\chi_m}^2 \right). \tag{5.149}$$

When diagonalizing M_ν, two non-zero Majorana neutrino masses are obtained. The third eigenvalue is always zero. This is compatible with current experimental limits and allows to set an absolute mass scale for neutrinos. This allows to determine all masses. For the presence of three massive neutrinos, additional fields have to be introduced, at least an extra scalar or fermion singlet.

5.2.3.1 *Casas-Ibarra parametrization*

Within this realization of T12A, one neutrino mass m_{ν_1} is always zero. The absolute mass scale is set. Under the assumption of normal hierarchy, this allows to constrain the two other neutrino masses $m_{\nu_{2,3}}$. Following the steps in [254], it is possible to obtain a relation between the neutrino couplings g_{ij} and the observed squared mass differences and mixing angles, such that the experimental observations can be used as an input to generate matching couplings g_{ij}.
It is known that the neutrino mass matrix M_ν is diagonalized by the PMNS matrix U_ν:

$$U_\nu^T M_\nu U_\nu = D_\nu := \mathrm{diag}\left(0, m_{\nu_2}, m_{\nu_3}\right). \tag{5.150}$$

M_ν, the neutrino mass matrix, is defined by Eq. 5.147 and depends on the symmetric matrix M. M can be diagonalized by U_M to obtain $U_M^T M U_M = D_M = \mathrm{diag}\left(E_1, E_2\right)$ with the eigenvalues

$$E_1 = \frac{1}{2}(M_{11} + M_{22} - \sqrt{(M_{11} - M_{22})^2 + 4M_{12}}), \tag{5.151}$$

$$E_2 = \frac{1}{2}(M_{11} + M_{22} + \sqrt{(M_{11} - M_{22})^2 + 4M_{12}}). \tag{5.152}$$

Accordingly, the unitary transformation matrix

$$U_M = \begin{pmatrix} \cos(\kappa) & -\sin(\kappa) \\ \sin(\kappa) & \cos(\kappa) \end{pmatrix} \tag{5.153}$$

is given in terms of one mixing angle κ, which is defined by

$$\tan(2\kappa) = \frac{2M_{12}}{M_{11} - M_{22}}. \tag{5.154}$$

Using the diagonalization transformation, it is possible to rewrite Eq. 5.150 to

$$D_\nu = U_\nu^T g^T U_M D_M U_M^T g U_\nu. \tag{5.155}$$

This equation can be simplified by means of properties of diagonal matrices like $D = D^{\frac{1}{2}} D^{\frac{1}{2}}$, where only the square roots of the diagonal elements are taken. Furthermore, for all diagonal matrices D the relation $D^T = D$ is true. Multiplying Eq. 5.150 from left and right with $D_\nu^{-\frac{1}{2}}$, and establishing

$$R := D_M^{\frac{1}{2}} U_M^T g U_\nu D_\nu^{-\frac{1}{2}}, \tag{5.156}$$

an equation which R must obey is obtained:

$$R^T R = D_1 = \mathrm{diag}\,(0, 1, 1)\,. \tag{5.157}$$

Hence, any solution takes the form

$$R = \begin{pmatrix} 0 & \cos(\theta_R) & -\sin(\theta_R) \\ 0 & \sin(\theta_R) & \cos(\theta_R) \end{pmatrix}, \tag{5.158}$$

which is characterized by a single parameter θ_R. Transforming Eq. 5.158, while using the definition of R in Eq. 5.156, leads to an expression for the coupling g:

$$g = U_M D_M^{-\frac{1}{2}} R D_\nu^{\frac{1}{2}} U_\nu^T. \tag{5.159}$$

Within this transformation, it is assumed that all parameters in Eq. 5.159 are real for definiteness, and the phases in U_ν and R are set to zero.

5.2.3.2 *Correlations between neutrino masses and the dark sector*

The definition of the neutrino mass matrix in Eq. 5.147 links all dark matter parameters to neutrino masses. In absence of g_{ij} all neutrinos are massless, but also the other parameters enter the equation in the form of mass eigenstates and mixing matrix elements. More precisely, the fermion mixing matrix U_F introduces the Yukawa couplings y_1

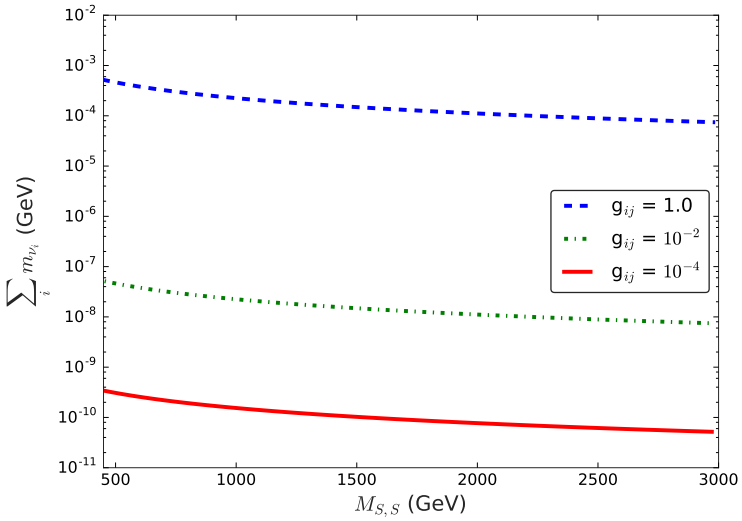

Figure 5.52: Influence of the scalar-fermion couplings g_{ij} on the sum of neutrino masses as a function of the singlet scalar mass parameter $M_{S,S}$.

and y_2. The scalar mixing matrix U_S contains all scalar couplings for singlets or doublets λ_S, λ_D etc. and the scalar mixing parameter A. This section contains numerical studies, with λ_S, λ_D, λ'_D and λ''_D mostly below 10^{-1} to put the main focus on the influence of the mixing parameters A, y_1 and y_2 as well as the fermion-scalar couplings g_{ij}. Fig. 5.52 shows the influence of scalar-fermion couplings g_{ij} on the sum of neutrino masses $\sum_i m_{\nu_i}$ as a function of the scalar singlet mass $M_{S,S}$. $M_{S,S}$ ranges from 450 to 3000 GeV. All other masses scale with $M_{S,S}$. The scaling factors are $M_{S,D} = 1.5M_{S,S}$, $M_{F,S} = 2M_{S,S}$ and $M_{F,D} = 2.5M_{S,S}$. Also, the Yukawa couplings are small $y_1 = 2 \times 10^{-2}$ and $y_2 = 10^{-1}$, as is the scalar mixing $A = 10^{-2}$ GeV. Thus, the lightest odd particle is always scalar and mostly singlet-like. The contributions from the vertex with g_{1i}, involving the singlet scalar and doublet fermion, dominate to some extent in the loop. Thus, an increase of the mass scale $M_{S,S}$ leads to a decreasing neutrino mass as expected by propagator suppression within the loop. A much larger influence comes from the neutrino-dark matter couplings g_{ij}. A drop from $g_{ij} = 1$ (dashed blue line) to 10^{-2} (dot dashed green line) or even to 10^{-4} (solid red line) yields an decrease of around four to six orders of magnitude for neutrino masses. This decrease is an expected behavior as g_{ij} enter the neutrino mass loop quadratically. Overall, it is possible to reach a viable region for the neutrino mass sum of $\mathcal{O}(10^{-11})$ eV only for small g_{ij} within this scenario.

A different scenario is shown in Fig. 5.53. It presents the sum of neutrino masses $\sum_i m_{\nu_i}$ as function of the fermion singlet mass parameter $M_{F,S}$. $M_{F,S}$ acts as common scale for all mass parameters,

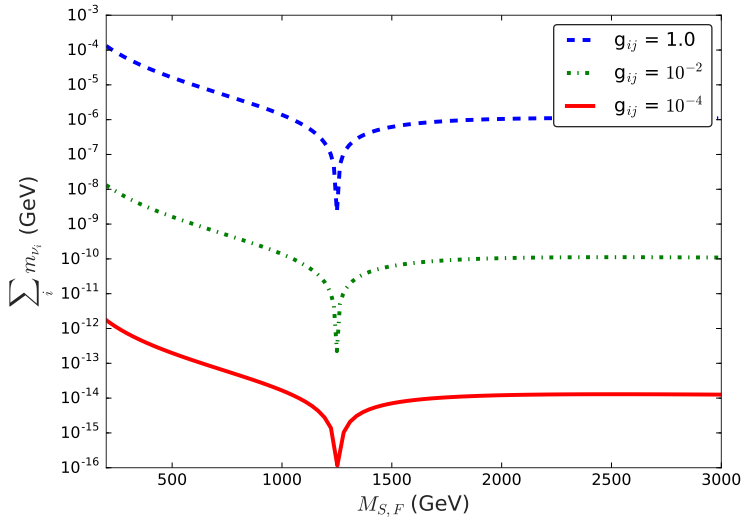

Figure 5.53: Influence of the scalar-fermion couplings g_{ij} on the sum of neutrino masses as a function of the singlet fermion mass parameter $M_{F,S}$.

which scale as $M_{S,S} = 2.5M_{F,S}$, $M_{S,D} = 3.5M_{F,S}$ and $M_{F,D} = 1.5M_{F,S}$. The lightest state is now fermionic. The Yukawa couplings for the new fermions remain comparably small with $y_1 = 4 \times 10^{-2}$ and $y_2 = 2 \times 10^{-2}$. A stronger scalar mixing $A = 10$ GeV, three orders of magnitude larger than in the previous scenario, is chosen. As $M_{S,S}$ is much larger than in Fig. 5.52, in addition to the larger mixing, the singlet scalar-doublet fermion part in the loop is not as dominant as before. Overall, the neutrino masses are at least one order of magnitude below the previous scenario and show a steep drop for small $M_{F,S}$. The most striking difference is a cancellation for $M_{F,S} = 1.25$ TeV. Terms in M enter with different signs, as the matrix elements M_{ij} contain sums over all neutral scalar and fermion states, leading to this effect. Beyond this dip, for larger $M_{F,S}$, the decrease with mass is less pronounced. Similarly as before, the same three values with the same color code for g_{ij} are shown. Outside the cancellation regions, quadratic scaling with g_{ij} is observed. It decreases the neutrino mass sum up to eight orders of magnitude for a four order of magnitude reduction in g_{ij}. The overall smaller values for $\sum_i m_{\nu_i}$ and the presence of the cancellation allow to reach viable neutrino masses for intermediate values of g_{ij} already.

APPROXIMATIONS FOR SMALL MIXING

As the parameter space is large with 17 free parameters, there are plenty of effects to illustrate which strongly depend on the parameter range. One example already mentioned, is the cancellation effect for a combination of masses and couplings, decreasing the neutrino

masses strongly. Different methods of exploring the variety of scenarios, lead to different interesting combinations of parameters. In order to disentangle different sectors, it is useful to make approximations for small mixings.
To start with a simple case, only proportionalities are presented without the exact formula. For small or vanishing scalar mixing the impact on masses of X_i and the mixing matrix U_S is given in Section 5.2.1.2. Similarly, Section 5.2.1.4 contains the formulas for small or vanishing fermion mixing. These simplifications can be used to simplify M from Eq. 5.147.
The first case considers vanishing $\lambda_S, \lambda_D, \lambda'_D, \lambda''_D$ and small mixing parameters $A, y_1, y_2 << 1$. Therefore, up to second order, the elements of M behave as

$$\begin{aligned} M_{11} &\propto A^2 const_1 - y^2 const_2 \\ M_{12} &\propto Ay \\ M_{22} &\propto A^2. \end{aligned} \tag{5.160}$$

The full result can be found together with different approximations in Appendix J. For either vanishing mixings and/or g_{ij} there are no neutrino masses in this case. The smallness of neutrino masses is controlled by a combination of g_{ij} and the mixing parameters in absence of the other scalar couplings.
Let's consider negligible mixing $y_1, y_2, A = 0$ next. In this case, the elements of M simplify to

$$\begin{aligned} M_{11} =& 0, \\ M_{12} =& 0, \\ M_{22} =& \big(M_{F,S} \big(\big(2M_{F,S}^2 \log\left(M_{F,S}^2\right) \\ & - \left(L^- v^2 + 2M_{S,D}^2\right) \log\left(\frac{L^- v^2}{2} + M_{S,D}^2\right)\big) \\ & \times \frac{2}{-L^- v^2 + 2M_{F,S}^2 - 2M_{S,D}^2} \\ & + \Bigg(\left(L^+ v^2 + 2M_{S,D}^2\right) \log\left(\frac{L^+ v^2}{2} + M_{S,D}^2\right) \\ & -2M_{F,S}^2 \log\left(M_{F,S}^2\right)\big) \\ & \times \frac{1}{-L^+ v^2 + 2M_{F,S}^2 - 2M_{S,D}^2}\Bigg)\Bigg) \\ & \times \frac{1}{16\pi^2}, \end{aligned} \tag{5.161}$$

where

$$\begin{aligned} L^+ :=& \lambda_D + \lambda'_D + \lambda''_D, \\ L^- :=& \lambda_D + \lambda'_D - \lambda''_D. \end{aligned} \tag{5.162}$$

Table 5.6: parameters used in Fig. 5.55, Fig. 5.56, Fig. 5.57 andFig. 5.54

Parameter	Fig. 5.55 and Fig. 5.56	Fig. 5.57	Fig. 5.54
λ_S	10^{-5}	10^{-5}	10^{-5}
λ_D	10^{-5}	10^{-5}	10^{-5}
λ'_D	10^{-5}	10^{-5}	10^{-5}
λ''_D	10^{-5}	10^{-5}	10^{-5}
A (GeV)	0	0	0
y_1	$10^{-7} - 10^{-4}$	$10^{-4} - 10^{0}$	10^{-6}
y_2	$10^{-7} - 10^{-4}$	$10^{-4} - 10^{0}$	$10^{-7} - 10^{-4}$
$M_{S,S}$ (GeV)	1000	1000	1000
$M_{S,D}$ (GeV)	$M_{S,S}/R_{D,S}$	$M_{S,S}/R_{D,S}$	$M_{S,S}/R_{D,S}$
$M_{F,S}$ (GeV)	$M_{S,S}/R_{S,F}$	$M_{S,S}/R_{S,F}$	$M_{S,S}/R_{S,F}$
$M_{F,D}$ (GeV)	$M_{S,S}/R_{D,F}$	$M_{S,S}/R_{D,F}$	$M_{S,S}/R_{D,F}$
g_{1i}	10^{-1}	10^{-1}	0.5
g_{2i}	10^{-5}	10^{-5}	10^{-4}

In the limit of vanishing λ_S, λ_D and λ'_D and small λ''_D the matrix element M_{22} becomes

$$\begin{aligned} M_{22} = &\left(\lambda''_D \left(M^3_{F,S} v^2 \log\left(M^2_{S,D}\right) + M^3_{F,S} v^2 \right.\right. \\ &\left.\left. - M^3_{F,S} v^2 \log\left(M^2_{F,S}\right) - M_{F,S} M^2_{S,D} v^2\right)\right) \\ &\times \frac{1}{16\pi^2 \left(M^2_{F,S} - M^2_{S,D}\right)^2}, \end{aligned} \tag{5.163}$$

which is proportional to λ''_D. Hence, this case features only one non-zero neutrino mass which is proportional to the scalar doublet mass splitting λ''_D. The smaller λ''_D, the smaller is this expression. Either λ''_D or g_{2i} can be very small (but not both simultaneously) in order to achieve viable neutrino masses.

Refraining from negligible fermion mixing, the analytic treatment of neutrino masses becomes more complex. The mixing matrix and masses are more complicated for the fermions than for the scalars. Full results can be found in Appendix J. It is useful to have a look at figures produced from the neutrino mass formula in order to understand the correlations.

A scenario is chosen, where the lightest odd particle is the scalar singlet and the scalar mixing A is still negligible. Additionally, the couplings g_{2i} of the scalar doublet to the neutrinos and leptons are chosen to be small – see Tab. 5.6. The largest influence on neutrino masses, therefore comes from the g_{1i} vertex with the fermion doublet and scalar singlet. As seen for the cancellation effects in Fig. 5.53, ratios between the mass parameters can be important. For this study they are introduced as $R_{D,S} = \frac{M_{S,S}}{M_{S,D}}$, $R_{S,F} = \frac{M_{S,S}}{M_{F,S}}$ and $R_{D,F} = \frac{M_{S,S}}{M_{F,D}}$.

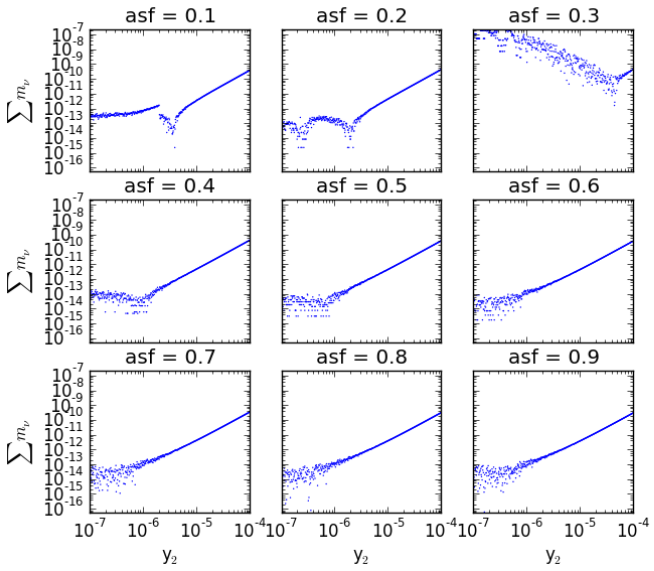

Figure 5.54: Plot showing the dependence of neutrino mass on y_2 for different fermionic singlet masses.

Which relate the mass parameters to $M_{S,S}$.
y_1 is fixed to 10^{-6} and y_2 to varies from 10^{-7} to 10^{-4}. The obtained neutrino masses are shown in Fig. 5.54. $R_{D,S}$ and $R_{D,F}$ are fixed to 0.3 and 0.6, respectively. The parameter $R_{S,F}$ ranges from 0.1 to 0.9 as labeled in the figure. All parameters are as indicated in Tab. 5.6, in particular $g_{2i} = 10^{-4}$ is much smaller than $g_{1i} = 0.5$. The neutrino masses exhibit a minimum located at different y_2 for varying $R_{S,F}$. As long as $R_{S,F}$ is larger than $R_{D,S} = 0.3$, the behavior is rather similar. For very small y_2, there are some fluctuations. As y_2 increases above 10^{-6}, the fluctuations are no longer visible, leaving a smooth increasing line. For $R_{S,F} = 0.3$ (upper right corner) the behavior changes drastically. For almost all y_2 the resulting neutrino masses are much higher than in the figures with larger $R_{S,F}$. Especially, for small values of y_2 there are neutrino masses up to seven orders of magnitude larger than for other mass combinations. For $R_{S,F}$ below 0.3 there is some minor difference as the curve exhibits several minima for y_2 around 10^{-6}. Hence, specific combinations of masses and mixings allow for very small neutrino masses, whereas away from this minimum the dependence on y_2 becomes milder. Conversely, there are regions with very small y_2 and still reasonably large neutrino masses.

Fig. 5.55 is a generalization of the previous Fig. 5.54. It depicts the plane y_1, y_2 with a color code for neutrino masses. The parameters are given in Tab. 5.6. For this plot, again, $R_{D,S}$ is 0.3, $R_{D,F}$ is 0.6. The value of $R_{S,F}$ is indicated on the figure. y_1 and y_2 cover a range from 10^{-7} to 10^{-4}. As in the previous scenario, for $R_{S,F}$ greater than $R_{D,S} = 0.3$, the figures look rather similar. If y_1 or y_2 is large, the neutrino masses become large as well. Decreasing both, going from the

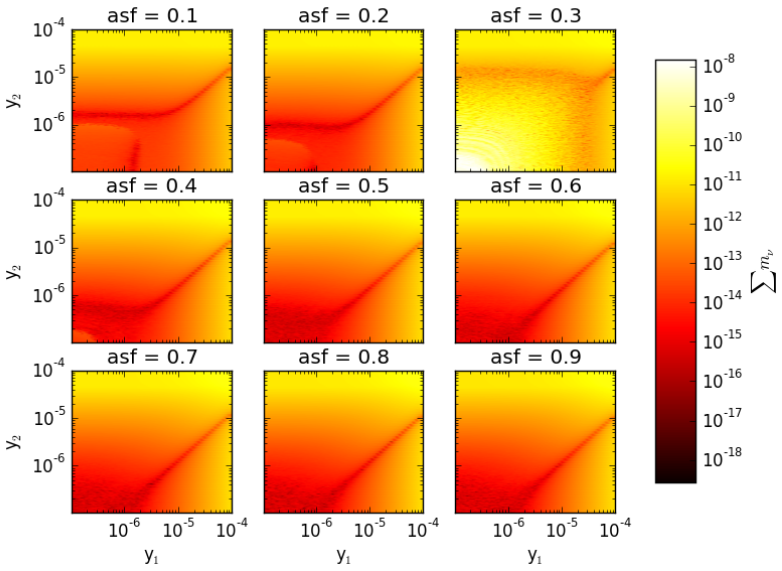

Figure 5.55: Color plot showing $\sum m_\nu$ as a function of the fermion Yukawa couplings y_1 and y_2 for different singlet fermion masses.

upper right corner to the down most left region of the plane, darkens the color as the neutrino mass decreases. This is overlaid by a valley of minima concentrated along a line from ($y_1 \approx 10^{-6}$,$y_2 \approx 10^{-7}$) to ($y_1 \approx 10^{-4}$,$y_2 \approx 10^{-5}$). In this region the neutrino masses are smaller than in the surrounding areas. This corresponds to a minimum in Fig. 5.54. In the plots for $R_{S,F} = 0.3$, $R_{S,F} = 0.1$ and $R_{S,F} = 0.2$ it can be seen, that the valley of minima continues on for either y_1 or y_2 being around 10^{-6} where as the other can be much smaller. When both y_1 and y_2 decrease below 10^{-6}, in these plots , the neutrino masses start to rise again. When $R_{S,F}$ is identical to $R_{D,S} = 0.3$, the lines of minima are still visible but their location changes from around 10^{-6} to 10^{-5}. The overall neutrino masses are much larger, especially for very small compared to the other figures. They can reach up to 10^{-8}. Hence, with certain mass combinations it is possible to have large neutrino masses even though the Yukawa couplings are rather small. Fig. 5.56 shows another selection of plots to investigate the dependence of neutrino mass sum on y_1 and y_2. Similarly as before, $M_{S,S}$ is set to 1 TeV while the scalar mixing is $A = 0$ GeV. To increase the strength of the interaction between scalar singlet and fermion doublet, g_{1i} is set to 0.1. All other couplings have no impact. They are set to 10^{-5}, so g_{2i}, λ_S, λ_D, λ'_D and λ''_D are negligible – see Tab. 5.6. The setting is the same as for Fig. 5.55, despite $R_{S,F} = 0.3$ is now fixed and $R_{D,F}$ is varied. $R_{D,S}$ is fixed at 0.3. This choice allows to disentangle the influence of the doublet scalar and singlet fermion coupling even more. For large $M_{F,D}$ – see upper left corner –. It is possible to obtain viable neutrino masses over the whole range of y_1 and y_2 which

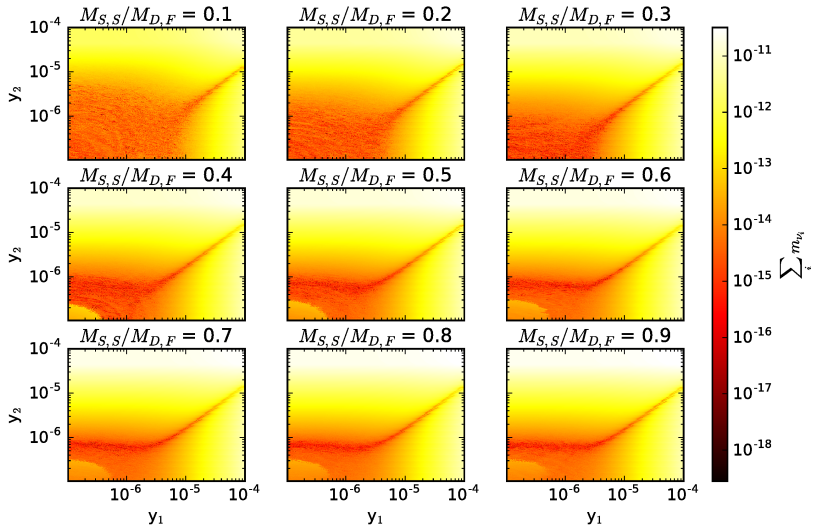

Figure 5.56: Influence on the ratio of the singlet scalar mass $M_{S,S} = 1$ TeV over the singlet fermion mass $M_{F,S}$ on the sum of neutrino masses in the plane of Yukawa couplings y_1–y_2. The doublet scalar and singlet fermion have been decoupled via $M_{S,S}/M_{S,D} = 0.6$ and $M_{S,S}/M_{F,S} = 0.3$.

become smaller for smaller couplings. For similar sized Yukawa couplings there is a region which features small neutrino masses (red). When only one coupling is large, the neutrino masses can be reasonably large. Yet the decrease of $M_{F,D}$ demands a reduction of the couplings in order to provide the same neutrino masses – see the bottom right plot in comparison to the upper left. Starting from $R_{S,F}$ around 0.4, which is larger than $R_{D,S}$, one observes again that for too small couplings the neutrino masses start to rise. This is similar to the effect of cancellation – compare for example Fig. 5.53. This leads to a line (horizontally and vertically) shaped valley of small neutrino masses which extended in a line for $y_1 \approx y_2$. Altogether, relations between masses play an important role in achieving the correct neutrino masses for small mixings. If the fermion Yukawa couplings are not too small the dependence on the mass ratios nearly vanishes. This is presented in Fig. 5.57. The figure shows the plane (y_1,y_2) with a similar color code as the previous Fig. 5.55. The factors for $M_{F,S}$ and $M_{F,D}$ are the same, but the range for y_1 and y_2 is between 10^{-4} and 1. All other parameters stay the same – see Tab. 5.6. The typical line of neutrino mass minima for a specific combination of y_1 and y_2 is visible in these plots as well. Altogether, there is a decrease in neutrino mass with decreasing couplings within each plot. The dependence on $R_{S,F}$ is rather mild. There are subtle changes increasing the neutrino masses as $R_{S,F}$ increases but the plots look rather similar.

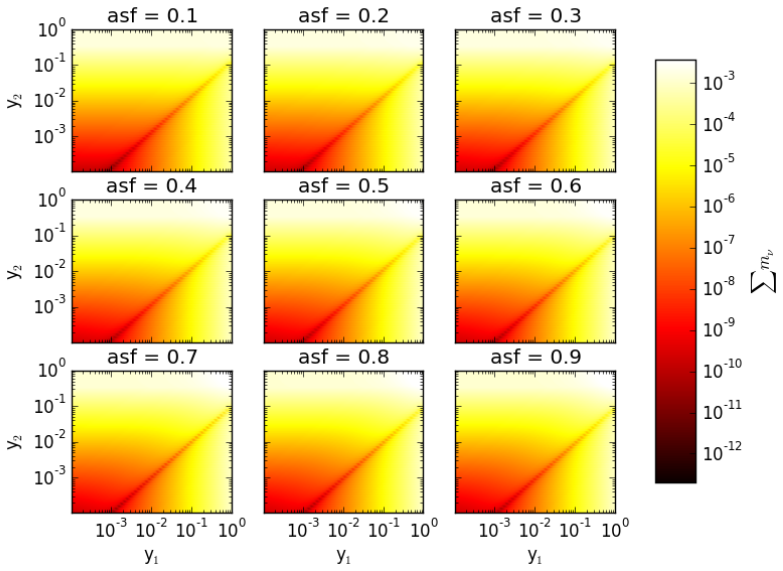

Figure 5.57: Color plot showing $\sum m_\nu$ as a function of the fermion Yukawa couplings y_1 and y_2 larger than 10^{-4} and for different singlet fermion masses.

5.2.4 *Lepton flavor violation*

The radiative generation of neutrino masses needs lepton flavor changing couplings within the Lagrangian. These couplings give rise to lepton flavor changing processes. Some important processes involve radiative transitions like $\mu \to e\gamma$ and probably $\mu \to e\gamma\gamma$ as well as leptonic decays $\mu \to eee$ and conversion in nuclei $N + \mu \to N + e$ or similar processes involving τ leptons. General calculations for loop diagrams in T12A and similar models are found in Appendix I, in particular in Section I.6 for $\mu \to e\gamma$, in Section I.7 for $\mu \to e\gamma\gamma$ and in Section I.8 for $\mu \to 3e$. There are also calculations, based on this loop classification, containing full squared amplitudes supported by the Mathematica [255] package FeynRules [256]. The results are cross checked with B. Herrmann using FORM [257]. The amplitudes will be made available within the bitbucket of the working group.
All lepton flavor changing processes are mediated by odd scalars and fermions in a loop. Either a scalar or a fermion has to be charged in order to carry charge of the incoming lepton. The corresponding vertices are summarized in Appendix E. The lepton flavor changing processes mentioned above scale with the couplings g_{ij}, the same couplings which give rise to neutrino masses. Neutrino masses always involve two $\mathbb{Z}_2$ odd neutral particles, so both mixing matrices U_F and U_S enter the equation. For charged leptons only one particle in the loop is neutral so it is either U_S or U_F contributing to the specific diagram. Without g_{ij}, not only neutrino masses vanish but also

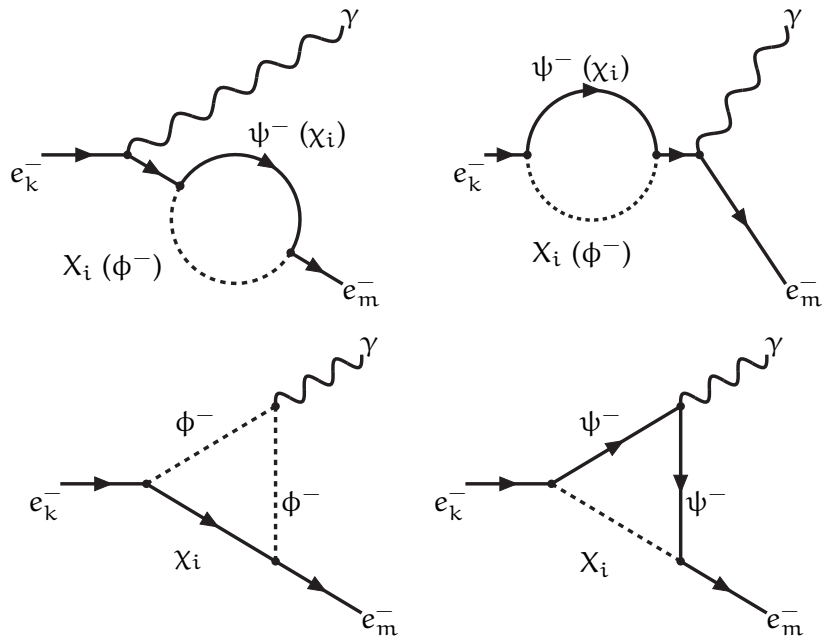

Figure 5.58: Radiative one-loop processes $e_k^- \to e_m^- \gamma$ violating lepton flavor.

lepton flavor violation.

For the radiative decay, like $\mu \to e\gamma$, the diagrams are shown in Fig. 5.58. They consist of two bubble type and two triangular topologies. The calculations are similar to the scotogenic model – Section 5.1 in particular Section 5.1.3. The difference is in the number of all particles which can run in the loop and in the couplings. When suppressing the external lepton masses the bubble diagrams only cancel the divergences, finite parts arise from the triangle diagrams. The branching ratio is then

$$\begin{aligned} \mathrm{BR}(\mu \to e\gamma) = \frac{3\alpha_{em}}{64\pi G_F^2} \Bigg[& \frac{1}{2m_{\psi^-}^4} \left(\sum_i g_{11} g_{12} U_{S,1i}^2 F_2\left(\frac{m_{X_i}^2}{m_{\psi^-}^2}\right) \right)^2 \\ & + \frac{1}{m_{\phi^-}^4} \left(\sum_i g_{21} g_{22} U_{F,1i}^2 F_2\left(\frac{m_{X_i}^2}{m_{\phi^-}^2}\right) \right)^2 \\ & + \frac{1}{m_{\phi^-}^2 m_{\psi^-}^2} \left(\sum_i g_{11} g_{12} U_{S,1i}^2 F_2\left(\frac{m_{X_i}^2}{m_{\psi^-}^2}\right) \right) \\ & \times \left(\sum_j g_{21} g_{22} U_{F,1j}^2 F_2\left(\frac{m_{X_j}^2}{m_{\phi^-}^2}\right) \right) \Bigg], \end{aligned} \tag{5.164}$$

with F_2 as in Eq. 5.104. Similar results are found for $\tau \to e\gamma$ (exchange g_{12} for g_{13}) and $\tau \to \mu\gamma$ (exchange g_{11} for g_{12} and g_{12} for g_{13}).

μe conversion in nuclei is described by the same diagrams as $\mu \to e\gamma$ shown in Fig. 5.58 with an off-shell photon which couples to the nucleus.

Leptonic decays like $\mu \to eee$ are presented in Fig. 5.60. Analogous to $\mu \to e\gamma$ two triangle and two bubble loops are present but also

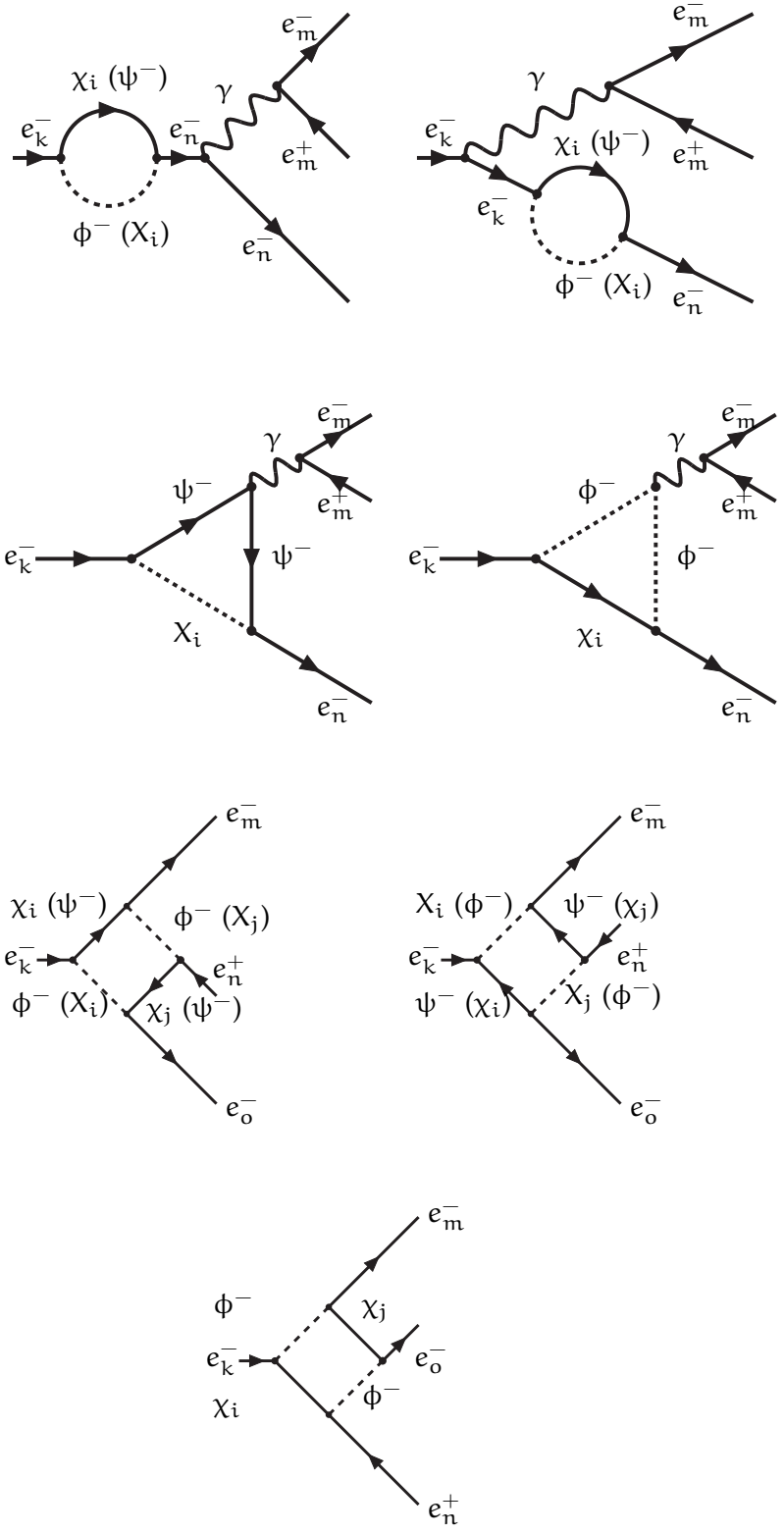

Figure 5.59: Loop diagrams contributing to the leptonic decays $e_k^- \to e_m^- e_n^+ e_o^-$

three additional box diagrams. The amplitudes involve either two or in case of the boxes four scalar-fermion couplings g_{ij}.
Alongside μ decays involving two photons in the final state can occur. They feature additional box diagrams with respect to $\mu \to e\gamma$. All topologies are shown in Fig. 5.60. Similar to $\mu \to e\gamma\gamma$ in the scotogenic model, this decay is not finite for soft or collinear photons. Current experimental limits are summarized in Chapter 4 see Tab. 4.1. The most stringent constraints come from $\mu \to e\gamma$ which restrict the parameter space mostly regarding the new couplings g_{ij}. Fig. 5.61 illustrates the dependence of $\mathrm{BR}(\mu \to e\gamma)$ on the singlet scalar mass parameter $M_{S,S}$ which acts as a common mass scale. All parameters are chosen as in Fig. 5.52. Curves are presented for $g_{ij} = 1$ (dashed blue line), $g_{ij} = 10^{-2}$ (dashed green line) and $g_{ij} = 10^{-4}$ (solid red line). Overall, the branching ratio decreases with increasing mass similarly, to neutrino masses due to propagator suppression in the loops. The dependence on g_{ij} is much stronger than on the mass. A drop of over eight orders of magnitude is observed when decreasing the couplings g_{ij}, going from 1 to 10^{-2}. A value of g_{ij} below 10^{-2} is sufficient to evade experimental limits. In comparison, neutrino masses demand g_{ij} below 10^{-4} in this scenario.

5.2.5 *Numerical results*

In this section numerical scans of the parameter space of T12A with focus on scalar dark matter are presented. Two different scans have been conducted. First, a random scan over the full parameter space is conducted. Second, a more restricted scan, enhancing coannihilation between fermion and scalars as well as lepton and neutrino final states, is performed. For both scans the relic density constraint $\Omega h^2 = 0.1186 \pm 0.0031$ is imposed, as well as limits on the Higgs doublet such that $M_H = 125$ GeV and it has Standard Model couplings [258]. The neutrino mass differences and mixing angles are taken from [259]. They are assumed to follow a normal distribution within the experimental limits:

$$\begin{aligned}
\sin^2\theta_{12} &= 0.30 \pm 0.013,\\
\sin^2\theta_{13} &= 0.0218 \pm 0.0010,\\
\sin^2\theta_{23} &= 0.452 \pm 0.052,\\
\Delta m^2_{12} &= (7.5 \pm 0.19) \times 10^{-5}\ \mathrm{eV}^2,\\
\Delta m^2_{23} &= (2.457 \pm 0.047) \times 10^{-4}\mathrm{eV}^2.
\end{aligned}$$

5.2.5.1 *Random scan*

For a first random scan, the free parameters are varied in the ranges shown in Tab. 5.7. Points with scalar dark matter, matching the relic density observations, are selected. Around 10^4 points are obtained.

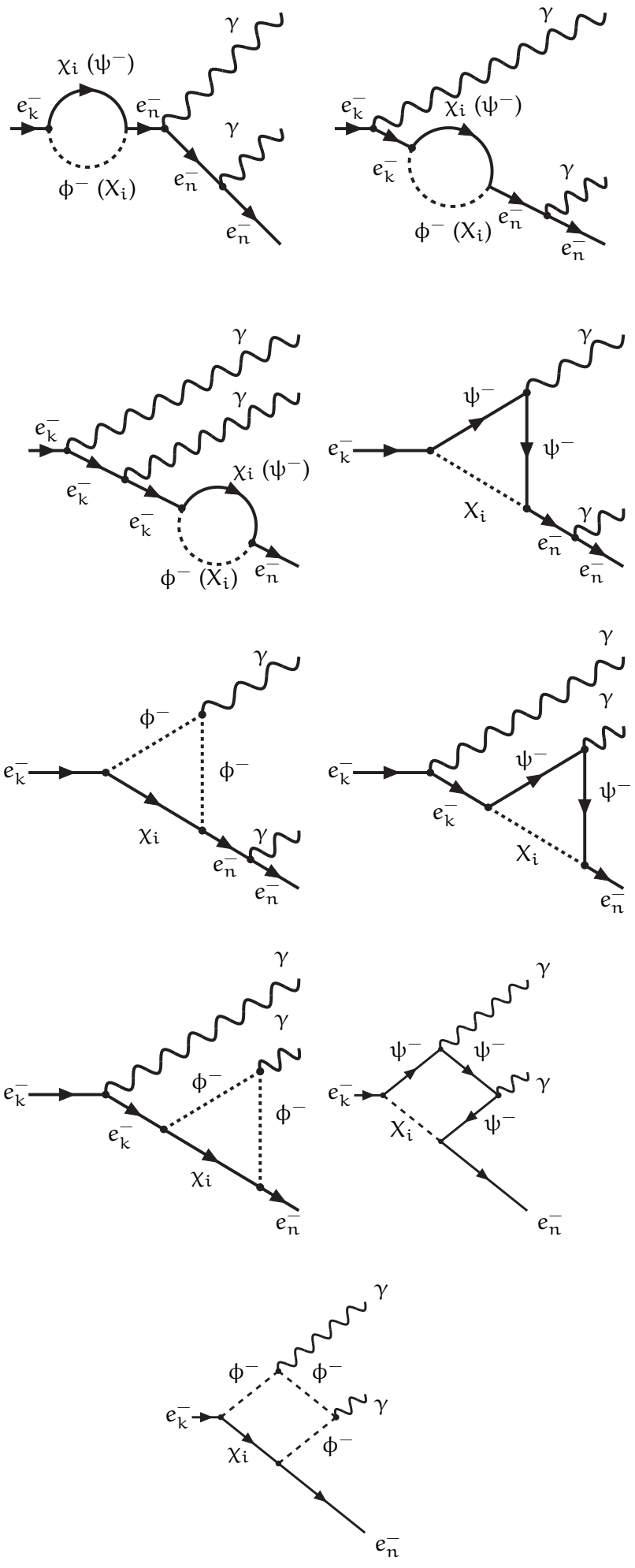

Figure 5.60: One-loop diagrams for the process $e_k^- \to e_m^- \gamma\gamma$

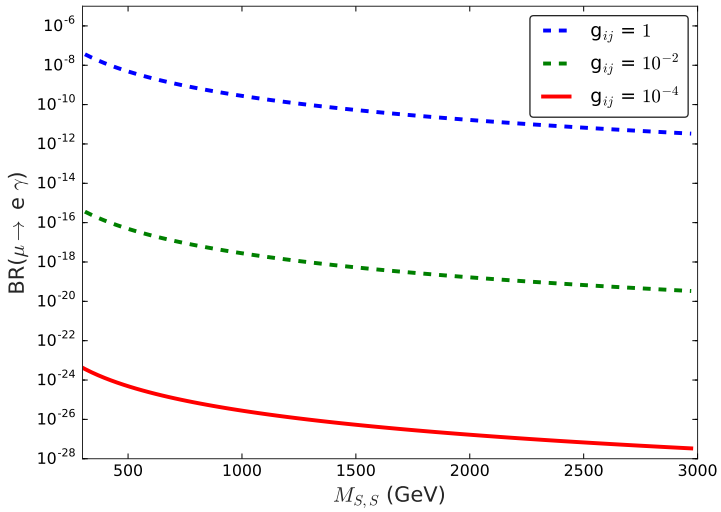

Figure 5.61: Influence of the scalar-fermion couplings g_{ij} on the branching ratio BR($\mu \to e\gamma$) as a function of the singlet scalar mass parameter $M_{S,S}$.

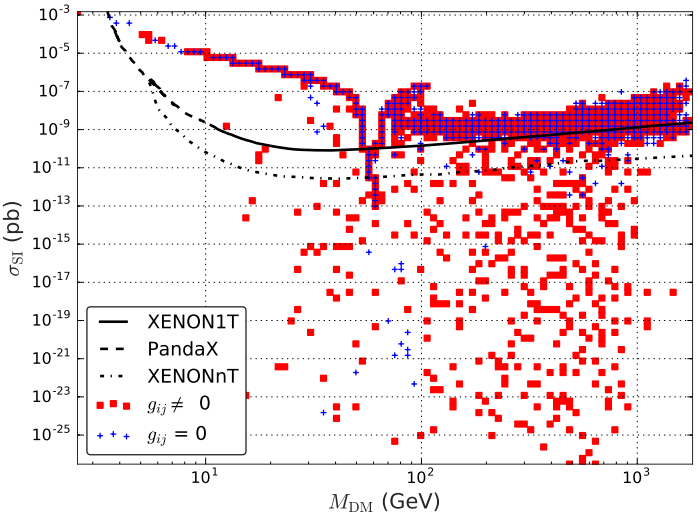

Figure 5.62: Direct detection cross section of scalar singlet dark matter as a function of its mass without (blue) and with (red) coupling of the scalar to the fermion sector.

All are compatible with the constraints mentioned above, including neutrino masses by use of the Casas-Ibarra parameterization – see Section 5.2.3.1. The range of g_{ij} is limited to be between -2π and 2π. Another set of $\mathcal{O}(10^4)$ points with zero neutrino masses as $g_{ij} = 0$ and correct relic density is produced. Fig. 5.62 shows all points with $g_{ij} \in [-2\pi, 2\pi]$ (red squares) and with $g_{ij} = 0$ (blue crosses) projected onto

Table 5.7: Parameters used for the first random scan

Parameter	Value
$\lambda_S, \lambda_D, \lambda'_D, \lambda''_D$	$\pm\pi(10^{-10} - 10^{0})$
A (GeV)	$(10^{-10} - 10^{4})$
y_1	$\pm(10^{-10} - 10^{0})$
y_2	$(10^{-10} - 10^{0})$
$M_{S,S}$, $M_{S,D}$, $M_{F,S}$, $M_{F,D}$ (GeV)	10 - 2000
g_{ij}	fixed to match observations or 0
$\cos(\theta_R)$	0 - $\pm$ 1

the plane of dark matter mass M_{DM} and spin-independent elastic scattering cross section σ_{SI}. The current direct detection bounds are shown as lines. For low masses, the most stringent limits come from PandaX (dashed black line) [101]. For larger dark matter mass, the strongest constraints are from XENON1T (dashed black line) [260]. Future prospects of XENONnT [112] are also shown as a dash dotted line. First, all points without fermion-scalar couplings (blue crosses) are considered. Since the mixing can be large, dark matter masses can be rather small. For such small masses below the Higgs resonance $M_{DM} \approx M_H/2$, direct detection and annihilation are closely related. Hence, the points gather in a small band to fulfill the relic density constraint. When approaching the Higgs resonance, the annihilation of dark matter becomes more and more efficient, demanding smaller couplings to obtain the correct relic density. Thus, the direct detection cross section decreases strongly towards the resonance and reaches very small values, down to 10^{-25} pb or less on the resonance. Similarly, to singlet-doublet scalar dark matter [242, 243], all points with masses below the resonance are excluded by direct detection experiments. Above the resonance region, the viable band broadens but it is still constrained, as the correlation between annihilation and scattering cross section is not reduced as much. Except for points on the resonance, all models will be probed by XENONnT. Allowing for $g_{ij} \neq 0$ (red squares) in order to obtain viable neutrino masses, opens up new annihilation channels as explained in Section 5.2.2 and offers coannihilation between scalars and fermions. This weakens the correlation of the relic density and direct detection. The new channels only contribute to relic density but not to dark matter nucleon scattering. This broadens the band of correct relic density. Consequently, it allows for cross sections way below the reach of future experiments. For mostly the entire mass range, cross section down to 10^{-25} pb and less even far away from the Higgs resonance can be found.

All 10^4 points, which are consistent with neutrino masses, are analyzed regarding lepton flavor violation. Fig. 5.63 shows these models

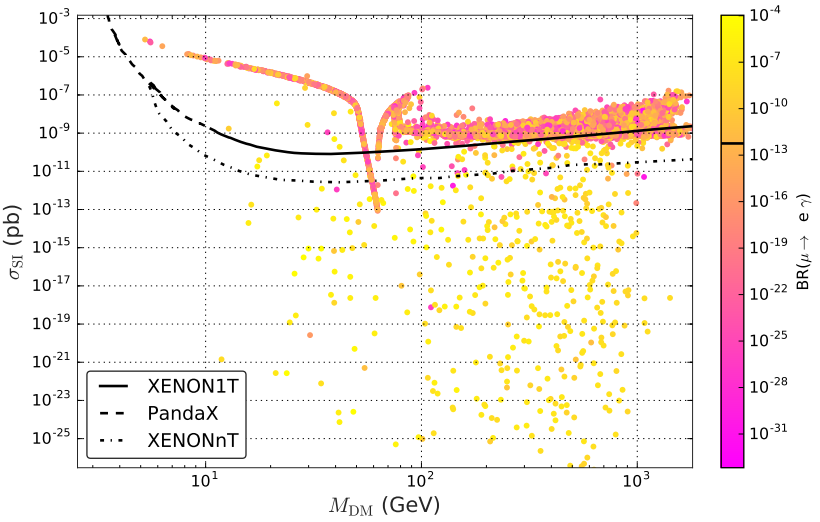

Figure 5.63: Direct detection cross section of scalar singlet dark matter as a function of its mass and its correlation with the lepton-flavor violating branching ratio BR($\mu \to e\gamma$) (colors).

in the same plane as Fig. 5.62 including a color code for the branching ratio of $\mu \to e\gamma$. The current limit is shown as a solid black line in the color bar. Most points, which feature small direct detection cross sections, need large values of g_{ij} in order to reach an acceptable relic density. In return, the large couplings give rise to large branching ratios for lepton flavor violating processes. Consequently, most points below XENON1T are excluded by lepton flavor experiments. Most points with a small branching ratio resemble the region which was found with $g_{ij} = 0$. Some of these viable points are below the current direct detection sensitivity but within the reach of future experiments allowing them to be probed soon. Fig. 5.64 contains points with non-zero neutrino masses. It shows the correlation between σ_{SI} and the singlet scalar coupling λ_S. The points have been structured in a grid to make effects more visible without overloading the figure by too much overlap. The different markers differentiate between points which are excluded by lepton flavor constraints (red squares) and points which lie beneath current constraints (blue crosses). The smallest values for σ_{SI} are reached for smallest values of λ_S. These points correspond to mostly singlet-like dark matter which couples to the Standard Model via λ_S. In return the larger λ_S, the larger is the minimal value of σ_{SI}. In order to obtain the correct relic density for these small couplings, the lepton channels and coannihilations have to be enhanced by large g_{ij}. Hence, all of these small σ_{SI} points are already excluded by lepton flavor constraints as explained for Fig. 5.63. A band of points compatible with lepton flavor violation covers the whole range of λ_S but features σ_{SI} above 10^{-9} pb. In Fig. 5.65 the

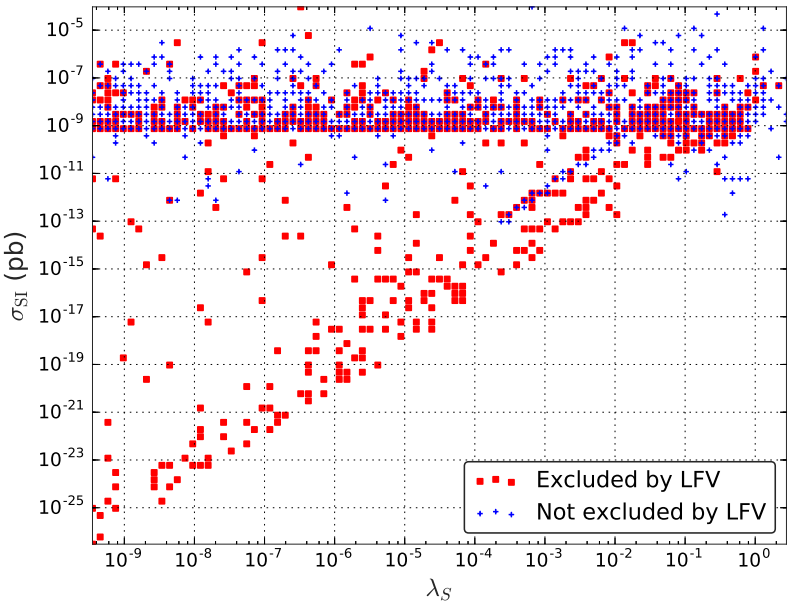

Figure 5.64: Direct detection cross section plotted against singlet scalar coupling λ_S.

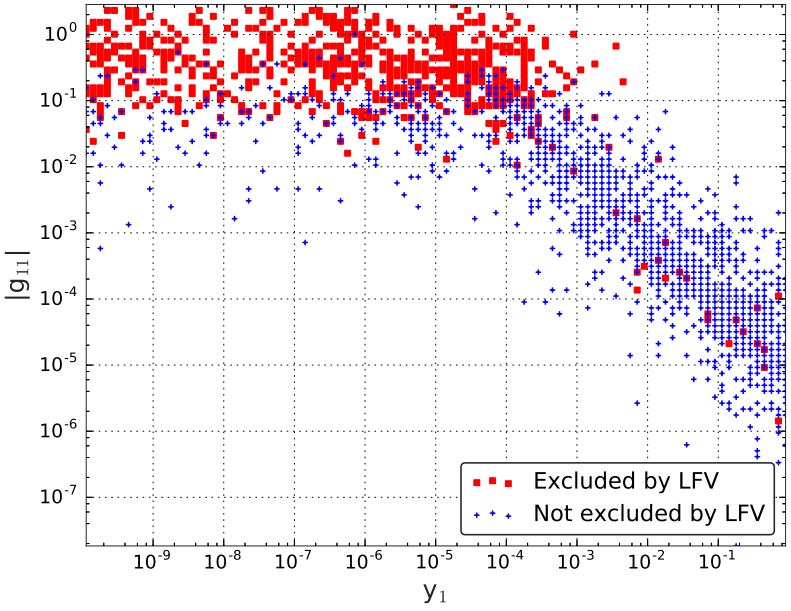

Figure 5.65: Correlation between y_1 and g_{11}.

correlation between y_1 and g_{11} for neutrino masses is shown. The same color code as in the previous figure is used to differentiate between points which are consistent with lepton flavor violation limits and which are excluded. In Section 5.2.3 some general studies of this correlation have been presented which are found in this figure as well. Either g_{11} or y_1 can be small but not both simultaneously to

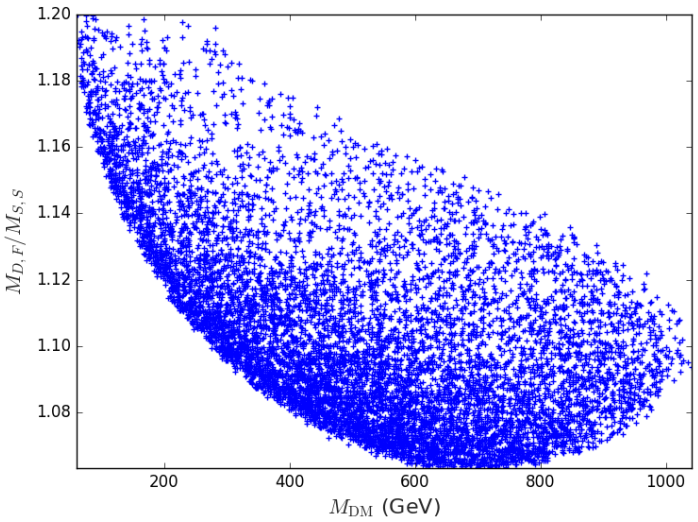

Figure 5.66: Ratio of $M_{F,S}$ and $M_{S,S}$ as a function of dark matter mass M_{DM} for all viable points in the coannihilation region.

obtain viable neutrino masses. For y_1 larger than 2×10^{-4} there is a strong correlation between g_{11} and y_1. A diagonal broad band of viable points is found across the plane. For smaller values of y_1 (below 10^{-4}) this correlation becomes weak. Furthermore, for large g_{ij}, most points of this scan are excluded by lepton flavor experiments.

5.2.5.2 *Coannihilation region*

Table 5.8: Parameters used for the coannihilation region random scan

Parameter	Value
λ_S	$\pm\pi(10^{-10} - 10^{-4}$
λ_D, λ'_D	$\pm\pi(10^{-10} - 10^{0})$
λ''_D	$\pi(10^{-10} - 10^{-4}$
A (GeV)	$(10^{-10} - 10^{-1})$
y_1	$\pm(10^{-10} - 10^{-4})$
y_2	$(10^{-10} - 10^{-4})$
$M_{S,S}$ (GeV)	10 - 1000
$M_{S,D}$ (GeV)	1.5 $M_{S,S}$ - 3000
$M_{F,S}$ (GeV)	$M_{F,D}$ - 3000
$M_{F,D}$ (GeV)	(1.05 - 1.2) $M_{S,S}$
g_{ij}	$\leqslant 2\pi$ (Casas-Ibarra parametrization)
$\cos(\theta_R)$	(0 - $\pm$ 1)

The first random scan gives an impression on how to incorporate lepton flavor violation limits. The focus in the second scan is on a region with enhanced coannhilation between fermions and scalars as well as leptonic final states. The parameter ranges are shown in Tab. 5.8. To obtain points, which are within this region and compatible with all current limits including lepton flavor violation, the parameter space is restricted to mostly singlet scalar dark matter. Therefore, the scalar mixing A is below 10^{-1} GeV and $M_{S,S}$ is always the lightest, varying between 10 and 1000 GeV. $M_{S,D}$ is at least 1.5 times as large and up to 3 TeV. To enhance coannihilation, the fermion doublet parameter $M_{F,D}$ is chosen to be 1.05 up to 1.2 times larger than $M_{S,S}$, whereas the fermion singlet is at least as heavy going up to 3 TeV. As the coupling λ_S of the singlet scalar to the Higgs is suppressed, coannihilation, as well as lepton and neutrino final states, become more important for the relic density. The fermion mixing is suppressed, since the Yukawas y_1 and y_2 are below 10^{-4}. Consequently, the vertex with g_{1i} influences coannihilation dominantly. Demanding at least 50% of the processes for dark matter annihilation in the early Universe are due to coannihilation with the fermions. $\mathcal{O}(10^4)$ points consistent with dark matter, neutrino mass and lepton flavor violation experiments are gathered.

Fig. 5.66 shows the ratio of $M_{F,S}$ and $M_{S,S}$ as a function of dark matter mass for all viable points. For small dark matter masses the ratio is rather large, up to the maximum allowed value of 1.2. For masses above 600 GeV the ratio tends to be in between 1.05 and 1.15. Regarding masses below 600 GeV there is a whole region which is not accessible within this framework as it is not possible to fulfill all constraints simultaneously. Starting at around 800 GeV the lower outline of the distribution displays another upswing. The smallest allowed value for 1.05 can no longer be reached. This rather sharp edge thins out for larger ratios, as it is easier to have measurable coannihilation contributions for small mass ratios. Since dark matter is mostly singlet-like and fermions also have small mixing, the couplings g_{1i} are constrained the most by dark matter observables as well as lepton flavor violation. Fig. 5.67 shows all viable points in the plane $|g_{11}| - |g_{12}|$ with color indicating the size of $|g_{13}|$. y_1 and y_2 are small. Hence, g_{ij} can be large and still provide sufficiently small neutrino masses. The distribution of points in the plane shows that either $|g_{11}|$ or $|g_{12}|$ can be large but not both. There are two separate regions. One for $|g_{11}|$ roughly above 10^{-1} and any value for $|g_{12}|$ from 10^{-6} up to 10^{-1} and a mirrored region where $|g_{12}|$ is above 10^{-1}. This twofold shape is due to the different size of squared neutrino mass differences. The value of $|g_{13}|$ increases along the short axis of the two elongated regions, for example with growing $|g_{11}|$, starting from 10^{-1}, $|g_{13}|$ increases. Overall $|g_{13}|$ is less constrained by lepton flavor

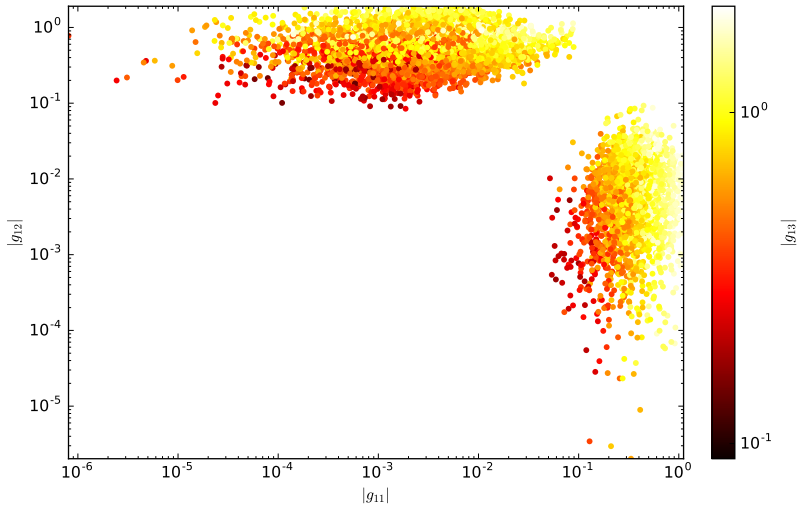

Figure 5.67: Viable scalar-fermion couplings in the plane $|g_{11}|$–$|g_{12}|$ (color code for $|g_{13}|$).

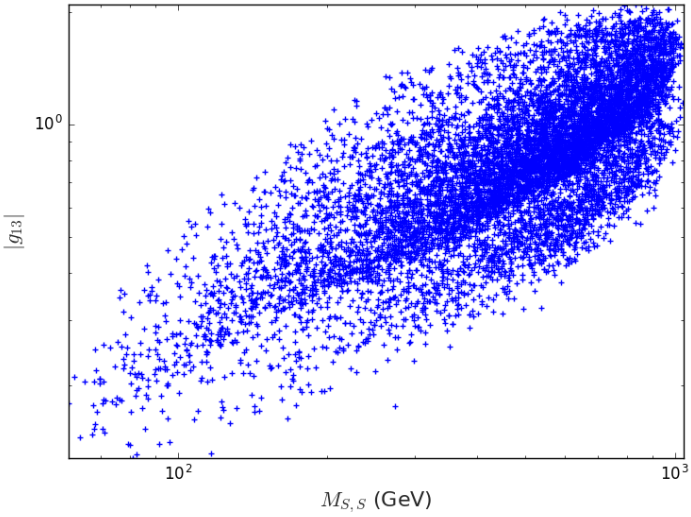

Figure 5.68: All points projected onto the plane of the singlet scalar mass parameter $M_{S,S}$ and the singlet scalar-fermion coupling g_{13}.

processes as the bounds for τ leptons are not as strict as for μ leptons.

As discussed before, the couplings g_{1i} and g_{2i} determine the neutrino masses and branching ratios for lepton flavor violating processes. Figure 5.68 shows a projection of all points onto the plane $M_{S,S}$ and $|g_{13}|$. There is a strong correlation between the singlet mass parameter and the neutrino couplings. As the mass increases, the absolute value of g_{13} needed to obtain the correct neutrino masses increases as well. There are two overlapping regions which correspond

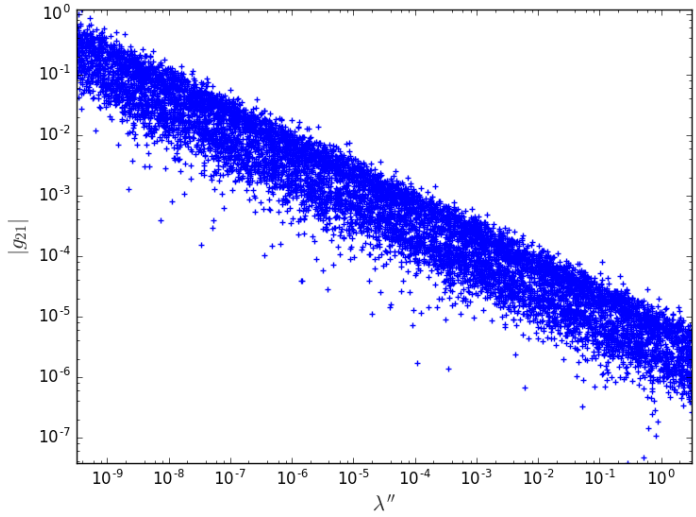

Figure 5.69: Correlation between the scalar doublet mass splitting λ''_D and the scalar doublet-fermion neutrino coupling g_{21}.

to the two regions in the previous figure. When the singlet scalar mass becomes larger, the suppression of neutrino masses grows, a larger $|g_{13}|$ is needed to balance it. As the most stringent lepton flavor violation limits do not come from processes involving the τ lepton, g_{13} is not as much influenced as g_{11} and g_{12} by the constraints. Yet, there are large regions of the parameter space which can not be reached due to neutrino mass constraints. As elaborated in Section 5.2.3, small mixings A, y_1 and y_2 lead to strong correlations in the parameter space when requiring all neutrino constraints. There is an expected anti-proportionality between λ''_D and g_{2i}. Fig. 5.69 shows all points projected onto the plane $(\lambda''_D, |g_{21}|)$. There is a clear correlation between the two parameters. The blue dots gather around a declining line. Any increase in λ''_D leads to a clear decrease in $|g_{21}|$. For λ''_D around 10^{-9}, the neutrino coupling cannot be smaller than 10^{-2} and not larger than 4. If λ''_D is as large as 10^{-1}, the value of g_{21} has to be between 10^{-6} and 3×10^{-5} in order to fulfill the neutrino constraints and satisfy all lepton flavor violation constraints. All other regions in the parameter space are excluded. In general, within the coannihilation region, g_{2i} are not as important for dark matter observables as g_{1i} due to the choice of singlet-like scalar dark matter. Overall, the neutrino couplings g_{ij} are chosen such that they result in neutrino masses compatible with experimental constraints. This is done by the Casas-Ibarra parametrization which depends on one single angle θ_R. Fig. 5.70 depicts the correlation between $|\theta_R|$ and $|g_{11}|$. The fact that there are two distinct areas for $|g_{11}|$, – compare to Fig. 5.67– also reflects in the allowed range of the parametrization angle. For $|g_{11}|$ larger than 10^{-1} there is a large portion of the range

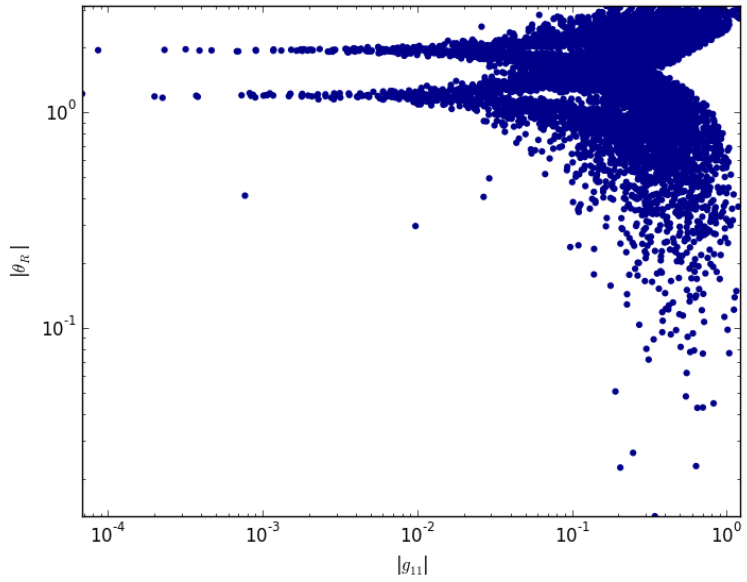

Figure 5.70: Correlation between the Casas-Ibarra angle θ_R and the fermion-scalar coupling g_{11}.

for θ_R covered. The angle can go up to the maximum value and down to 10^{-2}. There is a triangular shaped feature for $|g_{11}|$ above 3×10^{-1}, where no points are found. The smaller the coupling $|g_{11}|$ has to be, the more restricted is the choice of θ_R leading to viable results. For small $|g_{11}|$ the underlying mixing angle narrows down to two specific values. The angle is either around 1.2 or 1.9.

Fig. 5.71 shows the plane $|y_1| - y_2$ with both couplings being correlated to neutrino masses. The color code represents the ratio of $M_{S,S}$ to $M_{F,S}$. In Section 5.2.3 dependencies between the fermion Yukawa couplings and the resulting neutrino masses have been elaborated. Here similar patterns and also a similar stripe shape as in Fig. 5.67 are observed. Only one of the couplings, y_1 and y_2, can be small at the same time. There is a bulk of points for $|y_1|$ above 10^{-5} where y_2 can nearly take any value from around 10^{-5} to 10^{-10}. This stripe continues more sparsely for $|y_1|$ down to 10^{-7}. Another densely populated area is found for y_2 above 10^{-7} where y_1 can take any value below 10^{-5}. In the upper corner both y_1 and y_2 take a more diagonal shaped region in space being both simultaneously large. Points which feature both $|y_1|$ and y_2 below 10^{-7} or even below 10^{-8} are rather rare. The stripes for either $|y_1|$ or y_2 above 10^{-7} exhibit a similar pattern regarding the mass ratio $R_{S,F}$. The color code starts at blueish white for the largest values and fades to dark green for the smallest values of order 1. For $y_1|$ above 10^{-5} $R_{S,F}$ decreases with decreasing $|y_1|$. There is a color gradient transitioning from light blue to green. Similarly, for y_2 above 3×10^{-6} and $|y_1|$ below 10^{-5} the color fades

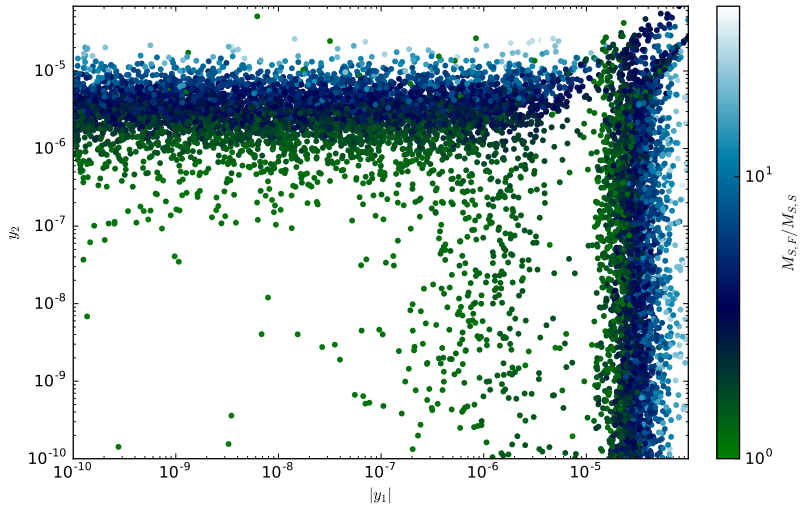

Figure 5.71: Viable Yukawa couplings in the plane $|y_1|$–$|y_2|$ (color code for the mass ratio $M_{F,S}/M_{S,S}$).

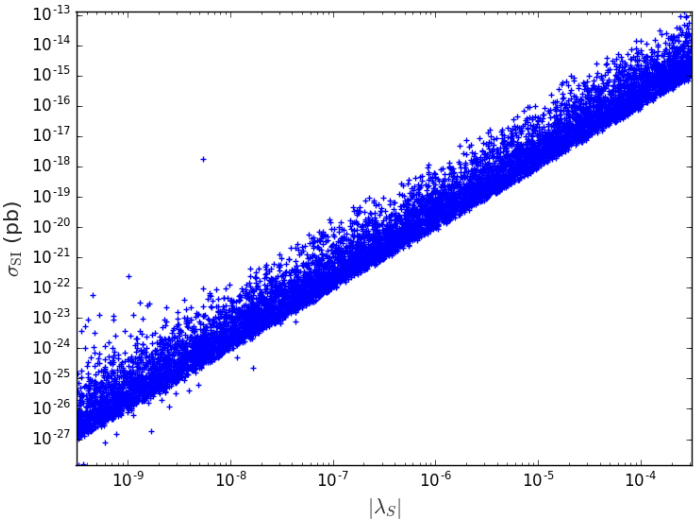

Figure 5.72: Spin independent direct detection cross section σ_{SI} as a function of λ_S for scalar dark matter.

along the y_2 direction over a bit larger area. One can see, that for $|y_1|$ and y_2 to be small simultaneously rather specific values of $R_{S,F}$ are required. This is only due to the neutrino mass constraints. The outcome of this figure is strongly related to the findings explained in Section 5.2.3 shown in Fig. 5.56, Fig. 5.55 and Fig. 5.57.

Within the coannihilation region, the suppression of λ_S leads to tiny direct detection cross sections. The dark matter-Higgs coupling is dominated by λ_S for mostly singlet-like scalars. Fig. 5.72 shows

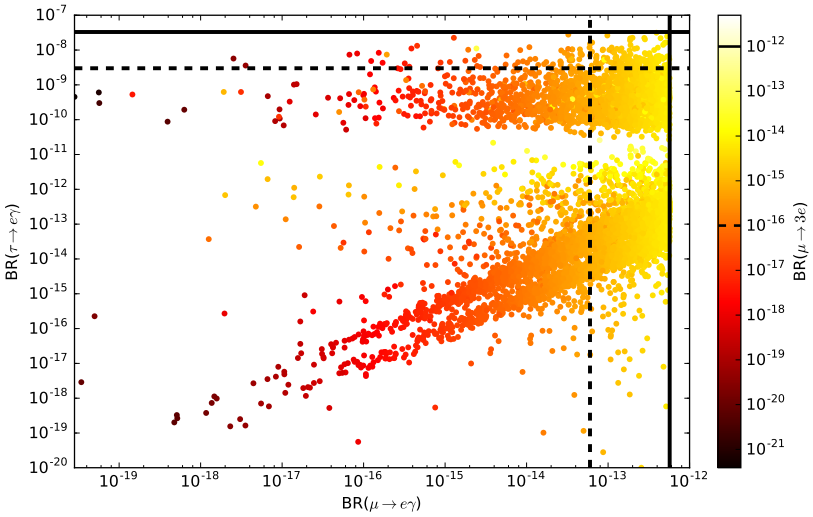

Figure 5.73: Predicted branching ratios for the most sensitive lepton-flavor violating processes BR($\mu \to e\gamma$), BR($\tau \to e\gamma$) and BR($\mu \to 3e$) (color) with current (full black lines) and future (dashed black lines) exclusion limits.

the spin-independent scattering cross section for dark matter σ_{SI} as a function of λ_S. As expected, a strong correlation is observed. The larger λ_S, the larger is σ_{SI}. Smallest values of around 10^{-27} pb are obtained for $\lambda_S \approx 10^{-10}$ up to the larges values of σ_{SI} of 10^{-13} pb for $\lambda_S \approx 2 \times 10^{-4}$. All points are beyond the reach of even XENONnT. Yet, similar to the models discussed before constraints can come from lepton flavor violating processes. Fig. 5.73 shows the three branching ratios of $\mu \to e\gamma$, $\tau \to e\gamma$ and $\mu \to eee$. The color code symbolizes the value of BR($\mu \to 3e$), starting with a light yellow for 10^{-12} going to a dark red for values around 10^{-21}. The solid and dashed lines correspond to the current and future experimental limits as stated in table 4.1. There are two rather separate regions within this plane.
A lot of points gather in a region with BR($\tau \to \gamma$) above 10^{-11} and the branching ratio for $\mu \to e\gamma$ extending from 10^{-12} down to below 10^{-19}. The other area is more along an increasing line with a huge spread surrounding it. These two areas correspond to the two separate regions found in the plane $|g_{11}|$ and $|g_{12}|$. The one, where $|g_{11}|$ stays at rather the same value, corresponds to the regions with BR($\tau \to e\gamma$) above 10^{-10}. Since $|g_{11}|$ influences the electron couplings and $|g_{12}|$ the muon couplings. The color gradient along this region corresponds to the decrease of $|g_{13}|$. The points along the inclined line exhibit a growing BR($\tau \to e\gamma$) for increasing BR($\mu \to e\gamma$. The value of BR($\mu \to 3e$) increases along this line. One can see that the current constraints on $\mu \to e\gamma$ put the strongest bounds on the parameter space. The solid line at 5.7×10^{-13} cuts directly through the distribu-

tion whereas the limit for $\tau \to e\gamma$ just touches the border of viable scenarios. All future sensitivities allow to probe more regions of the parameter space. Especially the limits on $\mu \to e\gamma$ and $\mu \to 3e$ allow to exclude a significant portion of points. Thus, even if all points within this scan are not accessible by direct detection, other experiments can restrict the parameter space in a complementary way.

5.2.6 *LHC constraints*

Several limits from Higgs invisible decays at the LHC and limits on charged scalar partners at LEP have been previously discussed in [261]. The first random scan in this work features scalar dark matter mixed from singlet and doublet fields, whereas the second scan provides mostly singlet scalar dark matter. Hence, the main focus here will be on scalar dark matter. If dark matter is dominated by the singlet component, it couples neither to the photon nor to the weak gauge bosons, but only to the Higgs boson through the coupling λ_S. Constraints from the LHC thus, currently come only from the invisible decay width of the Higgs boson in a mass region below 62.5 GeV. Current upper limits are at 67% for associated ZH production in ATLAS [262] and at 24% for a combination of different production channels in CMS [263]. Fig. 5.63 and Figure 8b in [263] show, that large couplings are already ruled out by direct detection and/or $\mathrm{BR}(\mu \to e\gamma)$.
If the doublet component dominates, an additional coupling to weak gauge bosons is present. Thus, more signatures at the LHC are possible. The couplings give rise to events with large transverse momentum imbalance paired with a single jet [262] and/or a vector boson [264]. In recent works the analysis is only treated for fermion dark matter as function of the mediator mass. However, under the assumption that the mediator is Z-like in coupling and mass and that spin is of minor importance, the results can be transferred. Figures 5 and 6 in [265] and figure 10 in [266] then limit dark matter mass to be between 50 and 100 GeV. Thus, LHC would exclude some models beyond Higgs resonance. In the case of fermion dark matter, which is not present in the two random scans, these limits apply more stringently.
Instead of producing dark matter directly, heavier $\mathbb{Z}_2$ odd charged or neutral scalar states can be produced, which subsequently decay into the lightest dark matter particle accompanied by W or Z boson leading to two or multi-lepton states and missing transverse energy [267]. The process is shown on the top panel of Fig. 5.74. The LHC data has mostly been analyzed in the context of charged scalar leptons within supersymmetric models (sleptons), scalar neutrinos are so far unconstrained. The results for charged sleptons can be translated to models like T12A, when assuming spin is of minor importance, since

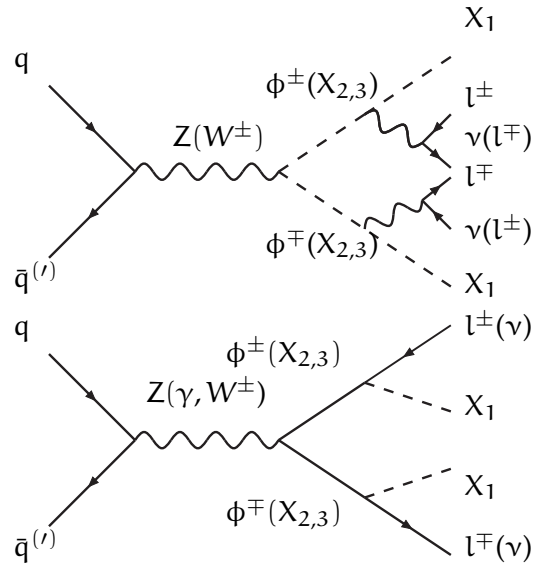

Figure 5.74: Typical diagrams for the production of heavy scalars (top) and fermions (bottom) decaying into two- or multi-lepton final states and missing transverse energy, carried away by scalar dark matter X_1 and neutrinos.

charged sleptons usually decay to fermionic neutralino dark matter. With spin being of little importance, this translates to decays into the lightest neutral scalars and gauge bosons. Under the assumption that the branching ratio for this process is one, the strongest constraints are obtained. Similar considerations are used by ATLAS [268] and CMS [269] regarding sleptons. Lower mass limits for sleptons of 520 GeV – see figure 6b in [268] – or 440 GeV – see figure 3 in [269] are found. Accordingly, the dark matter masses are limited in the 50 to 280 GeV or 40 to 220 GeV range. Looking at Fig. 5.63, this would exclude some points beneath the Higgs resonance. Yet, within T12A the constraints will be weaker ,as the leptonic branching fractions of $W-$ and $Z-$ bosons are 21 % for muons and 7 % for electrons reducing the limit. For charged scalars, heavier than 440 to 520 GeV or if they have different decay channels, the limits do not apply.

The bottom panel of Fig. 5.74 shows the production and subsequent decay of charged fermions. In the second random scan, the next lightest odd particle is mostly a doublet-like fermion, as such it can coannihilate with the scalar dark matter. Similar considerations as for charged scalars, allow to constrain this process. Well studied scenarios come again from supersymmetric frameworks. Within SUSY models, higgsino-like charginos and neutralinos correspond to the situation in T12A [239]. The masses have been constrained by ATLAS to be at least 95 to 145 GeV [270] – see figure 10 in the reference – and by CMS to be at least 100 to 170 GeV [271] – see figure 8 in the reference. This translates to a lower neutralino mass limits of 95 to 140 GeV or 100 to 150 GeV, respectively. Regarding the second scan, the limits are even lower as they have to be scaled with the fermion-

Table 5.9: Parameters used for Fig. 5.75

Parameter	Value
λ_H	0.26
λ_S	0.1
λ_D	0.2
λ'_D	0.3
λ''_D	0.4
A (GeV)	1
y_1	0.1
y_2	0.2
$M_{S,S}$ (GeV)	500
$M_{S,D}$ (GeV)	1000
$M_{F,S}$ (GeV)	800
$M_{F,D}$ (GeV)	1200
g_{ij}	0.1

scalar couplings g_{ij}. Regarding the first scan – see Fig. 5.63– the limits do not affect many models beyond the Higgs resonance. Still, the constraints are expected to be stronger since the leptonic branching ratios of Z and W bosons do not play an important role here. In the case of singlet-doublet fermion dark matter with scalar singlets the dark matter mass has to be above 510 GeV as shown in [239].

5.2.7 *One-loop mass corrections and outlook*

Since T12A introduces new fermions and scalars coupling to the Higgs doublet, the new particles can contribute to the one-loop mass corrections of the Higgs boson. Similar to the MSSM, the fermions and scalars enter the correction with different signs, which might allow for a cancellation between the possibly large loop contributions. As an outlook on this, the Higgs mass at one-loop has been calculated with SPheno as a function of the scalar or fermion mass parameter $M_{S,S}$ and $M_{F,D}$. In Tab. 5.9 all parameters are listed. Fig. 5.75 shows the results for the one-loop mass as a dashed line compared to the constant tree-level mass of around 125 GeV. In both cases, the effect becomes more pronounced for rather large masses. It might be interesting to analyze T12A with one-loop contributions to all masses.
Despite the radiative corrections, it might be worthwhile to look at internal bremsstrahlung for dark matter annihilation. As shown, for example, in [272] for singlet scalars radiation of a photon or gauge boson from the final state can reduce the velocity suppression for lepton final states substantially. This can impact both the evolution in

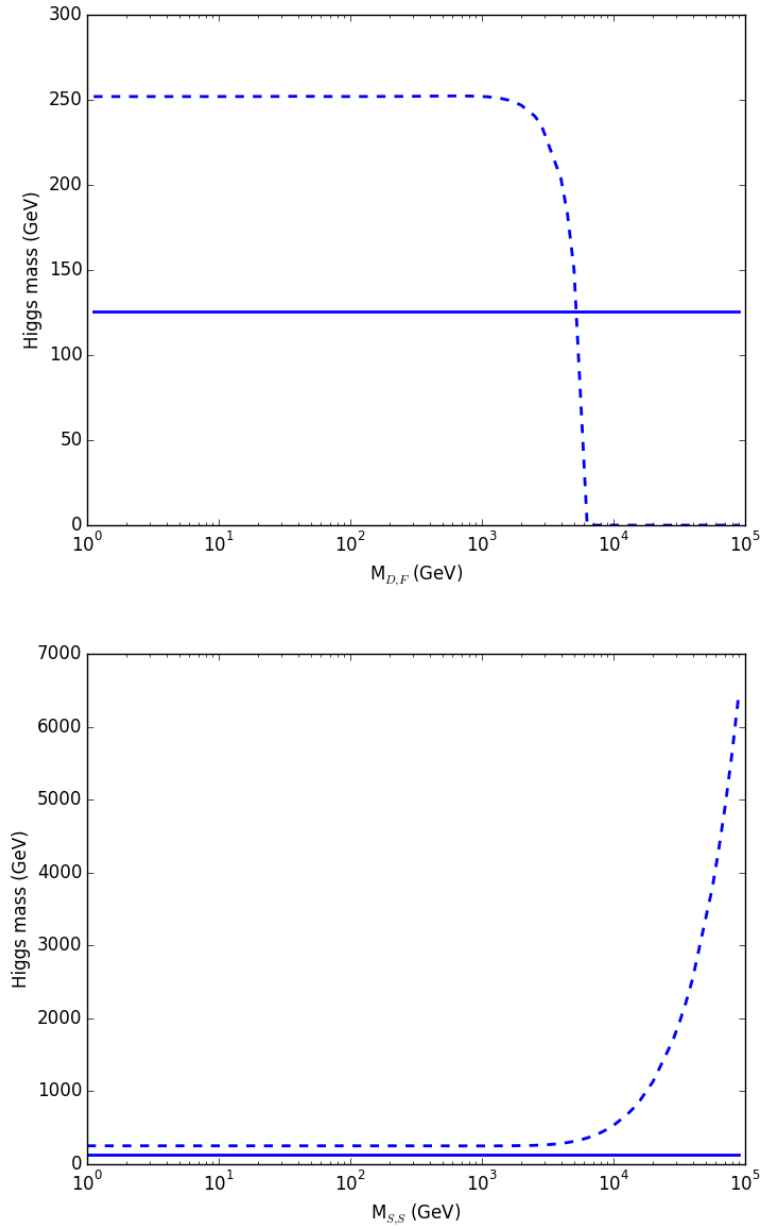

Figure 5.75: Influence of the scalar and fermion mass parameters $M_{F,D}$ and $M_{S,S}$ on the one-loop Higgs mass (dashed line) in comparison to the tree-level result (solid line).

the early Universe as well as the current indirect detection processes.

5.3 MODEL T13A

A model for radiative neutrino masses, similar to T12A, is T13A. It is also classified in [229] and it is of T13 topology with $\alpha = 0$. Recent

results are presented in [273], mostly based on work by D. Lamprea. Other studies of this model are found in [238, 239]. Concerning this work, calculations regarding dark matter annihilation are conducted.

5.3.1 *Model description*

The field content of T13A is close to the previous model. The same fields without a scalar doublet are sufficient to provide a T13 like diagram. Instead of the scalar doublet, another real scalar singlet is added to have two massive neutrinos. Otherwise, there are not enough degrees of freedom to fulfill all constraints in the neutrino sector. With respect to T12A, the scalars now obtain a family index such that ϕ_{S_1} and ϕ_{S_2} are the two scalar singlets. The discrete $\mathbb{Z}_2$ is again introduced for dark matter stability and prevention of tree level neutrino masses. Regarding the $SU(2)_L \bigotimes U(1)_Y \bigotimes \mathbb{Z}_2$ symmetry group, the new particles are

$$\begin{aligned}
\phi_{S_1} &\propto (1, 0, -), \\
\phi_{S_2} &\propto (1, 0, -), \\
\psi_S &\propto (1, 0, -), \\
\psi_{D_1} = \begin{pmatrix} \psi^0_{D_1,L'} \\ \psi^-_{D_1,L} \end{pmatrix} &\propto (2, -\frac{1}{2}, -), \\
\psi_{D_2} = \begin{pmatrix} -(\psi_{D_2,R})^\dagger, \\ (\psi^0_{D_2,R})^\dagger \end{pmatrix} &\propto (2, \frac{1}{2}, -).
\end{aligned} \tag{5.165}$$

The fermion Lagrangian is exactly the same as for T12A in Eq. 5.125. It introduces the same mixing and mass eigenstates, which can be found in Section 5.2.1.3. The scalar Lagrangian features only the singlet terms

$$\mathcal{L}_S = -\left(\frac{1}{2} M^2_{S,S_i} \phi^2_{S_i} + \frac{1}{2} \lambda_{S_i} \phi^2_{S_i} |H|^2\right), \tag{5.166}$$

for $i = 1, 2$, hence the singlet scalars have masses $m^2_{\phi_i} = M^2_{S,S_i} + \frac{1}{2} v^2 \lambda_{S_i}$. In the analysis of [273] the couplings λ_{S_i} are negligible. The coupling between the new particles and the Standard Model lepton doublets L_i also changed with regards to T12A. Only one of the two terms from Eq. 5.136 is present. Hence, there is only one type of vertex with g_{1ij}, which gains an additional index for the scalar family. The Lagrangian for the leptons is then

$$-\mathcal{L}_{lep} = g_{1ij} L_i \phi_{S_j} \psi_{D_2} + h.c. \tag{5.167}$$

5.3.2 *Neutrino masses*

After electro-weak symmetry breaking, the diagrams for neutrino mass generation look the same as for T12A, though, instead of three

neutral scalars there are only two neutral scalars. Still, neutrino masses are calculated in a similar fashion from the one-loop diagram in Fig. 5.76. Determined by Eq. 5.167, the coupling C_{ijk} between a neu-

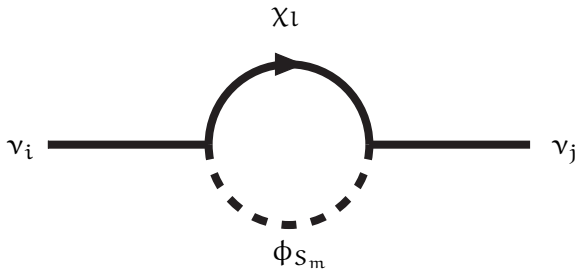

Figure 5.76: Neutrino-mass generation at one-loop in the model T13A after electro-weak symmetry breaking.

trino ν_i, a fermion χ_j and a scalar ϕ_{S_k} is

$$C_{ijk} = g_{1ik} U_{F,3j}. \tag{5.168}$$

Evaluating a similar amplitude for Majorana neutrino masses as in T12A Eq. 5.140, leads to the neutrino mass matrix elements

$$M_{\nu,ij} = \sum_m m_m \left(g_{1im} g_{1jm}\right). \tag{5.169}$$

The function m_m is defined by

$$m_m := \sum_l U_{F,3l}^2 \frac{1}{16\pi^2} \frac{M_{\chi_l}}{M_{\phi_m}^2 - M_{\chi_l}^2} \left(M_{\chi_l^2} \ln M_{\chi_l}^2 - M_{\phi_m}^2 \ln M_{\phi_m}^2\right). \tag{5.170}$$

And analogous to Eq. 5.147, the neutrino mass matrix M_ν can be expressed as

$$M_\nu = \begin{pmatrix} g_{111} & g_{121} & g_{131} \\ g_{112} & g_{122} & g_{132} \end{pmatrix}^T \begin{pmatrix} m_1 & 0 \\ 0 & m_2 \end{pmatrix} \begin{pmatrix} g_{111} & g_{121} & g_{131} \\ g_{112} & g_{122} & g_{132} \end{pmatrix}. \tag{5.171}$$

This shape is suitable to apply a Casas-Ibarra parametrization, in order to impose experimental constraints on the neutrino sector as a model input.

5.3.3 *Lepton flavor violation*

The presence of fermion-scalar couplings does not allow for lepton flavor conservation. Hence, they give rise to lepton flavor violating processes at one-loop level, again similar to T12A. The lepton flavor violation is mediated by singlet scalars ϕ_{S_i} and charged fermions ψ^-. The absence of a charged scalar ϕ^- reduces the number of diagrams,

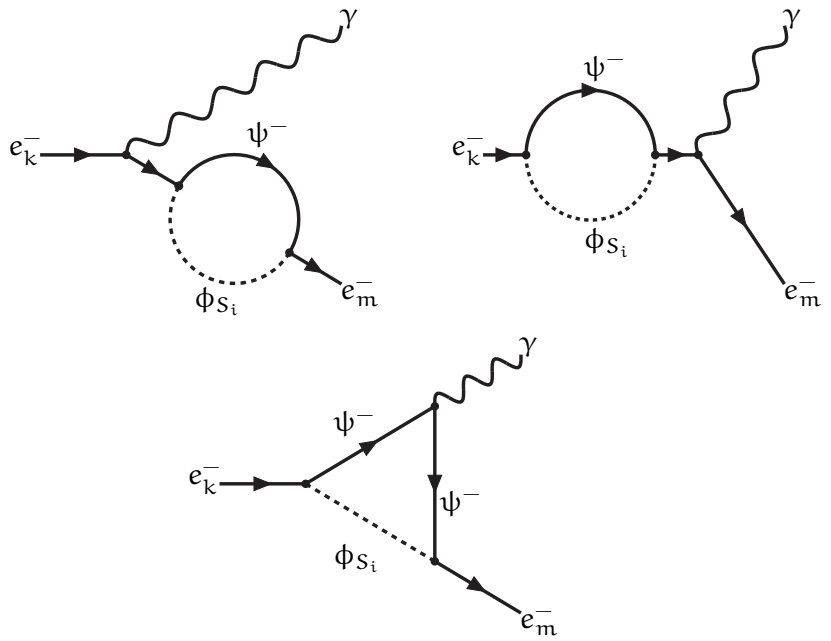

Figure 5.77: Radiative one-loop processes $e_k^- \to e_m^- \gamma$ violating lepton flavor in T13A.

yet the topologies are similar to T12A and the scotogenic model. In the scotogenic model, the situation is quite opposite, with a charged scalar and no charged fermion.
For $\mu \to e\gamma$, the process is shown in Fig. 5.77 – compare to Fig. 5.58 or Fig. 5.39. It features two bubble diagrams and one triangle diagram. The diagrams are also summarized in the overview in Section I.5. Using the couplings from Eq. 5.167 and following similar steps as in Section 5.2.4, the branching ratio is

$$\mathrm{BR}(\mu \to e\gamma) = \frac{3\alpha_{em}}{64\pi G_F^2} \frac{1}{m_{\psi^-}^4} \left(\sum_i g_{11i} g_{12i} F_2 \left(\frac{m_{\phi_{S_i}}^2}{m_{\psi^-}^2} \right) \right)^2 . \tag{5.172}$$

F_2 is the loop function defined in Eq. 5.104, which is found with Feynman parameters as in Section I.3 and Section I.4. With the adaption of couplings and masses, the process for radiative decays $\tau \to e\gamma$ and $\tau \to \mu\gamma$ is given by an analogous expression.

5.3.4 *Dark matter annihilation into lepton final states*

In T13A dark matter can be either a fermion or a singlet scalar, depending on which is the lightest neutral state. The fermionic part resembles the singlet-doublet fermion dark matter model and the scalar part consists of purely singlet scalars. Hence, all aspects summarized before, apply here. In addition, the fermion-scalar coupling gives rise to similar processes as in T12A. The focus in this section is on the ex-

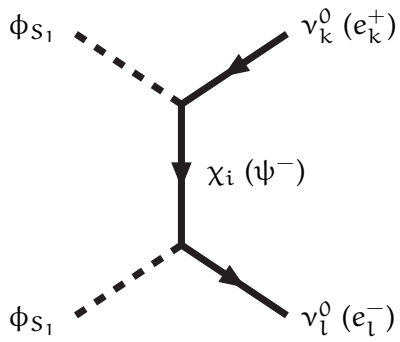

Figure 5.78: (Annihilation processes of scalar dark matter particles ϕ_{S_1} to SM leptons .

plicit calculations of dark matter annihilation cross sections for neutrino and lepton final states, both for fermion and scalar dark matter.

5.3.4.1 *Scalar dark matter*

The diagrams in Fig. 5.78 show the annihilation of singlet scalar dark matter within T13A to neutrino (left) or charged lepton (right) pairs. In principle, there is also an s-channel contribution mediated by a Higgs boson, but in the limit of zero lepton mass, this vanishes. The amplitudes describing the t-channel diagrams are

$$\begin{aligned} f_a &= \sum_i g_{1k1} g_{1l1} U^2_{F,3i} \overline{u}_3 \frac{\not{p}_2 - \not{p}_4 + m_{\chi_i}}{(p_2 - p_4)^2 - m^2_{\chi_i}} u_4, \\ f_b &= g_{1k1} g_{1l1} \overline{u}_3 P_L \frac{\not{p}_2 - \not{p}_4 + m_{\psi^-}}{(p_2 - p_4)^2 - m^2_{\psi^-}} P_R u_4, \end{aligned} \tag{5.173}$$

where the incoming scalars have momentum p_1 and p_2 and the outgoing Standard Model particles p_3 and p_4. In addition, the two exchange amplitudes for each process have to be taken into account, since the scalars are real:

$$\begin{aligned} f_{a,ex} &= \sum_i g_{1k1} g_{1l1} U^2_{F,3i} \overline{u}_3 \frac{\not{p}_1 - \not{p}_4 + m_{\chi_i}}{(p_1 - p_4)^2 - m^2_{\chi_i}} u_4, \\ f_{b,ex} &= g_{1k1} g_{1l1} \overline{u}_3 P_L \frac{\not{p}_1 - \not{p}_4 + m_{\psi^-}}{(p_1 - p_4)^2 - m^2_{\psi^-}} P_R u_4. \end{aligned} \tag{5.174}$$

The vertex between a scalar ϕ_{S_1} a fermion χ_i and a neutrino ν_k is determined by $g_{1k1} U_{F,3i}$, since all neutral fermions are Majorana fermions. For a charged lepton l_k^-, the vertex is governed by $g_{1kl} P_L$ including the left chirality projector P_L. Since dark matter is expected

to be much heavier than the leptons, the lepton masses are neglected in the following evaluation of the squared amplitudes.

$$\begin{aligned}
\overline{f_a f_a^\dagger} &= \sum_{i,j} C_{kl} F_{ij} \left((t - m_{\chi_i}^2) \left(t - m_{\chi_j}^2 \right) \right)^{-1} \\
&\quad \mathrm{Tr}\left[\not{p}_3 (m_{\chi_i} + \not{p}_2 - \not{p}_4) \not{p}_4 (m_{\chi_j} + \not{p}_2 - \not{p}_4) \right], \\
\overline{f_a f_{a,ex}^\dagger} &= \sum_{i,j} C_{kl} F_{ij} \left((t - m_{\chi_i}^2) \left(u - m_{\chi_j}^2 \right) \right)^{-1} \\
&\quad \mathrm{Tr}\left[\not{p}_3 (m_{\chi_i} + \not{p}_2 - \not{p}_4) \not{p}_4 (m_{\chi_j} + \not{p}_1 - \not{p}_4) \right], \\
\overline{f_{a,ex} f_{a,ex}^\dagger} &= C_{kl} F_{ij} \left((u - m_{\chi_i}^2) \left(u - m_{\chi_j}^2 \right) \right)^{-1} \\
&\quad \mathrm{Tr}\left[\not{p}_3 (m_{\chi_i} + \not{p}_1 - \not{p}_4) \not{p}_4 (m_{\chi_j} + \not{p}_1 - \not{p}_4) \right], \\
\overline{f_b f_b^\dagger} &= C_{kl} \left(\left(t - m_{\psi^-}^2 \right)^2 \right)^{-1} \\
&\quad \mathrm{Tr}\left[\not{p}_3 P_L (m_{\psi^-} + \not{p}_2 - \not{p}_4) P_R \not{p}_4 P_L (m_{\psi^-} + \not{p}_2 - \not{p}_4) P_R \right], \\
\overline{f_b f_{b,ex}^\dagger} &= C_{kl} \left(\left(t - m_{\psi^-}^2 \right) \left(u - m_{\psi^-}^2 \right) \right)^{-1} \\
&\quad \mathrm{Tr}\left[\not{p}_3 P_L (m_{\psi^-} + \not{p}_2 - \not{p}_4) P_R \not{p}_4 P_L (m_{\psi^-} + \not{p}_1 - \not{p}_4) P_R \right], \\
\overline{f_{b,ex} f_{b,ex}^\dagger} &= C_{kl} \left(\left(u - m_{\psi^-}^2 \right)^2 \right)^{-1} \\
&\quad \mathrm{Tr}\left[\not{p}_3 P_L (m_{\psi^-} + \not{p}_1 - \not{p}_4) P_R \not{p}_4 P_L (m_{\psi^-} + \not{p}_1 - \not{p}_4) P_R \right],
\end{aligned} \tag{5.175}$$

with the abbreviations $C_{kl} := g_{1k1}^2 g_{1l1}^2$ and $F_{ij} := U_{F,3i}^2 U_{F,3j}^2$. The traces are evaluated by using the trace theorems summarized in Appendix A and the result is

$$\begin{aligned}
\overline{f_a f_a^\dagger}^2 &= \sum_{i,j} C_{kl} F_{ij} \frac{2\left(\left(m_{\phi_{S_1}}^4 - tu \right) - (m_{\chi_i} m_{\chi_j}) s \right)}{\left(m_{\chi_i}^2 - t \right) \left(t - m_{\chi_j}^2 \right)}, \\
\overline{f_a f_{a,ex}^\dagger}^2 &= \sum_{i,j} C_{kl} F_{ij} \frac{2\left((m_{\chi_i} m_{\chi_j}) s + \left(m_{\phi_{S_1}}^4 - tu \right) \right)}{\left(m_{\chi_i}^2 - t \right) \left(m_{\chi_j}^2 - u \right)}, \\
\overline{f_{a,ex} f_{a,ex}^\dagger}^2 &= \sum_{i,j} C_{kl} F_{ij} \frac{2\left(\left(m_{\phi_{S_1}}^4 - tu \right) - (m_{\chi_i} m_{\chi_j}) s \right)}{\left(m_{\chi_i}^2 - u \right) \left(u - m_{\chi_j}^2 \right)}, \\
\overline{f_b f_b^\dagger}^2 &= C_{kl} \frac{\left(tu - m_{\phi_{S_1}}^4 \right)}{\left(m_{\psi^-}^2 - t \right)^2}, \\
\overline{f_b f_{b,ex}^\dagger}^2 &= C_{kl} \frac{\left(m_{\phi_{S_1}}^4 - tu \right)}{\left(m_{\psi^-}^2 - t \right) \left(m_{\psi^-}^2 - u \right)},
\end{aligned}$$

$$\overline{f_{b,ex} f_{b,ex}^{\dagger}}^{2} = C_{kl} \frac{\left(tu - m_{\phi_{S_1}}^4\right)}{\left(m_{\psi^-}^2 - u\right)^2}. \tag{5.176}$$

With the Mandelstam variables s, t and u. The variables and kinematics in such a $2 \to 2$ process are shown in Section B.3. The squared amplitudes for neutrino (a) and charged lepton (b) final states share a similar term $m_{\phi_{S_1}}^4 - tu$ with a factor 2 when neglecting the mixing matrix elements. In addition, the neutrino amplitudes have a term proportional to s. With respect to the center of mass system angle θ_{CMS} (between $\vec{p}_3$ and $\vec{p}_4$ t), the equation can be rewritten as

$$t = m_{\phi_{S_1}}^2 - \frac{1}{2}s + \sqrt{s} + \sqrt{\frac{s}{4} - m_{\phi_{S_1}}^2} \cos\theta_{CMS}. \tag{5.177}$$

The entire amplitude is obtained when adding the single contributions. In case of the neutrinos an additional minus sign has to be taken into account, since they are Majorana particles. Conducting the integration over $\cos\theta_{CMS}$ the results for the summed squared amplitudes from Eq. 5.176 can be expanded in the non-relativistic limit for small relative velocities v – c.f. Section B.3 – to

$$\begin{aligned} m_{\phi\phi\to l^+l^-} = \sum_{i,j} C_{kl} F_{ij} \\ &\left(32 m_{\phi_{S_1}}^4 v^2 \left(m_{\chi_i}^2 m_{\chi_j}^2 + m_{\phi_{S_1}}^2 (m_{\chi_i} + m_{\chi_j})^2 + m_{\phi_{S_1}}^4\right)\right) \\ &\frac{1}{3\left(m_{\chi_i}^2 + m_{\phi_{S_1}}^2\right)^2 \left(m_{\chi_j}^2 + m_{\phi_{S_1}}^2\right)^2} + O\left(v^3\right), \\ m_{\phi\phi\to\nu\nu} = C_{kl} \frac{16 m_{\phi_{S_1}}^8 v^4}{15\left(m_{\psi^-}^2 + m_{\phi_{S_1}}^2\right)^4} + O\left(v^5\right). \end{aligned} \tag{5.178}$$

The annihilation cross section times velocity is given by

$$\frac{d\sigma_{CMS} v}{d\Omega} = \frac{1}{64\pi^2} \frac{1}{4 m_{DM}^2} |\overline{F}|^2, \tag{5.179}$$

with the squared matrix element $|\overline{F}|^2$. Hence, one finds, similar to T12A,

$$\begin{aligned} \sigma v(\phi_{S_1}\phi_{S_1} \to l_k^+ l_l^-) &\propto v^4, \\ \sigma v(\phi_{S_1}\phi_{S_1} \to \nu_k^0 \nu_l^0) &\propto v^2. \end{aligned} \tag{5.180}$$

A summary of different integrals in $\cos\theta_{CMS}$ is presented in Section D.2, which have been used to perform the integration.

5.3.4.2 *Fermion dark matter*

In case of fermion dark matter, there is no t-channel diagram for annihilation to charged leptons, since there is no charged odd scalar. Yet,

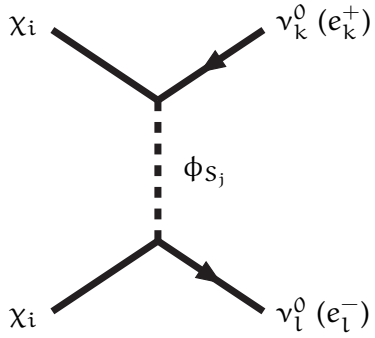

Figure 5.79: (Dark matter fermions χ_i annihilating to neutrinos.

an Z mediated s-channel contribution is possible, due to the mixing with the fermion doublet. However, as analyzed in [274], the final states for Z-mediated diagrams are not dominated by charged leptons. Below the W mass, the dominant annihilation channel, when only considering Z interactions, is $b\bar{b}$. For larger dark matter masses ZZ and W^+W^- final states, as well as ZH become more important. The only available final states, with regard to g_{1ij}, are neutrino pairs. The diagram for a pair of χ_i annihilating to neutrinos is shown in Fig. 5.79. For the lightest fermions χ_i, the amplitude and exchange amplitudes are

$$\begin{aligned} f_t &= \sum_j g_{1lj} g_{1kj} U^2_{F,3i} \overline{u}_3 u_1 \frac{i}{t - m^2_{\phi_{S_j}}} \overline{u}_4 u_2, \\ f_u &= \sum_j g_{1lj} g_{1kj} U^2_{F,3i} \overline{u}_3 u_2 \frac{i}{u - m^2_{\phi_{S_j}}} \overline{u}_4 u_1. \end{aligned} \tag{5.181}$$

All neutral fermions are Majorana fermions, thus, in order to fix a fermion flow and use the correct couplings, the conventions established in [275] are used. This allows to calculate the spin averaged squared elements

$$\begin{aligned} \overline{f_t f_t^\dagger} &= \sum_{j,m} \frac{4 C_{lkij} C_{lkim} \left(m^2_{\chi_i} - t\right)^2}{(t - m_{\phi_{S_j}})(t - m_{\phi_{S_m}})}, \\ \overline{f_t f_u^\dagger} &= \sum_{j,m} \frac{2 C_{lkij} C_{lkim} \left(m^4_{\chi_i} + m^2_{\chi_i}(s - 2t) + t(s + t)\right)}{(m_{\phi_{S_j}} - t)\left(-2m^2_{\chi_i} + m_{\phi_{S_m}} + s + t\right)}, \\ \overline{f_u f_u^\dagger} &= \sum_{j,m} \frac{4 C_{lkij} C_{lkim} \left(-m^2_{\chi_i} + s + t\right)^2}{\left(-2m^2_{\chi_i} + m_{\phi_{S_j}} + s + t\right)\left(-2m^2_{\chi_i} + m_{\phi_{S_m}} + s + t\right)}, \end{aligned} \tag{5.182}$$

with the short hand $C_{lkij} = g_{1kj} g_{1lj} U^2_{F,3i}$. In the non-relativistic limit and after the integration, the results for the entire amplitude F are obtained as

$$F = \frac{96 C_{lkij} C_{lkim} m^4_{\chi_i}}{\left(m^2_{\chi_i} + m_{\phi_{S_j}}\right)\left(m^2_{\chi_i} + m_{\phi_{S_m}}\right)} + O\left(v^2\right), \tag{5.183}$$

in which the t and u contributions for the neutrino final state are already summed.

5.3.5 *Summary of recent results*

In [273] the main focus is on scalar dark matter, which obtains a viable relic density mostly by processes involving g_{1ij}, while other couplings are suppressed. Thus, lepton final states are most important for dark matter annihilation. This channel features a velocity suppression of $\mathcal{O}(v^4)$ for charged leptons – see Eq. 5.180. Consequently, there is a huge impact today, as dark matter is expected to be ultra-non relativistic with small velocities. Therefore, indirect detection signals are suppressed. The annihilation into neutrino pairs has a somewhat milder dependence $\approx v^2$.
Similarly as for T12A, the impact of dark matter observables, neutrino masses and lepton flavor violation is investigated. The focus is on singlet scalar dark matter with λ_{S_i} negligibly small and no coannihilations between fermion and scalars. Therefore, the fermion doublet mass is chosen to be 1.2 times or more larger than the scalar mass parameter. In the analysis of the parameter space, it is found, that $M_{F,D}$ does not exceed M_{S,S_i} by more than a factor three and the large the scalar mass, the smaller the ratio.
Relic density, as well as measurable lepton flavor signals, demand sufficiently large g_{1ij}. Which, in return, limit the size of y_1 and y_2 in order to obtain viable neutrino masses. Furthermore, neutrino masses restrict the angle θ_R of the Casas-Ibarra parametrization to be around 0.35. The weakest bounds are found for g_{13j}, which is associated with τ leptons. Perturbativity on the couplings limits dark matter to be below 500 GeV, though.
Since λ_{S_i} vanish, there is no tree-level interaction between dark matter and quarks. Hence, direct detection bounds do not constrain the parameter space much. Strongest limits are expected from lepton flavor violation. Often the strictest bounds come from $\mu \to e\gamma$. Yet, in this situation the bound on $\mu \to e\gamma$ is not sufficient to have most other lepton flavor violation limits under control. For example $\mu \to eee$ can restrict quite a lot of the parameter space similar to μ conversion in nuclei. For both processes an increase in sensitivity in future experiments is expected, being able to probe the parameter space more.

Part IV

CONCLUSION

6 CONCLUSION

Currently the Standard Model of particle physics gives a good description for most observations. It includes all observed particles and forces. Many of its predictions have been confirmed experimentally. But, there are shortcomings. The strong evidence for neutrino masses and dark matter cannot be explained within the Standard model. It is therefore necessary to study different options how to extend the Standard Model.

In this work first an introduction and overview of dark matter evidence and candidates is given. Some focus is on different detection techniques along with current experimental limits in Chapter 2. Some analytic calculations, in a somewhat model independent way, for scalar and fermionic dark matter annihilation and direct detection are presented.

In Chapter 3 a short overview of neutrino oscillations is given. Neutrino oscillations demand massive neutrinos. In the next section neutrino mass generation via see-saw mechanisms is highlighted. And since lepton flavor violation comes along with radiative neutrino masses, corresponding constraints from experiments are presented in Chapter 4.

The main focus of this work is on models for radiative neutrino masses and dark matter in Chapter 5. Most emphasis is on the model T12A and some calculations for the model T13A regarding dark matter annihilation. First, different topologies for radiative neutrino masses are summarized and the scotogenic model, which has already been investigated in several works, is presented as an example, followed by the detailed introduction of the model T12A with special focus on the singlet-doublet scalar and singlet-doublet fermionic models. Both models are subsets of the model T12A, which links them together allowing for fermion-scalar couplings, which give rise to one loop neutrino masses. The mixing matrices and mass eigenstates for both singlet-doublet sectors are calculated in an analytic form, as well as in an approximation for small mixings. The correct implementation of the model is checked by reproducing existing figures of singlet-doublet dark matter. Then, the influence of the new fermion-scalar couplings is studied in different regions of the parameter space. Special focus is on co-annihilations between fermions and scalars, which give rise to new viable regions. In addition, the velocity dependencies of annihilation cross sections for neutrino and charged lepton final states are shown.

As the model T12A offers a mechanism of neutrino mass generation,

the loops are calculated in a similar fashion to the scotogenic model. For small couplings and mixings the approximations are performed. The analytic formula with respect to the fermion Yukawa couplings is investigated and it is found that cancellations can have a huge impact on neutrino masses, despite the expected propagator suppressions.
Lepton flavor violation processes are shown and an overview of different loop topologies is provided in the appendix along with one-loop integrals in the limit of negligible outer masses. This is somewhat independent of the model T12A and can be applied to similar models.
In the model T12A two separate random scans with emphasis on scalar dark matter are performed. In the first scan neutrino mass constraints are obtained by a Casas-Ibarra parametrization. Limits on the Higgs mass and couplings and the relic density constraint are used as well. The first scan shows the appearance of new viable regions in parameter space moderated by the fermion-scalar couplings. The viable regions are new with respect to the singlet-doublet scalar model. Lepton final states appear, which alter the relic density, while leaving direct detection cross sections unchanged. Hence, they disentangle the two observables and weaken the limits. This allows us to find models way below current and future direct detection experiments like XENON1t and XENONnt. Most of the models below current sensitivity are already excluded by lepton flavor violation experiments. Nearly all models, which are not yet excluded by direct detection and lepton flavor violation, lie within the reach of XENONnt. It is found, that direct detection experiments and lepton flavor searches are able to probe complementary regions of the parameter spaces.
The second scan is focused on singlet like scalar dark matter with small mixing and suppressed coupling to the Higgs. In addition to relic density, Higgs constraint and neutrino masses, also lepton flavor violation and direct detection limits are imposed. For this scan the lightest fermion is mostly doublet-like and close in mass to the scalar dark matter. The fermion Yukawa couplings are also small, which gives room for coannihilation between scalar and fermion and also gives importance to lepton final states for the relic density. It is found that the fermion Yukawas cannot be too small simultaneously due to neutrino masses and lepton flavor violation. The scalar-fermion couplings form two distinct regions in the parameter space for all viable models. Future experiments, which investigate $\mu \to e\gamma$ and $\mu \to eee$, will become sensitive enough to probe large amounts of the parameter space, whereas the sensitivity for $\tau \to e\gamma$ processes will not be good enough to place strong bounds.
LHC constraints on invisible Higgs decays have no further impact below the Higgs resonance, but mono-jet or di-lepton searches can add constraints for masses up to 280 GeV. The considerations are similar to MSSM scenarios. Yet, the actual constraints depend on the specific model parameters.

Briefly, one-loop mass corrections for Higgs mass are touched. As the fermion and scalar contributions to the radiative corrections enter with different signs, they might be able to compensate each other leading to the observed Higgs mass. Further, the one-loop corrections to all masses can possibly alter the viable parameter space for dark matter, giving an outlook on interesting phenomenology. In addition, it might be useful to investigate internal bremsstrahlung. As especially, the annihilation of scalar dark matter to Standard Model fermions is very velocity suppressed, up to order four. The radiation of a photon or gauge boson from the final state can weaken the suppression.

The models T12A and T13A, along with others from the classification, have a rather similar particle content, so some of the results and considerations can be applied to all of them.

In general, radiative neutrino mass models provide simultaneously two missing pieces to the Standard Model. Since they are minimal extensions of the Standard Model, the parameter space is of reasonable size but still offers interesting phenomenology.

Part V

APPENDIX

A

CONVENTIONS, γ MATRICES AND TRACE THEOREMS

A.1 CONVENTIONS

In the thesis, if not stated otherwise, natural units have been used so that $\hbar = c = k_B = 1$. This implies that energy, momentum and mass have the unit GeV and length and time GeV^{-1}

A.2 γ MATRICES

This and the following sections are based on [276]. The Dirac γ matrices are define by the Dirac algebra

$$\{\gamma^\mu, \gamma^\nu\} = \gamma^\mu\gamma^\nu + \gamma^\nu\gamma^\mu = 2g^{\mu\nu}, \tag{A.184}$$

with the metric tensor $g^{\mu\nu}$. In this work the notation $\not{p} = p_\mu\gamma^\mu$ is adapted. The four γ matrices allow to define γ^5 by

$$\gamma^5 := i\gamma^0\gamma^1\gamma^2\gamma^3\gamma^4, \tag{A.185}$$

which satisfies

$$\begin{aligned} \gamma_5^2 &= 1, \\ \{\gamma^5, \gamma^0\} &= 1, \\ \{\gamma^5, \gamma^\mu\} &= 0. \end{aligned} \tag{A.186}$$

For Hermitian conjugates of spinor matrix elements the following is true:

$$[\overline{u}(p,s)\Gamma u(p',s')]^\dagger = \overline{u}(p',s')\overline{\Gamma}u(p,s), \tag{A.187}$$

where Γ is any collection of γ matrices and $\overline{\Gamma} = \gamma^0\Gamma^\dagger\gamma$.

A.3 CHIRALITY PROJECTORS

With γ^5 the left- and right-handed chirality projectors P_L and P_R can be defined

$$\begin{aligned} P_L &= \frac{1}{2}\left(1 - \gamma^5\right), \\ P_R &= \frac{1}{2}\left(1 + \gamma^5\right). \end{aligned} \tag{A.188}$$

They obey

$$P_{L(R)}^2 = P_{L(R)},$$

$$\begin{aligned} P_L P_R &= P_R P_L = 0, \\ P_L + P_R &= 1. \end{aligned} \tag{A.189}$$

A.4 TRACE THEOREMS

With the Dirac algebra – see Eq. A.184 – the following identities for traces can be found:

$$\begin{aligned} \mathrm{Tr}(\not{a}\not{b}) &= 4ab, \\ \mathrm{Tr}(\not{a}\not{b}\not{c}\not{d}) &= 4[(ab)(cd) + (ad)(bc) - (ac)(bd)], \\ \mathrm{Tr}(\not{a}\gamma^5) &= 0, \\ \mathrm{Tr}(\not{a}\not{b}\gamma^5) &= 0, \\ \mathrm{Tr}(\Gamma) &= 0, \end{aligned} \tag{A.190}$$

where Γ is any odd number of γ matrices.

B

APPENDIX - KINEMATICS

The following sections contain an overview of different kinematics for particle interactions. They are based on [276–279].

B.1 KINEMATICS FOR $1 \to 2$ PROCESSES

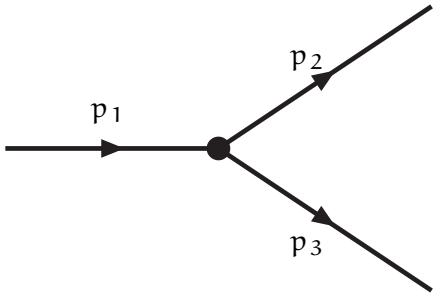

Figure B.80: Momenta for a $1 \to 2$ process.

Fig. B.80 shows a $1 \to 2$ decay with incoming four momentum p_1 and final state four momenta p_2 and p_3. Momentum conservation demands

$$p_1 = p_2 + p_3, \tag{B.191}$$

and for on-shell particles

$$p_i^2 = m_i^2, \tag{B.192}$$

holds. This allows to fix all possible scalar products

$$\begin{aligned} p_1 p_2 &= \frac{m_1^2 + m_2^2 - m_3^2}{2}, \\ p_1 p_3 &= \frac{m_1^2 + m_3^2 - m_2^2}{2}, \\ p_2 p_3 &= \frac{m_1^2 - m_2^2 - m_3^2}{2}. \end{aligned} \tag{B.193}$$

Hence phase space integration becomes trivial.

B.1.1 *Special case: one vanishing mass in the final state*

In the special case of one vanishing final state mass, e.g. for a photon, the mass and the momentum square are set to zero $p_3^2 = m_3^2 = 0$. Plugging this into Eq. B.193 gives

$$p_1 p_2 = \frac{m_1^2 + m_2^2}{2},$$

$$p_1 p_3 = \frac{m_1^2 - m_2^2}{2},$$
$$p_2 p_3 = \frac{m_1^2 - m_2^2}{2}. \tag{B.194}$$

B.2 KINEMATICS FOR $1 \to 3$ PROCESSES

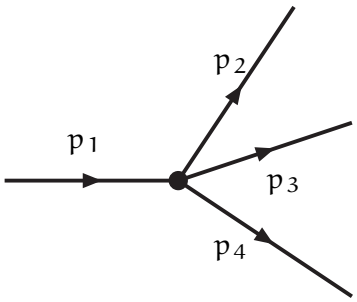

Figure B.81: Kinematics for a $1 \to 3$ process.

For a decay into three particles the schematic kinematics are shown in Fig. B.81. Momentum conservation and on-shell conditions are

$$p_1 = p_2 + p_3 + p_4, \tag{B.195}$$
$$p_i^2 = m_i^2. \tag{B.196}$$

They allow to pick two independent scalar products, such as for example $p_1 p_2$ and $p_1 p_3$ and express all quantities depending on this basis.

$$\begin{aligned} p_1 p_4 &= m_1^2 - p_1 p_2 - p_1 p_3, \\ p_2 p_3 &= \frac{m_1^2 + m_4^2 - m_2^2 - m_3^2 + 2 p_1 p_4}{2}, \\ p_2 p_4 &= p_1 p_2 - p_2 p_3 - m_2^2, \\ p_3 p_4 &= p_1 p_3 - p_2 p_3 - m_3^2. \end{aligned} \tag{B.197}$$

One can also identify the invariants, as in [279] ,

$$s = m_1^2, \tag{B.198}$$
$$s_1 = (p_1 - p_2)^2, \tag{B.199}$$
$$s_2 = (p_1 - p_3)^2, \tag{B.200}$$
$$s_3 = (p_1 - p_4)^2, \tag{B.201}$$

which are linked by

$$s + s_1 + s_2 + s_3 = m_1^2 + m_2^2 + m_3^2 + m_4^2, \tag{B.202}$$

and relate to $p_1 p_2$ and $p_1 p_3$ as

$$p_1 p_2 = \frac{m_1^2 + m_2^2 - s_1}{2}, \tag{B.203}$$
$$p_1 p_3 = \frac{m_1^2 + m_3^2 - s_2}{2}. \tag{B.204}$$

B.2.1 *Special case: two vanishing masses in the final state*

Processes, like, for example $\mu \to e\gamma\gamma$, have two massless particles in the final state. In addition to this ,they overlap with $\mu \to e\gamma$ for soft or collinear photons. With the assignment

$$\begin{aligned} p_1 &\to p_1, \\ p_2 &\to k_1, \\ p_3 &\to k_2, \\ p_4 &\to p_2, \end{aligned} \tag{B.205}$$

and $k_i^2 = 0$ the expressions for the scalar products Eq. B.197 and invariants Eq. B.201 and Eq. B.204 are

$$\begin{aligned} p_1p_2 =& m_1^2 - p_1k_1 - p_2k_2, \\ k_1k_2 =& \frac{m_1^2 + m_2^2 - 2p_1p_2}{2}, \\ p_2k_1 =& p_1k_1 - k_1k_2, \\ p_2k_2 =& p_1k_2 - k_1k_2, \\ s =& m_1^2, \\ s_1 =& (p_1 - k_1)^2 = (p_2 + k_2)^2 = m_1^2 - 2p_1k_1, \\ s_2 =& (p_1 - k_2)^2 = (p_2 + k_1)^2 = m_1^2 - 2p_1k_2, \\ s_3 =& (p_1 - p_2)^2 = (k_1 + k_2)^2. \end{aligned} \tag{B.206}$$

and

$$\begin{aligned} p_1k_1 =& \frac{m_1^2 - s_1}{2}, \\ p_1k_2 =& \frac{m_1^2 - s_2}{2}. \end{aligned} \tag{B.207}$$

The photons are associated with k_1 and k_2. In order to be able to perform a phase space integration, it is useful to link p_1k_1 and p_1k_2 to the energies and one angle appearing in the process to set limits matching to detector cuts.
In the center-of-mass (CMS) system, the outgoing momenta can be characterized by two angles. α, between p_2 and k_1 and β between k_1 and k_2 and the four-momenta can be expressed as

$$\begin{aligned} p_1 &= (E_1, 0), \\ p_2 &= (E_2, \vec{p_2}), \\ k_1 &= \left(E_{\gamma_1}, \vec{k_1}\right), \\ k_2 &= \left(E_{\gamma_2}, \vec{k_2}\right), \end{aligned} \tag{B.208}$$

which simplifies

$$s_1 = m_1^2 - 2m_1E_{\gamma_1},$$

$$s_2 = m_1^2 - 2m_1 E_{\gamma_2}, \tag{B.209}$$

and allows with Eq. B.206 to obtain

$$\begin{aligned} p_1 k_1 &= \frac{m_1^2 - s_1}{2}, \\ p_1 k_2 &= \frac{m_1^2 - s_2}{2}. \end{aligned} \tag{B.210}$$

The maximum value of s_1 is m_1^2, the minimal value is m_2^2 when both photons become soft. Hence

$$s_1 \in \left[m_2^2, m_1^2\right], \tag{B.211}$$

which translates to

$$E_{\gamma_1} = \frac{m_1^2 - s_1}{2m_1} \in \left[0, \frac{m_1^2 - m_2^2}{2m_1}\right]. \tag{B.212}$$

Therefore, cuts can account for soft photons. The angle between the two photons is restricted by cutting on the other photon energy E_{γ_2}. Considering energy and momentum conservation in the CMS system Eq. B.208 states

$$\begin{aligned} \alpha' &= \pi - \alpha, \\ 0 &= \vec{p_2} + \vec{k_1} + \vec{k_2}, \\ |\vec{p_2}|^2 &= E_2^2 - m_2^2, \\ |\vec{k_1}|^2 &= E_{\gamma_1}^2, \\ |\vec{k_2}|^2 &= E_{\gamma_2}^2. \end{aligned} \tag{B.213}$$

If β is 0, the photon becomes soft. If β is π it is collinear. The rule of cosine gives

$$\begin{aligned} &|\vec{k_2}|^2 + |\vec{k_1}|^2 - 2|\vec{k_1}||\vec{k_2}|\cos(\beta) = |\vec{p_2}|^2, \\ \Leftrightarrow\ &E_{\gamma_1}^2 + E_{\gamma_2}^2 - 2E_{\gamma_1}E_{\gamma_2}\cos(\beta) = E_2^2 - m_2^2, \end{aligned} \tag{B.214}$$

where due to energy conservation

$$m_1 = E_{\gamma_1} + E_{\gamma_2} + E_2. \tag{B.215}$$

One arrives at

$$\begin{aligned} E_{\gamma_2} &= \frac{m_1 E_{\gamma_1}}{E_{\gamma_1}(1 + \cos(\beta)) - m_1}, \\ p_1 k_1 &= m_1 E_{\gamma_1}, \\ p_1 k_2 &= m_1 E_{\gamma_2}. \end{aligned} \tag{B.216}$$

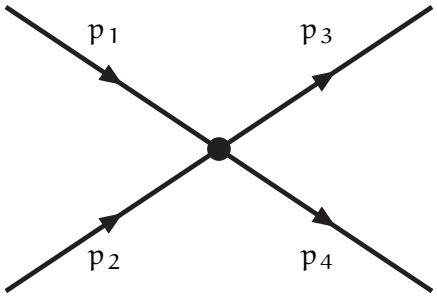

Figure B.82: Kinematics for a $2 \to 2$ process.

B.3 KINEMATICS FOR $2 \to 2$ PROCESSES

For example, the process of dark matter annihilation can be a $2 \to 2$ process. Considering two incoming dark matter particles with four-momenta p_1 and p_2. The outgoing particles have p_3 and p_4. As shown in Fig. B.82. The general relations for momentum conservation and on-shell particles

$$p_1 + p_2 = p_3 + p_4, \tag{B.217}$$

$$p_i^2 = m_i^2, \tag{B.218}$$

allow determine the invariants which are Mandelstam variables– see [276] –

$$\begin{aligned} s &= (p_1 + p_2)^2 = (p_3 + p_4)^2, \\ t &= (p_1 - p_3)^2 = (p_2 - p_4)^2, \\ u &= (p_1 - p_4)^2 = (p_2 - p_3)^2, \end{aligned} \tag{B.219}$$

which satisfy

$$\sum_i m_i^2 = s + t + u. \tag{B.220}$$

This allows tow identify following relations regarding all possible scalar products

$$\begin{aligned} p_1 p_2 &= \frac{s - m_1^2 - m_2^2}{2}, \\ p_1 p_3 &= \frac{m_1^2 + m_3^2 + t}{2}, \\ p_3 p_4 &= \frac{s - m_3^3 - m_4^2}{2}, \\ p_2 p_4 &= \frac{m_2^2 + m_4^2 - t}{2}, \end{aligned}$$

$$
\begin{aligned}
p_1 p_4 =& \frac{m_1^2 + m_4^2 - u}{2}, \\
p_2 p_3 =& \frac{m_2^2 + m_3^2 - u}{2}.
\end{aligned} \tag{B.221}
$$

In the center-of-mass system the four-momenta take the following form

$$
\begin{aligned}
p_1 =& (E_1, \vec{p_1}), \\
p_2 =& (E_2, -\vec{p_1}), \\
p_3 =& (E_3, \vec{p_3}), \\
p_4 =& (E_4, -\vec{p_3}),
\end{aligned} \tag{B.222}
$$

which results in

$$
s = (E_1 + E_2)^2. \tag{B.223}
$$

Utilizing the energy momentum relation and energy conservation gives

$$
E_2^2 = m_2^2 - m_1^2 + E_1^2, \tag{B.224}
$$

which can be used to rewrite

$$
\begin{aligned}
E_{1,2}^2 =& \frac{(s \pm (m_1^2 - m_2^2))^2}{4s}, \\
E_{3,4}^2 =& \frac{(s \pm (m_3^2 - m_4^2))^2}{4s}, \\
\vec{p_1}^{\,2} =& \frac{s^2 + (m_1^2 - m_2^2)^2 - 2s(m_1^2 + m_2^2)}{4s}, \\
\vec{p_3}^{\,2} =& \frac{s^2 + (m_3^2 - m_4^2)^2 - 2s(m_3^2 + m_4^2)}{4s}., \\
t =& m_1^2 + m_3^2 - 2E_1 E_3 + 2|\vec{p_1}||\vec{p_3}|\cos(\theta)
\end{aligned} \tag{B.225}
$$

with θ being the angle between $\vec{p_1}$ and $\vec{p_3}$. If $m_3 = m_4 = 0$, which is called case I, Eq. B.225 read as

$$
\begin{aligned}
E_{1,2}^2 =& \frac{(s \pm (m_1^2 - m_2^2))^2}{4s}, \\
E_{3,4}^2 =& \frac{s}{4}, \\
\vec{p_1}^{\,2} =& \frac{s^2 + (m_1^2 - m_2^2)^2 - 2s(m_1^2 + m_2^2)}{4s}, \\
\vec{p_3}^{\,2} =& \frac{s}{4}, \\
t =& m_1 + \frac{1}{2}(\cos(\theta)\sqrt{m_1^4 - 2m_1^2(m_2^2 + s) + (m_2^2 - s)^2}) \\
& - \sqrt{(m_1^2 - m_2^2 + s)^2}.
\end{aligned} \tag{B.226}
$$

When the two incoming masses are the same $m_1 = m_2 = m$ (case II) the equations are

$$\begin{aligned}
E_{1,2}^2 =& \frac{s}{4},\\
E_{3,4}^2 =& \frac{(s \pm (m_3^2 - m_4^2))^2}{4s},\\
\vec{p_1}^{\,2} =& \frac{s^2 - 4m^2 s}{4s},\\
\vec{p_3}^{\,2} =& \frac{s^2 + (m_3^2 - m_4^2)^2 - 2s(m_3^2 + m_4^2)}{4s},\\
t =& m_3^2 + m^2 - \frac{1}{2}(m_3^2 - m_4^2 + s)\\
&+ \cos(\theta)\sqrt{s(s-4m^2)(m_3^4 - 2m_3^2(m_4^2 + s)}.
\end{aligned} \tag{B.227}$$

If the incoming particles have the same mass m and the outgoing particles are massless (case III) one obtains

$$\begin{aligned}
p_1 p_2 =& \frac{s - 2m^2}{2},\\
p_3 p_4 =& \frac{s}{2},\\
p_1 p_3 =& p_2 p_4 = \frac{m^2 - t}{2},\\
p_1 p_4 =& p_2 p_3 = \frac{m^2 - u}{2},\\
2m^2 =& s + t + u,\\
E_1 =& E_2 = E_3 = E_4 := E,\\
E =& \frac{s}{4},\\
|\vec{p_1}| =& \frac{s - 4m^2}{2},\\
|\vec{p_3}| =& \frac{s}{4},\\
t =& m^2 + \frac{1}{2}\cos(\theta)\sqrt{s(s-4m^2)}\frac{1}{2}s.
\end{aligned} \tag{B.228}$$

In case III it is easy to express all quantities velocity dependent as

$$\begin{aligned}
|\vec{p_1}| =& \frac{1}{2}E\nu,\\
E^2 =& \frac{4m^2}{4 - \nu^2},\\
s =& \frac{16m^2}{4 - \nu^2},\\
|\vec{p_1}|^2 =& \frac{m^2\nu^2}{4 - \nu^2},\\
p_1 p_2 =& \frac{m^2(4 + \nu^2)}{4 - \nu^2},
\end{aligned}$$

$$
\begin{aligned}
|\vec{p_3}|^2 =& \frac{4m^2}{4-v^2}, \\
p_3 p_4 =& \frac{8m^2}{4-v^2}, \\
p_1 p_3 =& p_2 p_4 = \frac{2m^2(2+v\cos(\theta))}{4-v^2}, \\
p_1 p_4 =& p_2 p_3 = \frac{2m^2(2-v\cos(\theta))}{4-v^2}, \\
t =& \frac{-m^2(4+v^2)}{4-v^2} + \frac{4m^2 v}{4-v^2}\cos(\theta), \\
u =& \frac{-m^2(4+v^2)}{4-v^2} - \frac{4m^2 v}{4-v^2}\cos(\theta).
\end{aligned} \tag{B.229}
$$

In the non-relativistic limit the incoming particle have small velocities, thus it is useful to expand all quantities with respect to their relative velocity V. This can be used to express the annihilation cross sections as series in v disentangling the different contributions. Expanding around $v = 0$ leads to

$$s = 4m^2 + m^2 v^2 + \mathcal{O}v^3, \tag{B.230}$$

$$t = A + B\cos\theta, \tag{B.231}$$

$$u = A - b\cos\theta, \tag{B.232}$$

$$A = -m^2 - \frac{1}{2}m^2 v^2 + \mathcal{O}v^3, \tag{B.233}$$

$$B = m^2 + v + \mathcal{O}v^3. \tag{B.234}$$

C

DECAY WIDTH

This section give a short overview on the decay width for $1 \to 2$ and $1 \to 3$ decays based on [276]. The general decay width $d\Gamma$ for an initial particle with momentum p_{in} and mass M to a state with summed momentum p_{fin} is

$$\begin{aligned} d\Gamma =& (2\pi)^4 \delta^{(4)}(p_{in} - p_{fin}) |\overline{M}_{fi}|^2 \Pi_{f=1}^{n} \frac{d^3 p_{fin}}{(2\pi)^3} \\ =& \frac{1}{2E_i} |\overline{M}_{fi}|^2 d\phi^{(n)}, \end{aligned} \tag{C.235}$$

with the spin averaged squared matrix element $|\overline{M}_{fi}|^2$ which describes the transition. $d\phi^{(n)}$ is called the n-body phase-space. For two particles in the final state with four momenta $p_i = (E_i, \vec{p}_i)$ and masses m_i the phase-space element is

$$\begin{aligned} d\phi^{(2)} =& (2\pi)^4 \delta(M - E_1 - E_2) \delta^{(3)}(\vec{p}_1 + \vec{p}_2) \\ & \frac{d^3 p_1}{2E_1 (2\pi)^3} \frac{d^3 p_2}{2E_2 (2\pi)^3}. \end{aligned} \tag{C.236}$$

In oder to integrate over $d^3 p_1$, the momentum delta function is used and the result is

$$d\phi^{(2)} = \frac{1}{(2\pi)^4} \frac{1}{4E_1 E_2} \delta(M - E_1 - E_2) d^3 p_2, \tag{C.237}$$

with $E_1^2 = p_1^2 + m_1^2$. In polar coordinates $d^3 p_2$ can be written as $d\Omega p_2^2 dp_2$ which allows to transform the phase space element to

$$\begin{aligned} d\phi^{(2)} =& \frac{1}{16\pi^2} d\Omega \int_0^\infty \delta(M - E_1 - E_2 = \frac{p_2^2 dp_2}{E_1 E_2} \\ =& \frac{|p_2|}{16\pi^2 M} d\Omega. \end{aligned} \tag{C.238}$$

Furthermore, in the rest frame of the decaying particle, the following relation is true – compare Appendix B –

$$\begin{aligned} p_2^2 =& p_{cms}^2 \\ =& \frac{1}{4M^2} (M^2 - (m_1 + m_2)^2)(M^2 - (m_1 - m_2)^2), \end{aligned} \tag{C.239}$$

p_{cms} is the momentum in the center of mass system.
In the case of one massless final particle, the decay width becomes

$$d\Gamma = \frac{1}{2M} |\overline{M}| \frac{\sqrt{\frac{1}{4M^2} (M^2 - m_1^2)^2}}{16\pi^2 M} d\Omega. \tag{C.240}$$

In a similar fashion, the three-body phase space can be determined as

$$d\phi^{(3)} = \frac{1}{32\pi^3} dE_1 dE_2, \tag{C.241}$$

where the domain of integration is explained in Appendix B.

D

CROSS SECTION - ANNIHILATION

This section is based on [276, 280] In general, the differential cross section for dark matter annihilation in a $2 \to 2$ process is given by

$$d\sigma = \frac{1}{|\vec{v}|}\frac{1}{2E_1}\frac{1}{2E_2}|\overline{M}|^2 d\phi^{(2)}, \tag{D.242}$$

where the incoming particles have four-momenta $p_{1,2}$ and the outgoing have $p_{3,4}$. The phase space is the same as explained in Appendix C and the kinematics and Mandelstam variables in Appendix B. Similar to the decay width, the cross section formula can be transformed to

$$\frac{d\sigma_{cms}}{d\Omega} = \frac{|\vec{p_3}|}{|\vec{p_1}|}\frac{1}{64\pi^2(E_1+E_2)^2}|\overline{M}|^2, \tag{D.243}$$

within the CMS framework. In case of negligible masses in the final state Eq. D.243 simplifies to

$$\frac{d\sigma_{cms}}{d\Omega}v = \frac{1}{512\pi^2}\frac{1}{m^2}(4-v^2)|\overline{M}|^2. \tag{D.244}$$

The integration over Ω respectively $\cos\theta$ is explained in the next sections. All approximations within the non-relativistic limit can be found in Appendix C.

D.1 DIRECT DETECTION CROSS SECTION

In general for direct detection the cross section

$$d\sigma v = \frac{1}{s}\frac{d\Omega}{8\pi}|\overline{M}|^2\frac{1}{4\pi}(1-\frac{4m_f}{s})^{1/2}, \tag{D.245}$$

is true. Within in the nucleon the cross section can be written as

$$\sigma^{SI}_{n,p} = \frac{|\overline{M}|^2}{32\pi}\frac{f^2_{n,p}}{(M_{DM}+M_{n,p})^2}, \tag{D.246}$$

as long as the spin averaged squared matrix element is independent of t, which makes the integration trivial, otherwise the integral has to be conducted. In this expression $f_{n,p}$ are form-factors for either proton or neutron, and $M_{n,p}$ is the nucleon mass. For the proton the form-factors are

$$fp = \sum_{q=u,d,s} f^p_q + \frac{2}{9}\left(1 - \sum_{q=u,d,s} f^p_q\right). \tag{D.247}$$

D.2 COS θ INTEGRATION

In order to integrate the cross section, one can consider the different summands appearing within the the differential cross section containing the matrix element M and simplify them as far as possible. The Mandelstam variable t can be expressed as

$$t = A + B\cos(\theta), \tag{D.248}$$

where

$$A = m_1^2 + m_3^2 - 2E_1E_3, \tag{D.249}$$
$$B = 2|\vec{p_1}||\vec{p_3}|. \tag{D.250}$$

This allows to express the all combinations of four momenta and u as

$$\begin{aligned} u =& m_1^2 + m_2^2 + m_3^2 + m_4^2 - s - t \\ =& : C_{1234} - s - A - B\cos(\theta) =: \tilde{C}_{1234} - B\cos(\theta), \end{aligned} \tag{D.251}$$
$$p_1p_3 = \frac{m_1^2 + m_3^2}{2} - \frac{t}{2} =: C_{13} - \frac{t}{2}, \tag{D.252}$$
$$p_2p_4 = \frac{m_2^2 + m_4^2}{2} - \frac{t}{2} =: C_{24} - \frac{t}{2}, \tag{D.253}$$
$$p_1p_4 = \frac{-m_2^2 - m_3^2 + s + t}{2} =: -C_{23} + \frac{s}{2} + \frac{t}{2}, \tag{D.254}$$
$$p_2p_3 = \frac{-m_1^2 - m_4^2 + s + t}{2} =: -C_{14} + \frac{s}{2} + \frac{t}{2}. \tag{D.255}$$

Possible denominators for the matrix elements are

$$\begin{aligned} d_1 =& (t - m_a^2), \\ d_2 =& (t - m_a^2)(t - m_b^2), \\ d_3 =& (t - m_a^2)^2, \\ d_4 =& (u - m_a^2), \\ d_5 =& (u - m_a^2)(u - m_b^2), \\ d_6 =& (u - m_a^2)^2, \\ d_7 =& (t - m_a^2)(u - m_b^2), \\ d_8 =& (t - m_a^2)(u - m_a^2), \end{aligned} \tag{D.256}$$

where m_a, m_b are any masses of dark matter fermions or scalars. Nominators, which could possibly appear in $|\overline{M}|^2$, are

$$\begin{aligned} n_1 =& 1, \\ n_2 =& t, \\ n_3 =& t^2 = n_2^2, \\ n_4 =& u = (C_{1234} - s)n_1 - n_2 := \tilde{C}n_1 - n_2, \\ n_5 =& u^2 = \tilde{C}^2n_1 - 2\tilde{C}n_2 + n_2^2, \end{aligned}$$

$$
\begin{aligned}
n_6 =& ut = \tilde{C} n_2 - n_3, \\
p_1 p_3 =& n_1 C_{13} - \frac{1}{2} n_2, \\
p_2 p_4 =& n_1 C_{24} - \frac{1}{2} n_2, \\
p_1 p_4 =& n_1 C_{14} - \frac{1}{2} n_4, \\
p_2 p_3 =& n_1 C_{23} - \frac{1}{2} n_4.
\end{aligned} \tag{D.257}
$$

For later use, the relation

$$
\begin{aligned}
\ln\left(A + B - m^2\right) - \ln\left(A - B - m^2\right) =& \ln\left(\frac{(A - m^2 + B}{A - m^2 - B}\right) \\
=& \ln\left(\frac{1 + \frac{B}{A - m^2}}{1 - \frac{B}{A - m^2}}\right) \\
=& 2\operatorname{arctanh}\left(\frac{B}{A - m^2}\right),
\end{aligned} \tag{D.258}
$$

is useful. With the nominators and denominators one can define generic integrals and carry out the cosθ integration.

$$
\begin{aligned}
I_1 =& \int \frac{n_1}{d_1} d\cos\theta \\
=& \frac{1}{B}\left(\ln\left(A + B - m_a^2\right) - \ln\left(A - B - m_a^2\right)\right) \\
=& \frac{2}{B} \operatorname{arctanh}\left(\frac{B}{A - m_a^2}\right), \\
I_2 =& \int \frac{n_2}{d_1} d\cos\theta \\
=& \frac{m_a^2}{B} 2\operatorname{arctanh}\left(\frac{B}{A - m_a^2}\right) + 2, \\
I_3 =& \int \frac{n_3}{d_1} d\cos\theta \\
=& \frac{1}{B} 2\operatorname{arctanh}\left(\frac{B}{A - m_a^2}\right) + 2\left(A + m_a^2\right), \\
I_4 =& \int \frac{n_1}{d_2} d\cos\theta \\
=& \frac{1}{B\left(m_a^2 - m_b^2\right)} \\
& \left(2\operatorname{arctanh}\left(\frac{B}{A - m_a^2}\right) - 2\operatorname{arctanh}\left(\frac{B}{A - m_b^2}\right)\right), \\
I_5 =& \int \frac{n_2}{d_2} d\cos\theta \\
=& \frac{2}{B\left(m_a^2 - m_b^2\right)}
\end{aligned}
$$

$$\left(m_a^2 \operatorname{arctanh}\left(\frac{B}{A-m_a^2}\right) - m_b^2 \operatorname{arctanh}\left(\frac{B}{A-m_b^2}\right)\right),$$

$$\begin{aligned} I_6 =& \int \frac{n_3}{d_2} d\cos\theta \\ =& \frac{2}{B\left(m_a^2 - m_b^2\right)} \\ & \left(m_a^4 \operatorname{arctanh}\left(\frac{B}{A-m_a^2}\right) - m_b^2 \operatorname{arctanh}\left(\frac{B}{A-m_b^2}\right)\right), \end{aligned}$$

$$\begin{aligned} I_7 =& \int \frac{n_1}{d_3} d\cos\theta \\ =& \frac{2}{(A-m_a^2)^2 - B^2}, \end{aligned}$$

$$\begin{aligned} I_8 =& \int \frac{n_2}{d_3} d\cos\theta \\ =& \frac{2}{B} \operatorname{arctanh}\left(\frac{B}{A-m_a^2}\right) + \frac{2m_a^2}{(A-m_a^2)^2 - B^2}, \end{aligned}$$

$$\begin{aligned} I_9 =& \int \frac{n_3}{d_3} d\cos\theta \\ =& \frac{4m_a^2}{B} \operatorname{arctanh}\left(\frac{B}{A-m_a^2}\right) + 2 + \frac{2m_a^4}{(A-m_a^2)^2 - B^2}, \end{aligned}$$

$$\begin{aligned} I_{10} =& \int \frac{n_1}{d_4} d\cos\theta \\ =& \frac{-2}{B} \operatorname{arctanh}\left(\frac{B}{A-\tilde{C}+m_a^2}\right), \end{aligned}$$

$$\begin{aligned} I_{11} =& \int \frac{n_2}{d_4} d\cos\theta \\ =& \frac{2}{B}\left(m_a^2 - \tilde{C}\right) \operatorname{arctanh}\left(\frac{B}{A-\tilde{C}+m_a^2}\right) - 2, \end{aligned}$$

$$\begin{aligned} I_{12} =& \int \frac{n_3}{d_4} d\cos\theta \\ =& \frac{-2}{B}\left(\tilde{C} - m_a^2\right)^2 \operatorname{arctanh}\left(\frac{B}{A-\tilde{C}+m_a^2}\right) - 2\left(A + \tilde{C} - m_a^2\right), \end{aligned}$$

$$\begin{aligned} I_{13} =& \int \frac{n_1}{d_5} d\cos\theta \\ =& \frac{2}{B\left(m_a^2 - m_b^2\right)} \\ & \left(\operatorname{arctanh}\left(\frac{B}{A-\tilde{C}+m_b^2}\right) - \operatorname{arctanh}\left(\frac{B}{A-\tilde{C}+m_a^2}\right)\right), \end{aligned}$$

$$\begin{aligned} I_{14} =& \int \frac{n_2}{d_5} d\cos\theta \\ =& \frac{2}{B\left(m_a^2 - m_b^2\right)} \left(-\left(\tilde{C} - m_a^2\right) \operatorname{arctanh}\left(\frac{B}{A-\tilde{C}+m_a^2}\right)\right. \end{aligned}$$

$$
\begin{aligned}
&+\left(\tilde{C}-m_b^2\right)\operatorname{arctanh}\left(\frac{B}{A-\tilde{C}+m_b^2}\right)\Bigg),\\
I_{15}=&\int\frac{n_3}{d_5}\mathrm{d}\cos\theta\\
=&\frac{2}{B\left(m_a^2-m_b^2\right)}\left(\left(\tilde{C}-m_b^2\right)^2\operatorname{arctanh}\left(\frac{B}{A-\tilde{C}+m_b^2}\right)\right.\\
&\left.-\left(\tilde{C}-m_a^2\right)^2\operatorname{arctanh}\left(\frac{B}{A-\tilde{C}+m_a^2}\right)\right)+2,\\
I_{16}=&\int\frac{n_1}{d_6}\mathrm{d}\cos\theta\\
=&\frac{2}{\left(A-\tilde{C}+m_a^2\right)^2-B^2},\\
I_{17}=&\int\frac{n_2}{d_6}\mathrm{d}\cos\theta\\
=&\frac{2}{B}\operatorname{arctanh}\left(\frac{B}{A-\tilde{C}+m_a^2}\right)+\frac{2\left(\tilde{C}-m_a^2\right)}{\left(A-\tilde{C}+m_a^2\right)^2-B^2},\\
I_{18}=&\int\frac{n_3}{d_6}\mathrm{d}\cos\theta\\
=&\frac{4\left(\tilde{C}-m_a^2\right)}{B}\operatorname{arctanh}\left(\frac{B}{A-\tilde{C}+m_a^2}\right)+2\\
&+2\frac{\tilde{C}-m_a^2}{\left(A-\tilde{C}+m_a^2\right)^2-B^2},\\
I_{19}=&\int\frac{n_1}{d_7}\mathrm{d}\cos\theta\\
=&\frac{2}{B\left(\tilde{C}-m_a^2-m_b^2\right)}\\
&\left(\operatorname{arctanh}\left(\frac{B}{A-m_a^2}\right)-\operatorname{arctanh}\left(\frac{B}{A-\tilde{C}+m_b^2}\right)\right),\\
I_{20}=&\int\frac{n_2}{d_7}\mathrm{d}\cos\theta\\
=&\frac{2}{B\left(\tilde{C}-m_a^2-m_b^2\right)}\\
&\left(\left(m_b^2-\tilde{C}\right)\operatorname{arctanh}\left(\frac{B}{A-\tilde{C}+m_b^2}\right)\right.\\
&\left.+m_a^2\operatorname{arctanh}\left(\frac{B}{A-m_a^2}\right)\right),\\
I_{21}=&\int\frac{n_3}{d_7}\mathrm{d}\cos\theta\\
=&-2+\frac{2}{B\left(\tilde{C}-m_a^2-m_b^2\right)}\\
&\left(-\left(\tilde{C}-m_b^2\right)^2\operatorname{arctanh}\left(\frac{B}{A-\tilde{C}+m_b^2}\right)\right.
\end{aligned}
$$

$$+m_a^4 \operatorname{arctanh}\left(\frac{B}{A-m_a^2}\right)\Bigg).$$

E

COUPLINGS AND PROPAGATORS

E.1 GENERIC EXPRESSIONS

This section contains generic expression for propagators and couplings of scalars ϕ, fermions χ and vector bosons V. Note, the field type does not determine whether two particles are members of the same species. So ϕ_i and ϕ_j could for example be X_1 from T12A and the Higgs boson H. Chirality projectors P_L, P_R and γ matrices can be found in Appendix A. Momentum is chosen to run from left to right.

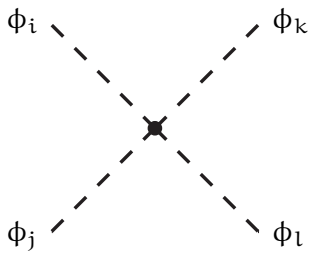

$$\boxed{i} = ig_i \tag{E.259}$$

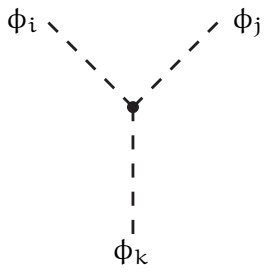

$$\boxed{i} = ig_i \tag{E.260}$$

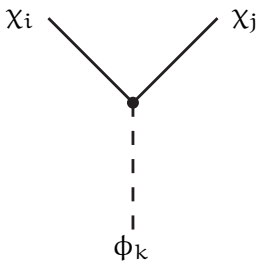

$$\boxed{i} = i(g_{iL}P_L + g_{iR}P_R) \tag{E.261}$$

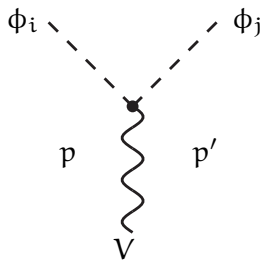

$$\boxed{i}^{\mu} = ig_i \left(p + p'\right)^{\mu} \tag{E.262}$$

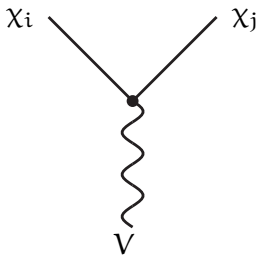

$$\boxed{i}^{\mu} = i\gamma^{\mu}\left(g_{iL}P_L + g_{iR}P_R\right) \tag{E.263}$$

$$\frac{i}{p^2 - M_\phi^2} \tag{E.264}$$

$$i\frac{\not{p} + M_\chi^2}{p^2 - M_\chi^2} \tag{E.265}$$

$$\frac{i}{p^2 - M_V^2}\left(-g^{\mu\nu} + xp^{\mu}p^{\nu}\right) \tag{E.266}$$

$$\text{with } x = \begin{cases} 0, \text{ for } V = \gamma \\ \frac{1}{M_V^2}, \text{ otherwise.} \end{cases} \tag{E.267}$$

E.2 STANDARD MODEL FERMIONS WITH HIGGS AND Z BOSONS

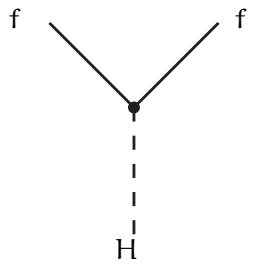

$$\boxed{i} = -i\frac{g}{2}\frac{m_f}{m_W} \tag{E.268}$$

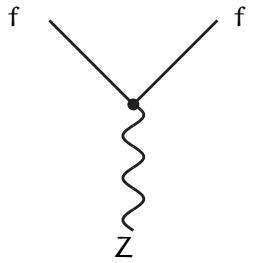

$$\boxed{i}^{\mu} = \frac{g}{\cos\theta_W}\gamma^{\mu}\left(g_V - g_A\gamma^5\right) \tag{E.269}$$

with $g_V = \frac{1}{2}I_3 - Q\sin^2\theta_W$ and $g_A = \frac{1}{2}I_3$

E.3 EXPRESSIONS IN T12A

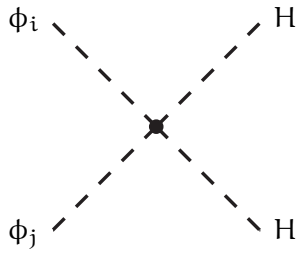

$$\begin{aligned}\boxed{i} =& \frac{1}{2}\left(\lambda_S U_{S,1i}U_{S,1j}\right.\\ &+\left(\lambda_D+\lambda'_D+\lambda''_D\right)U_{S,2i}U_{S,2j}\\ &\left.+(\lambda_D+\lambda'_D-\lambda''_D)U_{S,3i}U_{S,3j}\right)\end{aligned} \tag{E.270}$$

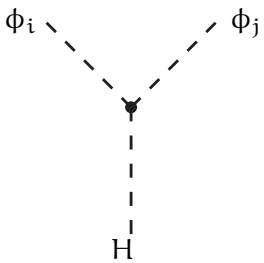

$$\begin{aligned}\boxed{i} =& v\left(1-\frac{1}{2}\delta_{ij}\right)\left(\lambda_S U_{S,1i}U_{S,1j}\right.\\ &+\left(\lambda_D+\lambda'_D+\lambda''_D\right)U_{S,2i}U_{S,2j}\\ &\left.+\left(\lambda_D+\lambda'_D-\lambda''_D\right)U_{S,3i}U_{S,3j}\right)\\ &+\left(1-\frac{1}{2}\delta_{ij}\right)\sqrt{2}\\ &\times A\left(U_{S,1i}U_{S,2j}+U_{S1i}U_{S2i}\right)\end{aligned} \tag{E.271}$$

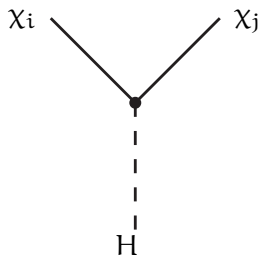

$$\boxed{i} = i\left(1 - \frac{1}{2}\delta_{ij}\right)\Big(y_1 \left(U_{F,1i}U_{F,2j} + U_{F,1j}U_{F,2i}\right) \\ y_2 \left(U_{F,1i}U_{F,3j} + U_{F,1j}U_{F,3i}\right)\Big) \tag{E.272}$$

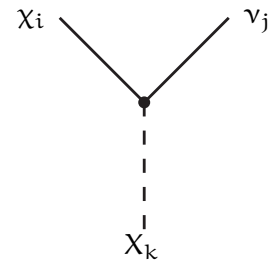

$$\begin{aligned} \boxed{i} =& g_{1j}U_{F,3i}U_{S,1k} \\ &+ g_{2j}U_{F,1i}U_{S,2k} \\ &- i\gamma^5 g_{2i}U_{F1i}U_{S,3k} \qquad \text{(E.273)} \\ =:& A_{ijk} - i\gamma^5 B_{ijk} \\ =& (A_{ijk} + iB_{ijk})P_L \\ &+ (A_{ijk} - iB_{ijk})P_R \qquad \text{(E.274)} \end{aligned}$$

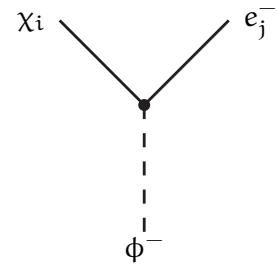

$$\boxed{i} = ig_{2j}U_{F,1i}P_L) \tag{E.275}$$

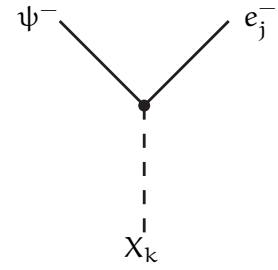

$$\boxed{i} = ig_{2j}U_{S,1k}P_L \tag{E.276}$$

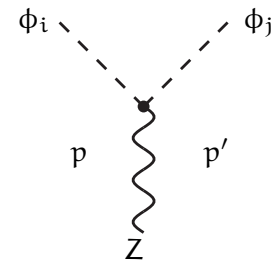

$$\boxed{i}^\mu = i\frac{g\cos 2\theta_W}{2\cos\theta_W}U_{2i}\delta_{3j}\left(p + p'\right)^\mu \tag{E.277}$$

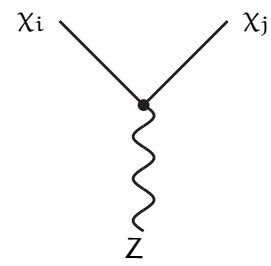

$$\boxed{i}^\mu = i\gamma^\mu\frac{g}{\cos\theta_W}\frac{1}{2}\left(U_{F,2i}^2 - U_{F,3i}^2\right) \tag{E.278}$$

F

DARK MATTER ANNIHILATION

There are plenty of dark matter annihilation processes, which heavily depend on the model. Even if they are viable within a model, not all annihilation channels contribute equally to the relic density. This chapter contains a small overview on some annihilation channels in generic way. Lepton and neutrino final states within T12A are especially shown.

F.1 SCALAR DARK MATTER

F.1.1 *Fermion final states*

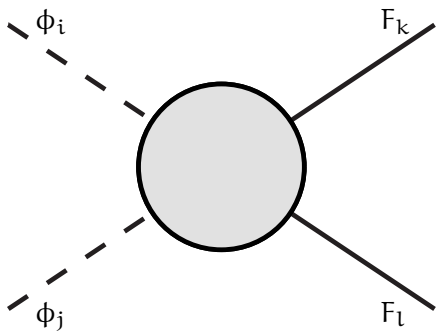

Figure F.83: Annihilation of fermion dark matter to two fermions

In the case of real scalar dark matter the diagrams in this section can be considered. Annihilation to lepton final states is closely linked to the direct detection diagrams shown in Section G.1. The generic diagrams for this process – see Fig. F.83 – are mostly the flipped versions of the diagrams found there. The generic vertices $\boxed{i}$ are summarized in Appendix E. Fig. G.124 and Fig. G.125 contains the generic diagrams for dark matter annihilation to lepton final states. Depending on the scalar and fermion indices, different relations between the vertices can be established. This is summarized in Tab. F.10. In general $\boxed{i}^*$ leads to $g^*_{i,L(R)} = g_{i,R(L)}$ and $\boxed{i}^{\nu *} = \boxed{i}$ demands $g^*_{i,L(R)} = g_{i,L(R)}$ for fermions.

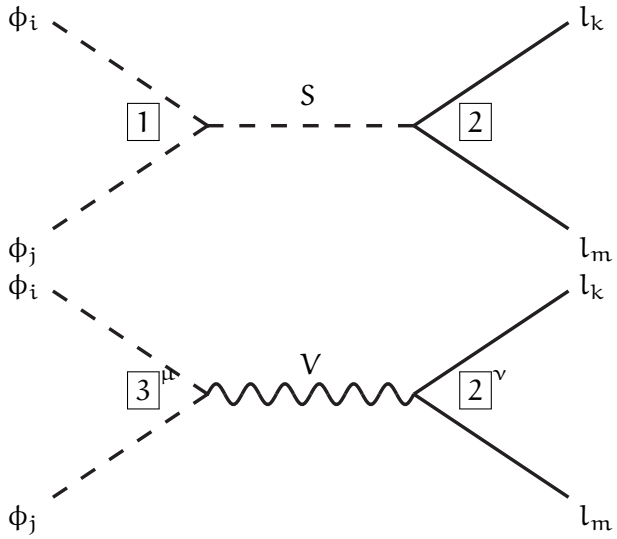

Figure F.84: Scalar dark matter annihilation to fermions: s-channel diagrams.

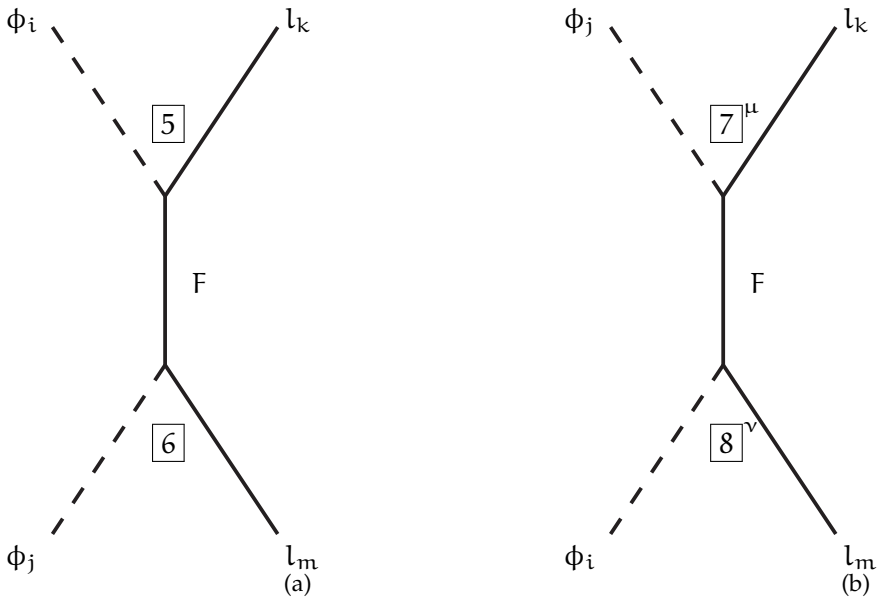

Figure F.85: t-channel diagrams for scalar to fermion processes.

The amplitudes corresponding to the diagrams are

$$
\begin{aligned}
f_1 =& \boxed{1} \frac{i}{s - m_S^2} \overline{u}_3 \boxed{2} v_4, \\
f_2 =& \boxed{3}^{\nu} (-g^{\mu\nu} + \frac{1}{m_V^2} (p_1 + p_2)^{\mu} (p_1 + p_2)^{\nu}) \\
& \times \frac{i}{s - m_V^2} \overline{u}_3 \boxed{4}^{\mu} v_4, \\
f_3 =& \overline{u}_3 \boxed{5} \frac{\not{p}_1 - \not{p}_3 + m_F}{t - m_F^2} \boxed{6} v_4,
\end{aligned}
$$

Table F.10: Vertex relations for scalar dark matter annihilation to fermion final states

Case	Vertex relations		
same scalar index $i = j$	$\boxed{5} = \boxed{7}$,	$\boxed{6} = \boxed{8}$	
same fermion index $k = l$	$\boxed{5}^* = \boxed{7}$,	$\boxed{6}^* = \boxed{8}$	
all Majorana fermions	$\boxed{i}^* = \boxed{i}$,	for $i = 2, 4-8$	

$$f_4 = \overline{u}_3 \boxed{7} \frac{\not{p}_1 - \not{p}_4 + m_F}{t - m_F^2} \boxed{8} v_4, \tag{F.279}$$

with momentum $p_{1(2)}$ for $\phi_{i(j)}$ and $p_{3(4)}$ for $l_{k(m)}$. The squared amplitudes are

$$\begin{aligned}
M_{1,1}^2 =& \frac{g_1 g_1^*}{(s - m_S^2)^2} \\
& \mathrm{Tr}\left[(m_3 + \not{p}_3).(g_{2L} P_L + g_{2R} P_R).\right. \\
& \left.(\not{p}_4 - m_4).(g_{2L}^* P_R + g_{2R}^* P_L)\right], \\
M_{1,2}^2 =& (g_1 g_3^* (p_1 + p_2)^\kappa \\
& \left(\frac{g^{\kappa\beta} g^{\alpha\sigma} (p_1 + p_2)^\alpha (p_1 + p_2)^\beta}{m_V^2} - g^{\kappa\sigma}\right)\Big) \\
& \times \frac{1}{(s - m_S^2)(s - m_V^2)} \\
& \mathrm{Tr}\left[(m_3 + \not{p}_3).(g_{2L} P_L + g_{2R} P_R).\right. \\
& \left.(\not{p}_4 - m_4).(g_{4L}^* P_R + g_{4R}^* P_L).\gamma^\sigma\right], \\
M_{1,3}^2 =& \frac{g_1}{(t - m_F^2)(s - m_S^2)} \\
& \mathrm{Tr}\left[(m_3 + \not{p}_3).(g_{2L} P_L + g_{2R} P_R).\right. \\
& (\not{p}_4 - m_4).(g_{6L}^* P_R + g_{6R}^* P_L) \\
& \left.(m_F + \not{p}_2 - \not{p}_4).(g_{5L}^* P_R + g_{5R}^* P_L)\right], \\
M_{1,4}^2 =& \frac{g_1}{(u - m_F^2)(s - m_S^2)} \\
& \mathrm{Tr}\left[(m_3 + \not{p}_3).(g_{2L} P_L + g_{2R} P_R).\right. \\
& (\not{p}_4 - m_4).(g_{8L}^* P_R + g_{8R}^* P_L) \\
& \left.(m_F + \not{p}_1 - \not{p}_4).(g_{7L}^* P_R + g_{7R}^* P_L)\right], \\
M_{2,2}^2 =& (g_3 g_3^* (p_1 + p_2)^\kappa (p_1 + p_2)^\mu \\
& \times \left(\frac{g^{\alpha\nu} (p_1 + p_2)^\alpha g^{\beta\mu} (p_1 + p_2)^\beta}{m_V^2} - g^{\mu\nu}\right)\Big) \\
& \times \frac{1}{(s - m_V^2)^2} \\
& \left(\frac{g^{\kappa\beta} g^{\alpha\sigma} (p_1 + p_2)^\alpha (p_1 + p_2)^\beta}{m_V^2} - g^{\kappa\sigma}\right)
\end{aligned}$$

$$
\begin{aligned}
&\mathrm{Tr}\left[(m_3+\not{p}_3).\gamma^\nu.(g_{4L}P_L+g_{4R}P_R).\right.\\
&\left.(\not{p}_4-m_4).(g^*_{4L}P_R+g^*_{4R}P_L).\gamma^\sigma\right], \qquad \text{(F.280)}\\
M^2_{2,3} =&(g_3(p_1+p_2)^\mu\\
&\left(\frac{g^{\alpha\nu}(p_1+p_2)^\alpha g^{\beta\mu}(p_1+p_2)^\beta}{m_V^2}-g^{\mu\nu}\right)\Big)\\
&\times\frac{1}{(t-m_F^2)\,(s-m_V^2)}\\
&\mathrm{Tr}\left[(m_3+\not{p}_3).\gamma^\nu.(g_{4L}P_L+g_{4R}P_R).\right.\\
&(\not{p}_4-m_4).(g^*_{6L}P_R+g^*_{6R}P_L)\\
&\left.(m_F+\not{p}_2-\not{p}_4).(g^*_{5L}P_R+g^*_{5R}P_L)\right],\\
M^2_{2,4} =&(g_3(p_1+p_2)^\mu\\
&\left(\frac{g^{\alpha\nu}(p_1+p_2)^\alpha g^{\beta\mu}(p_1+p_2)^\beta}{m_V^2}-g^{\mu\nu}\right)\Big)\\
&\times\frac{1}{(u-m_F^2)\,(s-m_V^2)}\\
&\mathrm{Tr}\left((m_3+\not{p}_3).\gamma^\nu.(g_{4L}P_L+g_{4R}P_R).\right.\\
&(\not{p}_4-m_4).(g^*_{8L}P_R+g^*_{8R}P_L)\\
&\left.(m_F+\not{p}_1-\not{p}_4).(g^*_{7L}P_R+g^*_{7R}P_L)\right),\\
M^2_{3,3} =&\frac{1}{(t-m_F^2)^2}\\
&\mathrm{Tr}\left[(m_3+\not{p}_3).(g_{5L}P_L+g_{5R}P_R).\right.\\
&(m_F+\not{p}_2-\not{p}_4).(g_{6L}P_L+g_{6R}P_R)\\
&(\not{p}_4-m_4).(g^*_{6L}P_R+g^*_{6R}P_L).\\
&\left.(m_F+\not{p}_2-\not{p}_4).(g^*_{5L}P_R+g^*_{5R}P_L)\right],\\
M^2_{3,4} =&\frac{1}{(t-m_F^2)\,(u-m_F^2)}\\
&\mathrm{Tr}\left[(m_3+\not{p}_3).(g_{5L}P_L+g_{5R}P_R).\right.\\
&(m_F+\not{p}_2-\not{p}_4).(g_{6L}P_L+g_{6R}P_R)\\
&(\not{p}_4-m_4).(g^*_{8L}P_R+g^*_{8R}P_L).\\
&\left.(m_F+\not{p}_1-\not{p}_4).(g^*_{7L}P_R+g^*_{7R}P_L)\right],\\
M^2_{4,4} =&\frac{1}{(u-m_F^2)^2}\\
&\mathrm{Tr}\left[m_3+\not{p}_3).(g_{7L}P_L+g_{7R}P_R).\right.\\
&(m_F+\not{p}_1-\not{p}_4).(g_{8L}P_L+g_{8R}P_R)\\
&(\not{p}_4-m_4).(g^*_{8L}P_R+g^*_{8R}P_L).\\
&\left.(m_F+\not{p}_1-\not{p}_4).(g^*_{7L}P_R+g^*_{7R}P_L)\right]. \qquad \text{(F.281)}
\end{aligned}
$$

The traces can be evaluated with the trace theorems given in Appendix A.

F.1.1.1 *Charged lepton final states in T12A*

Within T12A the charged leptons couple to the Higgs, but are also linked to the dark sector by g_{ij}. This allows for the diagrams shown in Fig. F.86 and Fig. F.87. Yet, the charged lepton masses are very

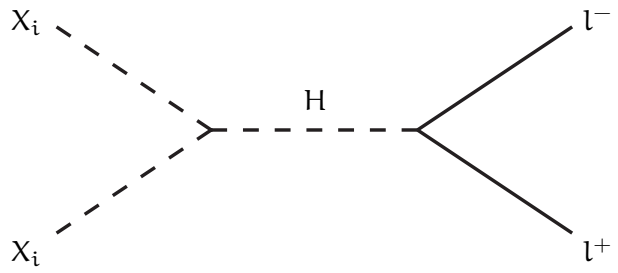

Figure F.86: s-channel diagram for scalar dark matter annihilating to charged leptons in T12A.

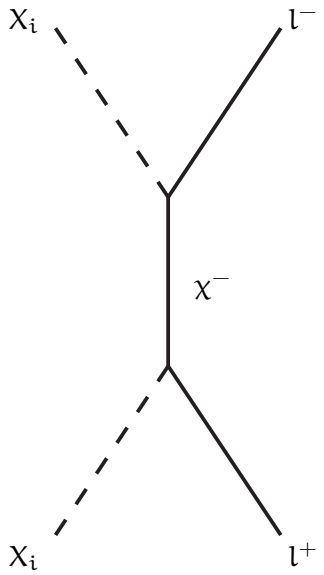

Figure F.87: t-channel diagram within T12A for scalar dark matter going to charged leptons.

small compared to the annihilating scalars, thus the s-channel diagram mediated by the Higgs does not contribute. Only f_3 and f_4 from Eq. F.279 have to be taken into account. For $M_{3,3}$ the trace can be evaluated in the case of matching scalar indices $i = j$. The expressions for g_i in the vertices are found in Section E.1. Notice $g_{5R,6L,7L,8R} = 0$ and $g_i^* = g_i$. Thus, with $m_1 = m_2 = m_{X_i}$ and $m_3 = m_4 = 0$, the evaluated trace leads to

$$M_{3,3}^2 = \frac{g_{5L}^2 g_{6R}^2 \left(tu - m_{X_i}^4\right)}{\left(m_{\psi^-}^2 - t\right)^2},$$

$$
\begin{aligned}
M_{3,4}^2 =& \frac{g_{5L}^2 g_{6R}^2 \left(2m_{X_i}^4 + 2m_{X_i}^2 (s-t-u) - s^2 + t^2 + u^2\right)}{2\left(m_{\psi^-}^2 - t\right)\left(m_{\psi^-}^2 - u\right)}, \\
M_{4,4}^2 =& \frac{g_{5L}^2 g_{6R}^2 \left(tu - m_{X_i}^4\right)}{\left(m_{\psi^-}^2 - u\right)^2}.
\end{aligned} \tag{F.282}
$$

The integration in $\cos\theta$ can be conducted with the integrals in Section D.2. In the non-relativistic limit the integrated squared amplitude $I_{3,3}$ is

$$
\begin{aligned}
I_{3,3} =& \frac{4 g_{5L}^2 g_{6R}^2 m_{X_i}^4 v^2}{3\left(m_{\psi^-}^2 + m_{X_i}^2\right)^2} \\
&+ \frac{2 g_{5L}^2 g_{6R}^2 v^4 \left(5 m_{\psi^-}^4 m_{X_i}^4 + m_{X_i}^8\right)}{15\left(m_{\psi^-}^2 + m_{X_i}^2\right)^4} + O\left(v^5\right), \\
I_{3,4} =& -\frac{4v^2 \left(g_{5L}^2 g_{6R}^2 m_{X_i}^4\right)}{3\left(m_{\psi^-}^2 + m_{X_i}^2\right)^2} \\
&- \frac{2v^4 \left(g_{5L}^2 g_{6R}^2 \left(5 m_{\psi^-}^4 m_{X_i}^4 - 3 m_{X_i}^8\right)\right)}{15\left(m_{\psi^-}^2 + m_{X_i}^2\right)^4} + O\left(v^5\right), \\
I_{4,3} =& -\frac{4v^2 \left(g_{5L}^2 g_{6R}^2 m_{X_i}^4\right)}{3\left(m_{\psi^-}^2 + m_{X_i}^2\right)^2} \\
&- \frac{2v^4 \left(g_{5L}^2 g_{6R}^2 \left(5 m_{\psi^-}^4 m_{X_i}^4 - 3 m_{X_i}^8\right)\right)}{15\left(m_{\psi^-}^2 + m_{X_i}^2\right)^4} + O\left(v^5\right), \\
I_{4,4} =& \frac{4 g_{5L}^2 g_{6R}^2 m_{X_i}^4 v^2}{3\left(m_{\psi^-}^2 + m_{X_i}^2\right)^2} \\
&+ \frac{2 g_{5L}^2 g_{6R}^2 v^4 \left(5 m_{\psi^-}^4 m_{X_i}^4 + m_{X_i}^8\right)}{15\left(m_{\psi^-}^2 + m_{X_i}^2\right)^4} + O\left(v^5\right).
\end{aligned} \tag{F.283}
$$

Individually the integrated amplitudes feature terms proportional to v^2, but when summing all contributions, they cancel each other and the resulting matrix element for the entire process is

$$
I_{summed} = \frac{16 g_{5L}^2 g_{6R}^2 m_{X_i}^8 v^4}{15\left(m_{\psi^-}^2 + m_{X_i}^2\right)^4} + O\left(v^5\right). \tag{F.284}
$$

F.1.1.2 *Neutrino final states in T12A*

T12A also offers the opportunity of neutrino final states. As the neutrinos do not couple directly to the Higgs boson, only the t-channel diagrams shown in Fig. F.88 mediate this process. For calculation, sim-

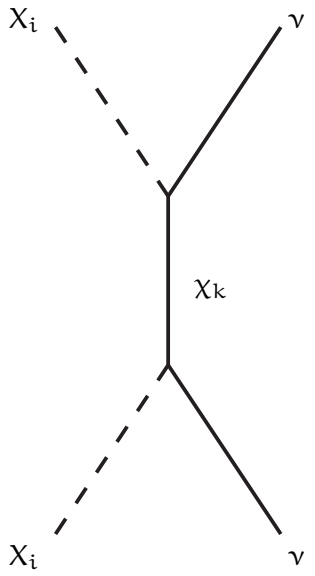

Figure F.88: Process for dark mater annihilating to neutrinos.

ilar to the charged lepton final state, only $f_{3,4}$ have to be considered, but now the mediator can be any of the three χ_j. Hence, one has to sum over all relevant contributions. The vertices will also be labeled with the index of the mediator. The squared amplitudes are

$$\begin{aligned}
M^2_{3,3} =& \frac{2\left(-m_{\chi_l} m_{\chi_j} s + m^4_{X_i} - 2m^2_{X_i} t + t(s+t)\right)}{\left(m^2_{\chi_l} - t\right)\left(t - m^2_{\chi_j}\right)} \\
& (A_{kji}A_{mji}A_{kli}A_{mli} + B_{kji}B_{mji}B_{kli}B_{mli}), \\
M^2_{3,4} =& \frac{2\left(m_{\chi_l} m_{\chi_j} s + m^4_{X_i} - 2m^2_{X_i} t + t(s+t)\right)}{\left(m^2_{\chi_l} - t\right)\left(m^2_{\chi_j} - 2m^2_{X_i} + s + t\right)} \\
& (A_{kji}A_{mji}A_{kli}A_{mli} + B_{kji}B_{mji}B_{kli}B_{mli}), \\
M^2_{4,4} =& -\frac{2\left(-m_{\chi_l} m_{\chi_j} s + m^4_{X_i} - 2m^2_{X_i} t + t(s+t)\right)}{\left(m^2_{\chi_l} - 2m^2_{X_i} + s + t\right)\left(m^2_{\chi_j} - 2m^2_{X_i} + s + t\right)} \\
& (A_{kji}A_{mji}A_{kli}A_{mli} + B_{kji}B_{mji}B_{kli}B_{mli}).
\end{aligned} \tag{F.285}$$

After summing the integrated squared amplitudes the outcome is

$$I_{summed} = \frac{32v^2\left(m^2_{\chi_l} m^2_{\chi_j} m^4_{X_i} + m^6_{X_i}(m_{\chi_l} + m_{\chi_j})^2 + m^8_{X_i}\right)}{3\left(m^2_{\chi_l} + m^2_{X_i}\right)^2\left(m^2_{\chi_j} + m^2_{X_i}\right)^2}$$

$$\times \left(A_{kji}A_{mji}A_{kli}A_{mli} + B_{kji}B_{mji}B_{kli}B_{mli}\right) + O\left(v^3\right), \tag{F.286}$$

in the non-relativistic limit. For the same neutrino index $k = m$ this simplifies to

$$\begin{aligned} I_{summed} = &\left(32v^2\left(m_{\chi_l}^2 m_{\chi_j}^2 m_{X_i}^4 + m_{X_i}^6 (m_{\chi_l} + m_{\chi_j})^2 + m_{X_i}^8\right)\right. \\ &\times \left.\left(A_{mji}^2 A_{mli}^2 + B_{mji}^2 B_{mli}^2\right)\right) \\ &\times \frac{1}{3\left(m_{\chi_l}^2 + m_{X_i}^2\right)^2\left(m_{\chi_j}^2 + m_{X_i}^2\right)^2} + O\left(v^3\right). \end{aligned} \tag{F.287}$$

F.1.2 *Vector final states*

One possible annihilation channel is annihilation into pairs of vector bosons as schematically shown in Fig. F.89 and generically in Fig. F.90, Fig. F.91 and Fig. F.92.

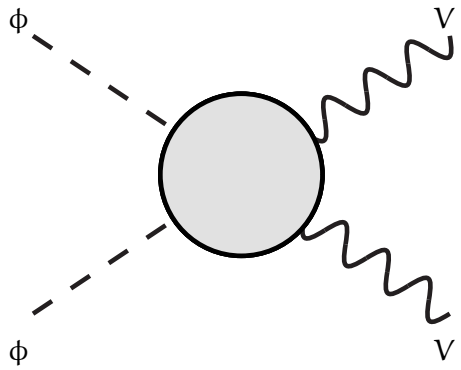

Figure F.89: Scalar to vector boson processes.

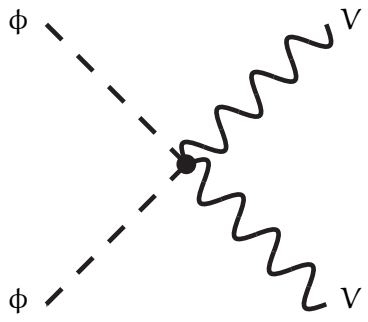

Figure F.90: Direct interaction between scalars and vector bosons.

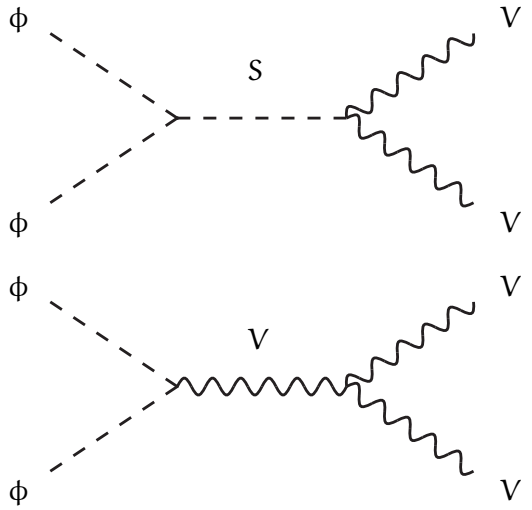

Figure F.91: s-channel contributions for scalar dark matter to vector bosons.

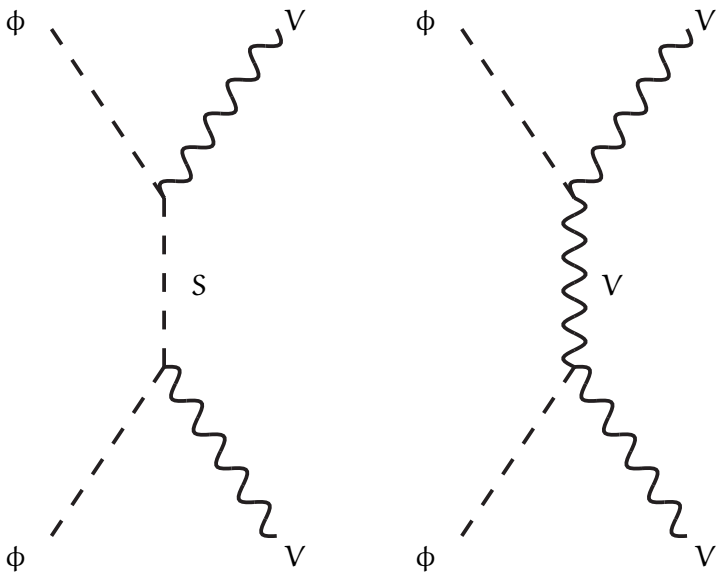

Figure F.92: Scalar to vector boson processes in t-channel diagrams.

F.1.3 *Scalar final states*

The process of scalar dark matter annihilation – see Fig. F.93 – can be mediated by the diagrams shown in Fig. F.94, Fig. F.96 and Fig. F.95.

F.2 FERMION DARK MATTER

Similar to scalar dark matter, fermionic dark matter has plenty of annihilation final states. Some of them are summarized in the sections below.

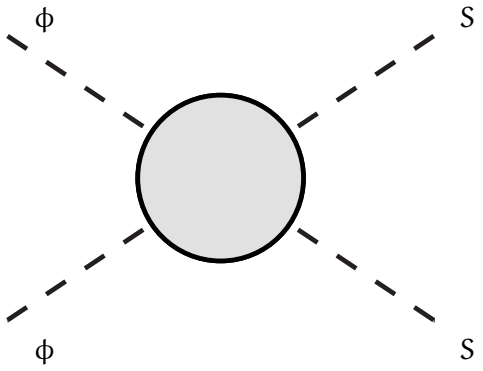

Figure F.93: Scalar to scalar processes.

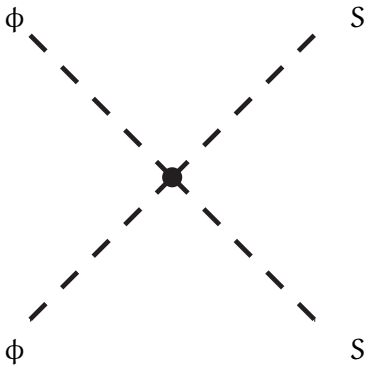

Figure F.94: Four fermion interaction.

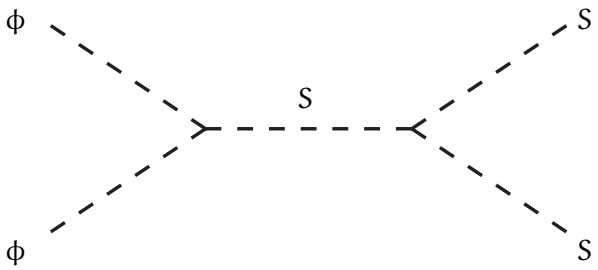

Figure F.95: s-channel diagram for a two scalar to two scalar process.

F.2.1 *Fermion final states*

The annihilation of fermion dark matter to fermions is schematically depicted in Fig. G.123, which is similar for direct detection. Fig. F.98, Fig. F.99 and Fig. F.100 show the diagrams for fermion dark matter. Similar to the scalar case, the relations between vertices depend on the exact particles. Further, it has an influence whether the fermions are Dirac or Majorana fermions. In the case of Dirac dark matter anni-

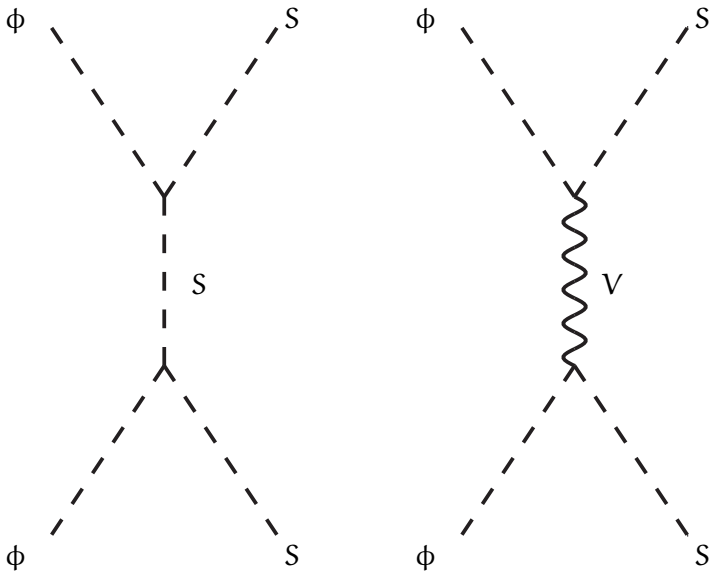

Figure F.96: t-channel contributions for scalar to scalar annihilation.

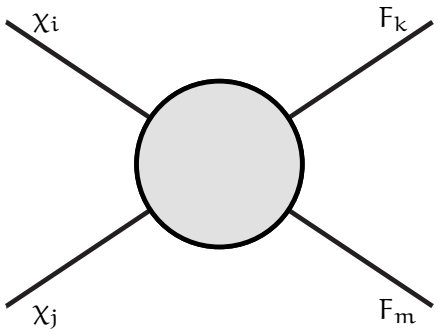

Figure F.97: Schematic sketch for fermion to fermion annihilation.

hilating to Dirac fermions, the right diagrams in Fig. F.99 and Fig. F.99 do no exist. For Majorana dark matter annihilating to Dirac fermions, $\boxed{i}^* = \boxed{i}$ is true for $i = 1, 3$ in the case of Dirac dark matter going to Majorana fermions i is 2 and 4. If all fermions are Majorana fermions, the relation holds for all i. Equations for different settings are listed in Tab. F.11.

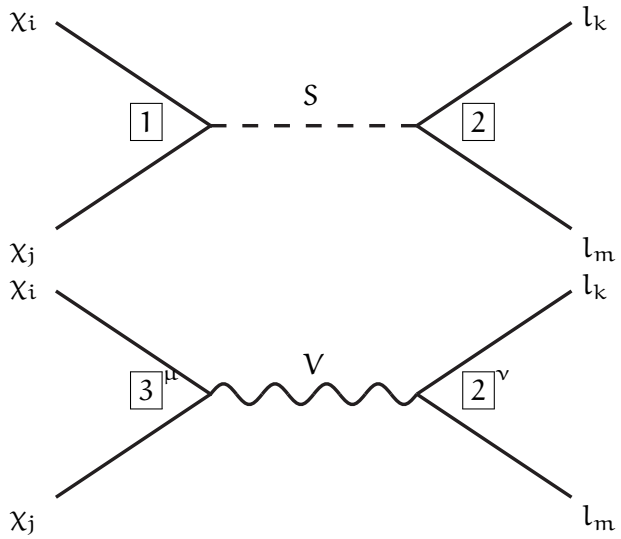

Figure F.98: Fermion dark matter annihilation to fermions: s-channel diagrams.

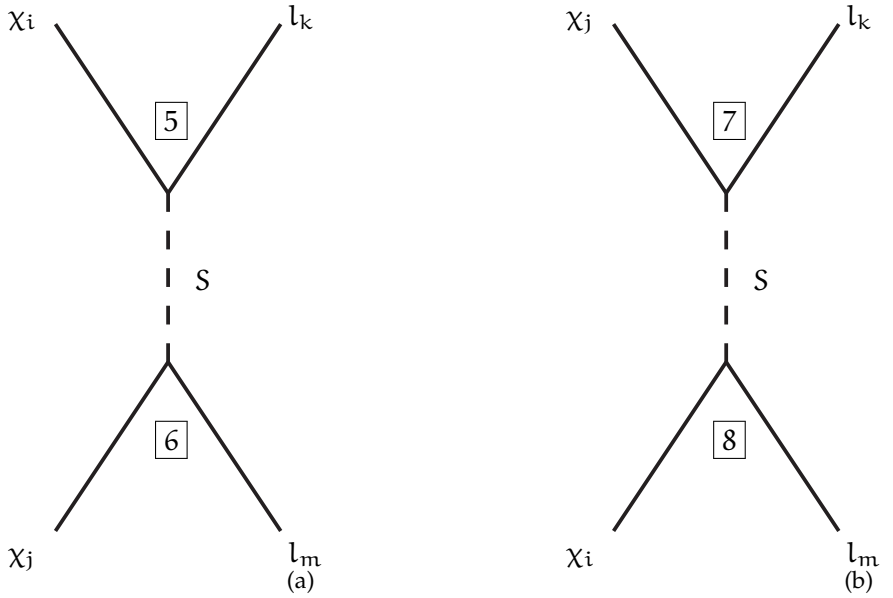

Figure F.99: t-channel diagrams for fermion to fermion processes mediated by a scalar.

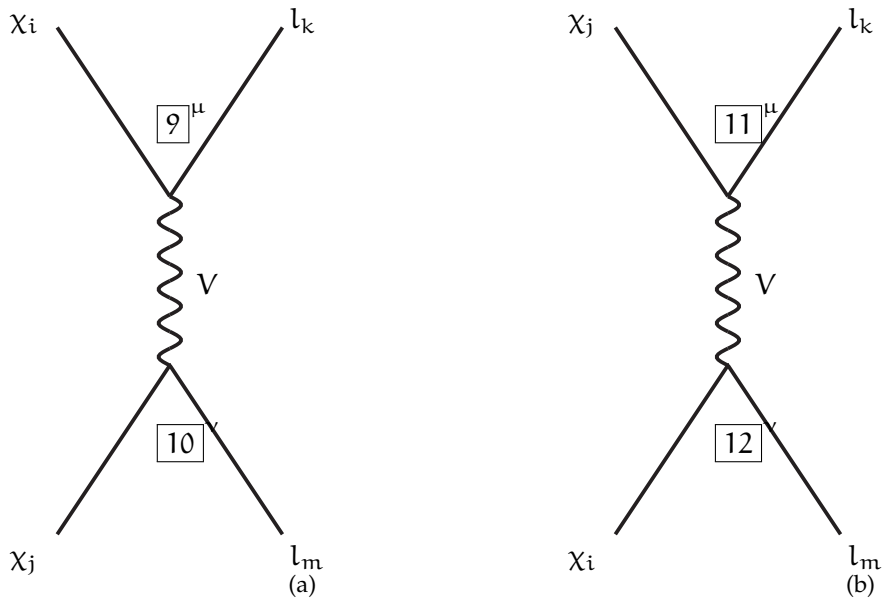

Figure F.100: t-channel diagrams for fermion to fermion processes mediated by a vector boson.

The amplitudes for the diagrams are

$$
\begin{aligned}
f_1 =& \bar{u}_3 \boxed{2} v_4 \frac{1}{s - m_S^2} \bar{v}_1 \boxed{1} u_1, \\
f_2 =& \bar{u}_3 \boxed{5} u_1 \frac{1}{t - m_S^2} \bar{v}_2 \boxed{6} v_4, \\
f_3 =& \bar{u}_3 \boxed{7} u_2 \frac{1}{u - m_S^2} \bar{v}_1 \boxed{8} v_4, \\
f_4 =& \bar{u}_3 \boxed{4}^{\mu} v_4 \frac{1}{s - m_V^2} (-g^{\mu\nu} + \frac{1}{m_V^2}(p_1 + p_2)^{\mu}(p_1 + p_2)^{\nu}) \bar{v}_1 \boxed{3}^{\nu} u_1, \\
f_5 =& \bar{u}_3 \boxed{9}^{\mu} u_1 \frac{1}{s - m_V^2} (-g^{\mu\nu} + \frac{1}{m_V^2}(p_1 - p_3)^{\mu}(p_1 - p_3)^{\nu}) \bar{v}_2 \boxed{11}^{\nu} v_4, \\
f_6 =& \bar{u}_3 \boxed{11}^{\mu} u_2 \frac{1}{s - m_V^2} (-g^{\mu\nu} + \frac{1}{m_V^2}(p_1 - p_3)^{\mu}(p_1 - p_3)^{\nu}) \bar{v}_1 \boxed{12}^{\nu} v_4.
\end{aligned}
\tag{F.288}
$$

The squared amplitudes are

Table F.11: Fermion to fermion annihilation overview

Case	all Dirac	Majorana DM	Majorana l	all Majorana
$i = j$		$\boxed{5} = \boxed{7}$, $\boxed{6} = \boxed{8}$, $\boxed{9}^{\mu} = \boxed{11}^{\mu}$, $\boxed{10}^{\nu} = \boxed{12}^{\nu}$	$\boxed{5}^{*} = \boxed{7}$, $\boxed{6}^{*} = \boxed{8}$, $\boxed{9}^{\mu *} = \boxed{11}^{\mu}$, $\boxed{10}^{\nu *} = \boxed{12}^{\nu}$	$\boxed{5} = \boxed{7}$ $\boxed{6} = \boxed{8}$ $\boxed{9}^{\mu} = \boxed{11}^{\mu}$ $\boxed{10}^{\nu} = \boxed{12}^{\nu}$
$k = l$		$\boxed{5}^{*} = \boxed{8}$, $\boxed{6}^{*} = \boxed{7}$, $\boxed{9}^{\mu *} = \boxed{12}^{\mu}$, $\boxed{10}^{\nu *} = \boxed{11}^{\nu}$	$\boxed{5} = \boxed{8}$, $\boxed{6} = \boxed{7}$, $\boxed{9}^{\mu} = \boxed{12}^{\mu}$, $\boxed{10}^{\nu} = \boxed{11}^{\nu}$	$\boxed{5} = \boxed{8}$, $\boxed{6} = \boxed{7}$ $\boxed{9}^{\mu} = \boxed{12}^{\mu}$, $\boxed{10}^{\nu} = \boxed{11}^{\nu}$
$i = j$, $k = l$	$\boxed{5}^{*} = \boxed{6}$, $\boxed{9}^{\mu *} = \boxed{10}^{\mu}$	$\boxed{5} = \boxed{6}^{*} = \boxed{7} = \boxed{8}^{*}$, $\boxed{9}^{\mu *} = \boxed{10}^{\mu} = \boxed{11}^{\mu} = \boxed{12}^{\mu *}$	$\boxed{5}^{*} = \boxed{6} = \boxed{7}^{*} = \boxed{8}$, $\boxed{9}^{\mu *} = \boxed{10}^{\mu} = \boxed{11}^{\mu *} = \boxed{12}^{\mu}$	$\boxed{5} = \boxed{6} = \boxed{7} = \boxed{8}$, $\boxed{9}^{\mu} = \boxed{10}^{\mu} = \boxed{11}^{\mu} = \boxed{12}^{\mu}$

$$
\begin{aligned}
M^2_{1,1} =& \frac{1}{\left(s - m^2_{S,schan}\right)^2} \\
& \mathrm{Tr}((m_1 + \not{p}_1).(g^*_{1L} P_R + g^*_{1R} P_L). \\
& (\not{p}_2 - m_2).(g_{1L} P_L + g_{1R} P_R) \\
& \mathrm{Tr}((m_3 + \not{p}_3).(g_{2L} P_L + g_{2R} P_R). \\
& (\not{p}_4 - m_4).(g^*_{2L} P_R + g^*_{2R} P_L))), \\
M^2_{1,2} =& \frac{1}{\left(t - m^2_{S,tchan}\right)\left(s - m^2_{S,schan}\right)} \\
& \mathrm{Tr}((\not{p}_2 - m_2).(g_{1L} P_L + g_{1R} P_R). \\
& (m_1 + \not{p}_1).(g^*_{5L} P_R + g^*_{5R} P_L) \\
& .(m_3 + \not{p}_3).(g_{2L} P_L + g_{2R} P_R). \\
& (\not{p}_4 - m_4).(g_{6L} P_R + g_{6R} P_L)), \\
M^2_{1,3} =& \frac{1}{\left(u - m^2_{S,tchan}\right)\left(s - m^2_{S,schan}\right)} \\
& \mathrm{Tr}((\not{p}_2 - m_2).(g_{1L} P_L + g_{1R} P_R). \\
& (m_1 + \not{p}_1).(g^*_{8L} P_R + g^*_{8R} P_L). \\
& (m_4 + \not{p}_4).(g_{2L} P_L + g_{2R} P_R). \\
& (\not{p}_3 - m_3).(g^*_{7L} P_R + g^*_{7R} P_L)), \\
M^2_{1,4} =& -\frac{\left(\frac{g^{\kappa\gamma} g^{\sigma\delta} (p_1+p_2)^{\delta} (p_1+p_2)^{\gamma}}{m^2_V} - g^{\kappa\sigma}\right)}{\left(s - m^2_{S,schan}\right)\left(s - m^2_V\right)} \\
& \mathrm{Tr}\left((\not{p}_2 - m_2).(g_{1L} P_L + g_{1R} P_R).\right.
\end{aligned}
$$

$$
\begin{aligned}
&(m_1 + \not{p}_1).(g_{3L}^* P_R + g_{3R}^* P_L).\gamma^\sigma \\
&\mathrm{Tr}\left((m_4 + \not{p}_4).(g_{2L} P_L + g_{2R} P_R).\right. \\
&\left.(\not{p}_3 - m_3).(g_{4L}^* P_L + g_{4R}^* P_R).\gamma^\kappa)\right), \\
M_{1,5}^2 =& \frac{\left(\frac{g^{\kappa\gamma} g^{\sigma\delta}(p_1-p_3)^\delta (p_1-p_3)^\gamma}{m_V^2} - g^{\kappa\sigma}\right)}{\left(s - m_{S,schan}^2\right)\left(t - m_V^2\right)} \\
&\mathrm{Tr}\left((\not{p}_2 - m_2).(g_{1L} P_L + g_{1R} P_R)\right. \\
&(m_1 + \not{p}_1).(g_{9L}^* P_R + g_{9R}^* P_L) \\
&\gamma^\sigma.(m_3 + \not{p}_3).(g_{2L} P_L + g_{2R} P_R). \\
&\left.(\not{p}_4 - m_4).(-g_{10L}^* P_L - g_{10R}^* P_R).\gamma^\kappa\right), \\
M_{1,6}^2 =& (\left(\frac{g^{\kappa\gamma} g^{\sigma\delta}(p_1 - p_4)^\delta (p_1 - p_4)^\gamma}{m_V^2} - g^{\kappa\sigma}\right) \\
&\mathrm{Tr}\left((\not{p}_2 - m_2).(g_{1L} P_L + g_{1R} P_R).\right. \\
&(m_1 + \not{p}_1).(g_{12L}^* P_R + g_{12R}^* P_L) \\
&\gamma^\sigma.(m_4 + \not{p}_4).(g_{2L} P_L + g_{2R} P_R). \\
&\left.(\not{p}_3 - m_3).(-g_{11L}^* P_L - g_{11R}^* P_R).\gamma^\kappa)\right) \\
&\frac{1}{\left(s - m_{S,schan}^2\right)\left(u - m_V^2\right)}, \\
M_{2,2}^2 =& (\mathrm{Tr}(\mathrm{Tr}((\not{p}_2 - m_2).(g_{6L} P_L + g_{6R} P_R). \\
&(\not{p}_4 - m_4).(g_{6L} P_R + g_{6R} P_L)) \\
&(m_1 + \not{p}_1).(g_{5L}^* P_R + g_{5R}^* P_L). \\
&(m_3 + \not{p}_3).(g_{5L} P_L + g_{5R} P_R))) \\
&\frac{1}{\left(t - m_{S,tchan}^2\right)^2}, \\
M_{2,3}^2 =& (\mathrm{Tr}((m_3 + \not{p}_3).(g_{5L} P_L + g_{5R} P_R). \\
&(m_1 + \not{p}_1).(g_{8L}^* P_R + g_{8R}^* P_L) \\
&(m_4 + \not{p}_4).(g_{6L} P_L + g_{6R} P_R). \\
&(m_2 + \not{p}_2).(g_{7L}^* P_R + g_{7R}^* P_L))) \\
&\frac{1}{\left(t - m_{S,tchan}^2\right)\left(u - m_{S,tchan}^2\right)}, \\
M_{2,4}^2 =& \left(\frac{g^{\kappa\gamma} g^{\sigma\delta}(p_1 + p_2)^\delta (p_1 + p_2)^\gamma}{m_V^2} - g^{\kappa\sigma}\right) \\
&\frac{1}{\left(t - m_{S,tchan}^2\right)\left(s - m_V^2\right)} \\
&\mathrm{Tr}\left((m_2 + \not{p}_2).(g_{3L}^* P_L + g_{3R}^* P_R).\gamma^\sigma.\right. \\
&(\not{p}_1 - m_1).(g_{5L} P_L + g_{5R} P_R) \\
&\left.(\not{p}_3 - m_3).(g_{4L}^* P_L + g_{4R}^* P_R).\gamma^\kappa.\right.
\end{aligned}
$$

$$
\begin{aligned}
&(m_4 + \not{p}_4).(g_{6L}P_L + g_{6R}P_R)\big)\,,\\
M^2_{2,5} =&(\left(\frac{g^{\kappa\rho}g^{\sigma\delta}(p_1-p_3)^\delta(p_1-p_3)^\rho}{m_V^2} - g^{\kappa\sigma}\right))\\
&\mathrm{Tr}\left((m_3+\gamma\cdot p_3).(g_{5L}P_L+g_{5R}P_R).\right.\\
&(m_1+\not{p}_1).(g^*_{9L}P_R+g^*_{9R}P_L)\\
&\gamma^\sigma\mathrm{Tr}\left((m_4+\gamma\cdot p_4).(g_{6L}P_L+g_{6R}P_R)\right.\\
&\left.(m_2+\gamma\cdot p_2).(g^*_{10L}P_R+g^*_{10R}P_L).\gamma^\kappa\right))\\
&\frac{1}{\left(t-m^2_{S,tchan}\right)\left(t-m_V^2\right)},\\
M^2_{2,6} =&(\left(\frac{g^{\kappa\gamma}g^{\sigma\delta}(p_1-p_4)^\delta(p_1-p_4)^\gamma}{m_V^2} - g^{\kappa\sigma}\right)\\
&\mathrm{Tr}\left((m_3+\not{p}_3).(g_{5L}P_L+g_{5R}P_R).\right.\\
&(m_1+\not{p}_1).(g^*_{12L}P_R+g^*_{12R}P_L)\\
&\gamma^\sigma.(m_4+\not{p}_4).(g_{6L}P_L+g_{6R}P_R).\\
&\left.(m_2+\not{p}_2).(g^*_{11L}P_R+g^*_{11R}P_L).\gamma^\kappa\right))\\
&\frac{1}{\left(t-m^2_{S,tchan}\right)\left(u-m_V^2\right)},\\
M^2_{3,3} =&\frac{}{\left(u-m^2_{S,tchan}\right)^2}\\
&\mathrm{Tr}((m_1+\not{p}_1).(g^*_{8L}P_R+g^*_{8R}P_L).\\
&(m_4+\not{p}_4).(g_{8L}P_L+g_{8R}P_R)\\
&\mathrm{Tr}((m_2+\not{p}_2).(g^*_{7L}P_R+g^*_{7R}P_L).\\
&(m_3+\not{p}_3).(g_{7L}P_L+g_{7R}P_R))),\\
M^2_{3,4} =&-(\left(\frac{g^{\kappa\gamma}g^{\sigma\delta}(p_1+p_2)^\delta(p_1+p_2)^\gamma}{m_V^2} - g^{\kappa\sigma}\right))\\
&\frac{1}{\left(u-m^2_{S,tchan}\right)\left(s-m_V^2\right)}\\
&\mathrm{Tr}\left((m_1+\not{p}_1).(g^*_{3L}P_R+g^*_{3R}P_L).\gamma^\sigma.\right.\\
&(\not{p}_2-m_2).(g_{7L}P_L+g_{7R}P_R)\\
&(\not{p}_3-m_3).(g^*_{4L}P_L+g^*_{4R}P_R).\gamma^\kappa.\\
&\left.(m_4+\not{p}_4).(g_{8L}P_L+g_{8R}P_R)\right)\,,\\
M^2_{3,5} =&\left(\frac{g^{\kappa\gamma}g^{\sigma\delta}(p_1-p_3)^\delta(p_1-p_3)^\gamma}{m_V^2} - g^{\kappa\sigma}\right)\\
&\frac{1}{\left(u-m^2_{S,tchan}\right)\left(t-m_V^2\right)}\\
&\mathrm{Tr}\left((m_1+\not{p}_1).(g^*_{9L}P_R+g^*_{9R}P_L).\gamma^\sigma.\right.\\
&\left.(m_3+\not{p}_3).(g_{7L}P_L+g_{7R}P_R)\right.
\end{aligned}
$$

$$
\begin{aligned}
&.(m_2+\not{p}_2).(g^*_{10L}P_R+g^*_{10R}P_L).\gamma^\kappa.\\
&(m_4+\not{p}_4).(g_{8L}P_L+g_{8R}P_R))\,,\\
M^2_{3,6} =&\left(\frac{g^{\kappa\gamma}g^{\sigma\delta}(p_1-p_4)^\delta(p_1-p_4)^\gamma}{m_V^2}-g^{\kappa\sigma}\right)\\
&\mathrm{Tr}\left((m_3+\not{p}_3).(g_{7L}P_L+g_{7R}P_R).\right.\\
&\left.(m_2+\not{p}_2).(g^*_{11L}P_R+g^*_{11R}P_L).\gamma^\kappa\right)\\
&\frac{1}{\left(u-m^2_{S,tchan}\right)\left(u-m_V^2\right)}\\
&\mathrm{Tr}\left((m_4+\not{p}_4).(g_{8L}P_L+g_{8R}P_R).\right.\\
&\left.(m_1+\not{p}_1).(g^*_{12L}P_R+g^*_{12R}P_L).\gamma^\sigma\right)\,,\\
M^2_{4,4} =&\left(\frac{g^{\alpha\mu}(p_1+p_2)^\alpha g^{\beta\nu}(p_1+p_2)^\beta}{m_V^2}-g^{\mu\nu}\right)\\
&\left(\frac{g^{\kappa\gamma}g^{\sigma\delta}(p_1+p_2)^\delta(p_1+p_2)^\gamma}{m_V^2}-g^{\kappa\sigma}\right)\\
&(\mathrm{Tr}\left((m_1+\not{p}_1).(g^*_{3L}P_R+g^*_{3R}P_L).\gamma^\sigma.\right.\\
&(\not{p}_2-m_2).\gamma^\mu.(g_{3L}P_L+g_{3R}P_R)\\
&\mathrm{Tr}\left((m_3+\not{p}_3).\gamma^\nu.(g_{4L}P_L+g_{4R}P_R).\right.\\
&\left.\left.(\not{p}_4-m_4).(g^*_{4L}P_R+g^*_{4R}P_L).\gamma^\kappa\right)\right))\\
&\frac{1}{\left(s-m_V^2\right)^2},\\
M^2_{4,5} =&\left(\frac{g^{\alpha\mu}(p_1+p_2)^\alpha g^{\beta\nu}(p_1+p_2)^\beta}{m_V^2}-g^{\mu\nu}\right)\\
&\left(\frac{g^{\kappa\gamma}g^{\sigma\delta}(p_1-p_3)^\delta(p_1-p_3)^\gamma}{m_V^2}-g^{\kappa\sigma}\right)\\
&\mathrm{Tr}\left((\not{p}_2-m_2).\gamma^\mu.(g_{3L}P_L+g_{3R}P_R)\right.\\
&(m_1+\not{p}_1).(g^*_{9L}P_R+g^*_{9R}P_L).\\
&\gamma^\sigma.(m_3+\not{p}_3).\gamma^\nu.(g_{4L}P_L+g_{4R}P_R)\\
&\left.(\not{p}_4-m_4).(-g^*_{10L}P_L-g^*_{10R}P_R).\gamma^\kappa\right))\\
&\frac{1}{\left(s-m_V^2\right)\left(t-m_V^2\right)},\\
M^2_{4,6} =&-\left(\frac{g^{\alpha\mu}(p_1+p_2)^\alpha g^{\beta\nu}(p_1+p_2)^\beta}{m_V^2}-g^{\mu\nu}\right)\\
&\left(\frac{g^{\kappa\gamma}g^{\sigma\delta}(p_1-p_4)^\delta(p_1-p_4)^\gamma}{m_V^2}-g^{\kappa\sigma}\right)\\
&\mathrm{Tr}\left((\not{p}_2-m_2).\gamma^\mu.(g_{3L}P_L+g_{3R}P_R).\right.\\
&(m_1+\not{p}_1).(g^*_{12L}P_R+g^*_{12R}P_L)\\
&\gamma^\sigma.(m_4+\not{p}_4).\gamma^\nu.(g_{4L}P_R+g_{4R}P_L).\\
&\left.(\not{p}_3-m_3).(-g^*_{11L}P_L-g^*_{11R}P_R).\gamma^\kappa\right)
\end{aligned}
$$

$$
\begin{aligned}
&\frac{1}{\left(s-m_V^2\right)\left(u-m_V^2\right)},\\
M^2_{5,5} = &\left(\frac{g^{\alpha\mu}(p_1-p_3)^\alpha g^{\beta\nu}(p_1-p_3)^\beta}{m_V^2}-g^{\mu\nu}\right)\\
&\left(\frac{g^{\kappa\gamma}g^{\sigma\delta}(p_1-p_3)^\delta(p_1-p_3)^\gamma}{m_V^2}-g^{\kappa\sigma}\right)\\
&\mathrm{Tr}\left((m_1+\not{p}_1).(g^*_{9L}P_R+g^*_{9R}P_L).\gamma^\sigma.\right.\\
&(m_3+\not{p}_3).\gamma^\mu.(g_{9L}P_L+g_{9R}P_R)\\
&\mathrm{Tr}\left((\not{p}_2-m_2).\gamma^\nu.(-g_{10L}P_R-g_{10R}P_L).\right.\\
&\left.\left.(\not{p}_4-m_4).(-g^*_{10L}P_L-g^*_{10R}P_R).\gamma^\kappa\right)\right)\\
&\frac{1}{\left(t-m_V^2\right)^2},\\
M^2_{5,6} = &\left(\frac{g^{\alpha\mu}(p_1-p_3)^\alpha g^{\beta\nu}(p_1-p_3)^\beta}{m_V^2}-g^{\mu\nu}\right)\\
&\left(\frac{g^{\kappa\gamma}g^{\sigma\delta}(p_1-p_4)^\delta(p_1-p_4)^\gamma}{m_V^2}-g^{\kappa\sigma}\right)\\
&\mathrm{Tr}\left((m_3+\not{p}_3).\gamma^\mu.(g_{9L}P_L+g_{9R}P_R)\right.\\
&(m_1+\not{p}_1).(g^*_{12L}P_R+g^*_{12R}P_L)\\
&\gamma^\sigma.(m_4+\not{p}_4).\gamma^\nu.(g_{10L}P_L+g_{10R}P_R)\\
&\left.(m_2+\not{p}_2).(g^*_{11L}P_R+g^*_{11R}P_L).\gamma^\kappa\right)\\
&\frac{1}{\left(t-m_V^2\right)\left(u-m_V^2\right)},\\
M^2_{6,6} = &\left(\frac{g^{\alpha\mu}(p_1-p_4)^\alpha g^{\beta\nu}(p_1-p_4)^\beta}{m_V^2}-g^{\mu\nu}\right)\\
&\left(\frac{g^{\kappa\gamma}g^{\sigma\delta}(p_1-p_4)^\delta(p_1-p_4)^\gamma}{m_V^2}-g^{\kappa\sigma}\right)\\
&\mathrm{Tr}\left((m_1+\not{p}_1).(g^*_{12L}P_R+g^*_{12R}P_L).\gamma^\sigma.\right.\\
&(m_4+\not{p}_4).\gamma^\mu.(g_{12L}P_L+g_{12R}P_R)\\
&\mathrm{Tr}\left((m_2+\not{p}_2).(g^*_{11L}P_R+g^*_{11R}P_L).\gamma^\kappa.\right.\\
&\left.\left.(m_3+\not{p}_3).\gamma^\nu.(g_{11L}P_L+g_{11R}P_R)\right)\right)\\
&\frac{1}{\left(u-m_V^2\right)^2}.
\end{aligned}
\tag{F.289}
$$

F.2.1.1 *Charged lepton Final States in T12A*

For charged lepton final states within T12A the three diagrams shown in Fig. F.101, Fig. F.102 and Fig. F.103 contribute. In principle the

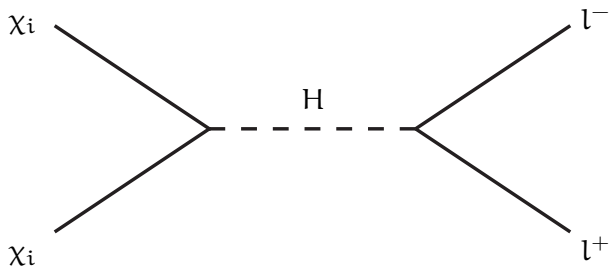

Figure F.101: s-channel diagram for fermion dark matter annihilating to charged leptons.

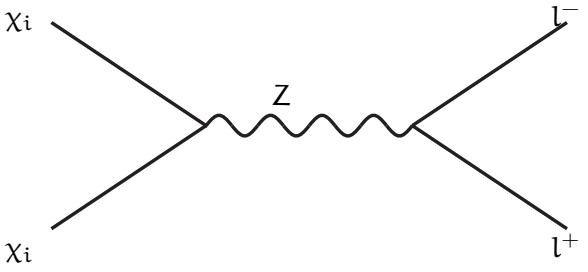

Figure F.102: s-channel diagram for fermion dark matter annihilating to charged leptons.

process mediated by the Z boson contributes, but it is more likely that the Z leads to different final states, as it is explained in [274]. Hence,

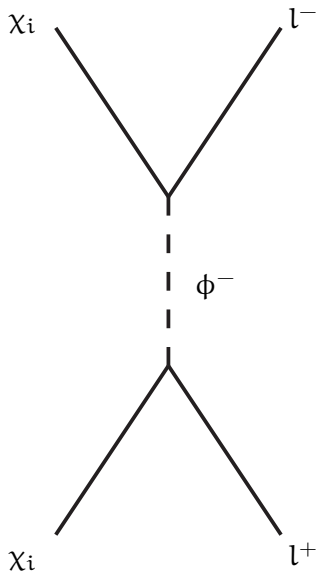

Figure F.103: Diagrams for χ_i annihilation to charged leptons within T12A.

it is not considered here. Only f_2 and f_3 contribute. The squared amplitudes are

$$
\begin{aligned}
M_{2,2}^2 =& \frac{g_{5L}^2 g_{6R}^2 \left(m_{\chi_i}^2 - t\right)^2}{\left(m_{\phi^-}^2 - t\right)^2}, \\
M_{2,3}^2 =& \frac{g_{5L}^2 g_{6R}^2 m_{\chi_i}^2 s}{\left(m_{\phi^-}^2 - t\right)\left(-2m_{\chi_i}^2 + m_{\phi^-}^2 + s + t\right)}, \\
M_{3,2}^2 =& \frac{g_{5L}^2 g_{6R}^2 m_{\chi_i}^2 s}{\left(m_{\phi^-}^2 - t\right)\left(-2m_{\chi_i}^2 + m_{\phi^-}^2 + s + t\right)}, \\
M_{3,3}^2 =& \frac{g_{5L}^2 g_{6R}^2 \left(-m_{\chi_i}^2 + s + t\right)^2}{\left(-2m_{\chi_i}^2 + m_{\phi^-}^2 + s + t\right)^2},
\end{aligned}
$$

for negligible lepton masses. After integration, the approximation in the non-relativistic limit yields

$$
\begin{aligned}
I_{2,2} =& \frac{8 g_{5L}^2 g_{6R}^2 m_{\chi_i}^4}{\left(m_{\chi_i}^2 + m_{\phi^-}^2\right)^2} \\
& - \frac{2v^2 \left(g_{5L}^2 g_{6R}^2 m_{\chi_i}^4 \left(m_{\chi_i}^4 + 6 m_{\chi_i}^2 m_{\phi^-}^2 - 7 m_{\phi^-}^4\right)\right)}{3\left(m_{\chi_i}^2 + m_{\phi^-}^2\right)^4} + O\left(v^3\right), \\
I_{2,3} =& \frac{8 g_{5L}^2 g_{6R}^2 m_{\chi_i}^4}{\left(m_{\chi_i}^2 + m_{\phi^-}^2\right)^2}
\end{aligned}
$$

$$
\begin{aligned}
&- \frac{2v^2\left(g_{5L}^2 g_{6R}^2 m_{\chi_i}^4\left(5m_{\chi_i}^4 + 6m_{\chi_i}^2 m_{\phi^-}^2 - 3m_{\phi^-}^4\right)\right)}{3\left(m_{\chi_i}^2 + m_{\phi^-}^2\right)^4} + O\left(v^3\right), \\
I_{3,2} =& \frac{8g_{5L}^2 g_{6R}^2 m_{\chi_i}^4}{\left(m_{\chi_i}^2 + m_{\phi^-}^2\right)^2} \\
&- \frac{2v^2\left(g_{5L}^2 g_{6R}^2 m_{\chi_i}^4\left(5m_{\chi_i}^4 + 6m_{\chi_i}^2 m_{\phi^-}^2 - 3m_{\phi^-}^4\right)\right)}{3\left(m_{\chi_i}^2 + m_{\phi^-}^2\right)^4} + O\left(v^3\right), \\
I_{3,3} =& \frac{8g_{5L}^2 g_{6R}^2 m_{\chi_i}^4}{\left(m_{\chi_i}^2 + m_{\phi^-}^2\right)^2} \\
&- \frac{2v^2\left(g_{5L}^2 g_{6R}^2 m_{\chi_i}^4\left(m_{\chi_i}^4 + 6m_{\chi_i}^2 m_{\phi^-}^2 - 7m_{\phi^-}^4\right)\right)}{3\left(m_{\chi_i}^2 + m_{\phi^-}^2\right)^4} + O\left(v^3\right).
\end{aligned}
$$

The summed matrix element, when taking into account the correct sign for the interfering diagrams, is

$$
I_{summed} = \frac{16g_{5L}^2 g_{6R}^2 m_{\chi_i}^4 v^2\left(m_{\chi_i}^4 + m_{\phi^-}^4\right)}{3\left(m_{\chi_i}^2 + m_{\phi^-}^2\right)^4} + O\left(v^3\right). \tag{F.290}
$$

The contribution from the Z diagram is suppressed by the mixing matrix entries, which appear as a difference.

F.2.1.2 *Neutrino final states in T12A*

Similar to charged leptons, T12A also allows for neutrino pairs in the final state. The corresponding diagrams are shown in Fig. F.104 and Fig. F.105 For neutrino final states only f_2 and f_3 have to be considered. The squared matrix elements are

$$
\begin{aligned}
M_{2,2}^2 =& \sum_{j,m} -\Big(4\left(m_{\chi_i}^2 - t\right)^2 (A_{kij}A_{kim}A_{lij}A_{lim} \\
&+B_{kij}B_{kim}B_{lij}B_{lim})) \\
&\times \frac{1}{\left(m_{\chi_j}^2 - t\right)\left(t - m_{\chi_m}^2\right)}, \\
M_{2,3}^2 =& \sum_{j,m} -(2\left(A_{kij}A_{lij}\right(\\
&A_{kim}A_{lim}\left(m_{\chi_i}^4 + m_{\chi_i}^2(s-2t) + t(s+t)\right) \\
&-B_{kim}B_{lim}\left(m_{\chi_i}^2 - t\right)\left(m_{\chi_i}^2 - s - t\right)) \\
&+B_{kij}B_{lij}\left(\right. \\
&B_{kim}B_{lim}\left(m_{\chi_i}^4 + m_{\chi_i}^2(s-2t) + t(s+t)\right) \\
&-A_{kim}A_{lim}\left(m_{\chi_i}^2 - t\right)\left(m_{\chi_i}^2 - s - t\right))))
\end{aligned}
$$

$$
\begin{aligned}
&\frac{1}{\left(t-m_{\chi_j}^2\right)\left(-2m_{\chi_i}^2+m_{\chi_m}^2+s+t\right)},\\
M_{3,2}^2 = &\sum_{j,m} -(2\left(A_{kij}A_{lij}\right.\\
&\left(A_{kim}A_{lim}\left(m_{\chi_i}^4+m_{\chi_i}^2(s-2t)+t(s+t)\right)\right.\\
&-B_{kim}B_{lim}\left(m_{\chi_i}^2-t\right)\left(m_{\chi_i}^2-s-t\right))\\
&+B_{kij}B_{lij}\left(B_{kim}B_{lim}\left(m_{\chi_i}^4+m_{\chi_i}^2(s-2t)+t(s+t)\right)\right.\\
&\left.\left.-A_{kim}A_{lim}\left(m_{\chi_i}^2-t\right)\left(m_{\chi_i}^2-s-t\right)\right)\right))\\
&\frac{1}{\left(t-m_{\chi_m}^2\right)\left(-2m_{\chi_i}^2+m_{\chi_j}^2+s+t\right)},\\
M_{3,3}^2 = &\sum_{j,m}(4\left(-m_{\chi_i}^2+s+t\right)^2\\
&(A_{kij}A_{kim}A_{lij}A_{lim}+B_{kij}B_{kim}B_{lij}B_{lim}))\\
&\frac{1}{\left(-2m_{\chi_i}^2+m_{\chi_j}^2+s+t\right)\left(-2m_{\chi_i}^2+m_{\chi_m}^2+s+t\right)}.
\end{aligned}
\tag{F.291}
$$

The vertices have been replaced according to the Majorana nature of χ and ν and the vertex within T12A. Further, the relation of the scalar mixing matrix $U_{S,1(2)i}U_{S,3j} = 0$ is used to simplify the results. The summed integrated matrix element is

$$
\begin{aligned}
I_{summed} = &\sum_{j,m}(32m_{\chi_i}^4(A_{kij}A_{lij}(3A_{kim}A_{lim}\\
&+B_{kim}B_{lim})+B_{kij}B_{lij}(A_{kim}A_{lim}+3B_{kim}B_{lim})))\\
&\frac{1}{\left(m_{\chi_i}^2+m_{\chi_j}^2\right)\left(m_{\chi_i}^2+m_{\chi_m}^2\right)}+O\left(v^2\right).
\end{aligned}
\tag{F.292}
$$

F.2.2 *Scalar final states*

Fig. F.106 and Fig. F.107 depict generic fermion to scalar annihilation processes.

F.2.3 *Vector final states*

Generic diagrams for fermion to vector boson annihilations are shown in Fig. F.108 and Fig. F.109.

F.3 COANNIHILATION BETWEEN FERMION AND SCALAR

The presence of scalars and fermions, which are close in mass, allow for coannihilation processes to become important. Some example di-

agrams for scalar-fermion and vector boson-fermion final states are presented in the following sections.

F.3.1 *Fermion scalar final state*

One possible final state for coannihilation is a fermion and a scalar as shown in Fig. F.110 and Fig. F.111.

F.3.1.1 *Neutrino-Higgs final states within T12A*

Since in T12A fermion-scalar couplings are present, coannihilation between the two species can take place. For a neutrino and a Higgs boson in the final state, the corresponding diagrams are shown in Fig. F.112.

F.3.2 *Vector boson fermion final state*

Similar to fermion-scalar final states, coannihilation also can feature fermion-vector boson channels as shown in Fig. F.113 and Fig. F.114

F.3.2.1 *Neutrino-Z final states within T12A*

Despite the neutrino Higgs final state, coannihilation in T12A can also feature a neutrino and a Z boson. The corresponding diagrams are shown in Fig. F.115 and Fig. F.116.

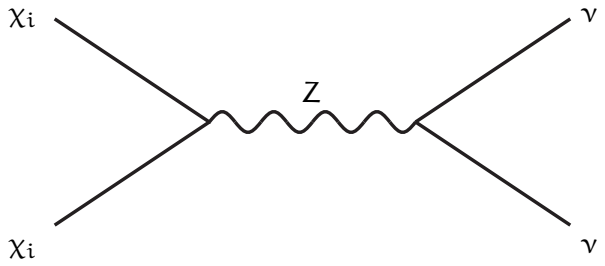

Figure F.104: Neutrino final state for fermion dark matter annihilation in T12A.

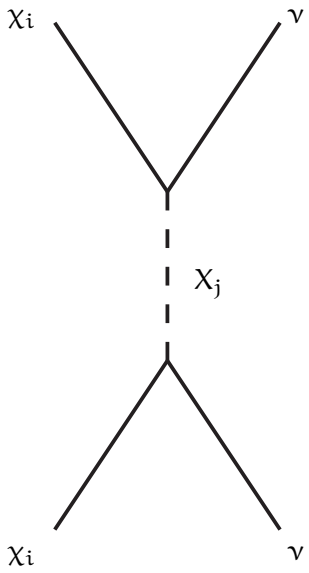

Figure F.105: t-channel diagram for neutrino final states within T12A.

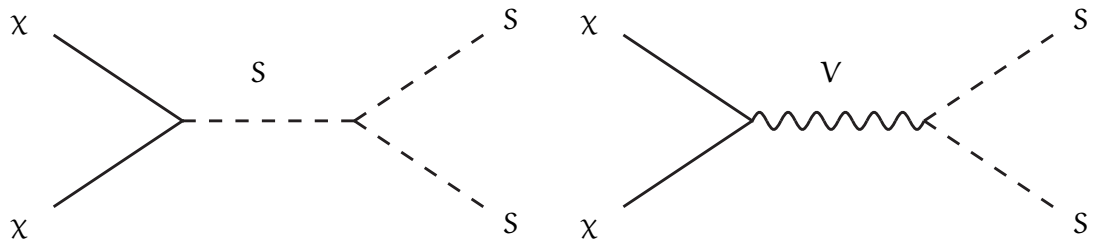

Figure F.106: Fermion dark matter annihilation to scalars: s-channel diagrams.

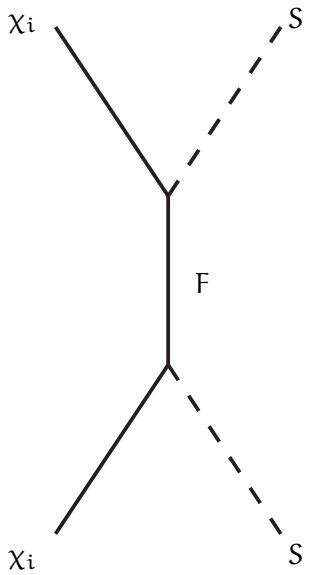

Figure F.107: t-channel diagrams for fermion to scalar processes.

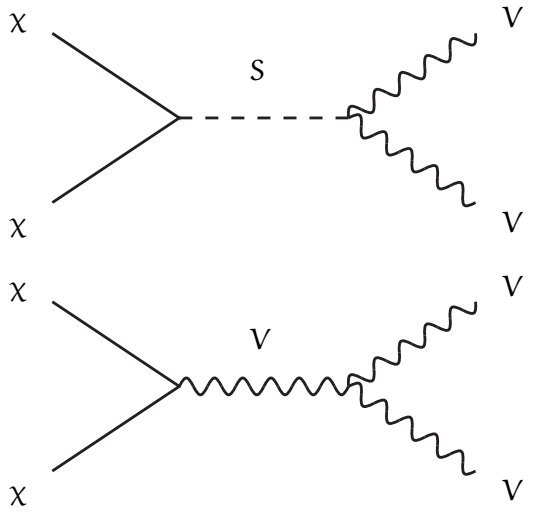

Figure F.108: s-channel diagrams for vector boson final sates.

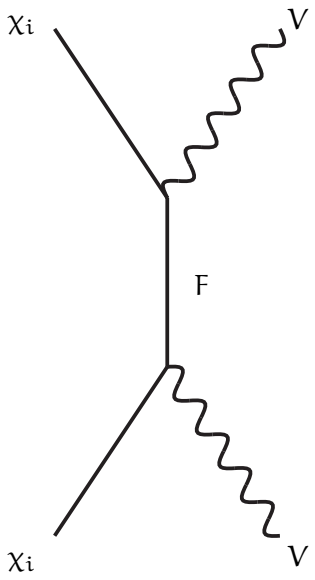

Figure F.109: Diagrams for dark matter fermions annihilating to vector bosons.

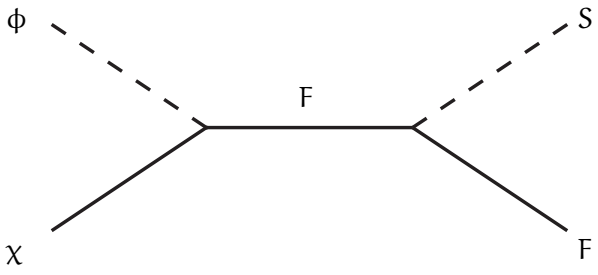

Figure F.110: Coannihilation between fermion and scalar dark matter to fermion scalar final states.

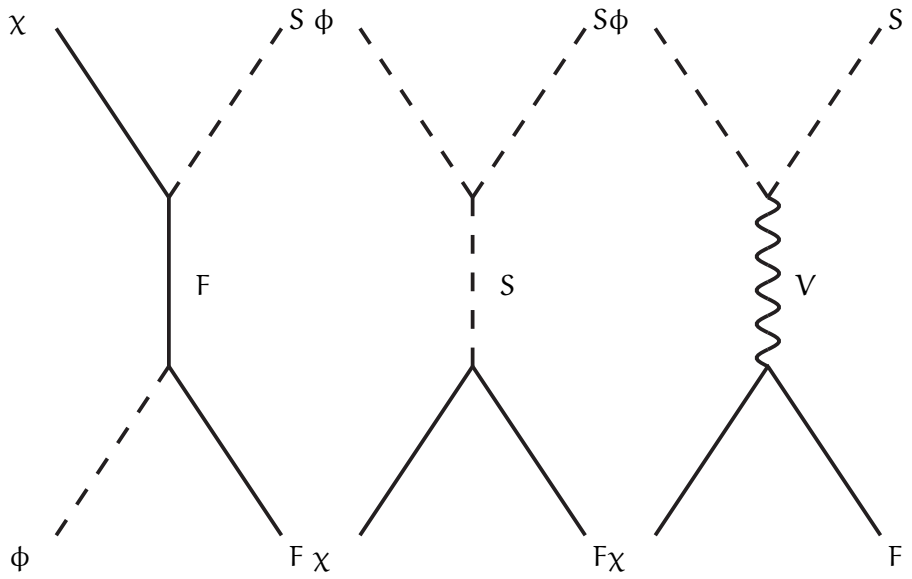

Figure F.111: t-channel diagrams for fermion to vector final sates.

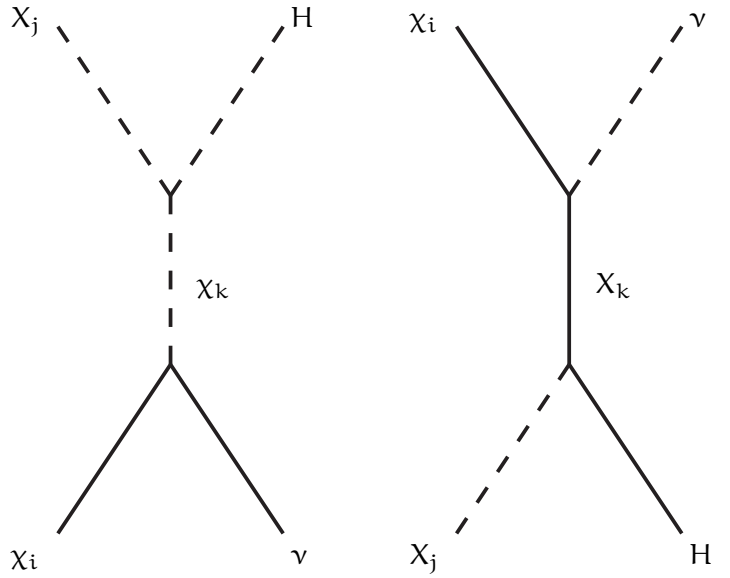

Figure F.112: Diagrams for χ_i and X_j co-annihilation within T12A.

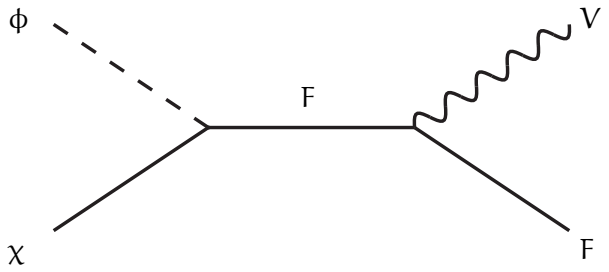

Figure F.113: s-channel diagram for fermion scalar coannihilation to a fermion and a vector boson.

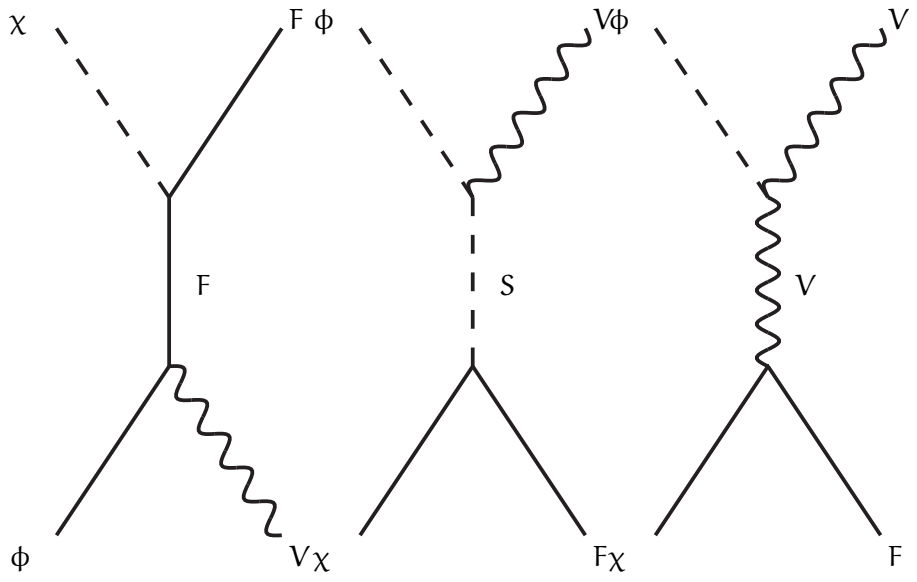

Figure F.114: t-channel contributions for fermion and vector boson final states.

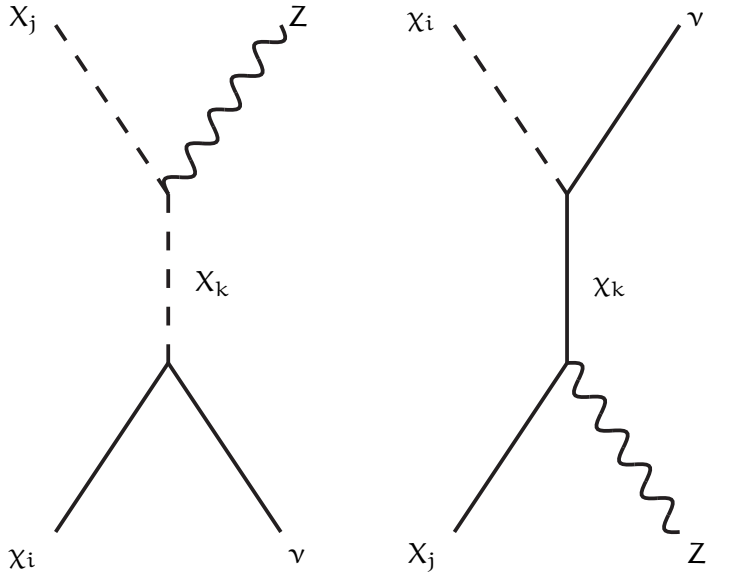

Figure F.115: Diagrams for χ_i and X_j co-annihilation within T12A.

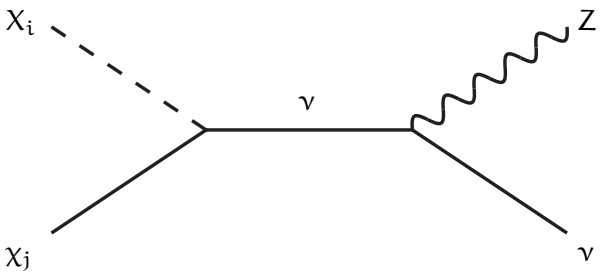

Figure F.116: s-channel diagram for χ_i and X_j coannihilation within T12A.

G

DIRECT DETECTION DIAGRAMS

Direct detection of dark matter is done by dark matter scattering off of nuclei. The sections beneath contain generic diagrams for this process as well as specific diagrams within T12A.

G.1 SCALAR DARK MATTER

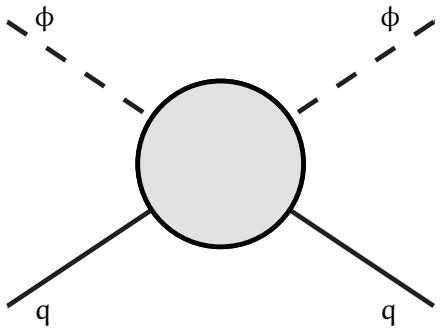

Figure G.117: Generic process of scalar - fermion scattering.

Fig. G.117 sketches scalar fermion scattering, which is the underlying process for scalar dark matter direct detection. This can also include scattering off of electrons instead of quarks when the model contains the appropriate couplings.

G.1.1 *Generic diagrams*

The figures in this section display different options how the direct detection process could be mediated.

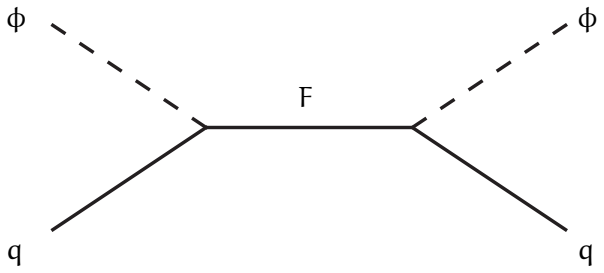

Figure G.118: s-channel diagrams

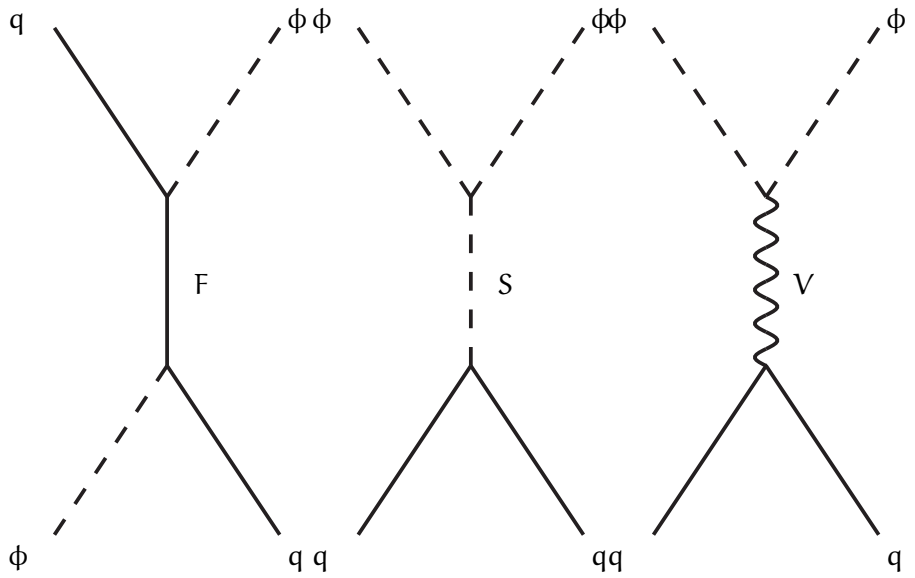

Figure G.119: t-channel diagrams

G.1.2 *Diagrams within T12A*

Not all of the above diagrams are realized within T12A. For direct detection based on nuclear recoil only the s-channel diagram mediated by a Higgs shown in Fig. G.120. Considering electron recoil, which

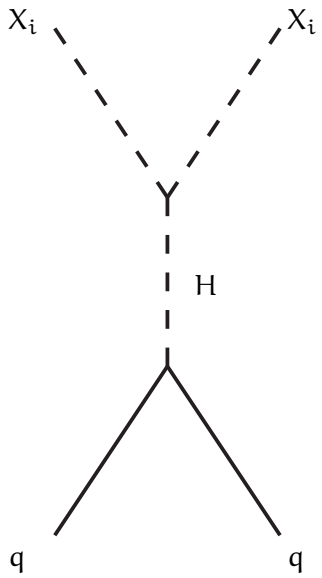

Figure G.120: s-channel diagrams for X_i and quark scattering within T12A.

is another possibility for direct detection, the s-channel diagram in Fig. G.121 and the two t-channel diagrams in Fig. G.122 contribute to this. The presence of scalars and fermions linking the dark sector to the Standard Model lepton sector allow for these processes. Even though the diagram mediated by a Higgs is negligibly small as the coupling to the electron scales with the electron mass.

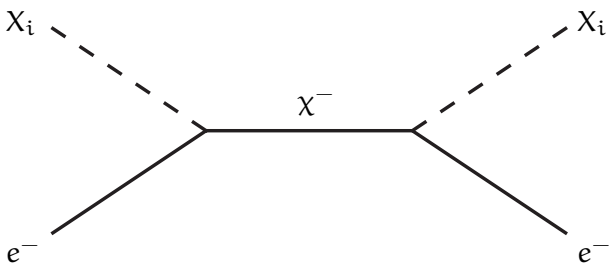

Figure G.121: s-channel diagram for X_i and e^- scattering within T12A.

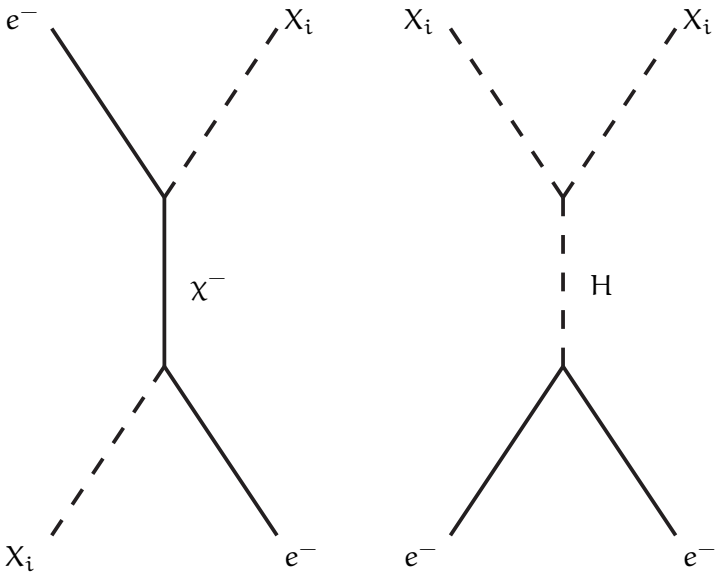

Figure G.122: t-channel diagrams for X_i and e^- scattering within T12A.

G.2 FERMION DARK MATTER

For fermion dark matter the direct detection process can be depicted by Fig. G.123.

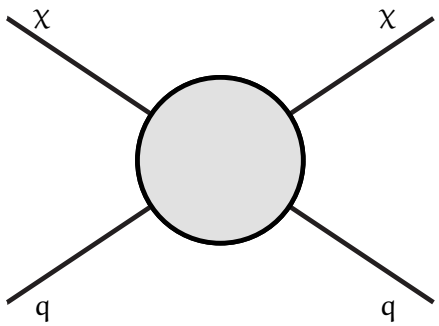

Figure G.123: Generic process of fermion - fermion scattering.

G.2.1 *Generic diagrams*

The diagrams in this section depict generic fermion-fermion scattering processes.

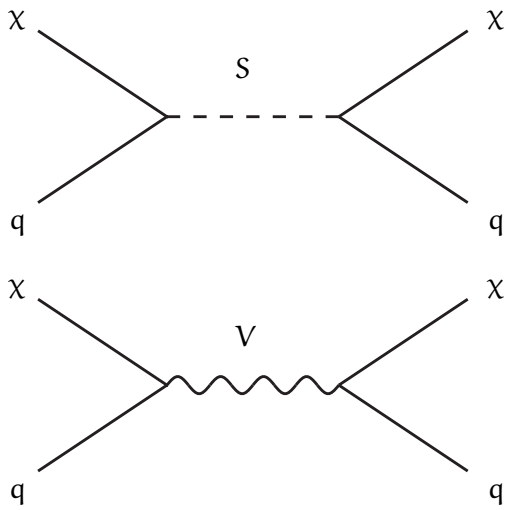

Figure G.124: s-channel diagrams for fermion - fermion scattering in the context of dark matter direct detection.

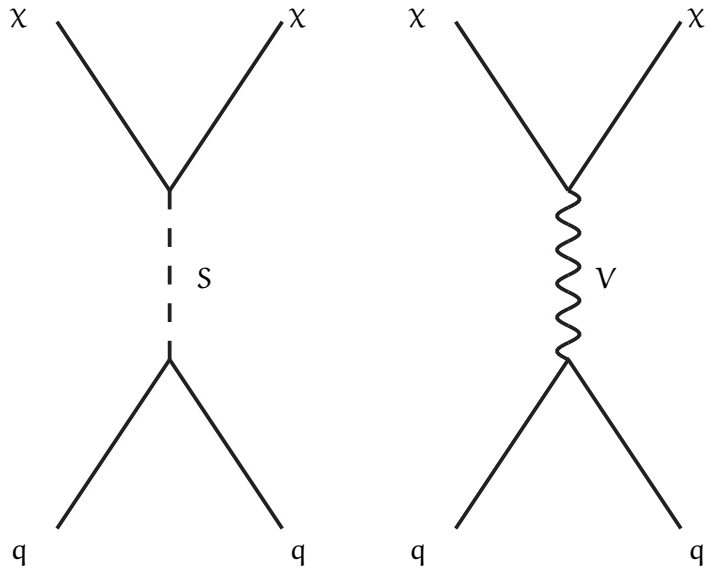

Figure G.125: t-channel diagrams for direct detection processes of fermion dark matter.

G.2.2 *Diagrams within T12A*

Within the model T12A not all of the diagrams shown in Fig. G.124 and Fig. G.125 are present. The realized diagrams for scattering off of

quarks are shown in Fig. G.126. Respectively Fig. G.127 and Fig. G.128 show the process of scattering off of electrons.

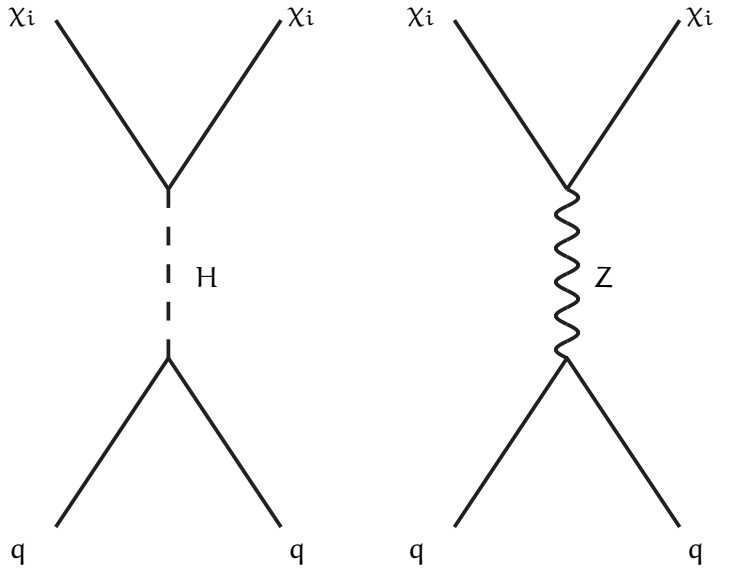

Figure G.126: Diagrams for χ_i and q interactions within T12A.

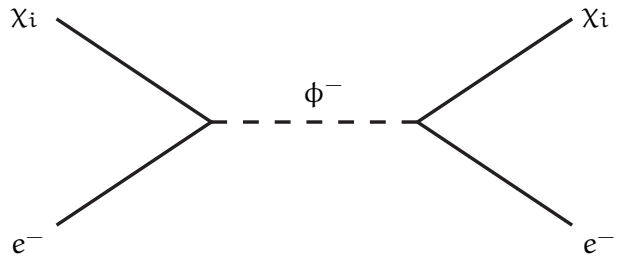

Figure G.127: s-channel diagram for χ_i and e^- scattering within T12A.

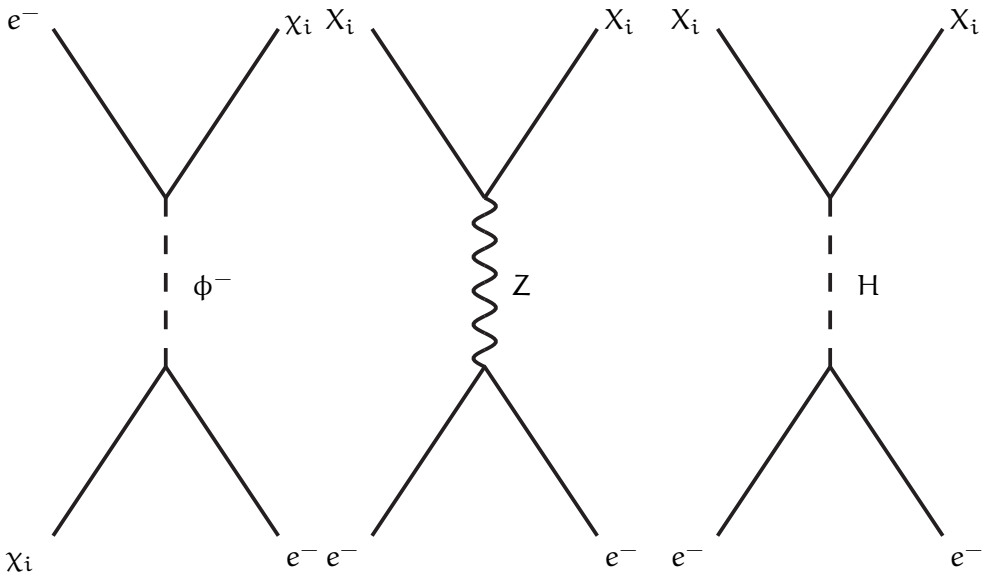

Figure G.128: Diagrams for χ_i and e^- interactions within T12A.

H

DIRECT DETECTION CROSS SECTION

H.1 GENERIC DIRECT DETECTION CROSS SECTION CALCULATION

For scalar dark matter the full set of squared amplitudes obtained following section Section 2.4.2 is

$$
\begin{aligned}
|\overline{M_{S,aa}}|^2 =& g_1 g_1^* \left(g_{2L}\left(2g_{2L}^* m_q^2 + 2g_{2R}^* m_q^2 - g_{2L}^* t\right)\right.\\
&\left.+g_{2R}\left(2g_{2L}^* m_q^2 + 2g_{2R}^* m_q^2 - g_{2R}^* t\right)\right)\\
&\frac{1}{\left(m_S^2 - t\right)^2},\\
|\overline{M_{S,ab}}|^2 =& \frac{g_1}{\left(m_F^2 - s\right)\left(m_S^2 - t\right)}\\
&\left(g_{2L}\left(\right.\right.\\
&g_{3R}^* m_q \left(2g_{4R}^* m_F m_q\right.\\
&\left.+g_{4L}^*\left(-m_{DM}^2 + m_q^2 + s\right)\right)\\
&+g_{3L}^*\left(g_{4R}^* m_q\left(-m_{DM}^2 + m_q^2 + s\right) + g_{4L}^* m_F\left(2m_q^2 - t\right)\right)\\
&+g_{2R}\left(\right.\\
&g_{3L}^* m_q\left(2g_{4L}^* m_F m_q + g_{4R}^*\left(-m_{DM}^2 + m_q^2 + s\right)\right)\\
&\left.\left.+g_{3R}^*\left(g_{4L}^* m_q\left(-m_{DM}^2 + m_q^2 + s\right) + g_{4R}^* m_F\left(2m_q^2 - t\right)\right)\right)\right),\\
|\overline{M_{S,ac}}|^2 =& \frac{g_1 g_5^* m_q}{\left(m_S^2 - t\right)\left(t - m_V^2\right)}\\
&\left(g_{2L}\left(g_{6R}^*\left(m_{DM}^2 - m_q^2 + s + t\right)\right.\right.\\
&\left.+g_{6L}^*\left(-2m_{DM}^2 - 2m_q^2 + 2s + t\right)\right)\\
&+g_{2R}\left(g_{6L}^*\left(m_{DM}^2 - m_q^2 + s + t\right)\right.\\
&\left.\left.+g_{6R}^*\left(-2m_{DM}^2 - 2m_q^2 + 2s + t\right)\right)\right),\\
|\overline{M_{S,bb}}|^2 =& \frac{1}{\left(m_F^2 - s\right)^2}\\
&\left(g_{3R}\left(g_{3L}^* m_q\left(g_{4R} m_F\left(2g_{4L}^* m_F m_q\right.\right.\right.\right.\\
&\left.\left.+g_{4R}^*\left(-m_{DM}^2 + m_q^2 + s\right)\right)\right.\\
&\left.+g_{4L}\left(2g_{4R}^* m_q s\right.\right.\\
&\left.\left.\left.+g_{4L}^* m_F\left(-m_{DM}^2 + m_q^2 + s\right)\right)\right)\right.\\
&+g_{3R}^*\left(g_{4R} m_F\left(g_{4L}^* m_q\left(-m_{DM}^2 + m_q^2 + s\right)\right.\right.\\
&\left.\left.+g_{4R}^* m_F\left(2m_q^2 - t\right)\right)\right.\\
&+g_{4L}\left(g_{4R}^* m_F m_q\left(-m_{DM}^2 + m_q^2 + s\right)\right.\\
&\left.\left.+g_{4L}^*\left(m_{DM}^4 - 2\left(m_q^2 + s\right)m_{DM}^2\right.\right.\right.
\end{aligned}
$$

$$
\begin{aligned}
&+m_q^4+s(s+t)))))\\
&+g_{3L}\,(g_{3R}^*m_q\,(g_{4L}m_F\,(2g_{4R}^*m_Fm_q\\
&+g_{4L}^*\left(-m_{DM}^2+m_q^2+s\right))\\
&+g_{4R}\left(2g_{4L}^*m_qs+g_{4R}^*m_F\left(-m_{DM}^2+m_q^2+s\right)\right))\\
&+g_{3L}^*\left(g_{4L}m_F\left(g_{4R}^*m_q\left(-m_{DM}^2+m_q^2+s\right)\right.\right.\\
&+g_{4L}^*m_F\left(2m_q^2-t\right))\\
&+g_{4R}\left(g_{4L}^*m_Fm_q\left(-m_{DM}^2+m_q^2+s\right)\right.\\
&+\left.\left.g_{4R}^*\left(m_{DM}^4-2\left(m_q^2+s\right)m_{DM}^2\right.\right.\right.\\
&\left.\left.\left.+m_q^4+s(s+t)\right)\right)\right)\right),
\end{aligned}
$$

$$
\begin{aligned}
|\overline{M_{S,bc}}|^2=&-\frac{g_5^*}{2\left(m_F^2-s\right)\left(m_V^2-t\right)}\\
&(g_{3L}\,(\\
&2g_{4L}m_Fm_q\left(g_{6R}^*\left(m_{DM}^2-m_q^2+s+t\right)\right.\\
&\left.+g_{6L}^*\left(-2m_{DM}^2-2m_q^2+2s+t\right)\right)\\
&+g_{4R}\left(4g_{6R}^*\left(m_{DM}^2-m_q^2+s\right)m_q^2\right.\\
&+g_{6L}^*\left(m_{DM}^4-2\left(m_q^2+2s\right)m_{DM}^2\right.\\
&\left.\left.+m_q^4+3s^2-4m_q^2s+4st\right)\right)\\
&+g_{3R}\,(\\
&2g_{4R}m_Fm_q\left(g_{6L}^*\left(m_{DM}^2-m_q^2+s+t\right)\right.\\
&+g_{6R}^*\left(-2m_{DM}^2-2m_q^2+2s+t\right)\right)\\
&+g_{4L}\left(4g_{6L}^*\left(m_{DM}^2-m_q^2+s\right)m_q^2\right.\\
&+g_{6R}^*\left(m_{DM}^4-2\left(m_q^2+2s\right)m_{DM}^2\right.\\
&\left.\left.\left.+m_q^4+3s^2-4m_q^2s+4st\right)\right)\right),
\end{aligned}
$$

$$
\begin{aligned}
|\overline{M_{S,cc}}|^2=&-\frac{g_5g_5^*}{\left(m_V^2-t\right)^2}\\
&\left(g_{6L}\left(2g_{6R}^*\left(t-4m_{DM}^2\right)m_q^2\right.\right.\\
&+g_{6L}^*\left(2m_{DM}^4+\left(8m_q^2-3t\right)m_{DM}^2\right.\\
&\left.\left.-2m_q^4+m_q^2(4s+t)-s(2s+3t)\right)\right)\\
&+g_{6R}\left(2g_{6L}^*\left(t-4m_{DM}^2\right)m_q^2\right.\\
&+g_{6R}^*\left(2m_{DM}^4+\left(8m_q^2-3t\right)m_{DM}^2\right.\\
&\left.\left.\left.-2m_q^4+m_q^2(4s+t)-s(2s+3t)\right)\right)\right).
\end{aligned}
\tag{H.293}
$$

The scalar squared amplitudes are given by

$$
\begin{aligned}
|\overline{M_{S,aa}}|^2=&\left(2g_1^2g_2^2\left(4m_q^2-t\right)\right)\times\frac{1}{\left(m_S^2-t\right)^2},\\
|\overline{M_{S,ab}}|^2=&\left(2g_1g_2g_3g_4\left(-2m_qm_{DM}^2+2m_q\left(m_q^2+s\right)\right.\right.\\
&\left.\left.+\,m_F\left(4m_q^2-t\right)\right)\right)
\end{aligned}
$$

$$
\begin{aligned}
&\times \frac{1}{\left(m_F^2 - s\right)\left(m_S^2 - t\right)}, \\
|\overline{M_{S,ac}}|^2 =& \left(2 g_1 g_2 g_5 g_6 m_q \left(m_{DM}^2 + 3 m_q^2 - 3s - 2t\right)\right) \\
&\times \frac{1}{\left(t - m_S^2\right)\left(t - m_V^2\right)}, \\
|\overline{M_{S,bb}}|^2 =& \left(2 g_3^2 g_4^2 \left(m_{DM}^4 - 2\left(m_q^2 + 2 m_F m_q + s\right) m_{DM}^2\right.\right. \\
&+ m_q^4 + s^2 + 2 m_q^2 s \\
&\left.\left. + 4 m_F m_q \left(m_q^2 + s\right) + m_F^2 \left(4 m_q^2 - t\right) + st\right)\right) \\
&\times \frac{1}{\left(m_F^2 - s\right)^2}, \\
|\overline{M_{S,bc}}|^2 =& -\left(g_3 g_4 g_5 g_6 \left(m_{DM}^4 - 2\left(-m_q^2 + m_F m_q + 2s\right) m_{DM}^2\right.\right. \\
&\left.\left. - 3 m_q^4 + 3 s^2 + 4st + m_F \left(-6 m_q^3 + 6 s m_q + 4 t m_q\right)\right)\right) \\
&\times \frac{1}{\left(m_F^2 - s\right)\left(m_V^2 - t\right)}, \\
|\overline{M_{S,cc}}|^2 =& -\left(2 g_5^2 g_6^2 \left(m_{DM}^2 - m_q^2 + s\right)\left(2 m_{DM}^2 + 2 m_q^2 - 2s - 3t\right)\right) \\
&\times \frac{1}{\left(m_V^2 - t\right)^2}
\end{aligned}
\tag{H.294}
$$

The fermionic amplitudes are way too long to be pleasantly displayed here.

H.2 DIRECT DETECTION CROSS SECTION WITHIN T12A

In T12A spin-independent direct detection processes of dark matter take place via t-channel exchange of Higgs bosons, as shown in Fig. G.120 and Fig. G.126. In principle, there is also a Z mediated process, but under the assumption of small mixing it is not as important. The couplings can be found in Appendix E. They are labeled here as following

$$
\begin{aligned}
&\boxed{1} \propto y_1 U_{F1i} U_{F2i} + y_2 U_{F1i} U_{F3i}, \\
&\boxed{2} \propto \frac{m_q}{v}, \\
&\boxed{3} \propto \frac{1}{2}(\lambda_S v U_{S1i}^2 + v(\lambda_D + \lambda_D')(U_{S2i}^2 + U_{S3i}^2) \\
&\quad + v\lambda_D''(U_{S2i}^2 - U_{S3i}^2)) + A U_{S1i} U_{S2i}.
\end{aligned}
\tag{H.295}
$$

Starting from the Feynman diagrams the amplitudes are

$$
\begin{aligned}
f_1 =& \overline{u}_3 \cdot \boxed{1} \cdot u_1 \cdot \frac{1}{(p_1 - p_3)^2 - m_H^2} \cdot \overline{u}_4 \cdot \boxed{2} \cdot u_2, \\
f_2 =& \boxed{3} \cdot \frac{1}{(p_1 - p_3)^2 - m_H^2} \cdot \overline{u}_4 \cdot \boxed{2} \cdot u_2.
\end{aligned}
\tag{H.296}
$$

Direct detection is calculated with approximately zero momentum-transfer, hence $p_1 = p_3$ and $p_2 = p_4$ and $p_i^2 = m_i^2$ can be used to obtain the squared amplitudes:

$$\begin{aligned}
|\overline{f_1}|^2 =& \frac{\boxed{1}^2\boxed{2}^2}{m_H^2} 16 m_\chi^2 m_q^2, \\
|\overline{f_2}|^2 =& \frac{\boxed{2}^2\boxed{3}^2}{m_H^2} 8 m_q^2.
\end{aligned} \tag{H.297}$$

Which results in the following cross sections with the formula from Appendix D

$$\begin{aligned}
\sigma_{p,\chi}^{SI} =& \boxed{1}^2\boxed{2}^2 \frac{1}{2\pi} \frac{m_\chi^2 m_q^2}{(m_\chi + m_q)^2} f_p^2 \frac{1}{m_H^2}, \\
\sigma_{p,\chi}^{SI} =& \boxed{2}^2\boxed{3}^3 \frac{1}{4\pi} \frac{m_\chi^2 m_q^2}{(m_\chi^2 + m_q^2)^2} f_p^2 \frac{1}{m_H^2}.
\end{aligned} \tag{H.298}$$

I

LOOP FUNCTIONS AND DIAGRAMS FOR LEPTON FLAVOR VIOLATION

I.1 DIMENSIONAL REGULARIZATION

This section is based on [281, 282]. Dimensional regularization is used to modify the four momenta appearing integrals. This technique allows to evaluate certain loop integrals and identify the finite parts and separate them from the divergent ones. This is useful as for example single diagrams for a process might be divergent, but the sum of all diagrams is not, and dimensional regularization allows to perform the integration.
For dimensional regularization a shift from 4 to D dimensions is conducted. A short notation for a D-dimensional integral is

$$\langle ... \rangle_q = \frac{(2\pi\mu)^{4-D}}{i\pi^2} \int d^D q ... \tag{I.299}$$

where μ is an arbitrary scale.
Useful definitions and identities are:

$$\epsilon := \frac{4-D}{2} \tag{I.300}$$

and

$$\Delta = \frac{2}{4-D} - \gamma_E + \log(4\pi), \tag{I.301}$$

$$\text{with} \tag{I.302}$$

$$\gamma_E = -\Gamma'(1) = 0.5772. \tag{I.303}$$

and

$$\Gamma(\epsilon) = \frac{1}{\epsilon} - \gamma_E + \log(4\pi), \tag{I.304}$$

$$(\frac{A_1}{\mu^2})^{-\epsilon} = 1 - \epsilon \log\left(\frac{A_1}{\mu^2}\right) \tag{I.305}$$

where

$$\gamma_E = -\Gamma'(1) \tag{I.306}$$

as well as

$$c_\epsilon := (4\pi)^\epsilon \Gamma(1+\epsilon), \tag{I.307}$$

$$\frac{c_\epsilon}{\epsilon} := \Delta.. \tag{I.308}$$

I.2 TENSOR REDUCTION AND PASSARINO-VELTMAN INTEGRALS

According to [282, 283] loop integrals can be simplified using the tensor reduction. It allows to express all integrals in terms of scalar Passarino-Veltman integrals and momenta. The arguments of the loop functions are suppressed, they are P_i and M_i according to the integral expression in $\langle\rangle_q$ with the ordering $X(P_0, \ldots, P_n, M_0, \ldots, M_n)$ for n denominator terms.

A integral

$$
\begin{aligned}
A_0 =& \left\langle \frac{1}{q^2 - M_0^2 + i\epsilon} \right\rangle_q \\
A^{\delta\nu} =& \left\langle \frac{q^\delta}{q^2 - M_0^2 + i\epsilon} \right\rangle_q \\
=& g^{\delta\nu} A_0
\end{aligned}
$$

B integral

$$
\begin{aligned}
B_0 =& \left\langle \frac{1}{q^2 - M_0^2 + i\epsilon} \frac{1}{(q - P_1)^2 - M_1^2} \right\rangle_q \\
B^\delta =& \left\langle \frac{q^\delta}{q^2 - M_0^2 + i\epsilon} \frac{1}{(q - P_1)^2 - M_1^2 + i\epsilon} \right\rangle_q \\
=& P_1^\delta B_1 \\
B^{\delta\nu} =& \left\langle \frac{q^\delta q^\nu}{q^2 - M_0^2 + i\epsilon} \frac{1}{(q - P_1)^2 - M_1^2 + i\epsilon} \right\rangle_q \\
=& g^{\delta\nu} B_{00} + P_1^\delta P_1^\nu B_{11} \\
B^{\delta\nu\mu} =& \left\langle \frac{q^\delta q^\nu q^\mu}{q^2 - M_0^2 + i\epsilon} \frac{1}{(q - P_1)^2 - M_1^2 + i\epsilon} \right\rangle_q \\
=& P_1^\delta P_1^\nu P_1^\mu B_{111} \\
&+ (g^{\delta\nu} P_1^\mu + g^{\delta\mu} P_1^\nu + g^{\nu\mu} P_1^\delta) B_{001}
\end{aligned}
$$

C integral

$$
\begin{aligned}
C_0 =& \left\langle \frac{1}{q^2 - M_0^2 + i\epsilon} \right. \\
& \left. \frac{1}{(q - P_1)^2 - M_1^2 + i\epsilon} \frac{1}{(q - P_2)^2 - M_2^2 + i\epsilon} \right\rangle_q \\
C^\delta =& \left\langle \frac{q^\delta}{q^2 - M_0^2 + i\epsilon} \right. \\
& \left. \frac{1}{(q - P_1)^2 - M_1^2 + i\epsilon} \frac{1}{(q - P_2)^2 - M_2^2 + i\epsilon} \right\rangle_q \\
=& P_1^\delta C_1 + P_2^\delta C_2
\end{aligned}
$$

$$
\begin{aligned}
C^{\delta\nu} =& \left\langle \frac{q^\delta q^\nu}{q^2 - M_0^2 + i\epsilon} \right. \\
& \left. \frac{1}{(q-P_1)^2 - M_1^2 + i\epsilon} \frac{1}{(q-P_2)^2 - M_2^2 + i\epsilon} \right\rangle_q \\
=& g^{\delta\nu} C_{00} \\
& + P_1^\delta P_1^\nu C_{11} \\
& + (P_1^\delta P_2^\nu + P_2^\delta P_1^\nu) C_{12} \\
& + P_2^\delta P_2^\nu C_{22} \\
C^{\delta\nu\mu} =& \left\langle \frac{q^\delta q^\mu q^\nu}{q^2 - M_0^2 + i\epsilon} \right. \\
& \left. \frac{1}{(q-P_1)^2 - M_1^2 + i\epsilon} \frac{1}{(q-P_2)^2 - M_2^2 + i\epsilon} \right\rangle_q \\
=& (g^{\delta\nu} P_1^\mu + g^{\delta\mu} P_1^\nu + g^{\nu\mu} P_1^\delta) C_{001} \\
& + (g^{\delta\nu} P_2^\mu + g^{\delta\mu} P_2^\nu + g^{\nu\mu} P_2^\delta) C_{002} \\
& + (P_1^\delta P_1^\nu P_2^\mu + P_1^\delta P_2^\nu P_1^\mu + P_2^\delta P_1^\nu P_1^\mu) C_{112} \\
& + (P_1^\delta P_2^\nu P_2^\mu + P_2^\delta P_1^\nu P_2^\mu + P_2^\delta P_2^\nu P_1^\mu) C_{122} \\
& + P_1^\delta P_1^\nu P_1^\mu C_{111} + P_2^\delta P_2^\nu P_2^\mu C_{222}
\end{aligned}
$$

D integral

$$
\begin{aligned}
D_0 =& \left\langle \frac{1}{q^2 - M_0^2 + i\epsilon} \frac{1}{(q-P_1)^2 - M_1^2 + i\epsilon} \right. \\
& \left. \frac{1}{(q-P_2)^2 - M_2^2 + i\epsilon} \frac{1}{(q-P_3)^2 - M_3^2 + i\epsilon} \right\rangle_q \\
D^\delta =& \left\langle \frac{q^\delta}{q^2 - M_0^2 + i\epsilon} \frac{1}{(q-P_1)^2 - M_1^2 + i\epsilon} \right. \\
& \left. \frac{1}{(q-P_2)^2 - M_2^2 + i\epsilon} \frac{1}{(q-P_3)^2 - M_3^2 + i\epsilon} \right\rangle_q \\
=& P_1^\delta D_1 + P_2^\delta D_2 + P_3^\delta D_3 \\
D^{\delta\nu} =& \left\langle \frac{q^\delta q^\nu}{q^2 - M_0^2 + i\epsilon} \frac{1}{(q-P_1)^2 - M_1^2 + i\epsilon} \right. \\
& \left. \frac{1}{(q-P_2)^2 - M_2^2 + i\epsilon} \frac{1}{(q-P_3)^2 - M_3^2 + i\epsilon} \right\rangle_q \\
=& g^{\delta\nu} D_{00} \\
& + P_1^\delta P_1^\nu D_{11} + P_2^\delta P_2^\nu D_{22} \\
& + P_3^\delta P_3^\nu D_{33} \\
& + (P_1^\delta P_2^\nu + P_2^\delta P_1^\nu) D_{12} \\
& + (P_1^\delta P_3^\nu + P_3^\delta P_1^\nu) D_{13} \\
& + (P_2^\delta P_3^\nu + P_3^\delta P_2^\nu) D_{23}
\end{aligned}
$$

$$
\begin{aligned}
D^{\delta\nu\mu} =& \left\langle \frac{q^\delta q^\nu q^\mu}{q^2 - M_0^2 + i\epsilon} \frac{1}{(q-P_1)^2 - M_1^2 + i\epsilon} \right. \\
& \left. \frac{1}{(q-P_2)^2 - M_2^2 + i\epsilon} \frac{1}{(q-P_3)^2 - M_3^2 + i\epsilon} \right\rangle_q \\
=& (g^{\delta\nu} P_1^\mu + g^{\delta\mu} P_1^\nu + g^{\nu\mu} P_1^\delta) D_{001} \\
& + (g^{\delta\nu} P_2^\mu + g^{\delta\mu} P_2^\nu + g^{\nu\mu} P_2^\delta) D_{002} \\
& + (g^{\delta\nu} P_3^\mu + g^{\delta\mu} P_3^\nu + g^{\nu\mu} P_3^\delta) D_{003} \\
& + P_1^\delta P_1^\nu P_1^\mu D_{111} + P_2^\delta P_2^\nu P_2^\mu D_{222} \\
& + P_3^\delta P_3^\nu P_3^\mu D_{333} \\
& + (P_1^\delta P_1^\nu P_2^\mu + P_1^\delta P_2^\nu P_1^\mu + P_2^\delta P_1^\nu P_1^\mu) D_{112} \\
& + (P_1^\delta P_1^\nu P_3^\mu + P_1^\delta P_3^\nu P_1^\mu + P_3^\delta P_1^\nu P_1^\mu) D_{113} \\
& + (P_1^\delta P_2^\nu P_2^\mu + P_2^\delta P_1^\nu P_2^\mu + P_2^\delta P_2^\nu P_1^\mu) D_{122} \\
& + (P_2^\delta P_2^\nu P_3^\mu + P_2^\delta P_3^\nu P_2^\mu + P_3^\delta P_2^\nu P_2^\mu) D_{223} \\
& + (P_1^\delta P_3^\nu P_3^\mu + P_3^\delta P_1^\nu P_3^\mu + P_3^\delta P_3^\nu P_1^\mu) D_{133} \\
& + (P_2^\delta P_3^\nu P_3^\mu + P_3^\delta P_2^\nu P_3^\mu + P_3^\delta P_3^\nu P_2^\mu) D_{233} \\
& + (P_1^\delta P_2^\nu P_3^\mu + P_1^\delta P_3^\nu P_2^\mu + P_2^\delta P_1^\nu P_3^\mu \\
& + P_2^\delta P_3^\nu P_1^\mu + P_3^\delta P_1^\nu P_2^\mu + P_3^\delta P_2^\nu P_1^\mu) D_{123}
\end{aligned}
$$

The coefficients for the reduction can be determined by applying Feynman parametrization. The integrals are calculated in the approximation of heavy masses M_i.

I.3 FEYNMAN PARAMETRIZATION AND GENERIC LOOP INTEGRALS IN D-DIMENSIONS

This section, which is based on [280, 282], explains the use of Feynman parameters. For any fraction with n denominators A_i the relation

$$
\begin{aligned}
\frac{1}{A_1 A_2 ... A_n} =& \int_0^1 dx_1 dx_2 ... dx_n \delta \left(\sum_{i=0}^{n} x_i - 1 \right) \\
& \times \frac{(n-1)!}{(x_1 A_1 + x_2 A_2 + ... + x_n A_n)^n}
\end{aligned}
\tag{I.309}
$$

is true. This is applied to loop integrals in l. Then, the integration over l is performed. All terms with an odd number of l's in the numerator vanish by symmetric integration. For an even number, the generic loop integrals I_n in D dimensions are used

$$
\begin{aligned}
I_n(A) =& \int d^D l \frac{1}{(l^2 - A + i\epsilon)^n} \\
=& i(-1)^n \pi^{D/2} \frac{\Gamma(n - D/2)}{\Gamma(n)} (A - i\epsilon)^{D/2-n},
\end{aligned}
\tag{I.310}
$$

and for any even number k the integrals are

$$\begin{aligned} I_{n,k}^{\mu_1\mu_2\ldots\mu_k}(A) =& \int d^D l \frac{l^{\mu_1} l^{\mu_2} \ldots l^{\mu_k}}{(l^2 - A + i\epsilon)^n} \\ =& T^{\mu_1\mu_2\ldots\mu_k} \frac{\Gamma(D/2)\Gamma(k/2+1/2)}{\Gamma(1/2)\Gamma(k+2+D/2)} \\ & \times \int d^D l \frac{(l^2)^{k/2}}{(l^2 - A + i\epsilon)^n}, \end{aligned} \tag{I.311}$$

at which

$$\begin{aligned} I_n, k(A) =& \int d^D l \frac{(l^2)^{k/2}}{(l^2 - A + i\epsilon)^n} \\ =& i(-1)^{n-k/2} \pi^{D/2} (A - i\epsilon)^{D/2-n+k/2} \\ & \frac{\Gamma(D/2+k/2)\Gamma(n-D/2-k/2)}{\Gamma(D/2)\Gamma(n)}, \end{aligned} \tag{I.312}$$

and

$$T^{\mu_1\mu_2\ldots\mu_k} = \frac{1}{k!}(g^{\mu_1\mu_2} g^{\mu_3\mu_4} \ldots g^{\mu_{k-1}\mu_k} + \text{all permutations}). \tag{I.313}$$

The special case for two Lorentz indices in the numerator is

$$\begin{aligned} \int d^D l \frac{l^\mu l^\nu}{(l^2 - A + i\epsilon)^n} =& i(-1)^{n-1} g^{\mu\nu} \pi^{D/2} \\ & \times (A - i\epsilon)^{D/2-n+1} \frac{\Gamma(n-D/2-1)}{\Gamma(n)}. \end{aligned} \tag{I.314}$$

If the integral converges, one can perform the limit $D \to 4$.

I.4 DEFINITION OF LOOP INTEGRALS AND APPROXIMATION FOR HEAVY MASSES

If the masses of the outgoing particles are much smaller compared to the masses in the loops, one can neglect them in the denominator since

$$P_i^2 \ll M_{loop}^2. \tag{I.315}$$

By means of Feynman-parametrization, which is explained in Section I.3, one can solve the approximated loop integrals to obtain functions, which only depend on the masses of particles in the loop.

B INTEGRAL

The generic B integral is

$$I_{B^i} \propto \int \frac{d^D q}{(2\pi)^D} \mu^{4-D} \frac{N_i}{(q^2 - M_0^2)(q + P_1)^2 - M_1^2)}, \tag{I.316}$$

where N_i is either of

$$\begin{aligned} N_0 &= 1, \\ N_1 &= q^\nu, \\ N_2 &= q^\nu q^\mu, \\ N_3 &= q^\nu q^\mu q^\delta. \end{aligned} \tag{I.317}$$

After applying Feynman parametrization and the approximation Eq. I.315 to the generic B integral Eq. I.316 the result is

$$I_{B^i} = \int_0^1 dx \int \frac{d^D q}{(2\pi)^d} \mu^{4-D} \frac{N_i}{(q^2 - A_B)^2}, \tag{I.318}$$

where

$$A_B = M_0^2 x + M_1^2 (x-1), \tag{I.319}$$

and N_i is one of

$$\begin{aligned} N_0 &= 1, \\ N_1 &= p_1^\mu (x-1), \\ N_2 &= q^\mu q^\nu + p_1^\mu p_1^\nu (x-1)^2 \\ N_3 &= q^\mu q^\nu p_1^\delta (x-1) + \text{cycl.} + p_1^\mu p_1^\nu p_1^\delta (x-1)^3. \end{aligned} \tag{I.320}$$

Here odd numbers of q^α have already been neglected, as they vanish in the dq^D integration. With the use of the definitions in Section I.1 for the divergent parts Δ and the generic integrals over q in Section I.3, this is transformed to

$$\begin{aligned} I_{B^0} &= \frac{i\pi^2}{(2\pi)^4} \left(\Delta - \log\left(\frac{M_0^2}{\mu^2}\right) + F(w) \right), \\ I_{B^1} &= \frac{i\pi^2}{(2\pi)^4} p_1^\mu \left(-\frac{1}{2}\Delta \frac{1}{2} \log\left(\frac{M_0^2}{\mu^2}\right) + G(w) \right), \\ I_{B^2} &= \frac{i\pi^2}{(2\pi)^4} \left(p_1^\mu p_1^\nu \left(\frac{1}{3}\Delta - \frac{1}{3}\log\left(\frac{M_0^2}{\mu^2}\right) + H(w) \right) \right. \\ &\quad + g^{\mu\nu} \left(\frac{1}{2}(M_0^2 + M_1^2)\Delta - \frac{1}{2}(M_0^2 + M_1^2)\log\left(\frac{M_0^2}{\mu^2}\right) \right. \\ &\quad \left. \left. + M_1^2 I(w) \right) \right), \\ I_{B^3} &= \frac{i\pi^2}{(2\pi)^4} \left(p_1^\mu p_1^\nu p_1^\delta \left(-\frac{1}{4}\Delta + \frac{1}{4}\log\left(\frac{M_0^2}{\mu^2}\right) + J(w) \right) \right. \\ &\quad \left. + g^{\mu\nu} p_1^\delta \left(-\frac{1}{2}\Delta - \frac{1}{2}\log\left(\frac{M_0^2}{\mu^2}\right) - G(w) \right) \right), \end{aligned} \tag{I.321}$$

with $w = \frac{M_0^2}{M_1^2}$ and the arbitrary scale μ. The loop functions are

$$F(w) = (-1 + w + \log(w)) \frac{1}{-1+w},$$

$$
\begin{aligned}
G(w) &= \left(-1+4w-3w^2+(-2+4w)\log(w)\right)\frac{1}{4(-1+w)^2},\\
H(w) &= \left(-2+9w-18w^2+11w^3\right.\\
&\quad \left.-6(1-3w+3w^2)\log(w)\right)\frac{1}{18(-1+w)^3},\\
I(w) &= \left(-1+w^2-2\log(w)\right)\frac{1}{4(-1+w)},\\
J(w) &= \left(-3+16w-36w^2+48w^3-25w^4\right.,\\
&\quad \left.+12(-1+4w-6w^2+4w^3)\log(w)\right)\frac{1}{48(-1+w)^4}.
\end{aligned}
\tag{I.322}
$$

C INTEGRAL

The generic C-Integrals are given by

$$
\begin{aligned}
I_{C^i} =& \int \frac{d^D q}{(2\pi)^D}\mu^{4-D}\\
&\frac{N_i}{(q^2-M_0^2)((q+P_1)^2-M_1^2)((q+P_2)^2-M_2^2)},
\end{aligned}
\tag{I.323}
$$

with the same nominators as in Eq. I.317. After utilizing the parametrization and the approximation Eq. I.315 one is left with

$$
I_{C^i} = 2\int dx dy \delta(1-x-y)\int \frac{d^D q}{(2\pi)^D}\mu^{4-D}\frac{N_i}{(l-A_C)^3},
\tag{I.324}
$$

at which

$$
A_C = M_0^2 x + M_1^2 y + M_2^2 z.
\tag{I.325}
$$

The nominators are

$$
\begin{aligned}
N_0 =& 1,\\
N_1 =& -p_1^\mu y - p_2^\mu z,\\
N_2 =& q^\mu q^\nu + (-p_1^\mu y - p_2^\nu z)(-p_1^\nu y - p_2^\nu z),\\
N_3 =& q^\mu q^\nu q^\delta + (-p_1^\mu y - p_2^\nu z)(-p_1^\nu y - p_2^\nu z)(-p_1^\delta y - p_2^\delta z),
\end{aligned}
\tag{I.326}
$$

without the contributions, that vanish in $d^D q$ integrals. In order to simplify the output even more, one can assume that two of the three masses are identical. Hence, there are three cases to be considered

$$
\begin{aligned}
&\text{I}: && M_1 = M_2, w = \frac{M_0^2}{M_2^2},\\
&\text{II}: && M_0 = M_2, w = \frac{M_0^2}{M_1^2},\\
&\text{III}: && M_1 = M_2, w = \frac{M_1^2}{M_0^2}.
\end{aligned}
\tag{I.327}
$$

Case	m
I	M_2
II	M_1
III	M_0

Table I.12: Arguments for C^0 integral.

Case	Co_1	Co_2	m
I	$L(w)$	$M(w)$	M_2
II	$M(w)$	$L(w)$	M_1
III	$L(w)$	$L(w)$	M_0

Table I.13: Arguments and functions for I_{C^1}

For the first integral the result is

$$I_{C^0} = -\frac{i\pi^2}{(2\pi)^4}\frac{1}{m}K(w), \tag{I.328}$$

with

$$K(w) = \frac{1-w+w\log(w)}{(-1+w)^2} \tag{I.329}$$

$$\tag{I.330}$$

and m is given in Tab. I.12. The results for I_{C^1} are

$$I_{C^1} = -\frac{i\pi^2}{(2\pi)^4}\frac{1}{m^2}\left(p_1^\mu Co_1 + p_2^\mu Co_2\right), \tag{I.331}$$

with the scalar functions for the three cases summarized in Tab. I.13 with the functions

$$\begin{aligned} L(w) =& -\frac{3-4w+w^2+2\log(w)}{4(-1+w)^3}, \\ M(w) =& \frac{1-w^2+2\log(w)}{2(-1+w)^3}. \end{aligned} \tag{I.332}$$

In the case of an integral with two indices the outcome is

$$\begin{aligned} I_{C^2} =& \frac{i\pi^2}{(2\pi)^4}\left(g^{\mu\nu}\left(\frac{1}{2}\Delta - \frac{1}{2}\log\left(\frac{M_0^2}{\mu^2}\right) + Co_{00}\right)\right. \\ &\left. + \frac{1}{m}\left(p_1^\mu p_1^\nu Co_{11} + \left(p_1^\mu p_2^\nu + p_2\mu p_1^\nu\right)Co_{12} + p_2^\mu p_2^\nu Co_{22}\right)\right), \end{aligned} \tag{I.333}$$

with the coefficients shown in Tab. I.14 .

Case	Co_{00}	Co_{11}	Co_{22}	Co_{12}	m
I	N(w)	O(w)	P(w)	Q(w)	M_2
II	N(w)	P(w)	O(w)	Q(w)	M_1
III	R(w)	O(w)	O(w)	O(w)	M_0

Table I.14: Overview for I_{C^2}

Case	Co_{001}	Co_{002}	Co_{111}	Co_{112}	Co_{122}	Co_{222}	m
I	S(w)	T(w)	U(w)	V(w)	W(w)	X(w)	M_2
II	T(w)	S(w)	X(w)	W(w)	V(w)	U(w)	M_1
III	Y(w)	Y(w)	U(w)	U(w)	U(w)	U(w)	M_0

Table I.15: Results for I_{C^3}.

The corresponding new functions are

$$\begin{aligned}
N(w) =& \frac{3-4w+w^2+2\log(w)}{4(-1+w)^2},\\
O(w) =& \frac{11-18w+9w^2-2w^3+6\log(w)}{18(-1+w)^4},\\
P(w) =& \frac{-1+6w-3w^2-2w^3+6w^2\log(w)}{6(-1+w)^4},\\
Q(w) =& -\frac{2+3w-6w^2+6\log(w)}{12(-1+w)^4},\\
R(w) =& \frac{3-4w+w^2-2(-2+w)w\log(w)}{4(-1+w)^2}.
\end{aligned} \tag{I.334}$$

The result for I_{C^3} is

$$\begin{aligned}
I_{C^3} =& \frac{i\pi^2}{(2\pi)^4}\Big(g^{\nu\delta}\\
&\left(\left(p_1^\mu+p_2^\mu\right)\left(\frac{1}{6}\left(-\Delta+\log\left(\frac{M_0^2}{\mu^2}\right)\right)\right)+p_1^\mu Co_{001}+p_2^\mu C_{002}\right)\\
&+\text{cycl.}\\
&+\frac{1}{m^2}\left(p_1^\nu p_1^\mu p_1^\delta Co_{111}+\left(p_1^\nu p_1^\mu p_2^\delta+p_1^\nu p_2^\mu p_1^\delta+p_2^\nu p_1^\mu p_1^\delta\right)Co_{112}\right.\\
&\left.+\left(p_1^\nu p_2^\mu p_2^\delta+p_2^\nu p_1^\mu p_2^\delta+p_2^\nu p_2^\mu p_1^\delta\right)Co_{122}+p_2^\nu p_2^\mu p_2^\delta Co_{222}\right)\Big),
\end{aligned} \tag{I.335}$$

with the arguments shown in Tab. I.15. and the functions

$$S(w) = \frac{11-18w+9w^2-2w^3+6\log(w)}{36(-1+w)^3},$$

$$
\begin{aligned}
T(w) =& \frac{5-27w+27w^2-5w^3+(6-18w)\log(w)}{36(-1+w)^3},\\
U(w) =& -\frac{25-48w+36w^2-16w^3+3w^4+12\log(w)}{48(-1+w)^5},\\
V(w) =& \frac{3+10w-18w^2+6w^3-w^4+12w\log(w)}{36(-1+w)^5},\\
W(w) =& -\frac{-1+8w-8w^3+w^4+12w^2\log(w)}{24(-1+w)^5},\\
X(w) =& \frac{1-6w+18w^2-10w^3-3w^4+12w^3\log(w)}{12(-1+w)^5}.
\end{aligned}
\tag{I.336}
$$

D INTEGRAL

The D-type integrals are defined as

$$
\begin{aligned}
I_{D^i} =& \int \frac{d^D q}{(2\pi)^D}\mu^{4-D}\\
&\frac{N_i}{(q^2-M_0^2)((q+P_1)^2-M_1^2)((q+P_2)^2-M_2^2)}\\
&\frac{1}{((q+P_3)^2-M_3^2)},
\end{aligned}
\tag{I.337}
$$

with N_i as in Eq. I.317. After applying the Feynman parameters and using the approximation Eq. I.315, one is left with

$$
\int \Pi_{i=0}^{3} dx_i \delta(1-\sum_{i=0}^{3} x_i) 6 \int \frac{d^D q}{(2\pi)^D}\mu^{4-D}\frac{N_i}{(l^2-A_D)^4},
\tag{I.338}
$$

where

$$
\begin{aligned}
A_D =& M_0^2 x_0 + M_1^2 x_1 + M_2^2 x_2 + M_3^2 x_3,\\
N_0 =& 1,\\
N_1 =& -p_1^\gamma x_1 - p_2^\gamma x_2 - p_3^\gamma x_3,\\
N_2 =& (-p_1^\gamma x_1 - p_2^\gamma x_2 - p_3^\gamma x_3)(-p_1^\mu x_1 - p_2^\mu x_2 - p_3^\mu x_3)\\
N_3 =& (-p_1^\gamma x_1 - p_2^\gamma x_2 - p_3^\gamma x_3)(-p_1^\mu x_1 - p_2^\mu x_2 - p_3^\mu x_3).\\
&(-p_1^\delta x_1 - p_2^\delta x_2 - p_3^\delta x_3).
\end{aligned}
\tag{I.339}
$$

Case	Do_0	m
I	Z(w)	M_2
II	Z(w)	M_1
III	Z(w)	M_1
IV	AA(w)	M_3
V	AA(w)	M_2
VI	AA(w)	M_1
VII	AA(w) · w	M_1

Table I.16: Coefficients for I_{D^0}

Similarly to the C integrals, it is useful to consider some simplifications

$$\begin{aligned}
\text{I} \qquad & M_0 = M_1, M_2 = M_3, w = \frac{M_0^2}{M_2^2}, \\
\text{II} \qquad & M_0 = M_2, M_1 = M_3, w = \frac{M_0^2}{M_1^2}, \\
\text{III} \qquad & M_0 = M_3, M_1 = M_2, w = \frac{M_0^2}{M_1^2}, \\
\text{IV} \qquad & M_0 = M_1 = M_2, w = \frac{M_0^2}{M_3^2}, \\
\text{V} \qquad & M_0 = M_1 = M_3, w = \frac{M_0^2}{M_2^2}, \\
\text{VI} \qquad & M_0 = M_2 = M_3, w = \frac{M_0^2}{M_1^2} \\
\text{VII} \qquad & M_1 = M_2 = M_3, w = \frac{M_0^2}{M_1^2}.
\end{aligned} \tag{I.340}$$

Within these cases

$$I_{D^0} = \frac{i\pi^2}{(2\pi)^4} \frac{1}{m^2} Do_0, \tag{I.341}$$

is the outcome, where the coefficients Do_0 and m are summarized in Tab. I.16. The new functions are

$$\begin{aligned}
Z(w) &= \frac{2 - 2w + (1+w)\log(w)}{(-1+w)^3}, \\
AA(w) &= \frac{-1 + w^2 - 2w\log(w)}{2w(-1+w)^3}.
\end{aligned} \tag{I.342}$$

Case	Do_1	Do_2	Do_3	m
I	BA(w)	CA(w)	CA(w)	M_2
II	CA(w)	BA(w)	CA(w)	M_1
III	CA(w)	CA(w)	BA(w)	M_1
IV	Q(w)/w	Q(w)/w	BA(w)	M_3
V	Q(w)/w	BA(w)	Q(w)/w	M_2
VI	BA(w)	Q(w)/w	Q(w)/w	M_1
VII	P(w)/2	P(w)/2	P(w)/2	M_1

Table I.17: Coefficients for I_{D^1}

.

The integral with one index leads to

$$I_{D^1} = \frac{i\pi^2}{(2\pi)^4}\frac{1}{m^4}\left(p_1^\mu Do_1 + p_2^\mu Do_2 + p_3^\mu Do_3\right), \tag{I.343}$$

where the coefficients are shown in Tab. I.17. The new functions are

$$\begin{aligned} BA(w) =& \frac{5-4w-w^2+(2+4w)\log(w)}{4(-1+w)^4}, \\ CA(w) =& -\frac{1+4w-5w^2+2w(2+w)\log(w)}{4(-1+w)^4}. \end{aligned} \tag{I.344}$$

The integral for two indices is solved as

$$\begin{aligned} I_{D^2} =& \frac{i\pi^2}{(2\pi)^4}\left(\frac{1}{m^2}g^{\mu\nu}Do_{00} + \frac{1}{m^4}\left(p_1^\mu p_1^\nu Do_{11}\right.\right. \\ &+ \left(p_1^\mu p_2^\nu + p_1^\mu p_2^\nu\right)Do_{12} \\ &+ \left(p_1^\mu p_3^\nu + p_3^\mu p_1^\nu\right) + Do_{13}\left(p_2^\mu p_3^\nu + p_3^\mu p_2^\nu\right)Do_{23}\ , \\ &\left.\left.+\ p_2^\mu p_2^\nu Do_{22} + p_3^\mu p_3^\nu Do_{33}\right)\right) \end{aligned} \tag{I.345}$$

at which the option for the different cases are shown in Tab. I.18. The resulting functions are

$$\begin{aligned} DA(w) =& \frac{17-9w-9w^2+w^3+6(1+3w)\log(w)}{18(-1+w)^5}, \\ EA(w) =& \frac{-1+9w+9w^2-17w^3+6w^2(3+w)\log(w)}{18(-1+w)^5}, \\ FA(w) =& \frac{-1-9w+9w^2+w^3-6w(1+w)\log(w)}{12(-1+w)^5}, \\ GA(w) =& \frac{-3-10w+18w^2-6w^3+w^4-12w\log(w)}{36w(-1+w)^5}, \\ HA(w) =& \frac{-1+6w-18w^2+10w^3+3w^4-12w^3\log(w)}{72(-1+w)^6}. \end{aligned} \tag{I.346}$$

Case	Do_{00}	Do_{11}	Do_{12}	Do_{13}
I	M(w)	DA(w)	FA(w)	FA(w)
II	M(w)	EA(w)	FA(w)	EA(w)/2
III	M(w)	EA(w)	EA(w)/2	FA(w)
IV	L(w)	GA(w)	GA(w)/2	DA(w)/2
V	L(w)	GA(w)	DA(w)/2	GA(w)/2
VI	L(w)	2 FA(w)	DA(w)/2	DA(w)/2
VII	IA(w)	HA(w)	HA(w)/2	HA(w)/2)

Case	m	Do_{23}	Do_{22}	Do_{33}
I	M_2	EA(w)/2	EA(w)	EA(w)
II	M_1	FA(w)	DA(w)	EA(w)
III	M_1	FA(w)	EA(w)	DA(w)
IV	M_2	DA(w)/2	GA(w)	2 FA(w)
V	M_2	DA(w)/2	2 FA(w)	GA(w)
VI	M_1	GA(w)/2	GA(w)	GA(w)
VII	M_1	HA(w)/2	HA(w)	HA(w

Table I.18: Coefficients for I_{D^3} in the approximation.

$$IA(w) = \frac{1 - 4w + 3w^2 - 2w^2 \log(w)}{4(-1+w)^3} \tag{I.347}$$

Considering the last D integral, one obtains

$$I_{D^3} = \frac{i\pi^2}{(2\pi)^4}\left(-g^{\mu\nu} I^{\delta}_{D^1} + \text{cycl.} + \frac{1}{m^4}\tilde{I}_{D^3}\right) \tag{I.348}$$

$$\begin{aligned}
\tilde{I}_{D^3} =& p_1^\nu p_1^\mu p_1^\delta Do_{111} \\
&+ (p_1^\nu p_1^\mu p_2^\delta + p_1^\nu p_2^\mu p_1^\delta + p_2^\nu p_1^\mu p_1^\delta)\, Do_{112} \\
&+ (p_1^\nu p_1^\mu p_3^\delta + p_1^\nu p_3^\mu p_1^\delta + p_3^\nu p_1^\mu p_1^\delta)\, Do_{113} \\
&+ (p_1^\nu p_2^\mu p_2^\delta + p_2^\nu p_1^\mu p_2^\delta + p_2^\nu p_2^\mu p_1^\delta)\, Do_{122} \\
&+ (p_1^\nu p_2^\mu p_3^\delta + p_1^\nu p_3^\mu p_2^\delta + p_2^\nu p_1^\mu p_3^\delta \\
&+ p_2^\nu p_3^\mu p_1^\delta + p_3^\nu p_1^\mu p_2^\delta + p_3^\nu p_2^\mu p_1^\delta)\, Do_{123} \\
&+ (p_1^\nu p_3^\mu p_3^\delta + p_3^\nu p_1^\mu p_3^\delta + p_3^\nu p_3^\mu p_1^\delta)\, Do_{133} \\
&+ p_2^\nu p_2^\mu p_2^\delta Do_{222} \\
&+ (p_2^\nu p_2^\mu p_3^\delta + p_2^\nu p_3^\mu p_2^\delta + p_3^\nu p_2^\mu p_2^\delta)\, Do_{223} \\
&+ (p_2^\nu p_2^\mu p_3^\delta + p_3^\nu p_2^\mu p_3^\delta + p_3^\nu p_3^\mu p_2^\delta)\, Do_{233}. \\
&+ p_3^\nu p_3^\mu p_3^\delta Do_{333}.
\end{aligned} \tag{I.349}$$

The Tab. I.19 lists the coefficients for the different cases. The new

Case	Do_{111}	Do_{112}	Do_{113}	Do_{122}	Do_{123}
I	JA(w)	KA(w)	KA(w)	LA(w)	LA(w)/2
II	MA(w)	LA(w)	MA(w)/3	KA(w)	LA(w)/2
III	MA(w)	MA(w)/3	LA(w)	MA(w)/3	LA(w)/2
IV	NA(w)	NA(w)/3	PA(w)	NA(w)/3	PA(w)/2
V	NA(w)	PA(w)	NA(w)/3	KA(w)	PA(w)/2
VI	3 LA(w)	KA(w)	KA(w)	PA(w)	PA(w)/2
VII	QA(w)	QA(w)/3	QA(w)/3	QA(w)/3	QA(w)/6

Case	Do_{133}	Do_{222}	Do_{223}	Do_{233}	Do_{333}	m
I	LA(w)	MA(w)	MA(w)/3	MA(w)/3	MA(w)	M_2
II	MA(w)/3	JA(w)	KA(w)	LA(w)	MA(w)	M_1
III	KA(w)	MA(w)	LA(w)	KA(w)	JA(w)	M_1
IV	KA(w)	NA(w)	PA(w)	KA(w)	3LA(w)	M_3
V	NA(w)/3	3LA(w)	KA(w)	PA(w)	NA(w)	M_2
VI	PA(w)	NA(w)	NA(w)/3	NA(w)/3	NA(w)	M_1
VII	QA(w)/3	QA(w)	QA(w)/3	QA(w)/3	QA(w)	M_1

Table I.19: Overview for I_{D^4}

functions are

$$\begin{aligned}
JA(w) =& -\left(-37+8w+36w^2-8w^3+w^4\right.\\
&\left.-12(1+4w)\log(w)\right)\frac{1}{48(-1+w)^6},\\
KA(w) =& -\left(3+44w-36w^2-12w^3+w^4\right.\\
&\left.+12w(2+3w)\log(w)\right)\frac{1}{72(-1+w)^6},\\
LA(w) =& \left(-1+12w+36w^2-44w^3-3w^4\right.\\
&\left.+12w^2(3+2w)\log(w)\right)\frac{1}{72(-1+w)^6},\\
MA(w) =& -\left(1-8w+36w^2+8w^3-37w^4\right.\\
&\left.+12w^3(4+w)\log(w)\right)\frac{1}{48w^6},\\
NA(w) =& -\left(12+65w-120w^2+60w^3-20w^4\right.\\
&\left.+3w^5+60w\log(w)\right)\frac{1}{240w(-1+w)^6},\\
PA(w) =& -\left(-37+8w+36w^2-8w^3+w^4\right.\\
&\left.-12(1+4w)\log(w)\right)\frac{1}{144(-1+w)^6},
\end{aligned}$$

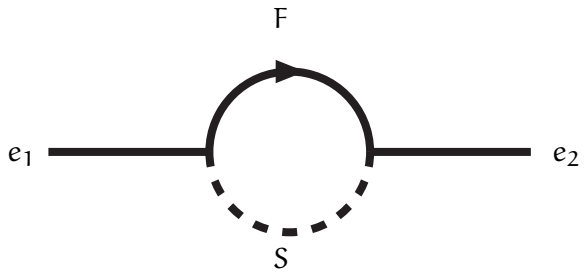

Figure I.129: Loop for I_A.

$$QA(w) = \left(-3 + 20w - 60w^2 + 120w^3 - 65w^4 \right.$$
$$\left. -12w^5 + 60w^4 \log(w)\right) \frac{1}{240\,(-1+w)^6}. \tag{I.350}$$

I.5 LOOP TOPOLOGIES FOR LFV WITHIN T12A AND SIMILAR MODELS

This section contains a general description of loop topologies, that can appear in LFV processes within minimal models, containing additional neutral and charged fermions as well as scalars coupling to the Standard Model lepton doublets. The loops feature fermions F and scalars S, which might be charged and can contribute to processes with neutrinos or charged leptons e_i. The arguments of the loop functions are given as

$$\begin{aligned} B =& B(P_1, M_0, M_1), \\ C =& C(P_1, P_2, M_0, M_1, M_2), \\ D =& D(P_1, P_2, P_3, M_0, M_1, M_2). \end{aligned} \tag{I.351}$$

To obtain the loop functions in the approximation of massless leptons, the functions in Section I.4 are used. The integral I_A in the amplitude described by Fig. I.129 can be expressed as

$$I_A = (\gamma^\delta B^\delta + m_f B^0), \tag{I.352}$$

with the arguments given in Tab. I.20. For further reduction of the

Loop function argument	P_1	M_0	M_1
equivalent	$-p$	m_F	m_S

Table I.20: Arguments for Fig. I.129

tensor integrals see Section I.2. The triangular loop, coming along with emission of photons from charged scalars, shown in Fig. I.130, is reduced to

$$I_B^\nu = 2\gamma^\delta C^{\delta\nu} + \gamma^\delta(-2p^\nu + k^\nu)C^\delta$$

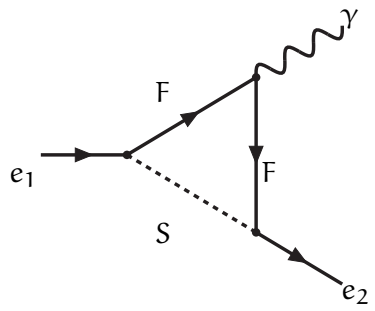

Figure I.130: Diagram for I_B.

$$+ 2m_F C^\nu + m_F(-2p^\nu + k^\nu C^0), \tag{I.353}$$

with the loop function arguments given in Tab. I.21. If the fermion

Loop function argument	P_1	P_2	M_0	M_1	M_2
equivalent	$-p$	$-p+k$	m_F	m_S	m_S

Table I.21: Loop arguments for I_B

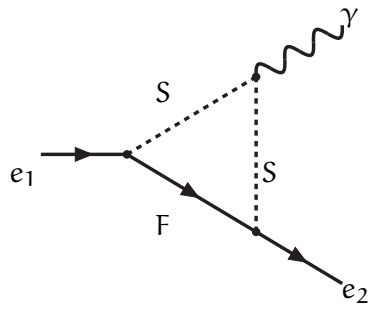

Figure I.131: Topology for integral I_C

line is charged and emits a photon the diagram is shown in Fig. I.131. The structure of the integral is

$$\begin{aligned} I_C^\nu =& \gamma^\delta\gamma^\nu\gamma^\lambda C^{\delta\lambda} + (\gamma^\delta\gamma^\nu m_f - \not{k}\gamma^\nu\gamma^\delta + m_F\gamma^\nu\gamma^\delta)C^\delta \\ &+ (-\not{k}\gamma^\nu m_F + m_f^2\gamma^\nu)C^0, \end{aligned} \tag{I.354}$$

where the arguments are as in Tab. I.22 In the box topology with

Loop function argument	P_1	P_2	M_0	M_1	M_2
equivalent	$-k$	$-p$	m_F	m_F	m_S

Table I.22: Table for I_C

charged scalars as in Fig. I.132, the integral is given by

$$I_D^{\nu\mu} = 4\gamma^\delta D^{\delta\nu\mu} + 4m_F D^{\nu\mu}$$

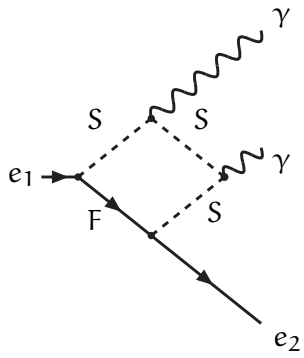

Figure I.132: Diagrams for I_D

$$
\begin{aligned}
&+ 2(-2p^\nu + k^\nu)\gamma^\delta D^{\delta\mu} + 2(-2p^{mu} + 2k_1^\mu + k_2^\mu)D^{\delta\nu} \\
&+ (-2p^\nu + k_1^\nu)(-2p^\mu + 2k_1^\mu + k_2^\mu)\gamma^\delta D^\delta \\
&+ 2m_F(-2p^\mu + 2k_1^\mu + k_2^\mu)D^\nu \\
&+ m_F(-2p^\nu + k_1^\nu)(-2p^\mu + 2k_1^\mu + k_2^\mu)D^0, \qquad \text{(I.355)}
\end{aligned}
$$

with the loop function arguments listed in Tab. I.23. The box with

Loop function argument	P_1	P_2	P_3	M_0	M_1	M_2	M_3
equivalent	$-p$	$-p+k_1$	$-p+k_1+k_2$	m_F	m_S	m_S	m_S

Table I.23: Arguments for loop functions in I_D from Fig. I.132

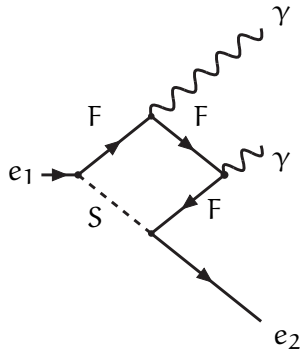

Figure I.133: Diagram for loop integral I_E.

charged fermions leads to

$$
\begin{aligned}
I_E^{\mu\nu} =& \gamma^\alpha\gamma^\mu\gamma^\beta\gamma^\nu\gamma^\delta D^{\alpha\beta\delta} \\
&+ (\gamma^\alpha\gamma^\mu\gamma^\beta\gamma^\nu m_F + \gamma^\alpha\gamma^\mu(-\not{k}_1 + m_F) \\
&+ (-\not{k}_1 + \not{k}_2 + m_F)\gamma^\mu\gamma^\alpha\gamma^\nu\gamma^\beta)D^{\alpha\beta} \\
&+ (\gamma^\alpha\gamma^\mu(-dsk_1 + m_F)\gamma^\nu m_F \\
&+ (-\not{k}_1 - \not{k}_2 + m_F)\gamma^\mu\gamma^\alpha\gamma^\nu m_F \\
&+ (-\not{k}_1 - \not{k}_2 + m_F)\gamma^\mu(-\not{k}_1 + m_F)\gamma^\mu\gamma^\alpha)D^\alpha \\
&+ ((-\not{k}_1 - \not{k}_2 + m_F)\gamma^\nu(-\not{k}_1 + m_F)\gamma^\nu m_F)D^0, \qquad \text{(I.356)}
\end{aligned}
$$

Loop function argument	P_1	P_2	P_3	M_0	M_1	M_2	M_3
equivalent	$-k_1-k_2$	$-k_1$	$-p$	m_F	m_F	m_F	m_S

Table I.24: Loop function arguments for I_E.

where the arguments are as shown in Tab. I.24. There are also loops, which allow for three final state fermions, such as Fig. I.134. One is

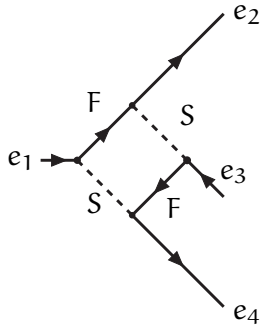

Figure I.134: Diagram with three final state fermions.

shown in Fig. I.134 and the integral is given by

$$\begin{aligned} I_F =& \bar{u}_2 \cdot \boxed{2} \cdot \gamma^\delta \cdot \boxed{1} \cdot u_1 \bar{u}_4 \cdot \boxed{4} \cdot \gamma^\lambda \cdot \boxed{3} \cdot u_3 D^{\delta\lambda} \\ &+ \bar{u}_2 \cdot \boxed{2} \cdot \gamma^\delta \cdot \boxed{1} \cdot u_1 \bar{u}_4 \cdot \boxed{4} \cdot (-\not{p}_2 + \not{p}_3 + m_{F_j}) \cdot \boxed{3} \cdot u_3 D^\delta \\ &+ \bar{u}_2 \cdot \boxed{2} \cdot m_{F_i} \cdot \boxed{1} \cdot u_1 \bar{u}_4 \cdot \boxed{4} \cdot \gamma^\delta \cdot \boxed{3} \cdot u_3 D^\delta \\ &+ \bar{u}_2 \cdot \boxed{2} \cdot m_{F_i} \cdot \boxed{1} \cdot u_1 \bar{u}_4 \cdot \boxed{4} \cdot (-\not{p}_2 - \not{p}_3 + m_{F_j}) \cdot \boxed{3} \cdot u_3 D^0, \end{aligned} \tag{I.357}$$

with the corresponding loop function arguments listed in Tab. I.25. One can also consider coupling to the Higgs instead of the pho-

Loop function argument	P_1	P_2	P_3	M_0
equivalent	$-p_2-p_3$	$-p_1$	$-p_2$	m_{F_i}

Loop function argument	M_1	M_2	M_3
equivalent	m_{F_j}	m_{S_m}	m_{S_n}

Table I.25: Argument set for I_F.

ton, which can lead to the triangle diagrams shown in Fig. I.135 and Fig. I.136. The corresponding loop integrals are for Fig. I.135

$$I_G = ((-\not{k} + m_F)\gamma^\delta + \gamma^\delta m_F) C^\delta + (-\not{k} + m_F) m_F C^0, \tag{I.358}$$

with the arguments as in Tab. I.26. and for Fig. I.136

$$I_H = \gamma^\delta C^\delta + m_F C^0, \tag{I.359}$$

where the arguments are given in Tab. I.26.

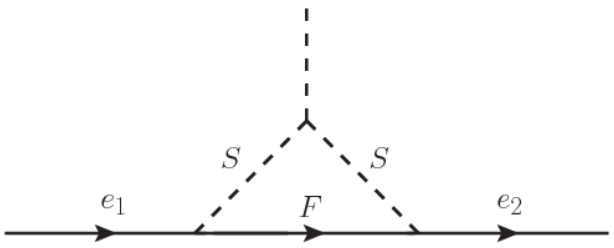

Figure I.135: Loop with Higgs.

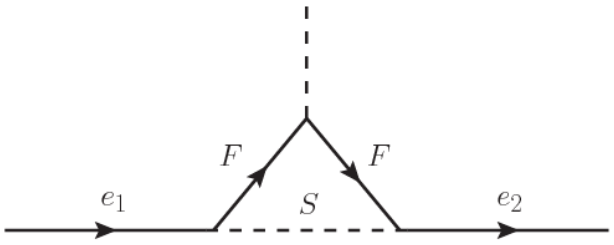

Figure I.136: Loop with Higgs.

Loop function argument	P_1	P_2	M_0	M_1	M_2
equivalent	$-k$	$-p$	m_F	m_F	m_S

Table I.26: Arguments for I_G.

Loop function argument	P_1	P_2	M_0	M_1	M_2
equivalent	$-p$	$-p+k$	m_F	m_S	m_S

Table I.27: Loop function arguments for Fig. I.136.

I.6 $e_1 \to e_2\gamma$ IN T12A AND SIMILAR MODELS

This section contains a short overview for the lepton flavor violating process of $e_1 \to e_2\gamma$ for example $\mu \to e\gamma$. In a generic way the couplings between a scalar and two fermions can be described by

$$\boxed{i} = g_{iL}P_L + g_{iR}P_R \tag{I.360}$$

see Appendix E. The coupling constant with photons is represented by $\boxed{o}$ in the following. The process $e_1 \to e_2\gamma$ within models like T12A can feature diagrams shown in Fig. I.137.The incoming lepton

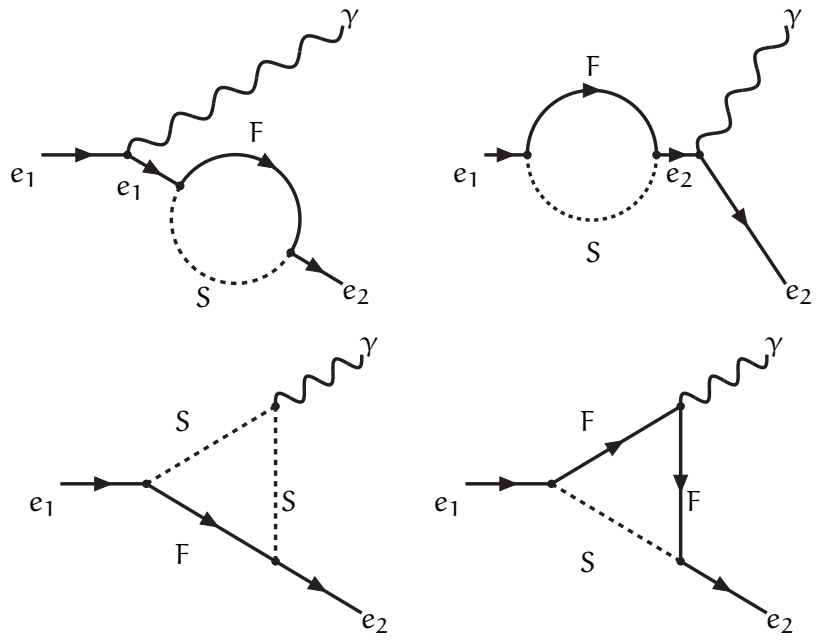

Figure I.137: Diagrams for $\mu \to e\gamma$.

Table I.28: Arguments for $e_1 \to e_2\gamma$

. The loop integrals can be found in Section I.4.

Function arguments	P_1	P_2	M_0	M_1	M_2
In F_1	$-p_2$	-	$m_F(m_{\psi_D^-})$	$m_{\phi_D^-}(m_S)$	-
In F_2	$-p_1$	-	$m_F(m_{\psi_D^-})$	$m_{\phi_D^-}(m_S)$	-
InF_3	$-p_1$	$-p_2$	m_F	$m_{\phi_D^-}$	$m_{\phi_D^-}$
In F_4	$-k$	$-p_1$	$m_{\psi_D^-}$	$m_{\psi_D^-}$	m_S

has momentum p_1, the outgoing p_2 and the photon k. In the loop q runs across the fermion line. The corresponding amplitudes are

$$\begin{aligned}
F_1 =& \epsilon^*_{1\nu}\bar{u}_2 \cdot \boxed{2} \cdot I_A \cdot \boxed{1} \cdot \frac{\not{p}_2 + m_1^2}{p_2^2 - m_1^2} \cdot \boxed{0} \cdot \gamma^\nu u_1 \\
F_2 =& \epsilon^*_{1\nu}\bar{u}_2 \cdot \boxed{0} \cdot \gamma^\nu \frac{\not{p}_1 + m_2}{p_1^2 - m_2^2} \cdot \boxed{2} \cdot I_A \cdot \boxed{1} \cdot u_1 \\
F_3 =& \epsilon^*_{1\nu}\bar{u}_2 \cdot \boxed{2} \cdot I_B^\nu \cdot \boxed{1} \cdot \boxed{0} \cdot u_1 \\
F_4 =& \epsilon^*_{1\nu}\bar{u}_2 \cdot \boxed{2} \cdot I_C^\nu \cdot \boxed{1} \cdot \boxed{0} \cdot u_1
\end{aligned} \tag{I.361}$$

where the arguments for the loop functions are summarized in Tab. I.28, The $-$ indicates when a charged particle runs in the loop,since there are several combinations. ϕ_D^- is a charged scalar and ψ_D^- a charged fermion. Kinematics and on-shell conditions fix

$$\begin{aligned}
p_1 &= p_2 + k_1 \\
p_1^2 &= m_1^2 \\
p_2^2 &= m_2^2
\end{aligned}$$

Table I.29: Arguments for loop functions in $e_1 \to e_2\gamma\gamma$

Function arguments	P_1	P_2	P_3
In F_1	$-p_2$	-	-
In F_2	$-p_1+k_1$	-	-
In F_3	$-p_1$	-	-
In F_4	$-p_1+k_1$	$-p_2$	-
In F_5	$-p_1$	$-p_1+k_1$	-
In F_6	$-k_2$	$-p_1+k_1$	-
In F_7	$-k_1$	$-p_1$	-
In F_8	$-p_1$	$-p_1+k_1$	$-p_2$
In F_9	$-k_1-k_2$	$-k_1$	$-p_1$

Function arguments	M_0	M_1	M_2	M_3
In F_1	$m_F(m_{\psi_D^-})$	$m_{\phi_D^-}(m_S)$	-	-
In F_2	$m_F(m_{\psi_D^-})$	$m_{\phi_D^-}(m_S)$	-	-
In F_3	$m_F(m_{\psi_D^-})$	$m_{\phi_D^-}(m_S)$	-	-
In F_4	m_F	$m_{\phi_D^-}$	$m_{\phi_D^-}$	-
In F_5	m_F	$m_{\phi_D^-}$	$m_{\phi_D^-}$	-
In F_6	$m_{\psi_D^-}$	$m_{\psi_D^-}$	m_S	-
In F_7	$m_{\psi_D^-}$	$m_{\psi_D^-}$	m_S	-
In F_8	m_F	$m_{\phi_D^-}$	$m_{\phi_D^-}$	$m_{\phi_D^-}$
In F_9	$m_{\psi_D^-}$	$m_{\psi_D^-}$	$m_{\psi_D^-}$	m_S

$$\begin{aligned} k_1^2 &= 0 \\ p_1p_2 &= \frac{m_1^2+m_2^2}{2} \\ p_1k_1 &= \frac{m_1^2-m_2^2}{2} \\ p_2k_1 &= \frac{m_1^2-m_2^2}{2}. \end{aligned} \tag{I.362}$$

see Appendix B. When calculating an actual branching ratio one has to consider possible summation over internal fermions and scalars. Depending on the model not all vertices may be present and thus reduce the number of corresponding diagrams.

I.7 PROCESS $e_1 \to e_2\gamma\gamma$

Considering lepton flavor violation, the process $e_1 \to e_2\gamma\gamma$ plays a role. The amplitudes for this process are shown in Fig. I.138. The leptons e_i have four-momentum p_i and the photons k_i. Any coupling

to the photon is labeled $\boxed{0}$, couplings between F, S and e_i is given as $\boxed{i}$. An overview on generic couplings is found in Appendix E. The amplitudes corresponding to the diagrams are

$$\begin{aligned}
F_1 =& \epsilon^*_{1\nu}\epsilon^*_{2\mu}\bar{u}_2 \cdot \boxed{2}\cdot I_A \cdot \boxed{1}\cdot \frac{\not{p}_2 + m_1}{p_2^2 - m_1^2}\cdot \boxed{0}\cdot \gamma^\mu \\
& \cdot \frac{\not{p}_1 - \not{k}_1 + m_1}{(p_1-k_1)^2 - m_1^2} \cdot \boxed{0}\cdot \gamma^\nu u_1, \\
F_2 =& \epsilon^*_{1\nu}\epsilon^*_{2\mu}\bar{u}_2\gamma^\mu \cdot \boxed{0}\cdot \frac{\not{p}_1 - \not{k}_1 + m_2}{(p_1-k_1)^2 - m_2^2}\cdot \boxed{2}\cdot I_A \\
& \cdot \boxed{1}\cdot \frac{\not{p}_1 - \not{k}_1 + m_1}{(p_1-k_1)^2 - m_1^2}\gamma^\nu \cdot \boxed{0}\cdot u_1, \\
F_3 =& \epsilon^*_{1\nu}\epsilon^*_{2\mu}\bar{u}_2\gamma^\mu \cdot \boxed{0}\cdot \frac{\not{p}_1 - ds k_1 + m_2}{(p_1-k_1)^2 - m_2^2}\cdot \gamma^\nu \\
& \cdot \boxed{0}\cdot \frac{\not{p}_1 - m_2}{p_1^2 - m_2^2} \cdot \boxed{2}\cdot I_A \cdot \boxed{1}\cdot u_1, \\
F_4 =& \epsilon^*_{1\nu}\epsilon^*_{2\mu}\bar{u}_2 \cdot \boxed{2}\cdot I_B \cdot \boxed{0}\cdot \boxed{1}\cdot \frac{\not{p}_1 - \not{k}_1 + m_1}{(p_1-k_1)^2 - m_1^2}\cdot \gamma^\nu \cdot \boxed{0}\cdot u_1, \\
F_5 =& \epsilon^*_{1\nu}\epsilon^*_{2\mu}\bar{u}_2\gamma^\mu \cdot \boxed{0}\cdot \frac{\not{p}_1 - \not{k}_1 + m_2}{(p_1-k_1)^2 - m_2^2}\cdot \boxed{2}\cdot I_B \cdot \boxed{0}\cdot \boxed{1}\cdot u_1, \\
F_6 =& \epsilon^*_{1\nu}\epsilon^*_{2\mu}\bar{u}_2 \cdot \boxed{2}\cdot I_C \cdot \boxed{0}\cdot \boxed{1}\cdot \frac{\not{p}_1 - \not{k}_1 + m_1}{(p_1-k_1)^2 - m_1^2}\cdot \gamma^\nu \cdot \boxed{0}\cdot u_1, \\
F_7 =& \epsilon^*_{1\nu}\epsilon^*_{2\mu}\bar{u}_2\gamma^\mu \cdot \boxed{0}\cdot \frac{\not{p}_1 - \not{k}_1 + m_2}{(p_1-k_1)^2 - m_2^2}\cdot \boxed{2}\cdot I_C \cdot \boxed{0}\cdot \boxed{1}\cdot u_1, \\
F_8 =& \epsilon^*_{1\nu}\epsilon^*_{2\mu}\bar{u}_2 \cdot \boxed{2}\cdot I_D \cdot \boxed{0}\cdot \boxed{0}\cdot \boxed{2}\cdot u_1, \\
F_9 =& \epsilon^*_{1\nu}\epsilon^*_{2\mu}\bar{u}_2 \cdot \boxed{2}\cdot I_E \cdot \boxed{0}\cdot \boxed{0}\cdot \boxed{2}\cdot u_1,
\end{aligned} \tag{I.363}$$

with the arguments listed in Tab. I.29. General expressions and solutions for the loop integrals are listed in Section I.4. Kinematics and on-shell conditions allow to reduce the expression, so that they only depend on two independent scalar products p_1k_1 and p_1k_2 and all other scalar products can be expressed depending on them – compare Appendix B.

$$\begin{aligned}
p_1^2 =& m_1^2, \\
p_2^2 =& m_2^2, \\
k_1^2 =& 0, \\
k_2^2 =& 0, \\
p_1p_2 =& m_1^2 - p_1k_1 - p_2k_2, \\
k_1k_2 =& \frac{m_1^2 + m_2^2 - 2p_1p_2}{2}, \\
p_2k_1 =& p_1k_1 - k_1k_2, \\
p_2k_2 =& p_1k_2 - k_1k_2.
\end{aligned} \tag{I.364}$$

Table I.30: Arguments for the loop integrals

Function arguments	P_1	P_2	P_3	M_0
in F_1	$-p_4$	-	-	$m_F(m_{\psi_D^-})$
in F_3	$-p_1$	-	-	$m_F(m_{\psi_D^-})$
in F_5	$-p_1+p_4$	$-p_1$	-	$m_{\psi_D^-}$
in F_7	$-p_1$	$-p_4$	-	m_F
in F_8	$-p_1$	$-p_4$	-	$m_F(m_{\psi_D^-})$
in F_9	$-p_3-p_4$	$-p_1$	$-p_4$ -	$m_F(m_{\psi_D^-}))$
s in F_{10}	$-p_3-p_4$	$-p_1$	$-p_3$ -	$m_F(m_{\psi_D^-})$

Function arguments	M_1	M_2	M_3
in F_1	$m_{\phi_D^-}(m_S)$	-	-
in F_3	$m_{\phi_D^-}(m_S)$	-	-
in F_5	$m_{\psi_D^-}$	m_S	-
in F_7	$m_{\phi_D^-}$	$m_{\phi_D^-}$	-
in F_8	$m_{\phi_D^-}(m_S)$	$m_{\phi_D^-}(m_S)$	-
in F_9	$m_F(m_{\psi_D^-})$	$m_{\phi_D^-}(m_{X_m})$	$m_{\phi_D^-}(m_{X_n})$
s in F_{10}	$m_F(m_{\psi_D^-})$	$m_{\phi_D^-}(m_{X_m})$	$m_{\phi_D^-}(m_{X_n})$

I.8 PROCESS: $e_1 \to e_2 e_2 e_3$

Fig. I.139 shows all diagrams for the process $e_1 \to e_2 e_3 e_4$. All loops from the process $e_1 \to e_2\gamma$ appear in addition to new box topologies. Only for box diagrams e_2 and e_3 do not have to be from the same lepton family. In all other diagrams, they are created as lepton anti-lepton pairs. In principle, there could also be processes with Higgs or Z bosons, but they are not as important, especially for very small lepton masses. The leptons e_i have momentum p_i. The coupling to photons is labeled $\boxed{0}$, the vertex between e_i, F and S is $\boxed{i}$. Generic expressions for the vertices are found in Appendix E. The corresponding amplitudes for Fig. I.139 are

$$\begin{aligned}
F_1 =& \bar{u}_4 \cdot \boxed{2} \cdot I_A \cdot \boxed{1} \cdot \frac{\not{p}_4 + m_1}{p_4^2 - m_1^2} \cdot \gamma^\mu \cdot \boxed{0} \cdot u_1 \bar{u}_3 \gamma^\nu \\
& \cdot \boxed{0} \cdot \frac{g^{\mu\nu}}{(p_1 - p_4)^2} u_2, \\
F_3 =& \bar{u}_4 \cdot \gamma^\mu \cdot \boxed{0} \cdot \frac{\not{p}_1 + m_3}{p_1^2 - m_3^3} \cdot \boxed{2} \cdot I_A \cdot \boxed{1} \cdot u_1 \bar{u}_3 \gamma^\nu \\
& \cdot \boxed{0} \cdot \frac{g^{\mu\nu}}{(p1 - p4)^2} u_2, \\
F_5 =& \bar{u}_4 \cdot \boxed{2} \cdot I_C^\mu \cdot \boxed{0} \cdot \boxed{1} \cdot u_1 \bar{u}_3 \cdot \gamma^\nu \cdot \boxed{0} \cdot \frac{g^{\mu\nu}}{(p1 - p4)^2} u_2,
\end{aligned}$$

$$
\begin{aligned}
F_7 =& \overline{u}_4 \cdot \boxed{2} \cdot I_B^{\mu} \cdot \ \boxed{0} \cdot \ \boxed{1} \cdot u_1 \overline{u}_3 \cdot \gamma^{\nu} \cdot \boxed{0} \cdot \frac{g^{\mu\nu}}{(p1-p4)^2} u_2, \\
F_8 =& \overline{u}_4 \cdot \boxed{2} \cdot I_H \cdot \ \boxed{9} \cdot \ \boxed{1} \cdot u_1 \overline{u}_3 \cdot \boxed{6} \cdot \frac{g^{\mu\nu}}{(p1-p4)^2} u_2, \\
F_9 =& \overline{u}_4 \cdot \boxed{2} \cdot \gamma^{\delta} \ \cdot \ \boxed{1} \cdot u_1 \overline{u}_3 \cdot \boxed{4} \cdot \gamma^{\lambda} \cdot \boxed{3} \cdot u_2 C^{\delta\lambda} \\
& + \overline{u}_4 \cdot \boxed{2} \cdot \gamma^{\delta} \ \cdot \ \boxed{1} \cdot u_1 \\
& \overline{u_3} \cdot \boxed{4} \cdot (-\not{p}_3 - \not{p}_4 + m_{F_j}) \cdot \boxed{3} \cdot u_2 C^{\delta} \\
& + \overline{u}_4 \cdot \boxed{2} \cdot m_{F_i} \cdot \boxed{1} \cdot u_1 \\
& \overline{u_3} \cdot \boxed{4} \cdot \gamma^{\delta} \cdot \boxed{3} \cdot u_2 C^{\delta} \\
& + \overline{u}_4 \cdot \boxed{2} \cdot m_{F_i} \cdot \boxed{1} \cdot u_1 \\
& \overline{u_3} \cdot \boxed{4} \cdot (-\not{p}_3 - \not{p}_4 + m_{F_j}) \cdot \boxed{3} \cdot u_2 C^{0}, \\
F_{10} =& \overline{u}_3 \cdot \boxed{2} \cdot \gamma^{\delta} \ \cdot \boxed{1} \cdot u_1 \\
& \overline{u_4} \cdot \boxed{4} \cdot \gamma^{\lambda} \cdot \boxed{3} \cdot u_2 C^{\delta\lambda} \\
& + \overline{u}_3 \cdot \boxed{2} \cdot \gamma^{\delta} \ \cdot \boxed{1} \cdot u_1 \\
& \overline{u_4} \cdot \boxed{4} \cdot (-\not{p}_3 - \not{p}_4 + m_{F_j}) \cdot \boxed{3} \cdot u_2 C^{\delta} \\
& + \overline{u}_3 \cdot \boxed{2} \cdot m_{F_i} \cdot \boxed{1} \cdot u_1 \\
& \overline{u_4} \cdot \boxed{4} \cdot (-\not{p}_3 - \not{p}_4 + m_{F_j}) \cdot \boxed{3} \cdot u_2 C^{\delta} \\
& + \overline{u}_3 \cdot \boxed{2} \cdot m_{F_i} \cdot \boxed{1} \cdot u_1 \\
& \overline{u_4} \cdot \boxed{4} \cdot (-\not{p}_3 - \not{p}_4 + m_{F_j}) \cdot \boxed{3} \cdot u_2 C^{0}. \qquad \text{(I.365)}
\end{aligned}
$$

The loop integrals can be found in Appendix B, their arguments are listed in Tab. I.30.

I.9 $\mu \to e\gamma$ EXAMPLE CALCULATION IN THE SCOTOGENIC MODEL

In the scotogenic model, as presented in Section 5.1.3, the loop integrals from Eq. 5.96, Eq. 5.97 and Eq. 5.98 are:

$$
\begin{aligned}
M_a =& \frac{-e y_{ie}^* y_{i\mu}}{2} \epsilon_{\nu}^* \overline{u}(p_e) P_r \gamma_{\delta} I_a^{\delta} \frac{\not{p}_e + m_{\mu}}{-m_{\mu}^2} u(p_{\mu}), \\
M_b =& \frac{-e y_{ie}^* y_{i\mu}}{2} \epsilon_{\nu}^* \overline{u}(p_e) P_r \gamma^{\nu} \frac{\not{p}_{\mu}}{m_{\mu}^2} \gamma_{\delta} I_b^{\delta} u(p_{\mu}), \\
M_c =& \frac{-e y_{ie}^* y_{i\mu}}{2} \epsilon_{\nu}^* \overline{u}(p_e) P_r \gamma_{\delta} I_c^{\delta\nu} u(p_{\mu}), \qquad \text{(I.366)}
\end{aligned}
$$

where

$$
\begin{aligned}
I_a^{\delta} =& \int \frac{q^{\delta}}{(q^2 - M_i^2)((q-p_e)^2 - m_{\eta^+}^2)} \frac{d^4 q}{(2\pi)^4}, \\
I_b^{\delta} =& \int \frac{q^{\delta}}{(q^2 - M_i^2)((q-p_{\mu})^2 - m_{\eta^+}^2)} \frac{d^4 q}{(2\pi)^4}, \\
I_c^{\delta\nu} =& \int \frac{q^{\delta}(2q^{\nu} - 2p_e^{\nu})}{(q^2 - M_i^2)((q-p_e)^2 - m_{\eta^+}^2)((q-p_{\mu})^2 - m_{\eta^+}^2)}
\end{aligned}
$$

$$\frac{d^4 q}{(2\pi)^4}. \tag{I.367}$$

The denominators after the parametrization are

$$\begin{aligned} D_a =& x(q^2 - M_i^2) + (1-x)((q-p_e)^2 - m_{\eta^+}^2), \\ D_b =& x(q^2 - M_i^2) + (1-x)((q-p_\mu)^2 - m_{\eta^+}^2), \\ D_c =& x(q^2 - M_i^2) + y((q-p_e)^2 - m_{\eta^+}^2) \\ &+ z((q-p_\mu)^2 - m_{\eta^+}^2) \end{aligned} \tag{I.368}$$

where $x + y + z = 1$. As the particles in the loop are heavy compared to muons and electrons, the masses of electron and muon become negligible. Thus, the denominators read as

$$\begin{aligned} D_a =& q^2 + 2qp_e(x-1) - m_{\eta^+}^2(1-x) - M_i^2 x, \\ D_b =& q^2 + 2qp_\mu(x-1) - m_{\eta^+}^2(1-x) - M_i^2 x, \\ D_c =& q^2 + 2q(-p_e y - p_\mu z) - m_{\eta^+}^2(y+z) - M_i^2 x. \end{aligned} \tag{I.369}$$

In order to complete the squares in each denominator, q is shifted appropriately

$$\begin{aligned} a:&\ q \to l = q + p_e(x-1), \\ b:&\ q \to l = q + p_\mu(x-1), \\ a:&\ q \to l = q - p_e y - p_\mu z. \end{aligned} \tag{I.370}$$

Hence, the denominators simplify to

$$D_a = D_b = D_c = l^2 - A_1, \tag{I.371}$$

with

$$A_1 = m_{\eta^+}^2(1-x) + M_i^2 x. \tag{I.372}$$

The numerators of the integrals have to be shifted as well, according to Eq. I.370.

$$\begin{aligned} N_a =& l^\delta, \\ N_b =& l^\delta + p_\mu^\delta(x-1), \\ N_c =& 2(l^\delta + p_\mu^\delta z)(l^\nu + p_e^\nu(1-y) + p_\mu^\nu z) \end{aligned} \tag{I.373}$$

where all terms with p_e^δ were omitted, as the electron mass is zero and therefore $\overline{u}(pe)\not{p}_6 = 0$. The loop integrals are evaluated with use of the generic integrals given in Section I.3. If the integral is finite, one can perform the limit $D \to 4$.
One is left with the integrals

$$I_a^\delta = \int_0^1 dx \int \frac{\mu^{4-D}}{(2\pi)^D} \frac{N_a}{(l^2 - A_1)^2} d^D l,$$

$$
\begin{aligned}
I_b^\delta &= \int_0^1 dx \int \frac{\mu^{4-D}}{(2\pi)^D} \frac{N_b}{(l^2 - A_1)^2} d^D l, \\
I_c \delta, \nu &= \int_0^1 dx dy dz \delta(x+y+z-1) \int \frac{\mu^{4-D}}{(2\pi)^D} \frac{N_c}{(l^2 - A_1)^3} d^D l.
\end{aligned}
\tag{I.374}
$$

I_a^δ is zero by means of symmetry, as all of these integrals with an odd number off l's in the numerator vanish. I_b^δ does not converge, so the limit of D to 4 can not be taken. $I_c^{\delta\nu}$ consists of one finite part $I_{c,conv}^{\delta\nu}$ and one part $I_{c,div}^{\delta\nu}$ where the limit can not be taken directly. For this part, the integration over z and y is already performed, as A_1 depends on x only. The integrals are

$$
\begin{aligned}
I_a^\delta &= 0, \\
I_b^\delta &= \int_0^1 dx \frac{\mu^{4-D}}{(2\pi)^D} i\pi^{D/2} \Gamma(2 - D/2) A_1^{D/2-2} p_\mu^\delta (1-x), \\
I_{c,div}^{\delta\nu} &= \int_0^1 dx \frac{\mu^{4-D}}{(2\pi)^D} ((-i) g^{\nu\delta} \pi^{D/2} A_1^{D/2-2} \Gamma(2 - D/2)(1-x), \\
I_{c,conv}^{\delta\nu} &= \int_0^1 dx dy dz \delta(x+y+z-1) \\
&\quad \frac{-i\pi^2}{(2\pi)^4} \frac{(p_e^\nu (1-y) + p_\mu^\nu z) p_\mu^\delta z}{A_1}.
\end{aligned}
\tag{I.375}
$$

With the definition of ϵ and Δ for the divergences as in Section I.1 the integrals simplify to

$$
\begin{aligned}
I_b^\delta &= \frac{i\pi^2}{(2\pi)^4} \pi^{-2\epsilon} p_\mu^\delta I_{div}, \\
I_c^{\delta\nu} &= \frac{-i\pi^2}{(2\pi)^4} \pi^{-2\epsilon} I_{div},
\end{aligned}
\tag{I.376}
$$

at which

$$
I_{div} := \int_0^1 dx (1-x)(\Delta - \Gamma(1+\epsilon) \log(\frac{A_1}{\mu^2})).
\tag{I.377}
$$

Introducing the simplified form of the divergent integrals Eq. I.376 to the amplitudes Eq. 5.97 and Eq. 5.98 results in

$$
\begin{aligned}
M_b &= K I_{div} \epsilon_\nu^* \bar{u}(p_e) P_R \gamma^\nu \frac{\not{p}_\mu}{m_{mu}^2} \not{p}_\mu u(p_\mu), \\
M_{c,div} &= K I_{div} \epsilon_\nu^* \bar{u}(p_e) P_R \gamma^\nu \frac{\not{p}_\mu}{m_{mu}^2} \not{p}_\mu u(p_\mu),
\end{aligned}
\tag{I.378}
$$

with the abbreviation

$$
K := \frac{-e y_{ie}^* y_{i\mu}}{2} \frac{i\pi^2}{(2\pi)^4} \pi^{-2\epsilon}.
\tag{I.379}
$$

As $\not{p}_\mu \not{p}_\mu = m_\mu^2$, both divergent parts cancel and one is left with the further evaluation of $I^{\delta\nu}_{c,conj}$ in Eq. I.375. The integration over x, y and z can be performed directly. If one uses

$$\zeta_i := \frac{M_i^2}{m_{\eta^+}^2} \tag{I.380}$$

and

$$p_e \nu = p_\mu^\nu, \tag{I.381}$$

as the kinematics give

$$p_\mu^\nu = p_e^\nu + k^\nu, \tag{I.382}$$

and the k^ν term does not give any contribution, when contracted with ϵ_ν^*, the outcome is

$$I^{\delta\nu}_{c,conv} = \frac{i\pi^2}{(2\pi)^4} \frac{1}{m_{\eta^+}^2} F_2(\zeta_i) p_\mu^\delta p\mu^\nu, \tag{I.383}$$

with the loop function F_2 defined as

$$F_2(x) := \frac{1 - 6x + 3x^2 + 2x^3 - 6x^2 \log x}{6(1-x)^4}. \tag{I.384}$$

Hence, the amplitude Eq. 5.98 is, after using $\not{p}_\mu u(p_\mu) = m_\mu u(p_\mu)$,

$$M_c = iK_2 \epsilon_\nu^* \overline{u}(p_e) P_R p_\mu^\nu u(p_\mu), \tag{I.385}$$

with

$$K_2 = \frac{-\pi^2 e y_{ie}^* y_{i\mu}}{2(2\pi)^4 m_\mu m_{\eta^+}^2} F_2(\zeta_i). \tag{I.386}$$

I.10 LOOPS IN THE SCOTOGENIC MODEL FOR $\mu \to e\gamma\gamma$

The calculations presented in this section are for the process of $\mu \to e\gamma\gamma$ in the scotogenic model described in Section 5.1.3. The amplitudes are

$$\begin{aligned}
M_1 =& K \epsilon_{1\mu}^* \epsilon_{2\nu}^* \overline{u}_2 \gamma^\nu \frac{\not{p}_1 - \not{k}_1}{(p_1 - k_1)^2} P_R \gamma_\delta I_1^\delta \\
& \frac{\not{p}_1 - \not{k}_1 + m_1}{(p_1 - k_1)^2 - m_1^2} \gamma^\mu u_1, \\
M_2 =& K \epsilon_{1\mu}^* \epsilon_{2\nu}^* \overline{u}_2 P_R \gamma_\delta I_2^{\delta\nu} \frac{\not{p}_1 - \not{k}_1 + m_1}{(p_1 - k_1)^2 - m_1^2} \gamma_\mu u_1, \\
M_3 =& K \epsilon_{1\mu}^* \epsilon_{2\nu}^* \overline{u}_2 \gamma^\nu \frac{\not{p}_1 - \not{k}_1}{(p_1 - k_1)^2} P_R \gamma_\delta I_3^{\delta\mu} u_1,
\end{aligned}$$

$$
\begin{aligned}
M_4 =& K\epsilon^*_{1\mu}\epsilon^*_{2\nu}\overline{u}_2 P_R\gamma_\delta I_4^\delta \frac{\not{p}_2 + m_1}{-m_1^2}\gamma^\nu \\
& \frac{\not{p}_1 - \not{k}_1 + m_1}{(p_1-k_1)^2 - m_1^2}\gamma^\mu u_1, \\
M_5 =& K\epsilon^*_{1\mu}\epsilon^*_{2\nu}\overline{u}_2\gamma^\nu \frac{\not{p}_1 - \not{k}_1}{(p_1-k_1)^2}\gamma^\mu \frac{\not{p}_1}{m_1^2} P_R\gamma_\delta I_5^\delta u_1, \\
M_6 =& K\epsilon^*_{1\mu}\epsilon^*_{2\nu}\overline{u}_2 P_R\gamma_\delta I_6^{\delta\mu\nu} u_1.
\end{aligned} \tag{I.387}
$$

Where p_1 is the muon momentum, p_2 is the electron momentum, the electron mass m_2 is set to zero, $k_{1,2}$ are the four-momenta of the photons from left to right which are associated with the index μ and ν. Momenta in the loop are always chosen such, that q runs along the fermion line. The amplitudes for the exchange diagrams are obtained when exchanging k_1 with k_2 and the indicesν and μ. u_1 is the spinor corresponding to the muon with mass m_1 and momentum p_1, $\overline{u}_2$ is associated with the electron, which has a negligible mass and momentum p_2, $\epsilon_1 = \epsilon(k_1)$ and $\epsilon_2 = \epsilon(k_2)$. The loop integrals are given by

$$
I_1^\delta = \int \frac{d^4q}{(2\pi)^4}\frac{q^\delta}{(q^2 - M_i^2)((q-p_1+k_1)^2 - m_{\eta^+}^2)}, \tag{I.388}
$$

$$
\begin{aligned}
I_2^{\delta\nu} =& \int \frac{d^4q}{(2\pi)^4}\frac{2q^\delta(q^\nu - p_2^\nu)}{(q^2 - M_i^2)((q-p_1+k_1)^2 - m_{\eta^+}^2)} \\
& \frac{1}{((q-p_2)^2 - m_{\eta^+}^2)},
\end{aligned} \tag{I.389}
$$

$$
\begin{aligned}
I_3^{\delta\mu} =& \int \frac{d^4q}{(2\pi)^4}\frac{2q^\delta(q^\mu - p_1^\mu)}{(q^2 - M_i^2)((q-p_1+k_1)^2 - m_{\eta^+}^2)} \\
& \frac{1}{((q-p_1)^2 - m_{\eta^+}^2)},
\end{aligned} \tag{I.390}
$$

$$
I_4^\delta = \int \frac{d^4q}{(2\pi)^4}\frac{q^\delta}{(q^2 - M_i^2)((q-p_2)^2 - m_{\eta^+}^2)}, \tag{I.391}
$$

$$
I_5^\delta = \int \frac{d^4q}{(2\pi)^4}\frac{q^\delta}{(q^2 - M_i^2)((q-p_1)^2 - m_{\eta^+}^2)}, \tag{I.392}
$$

$$
\begin{aligned}
I_6^{\delta\mu\nu} =& \int \frac{d^4q}{(2\pi)^4}\frac{4q^\delta(q^\nu - p_2^\nu)(q^\mu - p_1^\mu)}{(q^2 - M_i^2)} \\
& \frac{1}{((q-p_2-k_2)^2 - m_{\eta^+}^2)} \\
& \frac{1}{((q-p_2)^2 - m_{\eta^+}^2)}\frac{1}{((q-p_1)^2 - m_{\eta^+}^2)}.
\end{aligned} \tag{I.393}
$$

They can be solved within the approximation of heavy masses in the loop, as described in the following or the Passarino-Veltman functions

can be directly identified.
Kinematics fix

$$p_1 = p_2 + k_1 + k_2. \tag{I.394}$$

For the first diagram, Fig. 5.40 (a), the denominator is

$$D_1 = l^2 - A_1, \tag{I.395}$$

with

$$A_1 = m_{\eta^+}^2(1-x) + M_i^2 x. \tag{I.396}$$

After shifting q to $l = q + (k_1 + p_1)(x-1)$, the numerator becomes

$$N_1 = (k_1^\delta + p_1^\delta)(1-x). \tag{I.397}$$

The terms proportional to l^δ are omitted, as they vanish in the integration over l, due to symmetry arguments. In general, the relations

$$\begin{aligned} &p_2^\delta \to 0 \text{ as } \overline{u}_2 \not{p}_2 = 0, \\ &k_1^\mu \to 0 \text{ as } \epsilon_{\mu 1}^* k_1^\mu = 0, \\ &k_2^\nu \to 0 \text{ as } \epsilon_{\nu 2}^* k_2^\nu = 0, \end{aligned} \tag{I.398}$$

are used when treating the amplitudes.
The l integration of Eq. I.388 can then be performed. The result is, using the expressions Eq. I.300 and Eq. I.304 to Eq. I.308,

$$I_1^\delta = \frac{i\pi^2}{(2\pi)^4} \pi^{-2\epsilon} \int_0^1 dx N_1 (\Delta - \Gamma(1+\epsilon) \log(\frac{A_1}{\mu^2}). \tag{I.399}$$

For the second diagram in Fig. 5.40 (b) the denominator is

$$D_2 = l^2 - A_2, \tag{I.400}$$

with

$$\begin{aligned} A_2 =& m_{\eta^+}^2(y+z) + M_i^2 x \\ =& m_{\eta^+}^2(1-x) + M_i^2 x, \end{aligned} \tag{I.401}$$

with as $x + y + z = 1$ and the sift to

$$l = q + (k_1 - p_1)y - p_2 z. \tag{I.402}$$

When neglecting all odd powers of l in the integral, the numerator becomes

$$N_2 = N_{21} + N_{22}, \tag{I.403}$$

where

$$N_{21} = 4 l^\delta l^\nu,$$

$$N_{22} = 4(k_1^\delta - p_1^\delta)y(p_2^\nu + (k_1^\nu - p_1^\nu)y - p_2^\nu z). \tag{I.404}$$

For N_{21} the l integral is performed according to Eq. I.311 and for N_{22} Eq. I.310 is used. In the second integral, the limit $D \to 4$ is performed, as this integral is finite. After using the definitions Eq. I.300, Eq. I.380 and the relations Eq. I.304 to Eq. I.308 and performing the x, y and z integrals if possible, the result is

$$\begin{aligned} I_{21}^{\delta\nu} =& 2g^{\delta\nu}\frac{i\pi^2}{(2\pi)^4}\pi^{-2\epsilon}(4\pi)^\epsilon \left(\frac{1}{2}\Delta \right. \\ & \left. - \int_0^1 \log(\frac{A_2}{\mu^2})\delta(x+y+z-1)dxdydz\right), \\ I_{22}^{\delta\nu} =& \frac{-i\pi^2}{(2\pi)^4}(k_1^\delta - p_1^\delta)(p_1^\nu - k_1^\nu)\frac{F_2(\zeta_i)}{m_{\eta^+}^2}, \end{aligned} \tag{I.405}$$

with $F_2(x)$ as in Eq. 5.104.
For diagram Fig. 5.40 (c) the denominator is given by

$$\begin{aligned} D_3 =& x(q^2 - M_i^2) + y((q - p_1 + k_1)^2 - m_{\eta^+}^2) \\ & + z((q-p_1)^1 - m_{\eta^+}^2), \end{aligned} \tag{I.406}$$

where $x + y + z = 1$. The denominator simplifies to

$$D_3 = l^2 - A_2, \tag{I.407}$$

by shifting q to

$$l = q + k_1 y - p_1(y+z). \tag{I.408}$$

After neglecting all terms with odd numbers of ls, the numerator is

$$N_3 = N_{31} + N_{32}, \tag{I.409}$$

with

$$\begin{aligned} N_{31} =& 2l^\mu l^\delta, \\ N_{32} =& -2p_1^\mu(-1+y+z)(k_1^\delta y - p_1^\delta(y+z)). \end{aligned} \tag{I.410}$$

Analogous to $I_2^{\delta\nu}$ the l integration and most of the x, y and z integrals are performed. The final result is

$$\begin{aligned} I_{31}^{\delta\mu} =& 2g^{\mu\delta}\frac{i\pi^2}{(2\pi)^4}\pi^{-2\epsilon}(4\pi)^\epsilon \left(\frac{1}{2}\Delta \right. \\ & \left. - \int_0^1 \log(\frac{A_2}{\mu^2})\delta(1-x-y-z)dxdydz\right), \end{aligned} \tag{I.411}$$

$$I_{32}^{\delta\mu} = \frac{-i\pi^2}{(2\pi)^4}(k_1^\delta - 2p_1^\delta)p_1^\mu \frac{F_2(\zeta_i)}{m_{\eta^+}^2}. \tag{I.412}$$

For diagram 5.40 (d) the denominator after Feynman parametrization reads as

$$D_4 = x(q^2 - M_i^2) + (1-x)((q-p_2)^2 - m_{\eta^+}^2). \tag{I.413}$$

q is shifted to

$$l = q + p_2(x-1), \tag{I.414}$$

which results in

$$D_4 = l^2 - A_1. \tag{I.415}$$

Similarly, the numerator is shifted to

$$N_4 = p_2^\delta(1-x), \tag{I.416}$$

when omitting all l-odd terms. Due to Eq. I.398, the p_2^δ term makes the integral vanish.
For diagram 5.40 (e) the denominator, after Feynman parametrization ,is

$$D_5 = x(q^2 - M_i^2) + (1-x)((q-p_1)^2 + m_{\eta^+}^2). \tag{I.417}$$

In order to complete the square, all simplifications are applied and q is shifted to

$$l = q + p_1(x-1), \tag{I.418}$$

which results in

$$D_5 = l^2 - A_1. \tag{I.419}$$

The numerator without the l^δ term is then

$$N_5 = p_1^\delta(1-x). \tag{I.420}$$

Hence, one is left with the expression

$$I_5^\delta = \int_0^1 dx \int d^D l \frac{\mu^{4-D}}{(2\pi)^D} \frac{N_5}{(l^2 - A_1)^2}, \tag{I.421}$$

which simplifies to, when evaluating the l integral,

$$I_5^\delta = \frac{i\pi^2}{(2\pi)^4} \pi^{-2\epsilon} p_1^\delta \int_0^1 dx (1-x)(\Delta - \Gamma(1+\epsilon) \ln(\frac{A_1}{\mu^2}). \tag{I.422}$$

The process in diagram 5.40 (f) yields the denominator

$$\begin{aligned} D_6 =& x(q^2 - M_i^2) + y((q-p_2)^2 - m_{\eta^+}^2) \\ &+ z((q-p_2-k_2)^2 - m_{\eta^+}^2) + w((q-p_1)^2 - m_{\eta^+}^2), \end{aligned} \tag{I.423}$$

at which

$$x + y + z + w = 1. \tag{I.424}$$

Shifting q as

$$q = l + p_1 w + p_2 y + k_2 z + p_2 z \tag{I.425}$$

and using all simplifications, one is left with

$$D_6 = l^2 - A_6, \tag{I.426}$$

where

$$A_6 = M_i^2 x + m_{\eta^+}^2 (1 - x). \tag{I.427}$$

The numerator is

$$N_6 = q^\delta (2q^\nu 2p_2^\nu)(2q^\mu - 2p_1^\mu). \tag{I.428}$$

It is shifted according to Eq. I.425 and terms proportional to an odd number of l's are neglected:

$$N_6 = N_{61} l^\mu l^\nu + N_{62} l^\mu l^\delta + N_{63} l^\nu l^\delta + N_{64}, \tag{I.429}$$

with

$$\begin{aligned}
N_{61} =& 4(p_1^\delta w + k_2^\delta z), \\
N_{62} =& 4(p_1^\nu w + p_2^\nu (-1 + y + z)), \\
N_{63} =& 4(p_1^\mu (-1 + w) + p_2^\mu (y + z) + k_2^\mu z), \\
N_{64} =& 4(p_1^\delta w + k_2^\delta z)(p_1^\nu w + p_2^\nu (-1 + y + z)) \\
& (p_1^\mu (-1 + w) + p_2^\mu (y + z) + k_2^\mu z).
\end{aligned} \tag{I.430}$$

This leads to

$$\begin{aligned}
I_6^{\delta\mu\nu} =& 6(4\pi\mu^2)\pi^{-\epsilon}(2\pi)^{-4} \\
& \int dx dy dz dw \delta(x + y + z + w - 1) \qquad \text{(I.431)} \\
& \int d^D l \left(\frac{N_{61} l^\mu l^\nu}{(l^2 - A_6)^4} + \frac{N_{62} l^\mu l^\delta}{(l^2 - A_6)^4} \right. \\
& \left. + \frac{N_{63} l^\nu l^\delta}{(l^2 - A_6)^4} + \frac{N_{64}}{(l^2 - A_6)^4} \right). \qquad \text{(I.432)}
\end{aligned}$$

In order to perform the l integral on $I_6^{\delta\mu\nu}$, one can use Eq. I.310 and Eq. I.311 to obtain

$$I_6^{\delta\mu\nu} = \frac{i\pi^2}{(2\pi)^4}(-I_{61} g^{\mu\nu} - I_{62} g^{\mu\delta} - I_{63} g^{\nu\delta} + I_{64}), \tag{I.433}$$

with

$$I_{6i} = \int dx dy dz dw \delta(x + y + z + w - 1) \frac{N_{6i}}{A_6}, \text{ for } i = 1, 2, 3, 4,$$

$$
\begin{aligned}
I_{61} =& \frac{2}{3}(k_2^\delta + p_1^\delta \frac{G_2(\zeta_i)}{m_{\eta^+}^2},\\
I_{62} =& -2p_1^\nu \frac{F2(\zeta_i)}{m_{\eta^+}^2} + k_1^\nu \frac{H_1(\zeta_i)}{m_{\eta^+}^2},\\
I_{63} =& \frac{2}{3}p_2^\mu \frac{G_2(\zeta_i)}{m_{\eta^+}^2} - p_1^\mu \frac{H_1(\zeta_i)}{m_{\eta^+}^2},\\
I_{64} =& k_2^\delta \left(p_1^\mu \left(p_1^\nu H_2(\zeta_i) + p_2^\nu H_3(\zeta_i)\right)\right.\\
&\left. + k_2^\mu \left(p_1^\nu H_4(\zeta_i) + p_2^\nu H_5(\zeta_i)\right)\right)\\
&+ k_1^\delta (p_1^\mu (\frac{2}{3}p_1^\nu H_2(\zeta_i) + p_2^\nu H_6(\zeta_i))\\
&+ k_2^\mu (\frac{3}{2}p_1^\nu H_4(\zeta_i) + p_2^\nu H_7(\zeta_i))),
\end{aligned}
\tag{I.434}
$$

where $F_2(x)$ is as in Eq. 5.104 and the other functions are

$$
\begin{aligned}
G_2(x) =& \frac{2 - 9x + 18x^2 - 11x^3 + 6x^3 \log x}{6(1-x)^4},\\
H_1(x) =& \frac{5 - 27x + 27x^2 - 5x^3 + 6(-3+x)x^2 \log x}{9(1-x)^4},\\
H_2(x) =& \frac{37x^4 - 8x^3 - 12(x+4)x^3 \log x - 36x^2 + 8x - 1}{24(1-x)^4},\\
H_3(x) =& \left(-87x^4 + 376x^3 - 180x^2\right.\\
&\left. + 12(3x^2 - 4x - 24)x^2 \log x - 120x + 11\right) \frac{1}{72(1-x)^6},\\
H_4(x) =& \frac{-12x^5 - 65x^4 + 60x^4 \log x + 120x^3 - 60x^2 + 20x - 3}{120(1-x)^6},\\
H_5(x) =& \left(36x^5 - 175x^4 - 280x^3 - 60(x-8)x^3 \log x\right.\\
&\left. + 540x^2 - 140x + 19\right) \frac{1}{360(1-x)^6},\\
H_6(x) =& \frac{-31x^4 + 96x^3 - 36x^2 + 12(x^2-6)x^2 \log x - 32x + 3}{36(1-x)^6},\\
H_7(x) =& \left(24x^5 - 55x^4 - 200x^3 - 60(x-a)x^3 \log x\right.\\
&\left. + 300x^2 - 8x + 11\right) \frac{1}{360(1-x)^6}.
\end{aligned}
\tag{I.435}
$$

Using the results for the integrals from before, one can identify the divergent and scale dependent parts of the amplitudes:

$$
\begin{aligned}
M_1^D \propto& \bar{u}_2 P_R \gamma^\nu \frac{\not{p}_1 - \not{k}_1}{(p_1 - k_1)^2} (\not{k}_1 - \not{p}_1)(-\frac{1}{2}\Delta + F) \frac{\not{p}_1 - \not{k}_1 + m_1}{(p_1 - k_1)^2 - m_1^2} u_1\\
=& -\bar{u}_2 P_R \gamma^\nu (-\frac{1}{2}\Delta + F) \frac{\not{p}_1 - \not{k}_1 + m_1}{(p_1 - k_1)^2 - m_1^2} \gamma^\mu u_1,\\
M_2^D \propto& \bar{u}_2 P_R \gamma^\nu \frac{\not{p}_1 - \not{k}_1 + m_1}{(p_1 - k_1)^2 - m_1^2} \gamma^\mu u_1\\
\sim& -M_1^D,
\end{aligned}
$$

$$
\begin{aligned}
M_3^D &\propto \bar{u}_2 P_R \gamma^\nu \frac{\not{p}_1 - \not{k}_1}{(p_1 - k_1)^2} \gamma^\mu (\frac{1}{2}\Delta - F) u_1, \\
M_5^D &\propto \bar{u}_2 P_R \gamma^\nu \frac{\not{p}_1 - \not{k}_1}{(p_1 - k_1)^2} \gamma^\mu \frac{\not{p}_1^2}{m_1^2} (-\frac{1}{2}\Delta + F) u_1 \\
&\sim -M_3^D,
\end{aligned} \tag{I.436}
$$

with

$$
F = \int_0^1 (1-x) \log(\frac{A_1}{\mu^2}) dx. \tag{I.437}
$$

Adding up all amplitudes, it is found that the infinite parts cancel each other. The only finite contributions are obtained from the diagrams (b), (c) and (f) in Fig. 5.40 and their exchange diagrams, so only from $I_{2,3,6}$.
The resulting squared amplitudes are

$$
\begin{aligned}
M_{2,2}^2 =& \left(m_1^4 - m_1^2 p1k1 - 2p1k1(p1k1 + p1k2)\right) \\
&\times \frac{F_{2i} F_{2j} K_i K_j^* \left(m_1^2 - 2p1k1\right)^2}{m_{\eta^+}^4 p1k1^2}, \\
M_{2,3}^2 =& -\frac{2F_{2i} F_{2j} K_i K_j^* \left(m_1^2 - 2p1k1\right)\left(m_1^4 - m_1^2 p1k1\right)}{m_{\eta^+}^4 p1k1}, \\
M_{2,6}^2 =& \frac{F_{2i} K_i K_j^* \left(m_1^2 - 2p1k1\right)}{12 m_{\eta^+}^4 p1k1} \\
&\times \Big(F_{2j}\left(48\left(m_1^2 - p1k1\right)(p1k1 + p1k2)\right) \\
&+ G_{2j}\left(4\left(-5m_1^4 + 8m_1^2 p1k1 + 4p1k1 p1k2\right)\right) \\
&+ H_{1j}\left(6\left(m_1^4 + 2m_1^2(p1k2 - p1k1) - 4p1k1(p1k1 + p1k2)\right)\right) \\
&+ H_{2j}\left(12 m_1^2 m_{\eta^+}^2\left(m_1^2 - p1k1\right)\left(2m_1^2 - p1k1 - 2p1k2\right)\right) \\
&+ H_{3j}\left(3 m_1^2 m_{\eta^+}^2\left(m_1^2 - 2p1k1\right)\left(m_1^2 - 2p1k1 + 2p1k2\right)\right) \\
&+ H_{4j}\left(3 m_{\eta^+}^2\left(m_1^2 - 2p1k1\right)\left(m_1^2 - p1k1\right)\left(3m_1^2 - 2p1k2\right)\right) \\
&+ H_{5j}\left(12 m_{\eta^+}^2 p1k2\left(m_1^2 - 2p1k1\right)\left(m_1^2 - p1k1\right)\right) \\
&+ H_{6j}\left(6 m_1^2 m_{\eta^+}^2\left(m_1^2 - 2p1k1\right)\left(m_1^2 - 2p1k2\right)\right) \\
&+ H_{7j} 3 m_{\eta^+}^2\left(m_1^2 - 2p1k1\right)^2\left(m_1^2 - 2p1k2\right)\Big), \\
M_{3,3}^2 =& \left(2m_1^4 - 5m_1^2 p1k1 + 2p1k1(p1k1 + p1k2)\right) \\
&\times -\frac{4F_{2i} F_{2j} K_i K_j^* m_1^2}{m_{\eta^+}^4\left(m_1^2 - 2p1k1\right)}, \\
M_{3,6}^2 =& \frac{F_{2i} K_i K_j^*}{3 m_{\eta^+}^4\left(m_1^2 - 2p1k1\right)} \\
&\Big(F_{2j}\left(-6m_1^2\right. \\
&\left.\left(5m_1^4 - 6m_1^2(2p1k1 + p1k2) + 8p1k1(p1k1 + p1k2)\right)\right)
\end{aligned}
$$

$$
\begin{aligned}
&+G_{2j}\,(4\\
&\left(m_1^6+m_1^4 p1k2-2m_1^2\left(2p1k1^2+4p1k1p1k2+p1k2^2\right)\right.\\
&\left.\quad+4p1k1(p1k1+p1k2)^2\right))\\
&+H_{1j}\left(6m_1^2\left(4m_1^4-m_1^2(9p1k1+4p1k2)\right.\right.\\
&\left.\left.+2p1k1(2p1k1+3p1k2)\right)\right)\\
&+H_{2j}\left(-3m_1^4m_{\eta^+}^2\left(6m_1^4-m_1^2(13p1k1+8p1k2)\right.\right.\\
&\left.\left.+2p1k1(4p1k1+5p1k2)\right)\right)\\
&+H_{4j}\left(-3m_1^2m_{\eta^+}^2 p1k2\left(6m_1^4-m_1^2(13p1k1+8p1k2)\right.\right.\\
&\left.\left.+2p1k1(4p1k1+5p1k2)\right)\right),
\end{aligned}
$$

$$
\begin{aligned}
M_{6,6}^2=&\frac{K_i K_j^*}{18m_{\eta^+}^4}\\
&\left(F_{2i}\left(F_{2j}\left(288m_1^2\left(-m_1^2+p1k1+p1k2\right)\right)\right.\right.\\
&+\left.G_{2j}\left(24m_1^2\left(-3m_1^2+4p1k1+2p1k2\right)\right)\right.\\
&+\left.H_{1j}\left(72\left(m_1^2+2p1k1\right)\left(m_1^2-p1k1-p1k2\right)\right)\right.\\
&+\left.H_{2j}\left(18m_1^4m_{\eta^+}^2\left(5m_1^2-4p1k1-6p1k2\right)\right)\right.\\
&+\left.H_{3j}\left(36m_1^2m_{\eta^+}^2\left(m_1^2-2p1k1\right)\left(m_1^2-p1k1-p1k2\right)\right)\right.\\
&+\left.H_{4j}\left(18m_1^2m_{\eta^+}^2\left(m_1^2-2p1k1\right)\left(3m_1^2-2p1k2\right)\right)\right.\\
&+\left.H_{5j}\left(72m_{\eta^+}^2\left(m_1^4-2m_1^2p1k1\right)p1k2\right)\right.\\
&+\left.H_{6j}\left(36m_1^2m_{\eta^+}^2\left(m_1^2-2p1k2\right)\left(m_1^2-p1k1-p1k2\right)\right)\right.\\
&+\left.H_{7j}\left(36m_{\eta^+}^2\left(m_1^2-2p1k1\right)\left(m_1^2-2p1k2\right)\right.\right.\\
&\left.\left.\left(m_1^2-p1k1-p1k2\right)\right)\right)\\
&+G_{2i}\left(F_{2j}\left(24m_1^2\left(-3m_1^2+4p1k1+2p1k2\right)\right)\right.\\
&+\left.G_{2j}\left(64\left(2m_1^4-3p1k1m_1^2-2p1k1p1k2\right)\right)\right.\\
&+\left.H_{1j}\left(12\left(3m_1^4-2(3p1k1+5p1k2)m_1^2\right.\right.\right.\\
&\left.\left.\left.+4\left(p1k1^2+3p1k2p1k1+p1k2^2\right)\right)\right)\right.\\
&+\left.H_{2j}\left(-6m_1^2m_{\eta^+}^2\left(13m_1^4-19(p1k1+p1k2)m_1^2\right.\right.\right.\\
&\left.\left.\left.+2(2p1k1+p1k2)(p1k1+3p1k2)\right)\right)\right.\\
&+\left.H_{3j}\left(-12m_{\eta^+}^2\left(m_1^2-2p1k1\right)\left(m_1^2-p1k1-p1k2\right)\left(m_1^2+2p1k2\right)\right)\right.\\
&+\left.H_{4j}\left(-3m_{\eta^+}^2\left(5m_1^6+2(5p1k2-7p1k1)m_1^4\right.\right.\right.\\
&\left.\left.\left.+8(p1k1-2p1k2)(p1k1+p1k2)m_1^2+8p1k1p1k2^2\right)\right)\right.\\
&+\left.H_{5j}\left(-6m_{\eta^+}^2\left(m_1^2-2p1k1\right)\left(m_1^4+2(p1k2-p1k1)m_1^2+4p1k2^2\right)\right)\right.\\
&+\left.H_{6j}\left(-24m_{\eta^+}^2\left(m_1^2-p1k1\right)\right.\right.\\
&\left.\left.\left(m_1^2-2p1k2\right)\left(m_1^2-p1k1-p1k2\right)\right)\right.
\end{aligned}
$$

$$
\begin{aligned}
&+\ H_{7j}\left(-12m_{\eta^+}^2\left(m_l^4-3m_l^2p1k1+2p1k1^2\right)\right.\\
&\left.\left(m_l^2-2p1k2\right)\right)\\
&+H_{1i}\left(F_{2j}\left(72\left(m_l^2+2p1k1\right)\left(m_l^2-p1k1-p1k2\right)\right)\right.\\
&+\ G_{2j}\left(12\left(3m_l^4-2(3p1k1+5p1k2)m_l^2\right.\right.\\
&\left.\left.+4\left(p1k1^2+3p1k2p1k1+p1k2^2\right)\right)\right)\\
&+\ H_{1j}\left(36m_l^2\left(-3m_l^2+2p1k1+4p1k2\right)\right)\\
&+\ H_{2j}\left(9m_l^2m_{\eta^+}^2\left(m_l^2-p1k1\right)\left(5m_l^2-4p1k1-6p1k2\right)\right)\\
&+\ H_{3j}\left(-9m_l^2m_{\eta^+}^2\left(m_l^2-2p1k1\right)\left(m_l^2-2p1k2\right)\right)\\
&+\ H_{4j}\left(-9m_{\eta^+}^2\left((3p1k1-5p1k2)m_l^4+\left(-6p1k1^2\right.\right.\right.\\
&\left.\left.\left.+2p1k2p1k1+6p1k2^2\right)m_l^2+4p1k1^2p1k2\right)\right)\\
&+\ H_{5j}\left(18m_{\eta^+}^2\left(m_l^2-2p1k1\right)^2p1k2\right)\\
&+\ H_{6j}\left(-9m_l^2m_{\eta^+}^2\left(m_l^2-2p1k2\right)^2\right)\\
&+\ H_{7j}\left(-9m_{\eta^+}^2\left(m_l^2-2p1k1\right)\left(m_l^2-2p1k2\right)^2\right)\Big)\\
&+H_{2i}\left(F_{2j}\left(18m_l^4m_{\eta^+}^2\left(5m_l^2-4p1k1-6p1k2\right)\right)\right.\\
&+\ G_{2j}\left(-6m_l^2m_{\eta^+}^2\left(13m_l^4-19(p1k1+p1k2)m_l^2\right.\right.\\
&\left.\left.+2(2p1k1+p1k2)(p1k1+3p1k2)\right)\right)\\
&+\ H_{1j}\left(9m_l^2m_{\eta^+}^2\left(m_l^2-p1k1\right)\left(5m_l^2-4p1k1-6p1k2\right)\right)\\
&+\ H_{2j}\left(9m_l^4m_{\eta^+}^4\right.\\
&\left.\left(6m_l^4-(3p1k1+8p1k2)m_l^2-2p1k1p1k2\right)\right)\\
&+\ H_{3j}\left(9m_l^2m_{\eta^+}^4\left(m_l^2-2p1k1\right)\right.\\
&\left.\left(3m_l^2-2p1k2\right)\left(m_l^2-p1k1-p1k2\right)\right)\\
&+\ H_{4j}\left(9m_l^2m_{\eta^+}^4p1k2\right.\\
&\left.\left(6m_l^4-(3p1k1+8p1k2)m_l^2-2p1k1p1k2\right)\right)\\
&+\ H_{5j}\left(9m_l^2m_{\eta^+}^4\left(m_l^2-2p1k1\right)\left(3m_l^2-2p1k2\right)p1k2\right)\\
&+\ H_{6j}\left(18m_l^2m_{\eta^+}^4\left(m_l^2+p1k1\right)\right.\\
&\left.\left(m_l^2-2p1k2\right)\left(m_l^2-p1k1-p1k2\right)\right)\\
&+\ H_{7j}\left(18m_{\eta^+}^4p1k2\left(m_l^2+p1k1\right)\right.\\
&\left.\left.\left(m_l^2-2p1k2\right)\left(m_l^2-p1k1-p1k2\right)\right)\right)\\
&+H_{3i}\left(F_{2j}\left(36m_l^2m_{\eta^+}^2\left(m_l^2-2p1k1\right)\right)\right.\\
&\left.\left(m_l^2-p1k1-p1k2\right)\right)\\
&+\ G_{2j}\left(-12m_{\eta^+}^2\left(m_l^2-2p1k1\right)\right.
\end{aligned}
$$

$$
\begin{aligned}
&\left(m_l^2 - p1k1 - p1k2\right)\left(m_l^2 + 2p1k2\right)\Big) \\
&+\ H_{1j}\left(-9m_l^2 m_{\eta^+}^2\left(m_l^2 - 2p1k1\right)\left(m_l^2 - 2p1k2\right)\right) \\
&+\ H_{2j}\Big(9m_l^2 m_{\eta^+}^4\left(m_l^2 - 2p1k1\right) \\
&\left(3m_l^2 - 2p1k2\right)\left(m_l^2 - p1k1 - p1k2\right)\Big) \\
&+\ H_{3j}(0) \\
&+\ H_{4j}\Big(9m_{\eta^+}^4\left(m_l^2 - 2p1k1\right) \\
&\left(3m_l^2 - 2p1k2\right)\left(m_l^2 - p1k1 - p1k2\right)p1k2\Big) \\
&+\ H_{5j}\left(36m_{\eta^+}^4\left(m_l^2 - 2p1k1\right)\left(m_l^2 - p1k1 - p1k2\right)p1k2^2\right) \\
&+\ H_{6j}(0) \\
&+\ H_{7j}(0)\Big) \\
&+H_{4i}\left(F_{2j}\left(18m_l^2 m_{\eta^+}^2\left(m_l^2 - 2p1k1\right)\left(3m_l^2 - 2p1k2\right)\right)\right. \\
&+\ G_{2j}\Big(-3m_{\eta^+}^2 \\
&\left(5m_l^6 + 2(5p1k2 - 7p1k1)m_l^4\right. \\
&+8(p1k1 - 2p1k2)(p1k1 + p1k2)m_l^2 \\
&\quad\left.+8p1k1p1k2^2\right)\Big) \\
&+\ H_{1j}\Big(-9m_{\eta^+}^2\left((3p1k1 - 5p1k2)m_l^4\right. \\
&+\left(-6p1k1^2 + 2p1k2p1k1 + 6p1k2^2\right)m_l^2 \\
&\quad\left.+4p1k1^2 p1k2\right)\Big) \\
&+\ H_{2j}\Big(9m_l^2 m_{\eta^+}^4 p1k2 \\
&\left(6m_l^4 - (3p1k1 + 8p1k2)m_l^2 - 2p1k1p1k2\right)\Big) \\
&+\ H_{3j}\Big(9m_{\eta^+}^4\left(m_l^2 - 2p1k1\right) \\
&\left(3m_l^2 - 2p1k2\right)\left(m_l^2 - p1k1 - p1k2\right)p1k2\Big) \\
&+\ H_{4j}(0) \\
&+\ H_{5j}(0) \\
&+\ H_{6j}\Big(18m_{\eta^+}^4\left(m_l^2 + p1k1\right) \\
&\left(m_l^2 - 2p1k2\right)\left(m_l^2 - p1k1 - p1k2\right)p1k2\Big) \\
&+\ H_{7j}(0)\Big) \\
&+H_{5i}\left(F_j\left(72m_{\eta^+}^2\left(m_l^4 - 2m_l^2 p1k1\right)p1k2\right)\right. \\
&+\ G_{2j}\left(-6m_{\eta^+}^2\left(m_l^2 - 2p1k1\right)\left(m_l^4 + 2(p1k2 - p1k1)m_l^2 + 4p1k2^2\right)\right) \\
&+\ H_{1j}\left(18m_{\eta^+}^2\left(m_l^2 - 2p1k1\right)^2 p1k2\right) \\
&+\ H_{2j}\left(9m_l^2 m_{\eta^+}^4\left(m_l^2 - 2p1k1\right)\left(3m_l^2 - 2p1k2\right)p1k2\right) \\
&+\ H_{3j}\left(36m_{\eta^+}^4\left(m_l^2 - 2p1k1\right)\left(m_l^2 - p1k1 - p1k2\right)p1k2^2\right)
\end{aligned}
$$

$$
\begin{aligned}
&+ H_{4j}(0) \\
&+ H_{5j}(0) \\
&+ H_{6j}\Big(18m_{\eta^+}^4\left(m_l^2-2p1k1\right) \\
&\left(m_l^2-2p1k2\right)\left(m_l^2-p1k1-p1k2\right)p1k2\Big) \\
&+ H_{7j}(0)\Big) \\
&+H_{6i}\Big(F_{2j}\Big(36m_l^2m_{\eta^+}^2\left(m_l^2-2p1k2\right)\left(m_l^2-p1k1-p1k2\right)\Big) \\
&+ G_{2j}\Big(-24m_{\eta^+}^2\left(m_l^2-p1k1\right) \\
&\left(m_l^2-2p1k2\right)\left(m_l^2-p1k1-p1k2\right)\Big) \\
&+ H_{1j}\Big(-9m_l^2m_{\eta^+}^2\left(m_l^2-2p1k2\right)^2\Big) \\
&+ H_{2j}\Big(18m_l^2m_{\eta^+}^4\left(m_l^2+p1k1\right) \\
&\left(m_l^2-2p1k2\right)\left(m_l^2-p1k1-p1k2\right)\Big) \\
&+ H_{3j}(0) \\
&+ H_{4j}\Big(18m_{\eta^+}^4\left(m_l^2+p1k1\right) \\
&\left(m_l^2-2p1k2\right)\left(m_l^2-p1k1-p1k2\right)p1k2\Big) \\
&+ H_{5j}\Big(18m_{\eta^+}^4\left(m_l^2-2p1k1\right) \\
&\left(m_l^2-2p1k2\right)\left(m_l^2-p1k1-p1k2\right)p1k2\Big) \\
&+ H_{6j}(0) \\
&+ H_{7j}(0)\Big) \\
&+H_{7i}\Big(F_{2j}\Big(36m_{\eta^+}^2\left(m_l^2-2p1k1\right) \\
&\left(m_l^2-2p1k2\right)\left(m_l^2-p1k1-p1k2\right)\Big) \\
&+ G_{2j}\Big(-12m_{\eta^+}^2\left(m_l^4-3p1k1m_l^2+2p1k1^2\right)\left(m_l^2-2p1k2\right)\Big) \\
&+ H_{1j}\Big(-9m_{\eta^+}^2\left(m_l^2-2p1k1\right)\left(m_l^2-2p1k2\right)^2\Big) \\
&+ H_{2j}\Big(18m_{\eta^+}^4\left(m_l^2+p1k1\right) \\
&\left(m_l^2-2p1k2\right)\left(m_l^2-p1k1-p1k2\right)p1k2\Big)\Big)
\end{aligned}
$$

where the kinematic relations from Section B.2 for two vanishing masses have been applied.

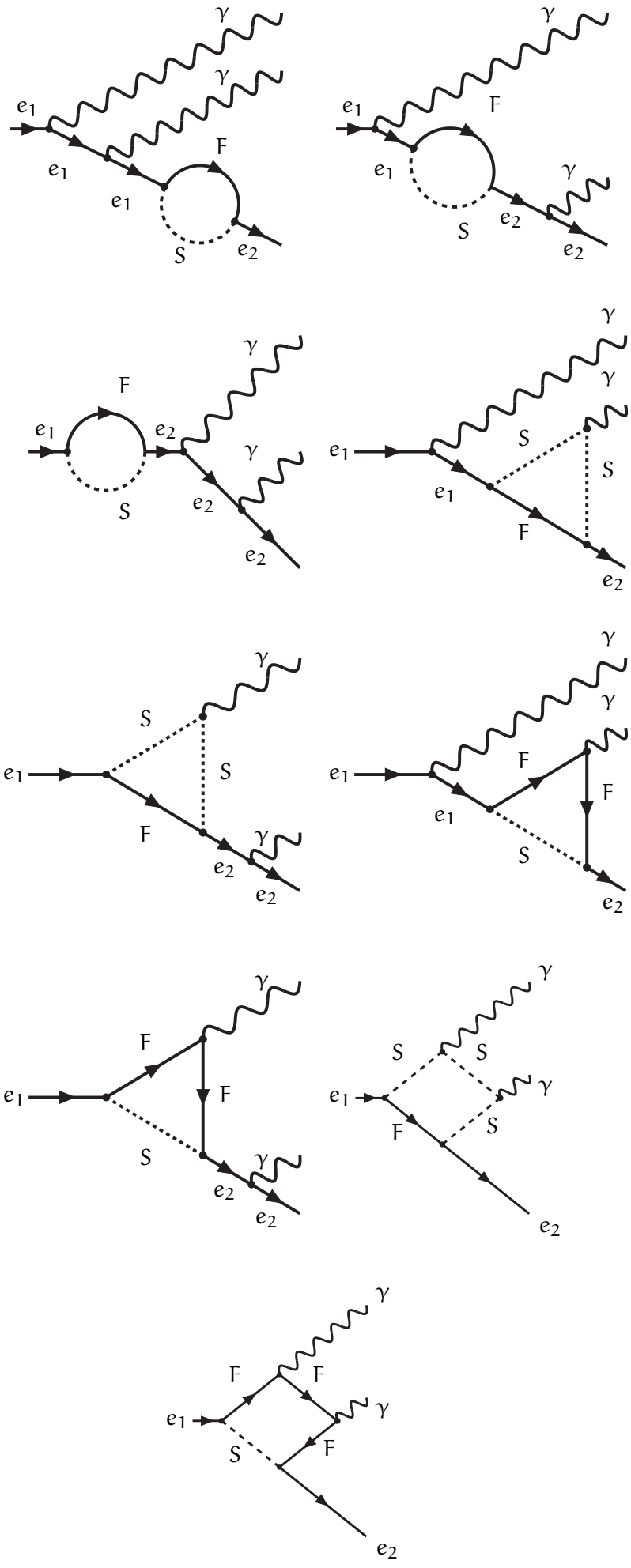

Figure I.138: Diagrams for $\mu \to e\gamma\gamma$.

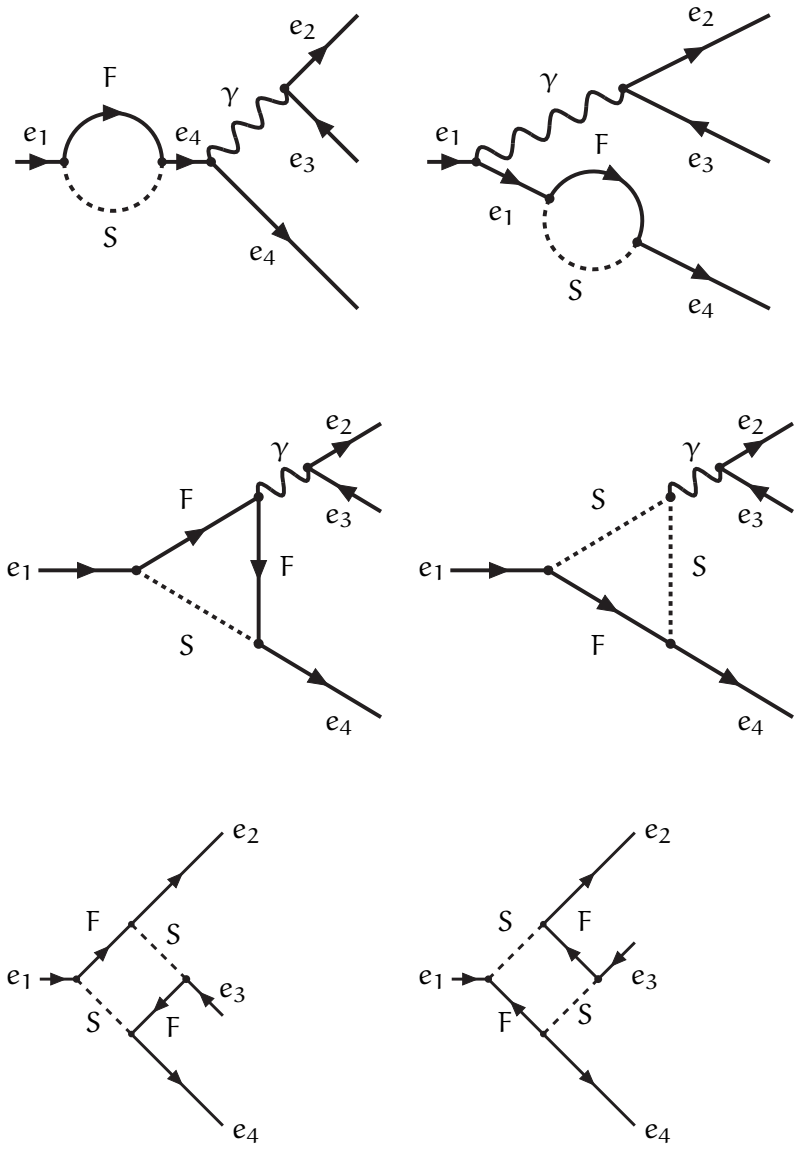

Figure I.139: Diagrams for $e_1 \to e_2 e_3 e_4$.

J

APPROXIMATION FOR NEUTRINO MASSES

The matrix M, defining the neutrino mass matrix M_ν as in Eq. 5.147, can be simplified in different ways depending on the model parameters. For the fermion and scalar mixing, the approximate mixing matrices and mass eigenstates are given in Section 5.2.1.2 and Section 5.2.1.4. They allow for further simplifications. This section contains the resulting elements of M.

J.0.1 $A = 0$ *and* $m_\lambda = 0$

For vanishing scalar and fermion mixing, $A = 0$ and $y_1, y_2 = 0$

$$\begin{aligned}
M_{11} =& 0, \\
M_{12} =& 0m \\
M_{22} =& \frac{M_{F,S}}{16\pi^2} \\
&\times \left(\frac{2M_{F,S}^2 \log\left(M_{F,S}^2\right) - \left(L^- v^2 + 2M_{S,D}^2\right) \log\left(\frac{L^- v^2}{2} + M_{S,D}^2\right)}{-L^- v^2 + 2M_{F,S}^2 - 2M_{S,D}^2} \right. \\
&\left. + \frac{\left(L^+ v^2 + 2M_{S,D}^2\right) \log\left(\frac{L^+ v^2}{2} + M_{S,D}^2\right) - 2M_{F,S}^2 \log\left(M_{F,S}^2\right)}{-L^+ v^2 + 2M_{F,S}^2 - 2M_{S,D}^2} \right),
\end{aligned} \tag{J.438}$$

is obtained, at which

$$\begin{aligned}
L^+ :=& \lambda_D + \lambda'_D + \lambda''_D, \\
L^- :=& \lambda_D + \lambda'_D - \lambda''_D.
\end{aligned} \tag{J.439}$$

In the limit of vanishing λ_S, λ_D and λ'_D and small λ''_D the result simplifies to

$$\begin{aligned}
M_{22} =& \lambda''_D \left(M_{F,S}^3 v^2 \log\left(M_{S,D}^2\right) + M_{F,S}^3 v^2 \right. \\
&\left. - M_{F,S}^3 v^2 \log\left(M_{F,S}^2\right) - M_{F,S} M_{S,D}^2 v^2 \right) \\
&\times \frac{1}{16\pi^2 \left(M_{F,S}^2 - M_{S,D}^2\right)^2},
\end{aligned} \tag{J.440}$$

which is proportional to λ''_D.

J.0.2 $\lambda_S = \lambda_D = \lambda'_D = \lambda''_D = 0$ *and* $A, m_\lambda \ll 1$

In the case of negligible scalar Higgs couplings, except for A and small fermion mixing, ($m_\lambda \ll 1$) the elements of M are

$$\begin{aligned} M_{11} &\propto m_\lambda^2, \\ M_{12} &\propto m_\lambda A, \\ M_{22} &\propto \mathrm{Const.} \end{aligned} \tag{J.441}$$

Or, more precise

$$\begin{aligned} M_{11} =& m_\lambda^2 \left(M_{F,S}(M_{F,D}-M_{F,S})(M_{F,D}+M_{F,S})\right. \\ & \times (M_{F,D}-M_{S,S})(M_{F,D}+M_{S,S}) \\ & \times \cos(2t)\left(M_{F,S}^2\left(M_{S,S}^2-M_{F,D}^2\right)\log\left(M_{F,S}^2\right)\right. \\ & + M_{F,D}^2\log\left(M_{F,D}^2\right)(M_{F,S}-M_{S,S})(M_{F,S}+M_{S,S}) \\ & \left.+M_{S,S}^2(M_{F,D}-M_{F,S})(M_{F,D}+M_{F,S})\log\left(M_{S,S}^2\right)\right) \\ & + M_{F,S}M_{S,S}^2\left(M_{F,D}^2-M_{F,S}^2\right)^2\left(M_{F,D}^2+M_{S,S}^2\right)\log\left(M_{S,S}^2\right) \\ & - 2M_{F,D}\sin(2t)\left((M_{F,D}-M_{F,S})(M_{F,D}+M_{F,S})\right. \\ & \times \left(M_{S,S}^4\left(M_{F,S}^2-M_{F,D}^2\right)\log\left(M_{S,S}^2\right)\right. \\ & +M_{F,D}^2(M_{F,D}-M_{S,S})(M_{F,D}+M_{S,S}) \\ & \left.\times (M_{F,S}-M_{S,S})(M_{F,S}+M_{S,S})\right) \\ & + M_{F,S}^4\left(M_{F,D}^2-M_{S,S}^2\right)^2\log\left(M_{F,S}^2\right) \\ & + M_{F,D}^2\log\left(M_{F,D}^2\right)\left(M_{F,D}^2\left(M_{S,S}^4-M_{F,S}^4\right)\right. \\ & \left.+2M_{F,S}^2M_{S,S}^2(M_{F,S}-M_{S,S})(M_{F,S}+M_{S,S})\right)\Big) \\ & + M_{F,S}^3\left(-\left(M_{F,D}^2+M_{F,S}^2\right)\right)\left(M_{F,D}^2-M_{S,S}^2\right)^2\log\left(M_{F,S}^2\right) \\ & + M_{F,D}^2M_{F,S}(M_{F,S}-M_{S,S})(M_{F,S}+M_{S,S}) \\ & \times \left(\log\left(M_{F,D}^2\right)\right. \\ & \left(M_{F,D}^4+M_{F,D}^2\left(M_{F,S}^2+M_{S,S}^2\right)-3M_{F,S}^2M_{S,S}^2\right) \\ & - 2(M_{F,D}-M_{F,S})(M_{F,D}+M_{F,S}) \\ & \left.\times (M_{F,D}-M_{S,S})(M_{F,D}+M_{S,S})\right)\Big) \\ & \times \frac{1}{32\pi^2\left(M_{F,D}^2-M_{F,S}^2\right)^2}\times\frac{1}{\left(M_{F,D}^2-M_{S,S}^2\right)^2} \\ & \times \frac{1}{\left(M_{F,S}^2-M_{S,S}^2\right)}, \\ M_{12} =& -Am_\lambda\left(Av\left(M_{F,D}^3\log\left(M_{F,D}^2\right)\right.\right. \\ & (M_{F,S}-M_{S,D})(M_{F,S}+M_{S,D}) \\ & (M_{F,S}-M_{S,S})(M_{F,S}+M_{S,S}) \\ & (M_{S,D}-M_{S,S})(M_{S,D}+M_{S,S}) \\ & + M_{F,S}^3(M_{F,D}-M_{S,D})(M_{F,D}+M_{S,D}) \\ & \times (M_{F,D}-M_{S,S})(M_{F,D}+M_{S,S}) \end{aligned}$$

$$
\begin{aligned}
&\times \log\left(M_{F,S}^2\right)\left(M_{S,D}-M_{S,S}\right)\left(M_{S,D}+M_{S,S}\right)\\
&+\left(M_{F,D}+M_{F,S}\right)\left(M_{S,D}^2\left(M_{F,D}-M_{S,S}\right)\left(M_{F,D}+M_{S,S}\right)\right.\\
&\times\left(M_{F,S}-M_{S,S}\right)\left(M_{F,S}+M_{S,S}\right)\\
&\times\log\left(M_{S,D}^2\right)\left(M_{S,D}^2-M_{F,D}M_{F,S}\right)\\
&+\left.M_{S,S}^2\left(M_{S,D}-M_{F,D}\right)\left(M_{F,D}+M_{S,D}\right)\right.\\
&\left(M_{S,D}-M_{F,S}\right)\left(M_{F,S}+M_{S,D}\right)\\
&\times\left.\log\left(M_{S,S}^2\right)\left(M_{F,D}M_{F,S}-M_{S,S}^2\right)\right)\\
&\times\left(M_{F,D}\cos(t)+M_{F,S}\sin(t)\right))\\
&\times\frac{1}{16\pi^2\left(M_{F,D}-M_{F,S}\right)}\times\frac{1}{\left(M_{F,D}+M_{F,S}\right)}\\
&\times\frac{1}{\left(M_{F,D}-M_{S,D}\right)}\times\frac{1}{\left(M_{F,D}+M_{S,D}\right)}\\
&\times\frac{1}{\left(M_{F,D}-M_{S,S}\right)}\times\frac{1}{\left(M_{F,D}+M_{S,S}\right)}\\
&\times\frac{1}{\left(M_{F,S}-M_{S,D}\right)}\times\frac{1}{\left(M_{F,S}+M_{S,D}\right)}\\
&\times\frac{1}{\left(M_{F,S}-M_{S,S}\right)}\times\frac{1}{\left(M_{F,S}+M_{S,S}\right)}\\
&\times\frac{1}{\left(M_{S,D}-M_{S,S}\right)}\times\frac{1}{\left(M_{S,D}+M_{S,S}\right)},
\end{aligned}
\tag{J.442}
$$

$$
\begin{aligned}
M_{22} =&-\left(M_{F,S}v^2\left(M_{F,S}^2\log\left(M_{F,S}^2\right)-M_{S,D}^2\log\left(M_{S,D}^2\right)\right)\right)\\
&\frac{1}{4\pi^2\left(M_{S,D}^2-M_{F,S}^2\right)}\times\frac{1}{\left(2M_{S,D}^2-2M_{S,S}^2\right)^2}\\
&+\left(M_{F,S}v^2\left(M_{F,S}^2\log\left(M_{F,S}^2\right)-M_{S,S}^2\log\left(M_{S,S}^2\right)\right)\right)\\
&\frac{1}{4\pi^2\left(M_{S,S}^2-M_{F,S}^2\right)}\times\frac{1}{\left(2M_{S,D}^2-2M_{S,S}^2\right)^2}\\
&+\left(M_{F,S}\left(M_{F,S}^2v^2\log\left(M_{S,D}^2\right)\right.\right.\\
&\left.\left.+M_{F,S}^2v^2-M_{F,S}^2v^2\log\left(M_{F,S}^2\right)-M_{S,D}^2v^2\right)\right)\\
&\frac{1}{16\pi^2\left(M_{F,S}^2-M_{S,D}^2\right)^2}\times\frac{1}{\left(M_{S,D}^2-M_{S,S}^2\right)}.
\end{aligned}
\tag{J.443}
$$

J.0.3 $A = 0$ *and* $m_\lambda \ll 1$

Vanishing scalar mixing $A = 0$ leads to

$$
\begin{aligned}
&M_{11} \propto m_\lambda^2,\\
&M_{12} \propto 0,\\
&M_{22} \propto m_\lambda^2 + \mathrm{Const.}
\end{aligned}
\tag{J.444}
$$

J.0.4 $A \ll 1$ *and* $m_\lambda = 0$

In the opposite case of negligible fermion mixing one finds

$$\begin{aligned}
&M_{11} \propto 0,\\
&M_{12} \propto 0,\\
&M_{22} \propto \mathrm{Const} + A^2.
\end{aligned} \tag{J.445}$$

The entire expression is

$$\begin{aligned}
M_{11} =& 0,\\
M_{12} =& 0,\\
M_{22} =& \left(\left(\left(M_{F,S}\left(M_{F,S}^2 \log\left(M_{F,S}^2\right)\right.\right.\right.\right.\\
&-\frac{1}{2}\left(\lambda_D v^2+\lambda'_D v^2+\lambda''_D v^2+2M_{S,D}^2\right)\\
&\left.\left.\left.\left.\times\log\left(\frac{1}{2}\left(\lambda_D v^2+\lambda'_D v^2+\lambda''_D v^2+2M_{S,D}^2\right)\right)\right)\right)\right)\\
&\times\frac{1}{8\pi^2\left(\lambda_D v^2+\lambda'_D v^2+\lambda''_D v^2-2M_{F,S}^2+2M_{S,D}^2\right)}\\
&-\left(M_{F,S}\left(M_{F,S}^2\log\left(M_{F,S}^2\right)\right.\right.\\
&\left.-\left(\frac{1}{2}v^2(\lambda_D+\lambda'_D-\lambda''_D)+M_{S,D}^2\right)\right.\\
&\left.\left.\times\log\left(\frac{1}{2}v^2(\lambda_D+\lambda'_D-\lambda''_D)+M_{S,D}^2\right)\right)\right)\\
&\left.\times\frac{1}{16\pi^2\left(\frac{1}{2}v^2(\lambda_D+\lambda'_D-\lambda''_D)-M_{F,S}^2+M_{S,D}^2\right)}\right)\\
&+O\left(A^3\right)\Big)\\
&+A^2\left(\left(M_{F,S}v^2\right.\right.\\
&\left(-\left(\left(v^2(-\lambda_S+\lambda_D+\lambda'_D+\lambda''_D)\right.\right.\right.\\
&\left.\left.\left.+2M_{S,D}^2-2M_{S,S}^2\right)\right.\\
&\times\left(2M_{F,S}^2\left(\log\left(M_{F,S}^2\right)\right.\right.\\
&\left.\left.-\log\left(\frac{1}{2}v^2(\lambda_D+\lambda'_D+\lambda''_D)+M_{S,D}^2\right)\right)\right.\\
&\left.+v^2(\lambda_D+\lambda'_D+\lambda''_D)-2M_{F,S}^2+2M_{S,D}^2\right))\\
&\times\frac{1}{\left(v^2(\lambda_D+\lambda'_D+\lambda''_D)-2M_{F,S}^2+2M_{S,D}^2\right)^2}\\
&+\left(\left(\lambda_S v^2+2M_{S,S}^2\right)\log\left(\frac{\lambda_S v^2}{2}+M_{S,S}^2\right)\right.\\
&\left.-2M_{F,S}^2\log\left(M_{F,S}^2\right)\right)\\
&\frac{1}{-\lambda_S v^2+2M_{F,S}^2-2M_{S,S}^2}\\
&+\left(2M_{F,S}^2\log\left(M_{F,S}^2\right)\right.
\end{aligned}$$

$$
\begin{aligned}
&- \left(v^2(\lambda_D + \lambda'_D + \lambda''_D) + 2M^2_{S,D}\right) \\
&\times \log\left(\frac{1}{2}v^2(\lambda_D + \lambda'_D + \lambda''_D) + M^2_{S,D}\right)\Bigg) \\
&\frac{1}{-v^2(\lambda_D + \lambda'_D + \lambda''_D) + 2M^2_{F,S} - 2M^2_{S,D}}\Bigg)\Bigg) \\
&\times \frac{1}{4\pi^2\left(v^2(-\lambda_S + \lambda_D + \lambda'_D + \lambda''_D) + 2M^2_{S,D} - 2M^2_{S,S}\right)^2}\Bigg).
\end{aligned}
\tag{J.446}
$$

J.0.5 $A \ll 1$ *and* $m_\lambda \ll 1$

For the case of small mixing in both sectors the matrix elements follow the proportionalities

$$
\begin{aligned}
M_{11} &\propto m^2_\lambda, \\
M_{12} &\propto A m_\lambda, \\
M_{22} &\propto A^2 + m^2_\lambda + \mathrm{Const.}
\end{aligned}
\tag{J.447}
$$

Whereas the full results are very lengthy and therefore not displayed here.

BIBLIOGRAPHY

[1] Planck Collaboration et al. "Planck 2015 results. XIII. Cosmological parameters." In: (2015). DOI: 10.1051/0004-6361/201525830. eprint: arXiv:1502.01589.

[2] C. L. Bennett et al. "Nine-Year Wilkinson Microwave Anisotropy Probe (WMAP) Observations: Final Maps and Results." In: (2012). DOI: 10.1088/0067-0049/208/2/20. eprint: arXiv:1212.5225.

[3] P. Binétruy. "Cosmology and Gravitation: the grand scheme for High-Energy Physics." In: (2015). DOI: 10.5170/CERN-2014-008.217. eprint: arXiv:1504.07050.

[4] V. C. Rubin et al. "Motion of the Galaxy and the local group determined from the velocity anisotropy of distant SC I galaxies. II - The analysis for the motion." In: 81 (Sept. 1976), pp. 719–737. DOI: 10.1086/111943.

[5] J. H. Oort. "The force exerted by the stellar system in the direction perpendicular to the galactic plane and some related problems." In: 6 (Aug. 1932), p. 249.

[6] F. Zwicky. "Die Rotverschiebung von extragalaktischen Nebeln." In: *Helvetica Physica Acta* 6 (1933), pp. 110–127.

[7] J. S. Sanders et al. "Linear Structures in the Core of the Coma Cluster of Galaxies." In: (2013). DOI: 10.1126/science.1238334. eprint: arXiv:1309.4866.

[8] J.-P. Kneib et al. "Hubble Space Telescope Observations of the Lensing Cluster Abell 2218." In: *The Astrophysical Journal* 471.2 (1996), p. 643. URL: http://stacks.iop.org/0004-637X/471/i=2/a=643.

[9] V. C. Rubin and W. K. Ford Jr. "Rotation of the Andromeda Nebula from a Spectroscopic Survey of Emission Regions." In: 159 (Feb. 1970), p. 379. DOI: 10.1086/150317.

[10] T. S. van Albada et al. "Distribution of dark matter in the spiral galaxy NGC 3198." In: 295 (Aug. 1985), pp. 305–313. DOI: 10.1086/163375.

[11] M. Milgrom. "A modification of the Newtonian dynamics as a possible alternative to the hidden mass hypothesis." In: 270 (July 1983), pp. 365–370. DOI: 10.1086/161130.

[12] A. Blondel et al. *Research Proposal for an Experiment to Search for the Decay -> eee*. 2013. eprint: arXiv:1301.6113.

[13] NASA. URL: http://chandra.harvard.edu/.

[14] Douglas Clowe et al. "A direct empirical proof of the existence of dark matter." In: (2006). DOI: 10.1086/508162. eprint: arXiv:astro-ph/0608407.

[15] Sidney Liebes. "Gravitational Lenses." In: *Phys. Rev.* 133 (3B 1964), B835–B844. DOI: 10.1103/PhysRev.133.B835. URL: https://link.aps.org/doi/10.1103/PhysRev.133.B835.

[16] VR Eshleman. "Gravitational Lens of the Sun: Its Potential for Observations and Communications over Interstellar Distances." In: *Science (New York, N.Y.)* 205.4411 (1979), 1133—1135. ISSN: 0036-8075. DOI: 10.1126/science.205.4411.1133. URL: https://doi.org/10.1126/science.205.4411.1133.

[17] C. Alcock et al. "The MACHO Project: Microlensing Results from 5.7 Years of Large Magellanic Cloud Observations." In: 542 (Oct. 2000), pp. 281–307. DOI: 10.1086/309512. eprint: astro-ph/0001272.

[18] P. Tisserand et al. "Limits on the Macho Content of the Galactic Halo from the EROS-2 Survey of the Magellanic Clouds." In: (2006). DOI: 10.1051/0004-6361:20066017. eprint: arXiv:astro-ph/0607207.

[19] Maruša Bradač et al. "Revealing the Properties of Dark Matter in the Merging Cluster MACS J0025.4–1222." In: *The Astrophysical Journal* 687.2 (2008), p. 959. URL: http://stacks.iop.org/0004-637X/687/i=2/a=959.

[20] David Harvey et al. "The non-gravitational interactions of dark matter in colliding galaxy clusters." In: (2015). DOI: 10.1126/science.1261381. eprint: arXiv:1503.07675.

[21] G. F. Smoot et al. "Structure in the COBE differential microwave radiometer first-year maps." In: 396 (Sept. 1992), pp. L1–L5. DOI: 10.1086/186504.

[22] G. Hinshaw et al. "Nine-Year Wilkinson Microwave Anisotropy Probe (WMAP) Observations: Cosmological Parameter Results." In: (2012). DOI: 10.1088/0067-0049/208/2/19. eprint: arXiv:1212.5226.

[23] C. L. Bennett et al. "First-Year Wilkinson Microwave Anisotropy Probe (WMAP) Observations: Preliminary Maps and Basic Results." In: 148 (Sept. 2003), pp. 1–27. DOI: 10.1086/377253. eprint: astro-ph/0302207.

[24] J. C. Mather et al. "Measurement of the cosmic microwave background spectrum by the COBE FIRAS instrument." In: 420 (Jan. 1994), pp. 439–444. DOI: 10.1086/173574.

[25] D. J. Fixsen et al. "Cosmic microwave background dipole spectrum measured by the COBE FIRAS instrument." In: 420 (Jan. 1994), pp. 445–449. DOI: 10.1086/173575.

[26] D. J. Fixsen et al. "The Cosmic Microwave Background Spectrum from the Full COBE FIRAS Data Set." In: 473 (Dec. 1996), p. 576. DOI: 10.1086/178173. eprint: astro-ph/9605054.

[27] R. K. Sachs and A. M. Wolfe. "Perturbations of a Cosmological Model and Angular Variations of the Microwave Background." In: 147 (Jan. 1967), p. 73. DOI: 10.1086/148982.

[28] R. A. Alpher, H. Bethe, and G. Gamow. "The Origin of Chemical Elements." In: *Physical Review* 73 (Apr. 1948), pp. 803–804. DOI: 10.1103/PhysRev.73.803.

[29] R. H. Dicke et al. "Cosmic Black-Body Radiation." In: 142 (July 1965), pp. 414–419. DOI: 10.1086/148306.

[30] A. A. Penzias and R. W. Wilson. "A Measurement of Excess Antenna Temperature at 4080 Mc/s." In: 142 (July 1965), pp. 419–421. DOI: 10.1086/148307.

[31] F. K. Hansen et al. "Foreground Subtraction of Cosmic Microwave Background Maps using WI-FIT (Wavelet based hIgh resolution Fitting of Internal Templates)." In: (2006). DOI: 10.1086/506015. eprint: arXiv:astro-ph/0603308.

[32] Wayne Hu, Naoshi Sugiyama, and Joseph Silk. "The Physics of Microwave Background Anisotropies." In: (1996). DOI: 10.1038/386037a0. eprint: arXiv:astro-ph/9604166.

[33] R. Tojeiro. *Understanding the Cosmic Microwave Background Temperature Power Spectrum*. 2016. URL: http://www.roe.ac.uk/ifa/postgrad/pedagogy/2006_tojeiro.pdf.

[34] J. A. Peacock. *Cosmological Physics*. Jan. 1999, p. 704.

[35] N. Kaiser and J. Silk. "Cosmic microwave background anisotropy." In: 324 (Dec. 1986), pp. 529–537. DOI: 10.1038/324529a0.

[36] The Virgo Consortium et al. "Evolution of structure in cold dark matter universes." In: (1997). DOI: 10.1086/305615. eprint: arXiv:astro-ph/9709010.

[37] Simon Folkes et al. "The 2dF Galaxy Redshift Survey: spectral types and luminosity functions." In: *Monthly Notices of the Royal Astronomical Society* 308.2 (), pp. 459–472. DOI: 10.1046/j.1365-8711.1999.02721.x. eprint: https://onlinelibrary.wiley.com/doi/pdf/10.1046/j.1365-8711.1999.02721.x. URL: https://onlinelibrary.wiley.com/doi/abs/10.1046/j.1365-8711.1999.02721.x.

[38] Matthew Colless et al. "The 2dF Galaxy Redshift Survey: Spectra and redshifts." In: (2001). DOI: 10.1046/j.1365-8711.2001.04902.x. eprint: arXiv:astro-ph/0106498.

[39] V. Springel et al. "Simulations of the formation, evolution and clustering of galaxies and quasars." In: 435 (June 2005), pp. 629–636. DOI: 10.1038/nature03597. eprint: astro-ph/0504097.

[40] B. Moore et al. "Dark Matter Substructure within Galactic Halos." In: 524 (Oct. 1999), pp. L19–L22. DOI: 10.1086/312287. eprint: astro-ph/9907411.

[41] A. Klypin et al. "Where Are the Missing Galactic Satellites?" In: 522 (Sept. 1999), pp. 82–92. DOI: 10.1086/307643. eprint: astro-ph/9901240.

[42] D. P. Bennett et al. *The MACHO Project Dark Matter Search*. 1995. eprint: arXiv:astro-ph/9510104.

[43] M. Milgrom. "Dynamics with a non-standard inertia-acceleration relation: an alternative to dark matter." In: (1993). DOI: 10.1006/aphy.1994.1012. eprint: arXiv:astro-ph/9303012.

[44] Laura Lopez-Honorez et al. "Constraints on warm dark matter from the ionization history of the Universe." In: (2017). DOI: 10.1103/PhysRevD.96.103539. eprint: arXiv:1703.02302.

[45] Rennan Barkana, Zoltan Haiman, and Jeremiah P. Ostriker. "Constraints on Warm Dark Matter from Cosmological Reionization." In: (2001). DOI: 10.1086/322393. eprint: arXiv:astro-ph/0102304.

[46] Paul Bode, Jeremiah P. Ostriker, and Neil Turok. "Halo Formation in Warm Dark Matter Models." In: (2000). DOI: 10.1086/321541. eprint: arXiv:astro-ph/0010389.

[47] G. Jungman, M. Kamionkowski, and K. Griest. "Supersymmetric Dark Matter." In: (1995). DOI: 10.1016/0370-1573(95)00058-5. eprint: arXiv:hep-ph/9506380.

[48] Jonathan M. Cornell, Stefano Profumo, and William Shepherd. "Dark Matter in Minimal Universal Extra Dimensions with a Stable Vacuum and the "Right" Higgs." In: (2014). DOI: 10.1103/PhysRevD.89.056005. eprint: arXiv:1401.7050.

[49] R. D. Peccei and Helen R. Quinn. "CP Conservation in the Presence of Pseudoparticles." In: *Phys. Rev. Lett.* 38 (25 1977), pp. 1440–1443. DOI: 10.1103/PhysRevLett.38.1440. URL: https://link.aps.org/doi/10.1103/PhysRevLett.38.1440.

[50] R. D. Peccei. "The Strong CP Problem and Axions." In: (2006). DOI: 10.1007/978-3-540-73518-2_1. eprint: arXiv:hep-ph/0607268.

[51] Javier Redondo and Andreas Ringwald. "Light shining through walls." In: (2010). DOI: 10.1080/00107514.2011.563516. eprint: arXiv:1011.3741.

[52] Ian Aitchison. *Supersymmetry in Particle Physics: An Elementary Introduction*. Cambridge University Press, 2007. DOI: 10.1017/CBO9780511619250.

[53] Julia Harz et al. *Precise Prediction of the Dark Matter Relic Density within the MSSM*. 2015. eprint: arXiv:1510.06295.

[54] Graham G. Ross, Kai Schmidt-Hoberg, and Florian Staub. "Revisiting fine-tuning in the MSSM." In: (2017). DOI: 10.1007/JHEP03(2017)021. eprint: arXiv:1701.03480.

[55] J. C. Costa et al. "Likelihood Analysis of the Sub-GUT MSSM in Light of LHC 13-TeV Data." In: (2017). DOI: 10.1140/epjc/s10052-018-5633-3. eprint: arXiv:1711.00458.

[56] J. Wess and B. Zumino. "Supergauge transformations in four dimensions." In: *Nuclear Physics B* 70 (Feb. 1974), pp. 39–50. DOI: 10.1016/0550-3213(74)90355-1.

[57] Carlos Munoz. "Models of Supersymmetry for Dark Matter." In: (2017). DOI: 10.1051/epjconf/201713601002. eprint: arXiv:1701.05259.

[58] Alexandre Arbey, Marco Battaglia, and Farvah Mahmoudi. "The Higgs boson, Supersymmetry and Dark Matter: Relations and Perspectives." In: (2015). DOI: 10.1002/andp.201500007. eprint: arXiv:1504.05091.

[59] Claudia Seitz, on behalf of the ATLAS, and CMS Collaborations. *Searches for strong production of supersymmetry at ATLAS and CMS*. 2017. eprint: arXiv:1710.05327.

[60] Andrea Ventura. *Searches for supersymmetry*. 2017. eprint: arXiv:1711.00152.

[61] ATLAS Collaboration. "Search for dark matter and other new phenomena in events with an energetic jet and large missing transverse momentum using the ATLAS detector." In: (2017). DOI: 10.1007/JHEP01(2018)126. eprint: arXiv:1711.03301.

[62] ATLAS Collaboration. "Search for new phenomena in final states with an energetic jet and large missing transverse momentum in pp collisions at $\sqrt{s} = 13$ TeV using the ATLAS detector." In: (2016). DOI: 10.1103/PhysRevD.94.032005. eprint: arXiv:1604.07773.

[63] Alexandre Alves et al. *Dirac-Fermionic Dark Matter in* $U(1)_X$ *Models*. 2015. eprint: arXiv:1506.06767.

[64] G. Bélanger et al. "Impact of semi-annihilations on dark matter phenomenology - an example of Z_N $symmetric scalar dark matter$." In: (2012). DOI: 10.1088/1475-7516/2012/04/010. eprint: arXiv:1202.2962.

[65] Michael Gustafsson. "The Inert Doublet Model and its Phenomenology." In: (2011). eprint: arXiv:1106.1719.

[66] Debasish Borah and Aritra Gupta. "A New Viable Region of Inert Higgs Doublet Dark Matter Model with Scotogenic Extension." In: (2017). DOI: 10.1103/PhysRevD.96.115012. eprint: arXiv:1706.05034.

[67] Yeong Gyun Kim, Kang Young Lee, and Seodong Shin. "Singlet fermionic dark matter." In: (2008). DOI: 10.1088/1126-6708/2008/05/100. eprint: arXiv:0803.2932.

[68] Mohammadmahdi Ettefaghi and Reza Moazzemi. "Analyzing of singlet fermionic dark matter via the updated direct detection data." In: (2017). DOI: 10.1140/epjc/s10052-017-4894-6. eprint: arXiv:1705.07571.

[69] James M. Cline et al. "Update on scalar singlet dark matter." In: (2013). DOI: 10.1103/PhysRevD.88.055025. eprint: arXiv:1306.4710.

[70] E. C. F. S. Fortes et al. *Scalar Dark Matter Candidates in Two Inert Higgs Doublet Model*. 2014. eprint: arXiv:1407.4749.

[71] G. Belanger et al. "Light mixed sneutrinos as thermal dark matter." In: (2010). DOI: 10.1088/1475-7516/2010/11/017. eprint: arXiv:1008.0580.

[72] J. Alberto Casas et al. "Reopening the Higgs portal for Singlet Scalar Dark Matter." In: (2017). DOI: 10.1007/JHEP05(2017)036. eprint: arXiv:1701.08134.

[73] Teruki Kamon, P. Ko, and Jinmian Li. "Characterizing Higgs portal dark matter models at the ILC." In: (2017). DOI: 10.1140/epjc/s10052-017-5240-8. eprint: arXiv:1705.02149.

[74] Martin Hoferichter et al. "Improved limits for Higgs-portal dark matter from LHC searches." In: (2017). DOI: 10.1103/PhysRevLett.119.181803. eprint: arXiv:1708.02245.

[75] Bjoern Penning. *The Pursuit of Dark Matter at Collider - An Overview*. 2017. eprint: arXiv:1712.01391.

[76] F. J. Kerr and D. Lynden-Bell. "Review of galactic constants." In: 221 (Aug. 1986), pp. 1023–1038. DOI: 10.1093/mnras/221.4.1023.

[77] Anne M. Green. "Astrophysical uncertainties on direct detection experiments." In: (2011). DOI: 10.1142/S0217732312300042. eprint: arXiv:1112.0524.

[78] M. Angeles Perez-Garcia, Joseph Silk, and Jirina R. Stone. "Dark Matter, Neutron Stars, and Strange Quark Matter." In: *Phys. Rev. Lett.* 105 (14 2010), p. 141101. DOI: 10.1103/PhysRevLett.105.141101. URL: https://link.aps.org/doi/10.1103/PhysRevLett.105.141101.

[79] Teresa Marrodan Undagoitia and Ludwig Rauch. "Dark matter direct-detection experiments." In: (2015). DOI: 10.1088/0954-3899/43/1/013001. eprint: arXiv:1509.08767.

[80] C. Levy et al. "Xenon Bubble Chambers for Direct Dark Matter Detection." In: (2016). DOI: 10.1088/1748-0221/11/03/C03003. eprint: arXiv:1601.05131.

[81] C. Tomei. "SABRE: Dark matter annual modulation detection in the northern and southern hemispheres." In: *Nuclear Instruments and Methods in Physics Research A* 845 (Feb. 2017), pp. 418–420. DOI: 10.1016/j.nima.2016.06.007.

[82] R. Bernabei et al. "First results from DAMA/LIBRA and the combined results with DAMA/NaI." In: (2008). DOI: 10.1140/epjc/s10052-008-0662-y. eprint: arXiv:0804.2741.

[83] R. Bernabei et al. "No role for muons in the DAMA annual modulation results." In: (2012). DOI: 10.1140/epjc/s10052-012-2064-4. eprint: arXiv:1202.4179.

[84] R. Bernabei et al. "Performances of the $\perp$ 100kgNaI(Tl)set − upoftheDAMAexperimentatGranSasso.." In: *Nuovo Cimento A Serie* 112 (June 1999), pp. 545–575. DOI: 10.1007/BF03035868.

[85] DEAP Collaboration et al. "DEAP-3600 Dark Matter Search." In: (2014). DOI: 10.1016/j.nuclphysbps.2015.09.048. eprint: arXiv:1410.7673.

[86] K. Rielage et al. *Update on the MiniCLEAN Dark Matter Experiment*. 2014. eprint: arXiv:1403.4842.

[87] K. Abe et al. "XMASS detector." In: (2013). DOI: 10.1016/j.nima.2013.03.059. eprint: arXiv:1301.2815.

[88] C. E. Aalseth et al. "Search for an Annual Modulation in a P-type Point Contact Germanium Dark Matter Detector." In: (2011). DOI: 10.1103/PhysRevLett.107.141301. eprint: arXiv:1106.0650.

[89] C. Amole et al. "Dark Matter Search Results from the PICO-60 C_3F_8 Bubble Chamber." In: (2017). DOI: 10.1103/PhysRevLett.118.251301. eprint: arXiv:1702.07666.

[90] M Felizardo et al. "Recent results from the SIMPLE dark matter search." In: *Journal of Physics: Conference Series* 375.1 (2012), p. 012011. URL: http://stacks.iop.org/1742-6596/375/i=1/a=012011.

[91] Z. Ahmed et al. "Results from a Low-Energy Analysis of the CDMS II Germanium Data." In: *Physical Review Letters* 106.13, 131302 (Apr. 2011), p. 131302. DOI: 10.1103/PhysRevLett.106.131302. arXiv: 1011.2482 [astro-ph.CO].

[92] R. Agnese et al. "Silicon Detector Dark Matter Results from the Final Exposure of CDMS II." In: *Physical Review Letters* 111.25, 251301 (Dec. 2013), p. 251301. DOI: 10.1103/PhysRevLett.111.251301.

[93] R. Agnese et al. "Search for Low-Mass Weakly Interacting Massive Particles with SuperCDMS." In: *Physical Review Letters* 112.24, 241302 (June 2014), p. 241302. DOI: 10.1103/PhysRevLett.112.241302. arXiv: 1402.7137 [hep-ex].

[94] M. Chapellier et al. "Dark Matter Search in the Edelweiss Experiment." In: (2001). DOI: 10.1142/9789812811363_0045. eprint: arXiv:astro-ph/0101204.

[95] E. Armengaud et al. "Axion searches with the EDELWEISS-II experiment." In: 11, 067 (Nov. 2013), p. 067. DOI: 10.1088/1475-7516/2013/11/067. arXiv: 1307.1488.

[96] Adriana E. Lita, Aaron J. Miller, and Sae Woo Nam. "Counting near-infrared single-photons with 95% efficiency." In: *Opt. Express* 16.5 (2008), pp. 3032–3040. DOI: 10.1364/OE.16.003032. URL: http://www.opticsexpress.org/abstract.cfm?URI=oe-16-5-3032.

[97] J Schieck et al. *Direct Dark Matter Search with the CRESST II Experiment*. 2016. eprint: arXiv:1611.02113.

[98] CRESST collaboration et al. *First results on low-mass dark matter from the CRESST-III experiment*. 2017. eprint: arXiv:1711.07692.

[99] J. Schieck for the CRESST collaboration. *Direct Dark Matter Search with the CRESST-II Experiment*. 2015. eprint: arXiv:1505.03289.

[100] D. S. Akerib et al. "The Large Underground Xenon (LUX) experiment." In: *Nuclear Instruments and Methods in Physics Research A* 704 (Mar. 2013), pp. 111–126. DOI: 10.1016/j.nima.2012.11.135. arXiv: 1211.3788 [physics.ins-det].

[101] A. Tan et al. "Dark matter search results from the commissioning run of PandaX-II." In: 93.12, 122009 (June 2016), p. 122009. DOI: 10.1103/PhysRevD.93.122009.

[102] J. Liu, X. Chen, and X. Ji. "Current status of direct dark matter detection experiments." In: *Nature Physics* 13 (Mar. 2017), pp. 212–216. DOI: 10.1038/nphys4039. arXiv: 1709.00688.

[103] XENON100 Collaboration et al. "The XENON100 Dark Matter Experiment." In: (2011). DOI: 10.1016/j.astropartphys.2012.01.003. eprint: arXiv:1107.2155.

[104] E. Aprile et al. "First Dark Matter Search Results from the XENON1T Experiment." In: (2017). DOI: 10.1103/PhysRevLett.119.181301. eprint: arXiv:1705.06655.

[105] Andrzej K. Drukier, Katherine Freese, and David N. Spergel. "Detecting cold dark-matter candidates." In: *Phys. Rev. D* 33 (12 1986), pp. 3495–3508. DOI: 10.1103/PhysRevD.33.3495. URL: https://link.aps.org/doi/10.1103/PhysRevD.33.3495.

[106] Christopher Savage et al. "Compatibility of DAMA/LIBRA dark matter detection with other searches." In: (2008). DOI: 10.1088/1475-7516/2009/04/010. eprint: arXiv:0808.3607.

[107] Jonathan H. Davis. "Fitting the annual modulation in DAMA with neutrons from muons and neutrinos." In: (2014). DOI: 10.1103/PhysRevLett.113.081302. eprint: arXiv:1407.1052.

[108] Andriy Kurylov and Marc Kamionkowski. "Generalized Analysis of Weakly-Interacting Massive Particle Searches." In: (2003). DOI: 10.1103/PhysRevD.69.063503. eprint: arXiv:hep-ph/0307185.

[109] R. Foot. "Can dark matter - electron scattering explain the DAMA annual modulation signal?" In: (2014). DOI: 10.1103/PhysRevD.90.121302. eprint: arXiv:1407.4213.

[110] Jonathan L. Feng, Jason Kumar, and Louis E. Strigari. "Explaining the DAMA Signal with WIMPless Dark Matter." In: (2008). DOI: 10.1016/j.physletb.2008.10.038. eprint: arXiv:0806.3746.

[111] The LZ Collaboration et al. *LUX-ZEPLIN (LZ) Conceptual Design Report*. 2015. eprint: arXiv:1509.02910.

[112] E. Aprile and Xenon Collaboration. "The XENONnT Dark Matter Experiment." In: *APS April Meeting Abstracts*. Jan. 2017, J9.003.

[113] Jan Conrad. *Indirect Detection of WIMP Dark Matter: a compact review*. 2014. eprint: arXiv:1411.1925.

[114] R. Schödel, D. Merritt, and A. Eckart. "The nuclear star cluster of the Milky Way: proper motions and mass." In: 502 (July 2009), pp. 91–111. DOI: 10.1051/0004-6361/200810922. arXiv: 0902.3892.

[115] C. S. Reynolds. "Astrophysics: Bringing black holes into focus." In: 455 (Sept. 2008), pp. 39–40. DOI: 10.1038/455039a.

[116] S. Gillessen et al. "Monitoring stellar orbits around the Massive Black Hole in the Galactic Center." In: (2008). DOI: 10.1088/0004-637X/692/2/1075. eprint: arXiv:0810.4674.

[117] B. Zitzer for the VERITAS Collaboration. *The VERITAS Dark Matter Program*. 2015. eprint: arXiv:1503.00743.

[118] The Veritas Collaboration et al. "Constraints on Cosmic Rays, Magnetic Fields, and Dark Matter from Gamma-Ray Observations of the Coma Cluster of Galaxies with VERITAS and Fermi." In: (2012). DOI: 10.1088/0004-637X/757/2/123. eprint: arXiv:1208.0676.

[119] Lucia Rinchiuso, Emmanuel Moulin, and for the H. E. S. S. Collaboration. *Dark matter searches toward the Galactic Centre halo with H.E.S.S.* 2017. eprint: arXiv:1711.08634.

[120] H. E. S. S. Collaboration et al. "Search for dark matter annihilation signatures in H.E.S.S. observations of Dwarf Spheroidal Galaxies." In: (2014). DOI: 10.1103/PhysRevD.90.112012. eprint: arXiv:1410.2589.

[121] Michele Doro. *A review of the past and present MAGIC dark matter search program and a glimpse at the future*. 2017. eprint: arXiv:1701.05702.

[122] J. Aleksić et al. "Optimized dark matter searches in deep observations of Segue 1 with MAGIC." In: (2013). DOI: 10.1088/1475-7516/2014/02/008. eprint: arXiv:1312.1535.

[123] Fermi/LAT Collaboration, : and W. B. Atwood. "The Large Area Telescope on the Fermi Gamma-ray Space Telescope Mission." In: (2009). DOI: 10.1088/0004-637X/697/2/1071. eprint: arXiv:0902.1089.

[124] The Fermi-LAT et al. "Searching for Dark Matter Annihilation in Recently Discovered Milky Way Satellites with Fermi-LAT." In: (2016). DOI: 10.3847/1538-4357/834/2/110. eprint: arXiv:1611.03184.

[125] G.A. Gómez-Vargas et al. "Dark matter implications of Fermi-LAT measurement of anisotropies in the diffuse gamma-ray background." In: *Nuclear Instruments and Methods in Physics Research Section A: Accelerators, Spectrometers, Detectors and Associated Equipment* 742 (2014). 4th Roma International Conference on Astroparticle Physics, pp. 149 –153. ISSN: 0168-9002. DOI: https://doi.org/10.1016/j.nima.2013.11.009. URL: http://www.sciencedirect.com/science/article/pii/S016890021301509X.

[126] Esra Bulbul et al. "Detection of An Unidentified Emission Line in the Stacked X-ray spectrum of Galaxy Clusters." In: (2014). DOI: 10.1088/0004-637X/789/1/13. eprint: arXiv:1402.2301.

[127] A. Boyarsky and O. Ruchayskiy. "Probing the nature of dark matter with deep XMMNewton observations of the dwarf spheroidal galaxies." In: *Astronomische Nachrichten* 338.2-3 (), pp. 287–292. DOI: 10.1002/asna.201713344. eprint: https://onlinelibrary.wiley.com/doi/pdf/10.1002/asna.201713344. URL: https://onlinelibrary.wiley.com/doi/abs/10.1002/asna.201713344.

[128] Hitomi Collaboration et al. "Hitomi constraints on the 3.5 keV line in the Perseus galaxy cluster." In: (2016). DOI: 10.3847/2041-8213/aa61fa. eprint: arXiv:1607.07420.

[129] Marcus Berg et al. "Constraints on Axion-Like Particles from X-ray Observations of NGC1275." In: (2016). DOI: 10.3847/1538-4357/aa8b16. eprint: arXiv:1605.01043.

[130] Yasaman Farzan and Amin Rezaei Akbarieh. "Decaying Vector Dark Matter as an Explanation for the 3.5 keV Line from Galaxy Clusters." In: (2014). DOI: 10.1088/1475-7516/2014/11/015. eprint: arXiv:1408.2950.

[131] Alexander Merle and Aurel Schneider. "Production of Sterile Neutrino Dark Matter and the 3.5 keV line." In: (2014). DOI: 10.1016/j.physletb.2015.07.080. eprint: arXiv:1409.6311.

[132] Nico Cappelluti et al. *Searching for the 3.5 keV Line in the Deep Fields with Chandra: the 10 Ms observations*. 2017. eprint: arXiv:1701.07932.

[133] J. Aleksić et al. "Optimized dark matter searches in deep observations of Segue 1 with MAGIC." In: (2013). DOI: 10.1088/1475-7516/2014/02/008. eprint: arXiv:1312.1535.

[134] E. Aliu et al. "VERITAS Deep Observations of the Dwarf Spheroidal Galaxy Segue 1." In: (2012). DOI: 10.1103/PhysRevD.85.062001. eprint: arXiv:1202.2144.

[135] H. E. S. S. Collaboration et al. "Search for dark matter annihilation signatures in H.E.S.S. observations of Dwarf Spheroidal Galaxies." In: (2014). DOI: 10.1103/PhysRevD.90.112012. eprint: arXiv:1410.2589.

[136] J. Buckley et al. *Cosmic Frontier Indirect Dark Matter Detection Working Group Summary*. 2013. eprint: arXiv:1310.7040.

[137] H. E. S. S. Collaboration et al. "Search for a Dark Matter annihilation signal from the Galactic Center halo with H.E.S.S." In: (2011). DOI: 10.1103/PhysRevLett.106.161301. eprint: arXiv:1103.3266.

[138] O. Adriani et al. "Ten Years of PAMELA in Space." In: (2018). DOI: 10.1393/ncr/i2017-10140-x. eprint: arXiv:1801.10310.

[139] M. Casolino et al. "Launch of the Space experiment PAMELA." In: (2007). DOI: 10.1016/j.asr.2007.07.023. eprint: arXiv:0708.1808.

[140] M. Aguilar et al. "First Result from the Alpha Magnetic Spectrometer on the International Space Station: Precision Measurement of the Positron Fraction in Primary Cosmic Rays of 0.5-350 GeV." In: *Physical Review Letters* 110.14, 141102 (Apr. 2013), p. 141102. DOI: 10.1103/PhysRevLett.110.141102.

[141] M. Aguilar et al. "The Alpha Magnetic Spectrometer (AMS) on the International Space Station: Part I – results from the test flight on the space shuttle." In: *Physics Reports* 366.6 (2002), pp. 331 –405. ISSN: 0370-1573. DOI: https://doi.org/10.1016/S0370-1573(02)00013-3. URL: http://www.sciencedirect.com/science/article/pii/S0370157302000133.

[142] Raghuveer Garani and Sergio Palomares-Ruiz. "Dark matter in the Sun: scattering off electrons vs nucleons." In: (2017). DOI: 10.1088/1475-7516/2017/05/007. eprint: arXiv:1702.02768.

[143] IceCube collaboration et al. "Search for dark matter annihilations in the Sun with the 79-string IceCube detector." In: (2012). DOI: 10.1103/PhysRevLett.110.131302. eprint: arXiv:1212.4097.

[144] The IceCube Collaboration. "First Year Performance of The IceCube Neutrino Telescope." In: (2006). DOI: 10.1016/j.astropartphys.2006.06.007. eprint: arXiv:astro-ph/0604450.

[145] ANTARES Collaboration. "ANTARES: the first undersea neutrino telescope." In: (2011). DOI: 10.1016/j.nima.2011.06.103. eprint: arXiv:1104.1607.

[146] IceCube Collaboration et al. "Multipole analysis of IceCube data to search for dark matter accumulated in the Galactic halo." In: (2014). DOI: 10.1140/epjc/s10052-014-3224-5. eprint: arXiv:1406.6868.

[147] ANTARES Collaboration et al. "Search of Dark Matter Annihilation in the Galactic Centre using the ANTARES Neutrino Telescope." In: (2015). DOI: 10.1088/1475-7516/2015/10/068. eprint: arXiv:1505.04866.

[148] M. G. Aartsen et al. "IceCube Search for Dark Matter Annihilation in nearby Galaxies and Galaxy Clusters." In: (2013). DOI: 10.1103/PhysRevD.88.122001. eprint: arXiv:1307.3473.

[149] IceCube Collaboration et al. "Search for annihilating dark matter in the Sun with 3 years of IceCube data." In: (2016). DOI: 10.1140/epjc/s10052-017-4689-9. eprint: arXiv:1612.05949.

[150] CDF Collaboration. "Limits on Extra Dimensions and New Particle Production in the Exclusive Photon and Missing Energy Signature in p pbar Collisions at sqrt(s) = 1.8 TeV." In: (2002). DOI: 10.1103/PhysRevLett.89.281801. eprint: arXiv:hep-ex/0205057.

[151] Lyndon Evans and Philip Bryant. "LHC Machine." In: *Journal of Instrumentation* 3.08 (2008), S08001. URL: http://stacks.iop.org/1748-0221/3/i=08/a=S08001.

[152] Giorgio Busoni et al. "On the Validity of the Effective Field Theory for Dark Matter Searches at the LHC." In: (2013). DOI: 10.1016/j.physletb.2013.11.069. eprint: arXiv:1307.2253.

[153] Ciaran A. J. O'Hare et al. "Readout strategies for directional dark matter detection beyond the neutrino background." In: (2015). DOI: 10.1103/PhysRevD.92.063518. eprint: arXiv:1505.08061.

[154] Daniel Abercrombie et al. *Dark Matter Benchmark Models for Early LHC Run-2 Searches: Report of the ATLAS/CMS Dark Matter Forum*. 2015. eprint: arXiv:1507.00966.

[155] Jalal Abdallah et al. *Simplified Models for Dark Matter and Missing Energy Searches at the LHC*. 2014. eprint: arXiv:1409.2893.

[156] The CMS Collaboration. "Observation of a new boson at a mass of 125 GeV with the CMS experiment at the LHC." In: (2012). DOI: 10.1016/j.physletb.2012.08.021. eprint: arXiv:1207.7235.

[157] G. Aad et al. "The ATLAS Experiment at the CERN Large Hadron Collider." In: *JINST* 3 (2008), S08003. DOI: 10.1088/1748-0221/3/08/S08003.

[158] CMS Collaboration. "Search for dijet resonances in proton-proton collisions at sqrt(s) = 13 TeV and constraints on dark matter and other models." In: (2016). DOI: 10.1016/j.physletb.2017.02.012. eprint: arXiv:1611.03568.

[159] D. S. Akerib et al. "Results from a search for dark matter in the complete LUX exposure." In: (2016). DOI: 10.1103/PhysRevLett.118.021303. eprint: arXiv:1608.07648.

[160] ATLAS Collaboration. "Summary of the ATLAS experiment's sensitivity to supersymmetry after LHC Run 1 - interpreted in the phenomenological MSSM." In: (2015). DOI: 10.1007/JHEP10(2015)134. eprint: arXiv:1508.06608.

[161] Paolo Gondolo and Graciela Gelmini. "Cosmic abundances of stable particles: Improved analysis." In: *Nucl. Phys.* B360 (1991), pp. 145–179. DOI: 10.1016/0550-3213(91)90438-4.

[162] J. Edsjo and P. Gondolo. "Neutralino Relic Density including Coannihilations." In: (1997). DOI: 10.1103/PhysRevD.56.1879. eprint: arXiv:hep-ph/9704361.

[163] Lawrence J. Hall et al. "Freeze-In Production of FIMP Dark Matter." In: (2009). DOI: 10.1007/JHEP03(2010)080. eprint: arXiv:0911.1120.

[164] Hiroshi Okada, Yuta Orikasa, and Takashi Toma. "Nonthermal dark matter models and signals." In: (2015). DOI: 10.1103/PhysRevD.93.055007. eprint: arXiv:1511.01018.

[165] Tarek Saab. "An Introduction to Dark Matter Direct Detection Searches & Techniques." In: (2012). DOI: 10.1142/9789814390163_0011. eprint: arXiv:1203.2566.

[166] J.D. Lewin and P.F. Smith. "Review of mathematics, numerical factors, and corrections for dark matter experiments based on elastic nuclear recoil." In: *Astroparticle Physics* 6.1 (1996), pp. 87–112. ISSN: 0927-6505. DOI: https://doi.org/10.1016/S0927-6505(96)00047-3. URL: http://www.sciencedirect.com/science/article/pii/S0927650596000473.

[167] W. Pauli. *Collection of Pauli's letters*. CERN document server. URL: https://cds.cern.ch/record/83282/.

[168] C. S. Wu et al. "Experimental Test of Parity Conservation in Beta Decay." In: *Phys. Rev.* 105 (4 1957), pp. 1413–1415. DOI: 10.1103/PhysRev.105.1413. URL: https://link.aps.org/doi/10.1103/PhysRev.105.1413.

[169] M. Goldhaber, L. Grodzins, and A. W. Sunyar. "Helicity of Neutrinos." In: *Phys. Rev.* 109 (3 1958), pp. 1015–1017. DOI: 10.1103/PhysRev.109.1015. URL: https://link.aps.org/doi/10.1103/PhysRev.109.1015.

[170] Bruce T. Cleveland et al. "Measurement of the Solar Electron Neutrino Flux with the Homestake Chlorine Detector." In: *The Astrophysical Journal* 496.1 (1998), p. 505. URL: http://stacks.iop.org/0004-637X/496/i=1/a=505.

[171] B. Pontecorvo. "Inverse β decay." In: *Chalk River Laboratory Report PD-205* (1946).

[172] Francesco Vissani. *Neutrino Sources and Properties*. 2014. eprint: arXiv:1412.8386.

[173] Chr. Weinheimer. "Vorlesung Nutrino- und Astoteilchenphysik." In: ().

[174] Y. Fukuda et al. "Measurement of the Flux and Zenith-Angle Distribution of Upward Throughgoing Muons by Super-Kamiokande." In: *Phys. Rev. Lett.* 82 (13 1999), pp. 2644–2648. DOI: 10.1103/PhysRevLett.82.2644. URL: https://link.aps.org/doi/10.1103/PhysRevLett.82.2644.

[175] SNO Collaboration. "Measurement of the rate of $\nu_e + d \rightarrow p + p + e^-$ interactions produced by 8B solar neutrinos at the Sudbury Neutrino Observatory." In: (2001). DOI: 10.1103/PhysRevLett.87.071301. eprint: arXiv:nucl-ex/0106015.

[176] T. Araki et al. "Measurement of Neutrino Oscillation with KamLAND: Evidence of Spectral Distortion." In: *Phys. Rev. Lett.* 94 (8 2005), p. 081801. DOI: 10.1103/PhysRevLett.94.081801. URL: https://link.aps.org/doi/10.1103/PhysRevLett.94.081801.

[177] S. M. Bilenky. "Neutrino. History of a unique particle." In: (2012). DOI: 10.1140/epjh/e2012-20068-9. eprint: arXiv:1210.3065.

[178] Petr Vogel, Liangjian Wen, and Chao Zhang. "Neutrino Oscillation Studies with Reactors." In: *Nature Commun.* 6 (2015), p. 6935. DOI: 10.1038/ncomms7935. arXiv: 1503.01059 [hep-ex].

[179] S.P. Mikheev and A.Y. Smirnov. "Resonance enhancement of oscillations in matter and solar neutrino spectroscopy." In: *Sov. J. Nucl. Phys. (Engl. Transl.); (United States)* 42:6 (Dec. 1985).

[180] L. Wolfenstein. "Neutrino oscillations in matter." In: *Phys. Rev. D* 17 (9 1978), pp. 2369–2374. DOI: 10.1103/PhysRevD.17.2369. URL: https://link.aps.org/doi/10.1103/PhysRevD.17.2369.

[181] Cédric Weiland. *Effects of fermionic singlet neutrinos on high- and low-energy observables*. 2013. eprint: arXiv:1311.5860.

[182] SNO Collaboration et al. "Combined Analysis of all Three Phases of Solar Neutrino Data from the Sudbury Neutrino Observatory." In: (2011). DOI: 10.1103/PhysRevC.88.025501. eprint: arXiv:1109.0763.

[183] S. Abe et al. "Precision Measurement of Neutrino Oscillation Parameters with KamLAND." In: *Phys. Rev. Lett.* 100 (22 2008), p. 221803. DOI: 10.1103/PhysRevLett.100.221803. URL: https://link.aps.org/doi/10.1103/PhysRevLett.100.221803.

[184] R. Wendell et al. "Atmospheric neutrino oscillation analysis with subleading effects in Super-Kamiokande I, II, and III." In: *Phys. Rev. D* 81 (9 2010), p. 092004. DOI: 10.1103/PhysRevD.81.092004. URL: https://link.aps.org/doi/10.1103/PhysRevD.81.092004.

[185] P. Adamson et al. "Measurement of the Neutrino Mass Splitting and Flavor Mixing by MINOS." In: *Phys. Rev. Lett.* 106 (18 2011), p. 181801. DOI: 10.1103/PhysRevLett.106.181801. URL: https://link.aps.org/doi/10.1103/PhysRevLett.106.181801.

[186] M. H. Ahn et al. "Indications of Neutrino Oscillation in a 250 km Long-Baseline Experiment." In: *Phys. Rev. Lett.* 90 (4 2003), p. 041801. DOI: 10.1103/PhysRevLett.90.041801. URL: https://link.aps.org/doi/10.1103/PhysRevLett.90.041801.

[187] F. P. An et al. "Observation of electron-antineutrino disappearance at Daya Bay." In: (2012). DOI: 10.1103/PhysRevLett.108.171803. eprint: arXiv:1203.1669.

[188] J. K. Ahn et al. "Observation of Reactor Electron Antineutrinos Disappearance in the RENO Experiment." In: *Phys. Rev. Lett.* 108 (19 2012), p. 191802. DOI: 10.1103/PhysRevLett.108.191802. URL: https://link.aps.org/doi/10.1103/PhysRevLett.108.191802.

[189] Thomas Hambye. *Leptogenesis from right-handed neutrino decays to right-handed leptons*. 2006. eprint: arXiv:hep-ph/0606182.

[190] Steven Weinberg. "Baryon- and Lepton-Nonconserving Processes." In: *Phys. Rev. Lett.* 43 (21 1979), pp. 1566–1570. DOI: 10.1103/PhysRevLett.43.1566. URL: https://link.aps.org/doi/10.1103/PhysRevLett.43.1566.

[191] J. Smirnov. "Effects of the Quantum Vacuum in Particle Physics and Cosmology." PhD thesis. Max-Planck-Institut für Kernphysik, Heidelberg, 2014. URL: http://archiv.ub.uni-heidelberg.de/volltextserver/17769/1/JuriSmirnovThesis.pdf.

[192] S. F. King. "Neutrino Mass Models." In: (2003). DOI: 10.1088/0034-4885/67/2/R01. eprint: arXiv:hep-ph/0310204.

[193] Francesco Capozzi et al. "Global constraints on absolute neutrino masses and their ordering." In: (2017). DOI: 10.1103/PhysRevD.95.096014. eprint: arXiv:1703.04471.

[194] Planck Collaboration et al. "Planck 2015 results. XI. CMB power spectra, likelihoods, and robustness of parameters." In: (2015). DOI: 10.1051/0004-6361/201526926. eprint: arXiv:1507.02704.

[195] Florian Beutler et al. "The 6dF Galaxy Survey: Baryon Acoustic Oscillations and the Local Hubble Constant." In: (2011). DOI: 10.1111/j.1365-2966.2011.19250.x. eprint: arXiv:1106.3366.

[196] Ashley J. Ross et al. "The Clustering of the SDSS DR7 Main Galaxy Sample I: A 4 per cent Distance Measure at z=0.15." In: (2014). DOI: 10.1093/mnras/stv154. eprint: arXiv:1409.3242.

[197] Lauren Anderson et al. "The clustering of galaxies in the SDSS-III Baryon Oscillation Spectroscopic Survey: Baryon Acoustic Oscillations in the Data Release 10 and 11 galaxy samples." In: (2013). DOI: 10.1093/mnras/stu523. eprint: arXiv:1312.4877.

[198] J. J. Gómez-Cadenas and Justo Martín-Albo. "Phenomenology of neutrinoless double beta decay." In: *PoS* GSSI14 (2015), p. 004. arXiv: 1502.00581 [hep-ex].

[199] A. Suzuki and Kam Land Collaboration. "Results from KamLAND Reactor Neutrino Detection." In: *Physica Scripta Volume T* 121 (Jan. 2005), pp. 33–38. DOI: 10.1088/0031-8949/2005/T121/004.

[200] K.-H. Ackermann et al. "The Gerda experiment for the search of $0\nu\beta\beta$ decay in 76Ge." In: *The European Physical Journal C* 73.3 (2013), p. 2330. ISSN: 1434-6052. DOI: 10.1140/epjc/s10052-013-2330-0. URL: https://doi.org/10.1140/epjc/s10052-013-2330-0.

[201] EXO-200 Collaboration et al. "Search for Majoron-emitting modes of double-beta decay of ^{136}Xe with EXO-200." In: (2014). DOI: 10.1103/PhysRevD.90.092004. eprint: arXiv:1409.6829.

[202] F. Rossi-Torres, M. M. Guzzo, and E. Kemp. *Boundaries on Neutrino Mass from Supernovae Neutronization Burst by Liquid Argon Experiments*. 2015. eprint: arXiv:1501.00456.

[203] C. B. Bratton et al. "Angular distribution of events from SN1987A." In: *Phys. Rev. D* 37 (12 1988), pp. 3361–3363. DOI: 10.1103/PhysRevD.37.3361. URL: https://link.aps.org/doi/10.1103/PhysRevD.37.3361.

[204] K. Hirata et al. "Observation of a neutrino burst from the supernova SN1987A." In: *Phys. Rev. Lett.* 58 (14 1987), pp. 1490–1493. DOI: 10.1103/PhysRevLett.58.1490. URL: https://link.aps.org/doi/10.1103/PhysRevLett.58.1490.

[205] Giulia Pagliaroli, Fernando Rossi-Torres, and Francesco Vissani. "Neutrino mass bound in the standard scenario for supernova electronic antineutrino emission." In: (2010). DOI: 10.1016/j.astropartphys.2010.02.007. eprint: arXiv:1002.3349.

[206] A. S. Dighe, M. T. Keil, and G. G. Raffelt. "Detecting the Neutrino Mass Hierarchy with a Supernova at IceCube." In: (2003). DOI: 10.1088/1475-7516/2003/06/005. eprint: arXiv:hep-ph/0303210.

[207] Hyper-Kamiokande Working Group et al. *A Long Baseline Neutrino Oscillation Experiment Using J-PARC Neutrino Beam and Hyper-Kamiokande*. 2014. eprint: arXiv:1412.4673.

[208] Susanne Mertens. "Direct Neutrino Mass Experiments." In: (2016). DOI: 10.1088/1742-6596/718/2/022013. eprint: arXiv:1605.01579.

[209] Thomas Thümmler and for the KATRIN Collaboration. "Introduction to direct neutrino mass measurements and KATRIN." In: (2010). DOI: 10.1016/j.nuclphysbps.2012.09.024. eprint: arXiv:1012.2282.

[210] R. G. Hamish Robertson. *KATRIN: an experiment to determine the neutrino mass from the beta decay of tritium*. 2013. eprint: arXiv:1307.5486.

[211] Ch. Kraus et al. "Final Results from phase II of the Mainz Neutrino Mass Search in Tritium Decay." In: (2004). DOI: 10.1140/epjc/s2005-02139-7. eprint: arXiv:hep-ex/0412056.

[212] V. N. Aseev et al. "An upper limit on electron antineutrino mass from Troitsk experiment." In: (2011). DOI: 10.1103/PhysRevD.84.112003. eprint: arXiv:1108.5034.

[213] Lorenzo Calibbi and Giovanni Signorelli. "Charged Lepton Flavour Violation: An Experimental and Theoretical Introduction." In: (2017). DOI: 10.1393/ncr/i2018-10144-0. eprint: arXiv:1709.00294.

[214] MEG Collaboration et al. *New constraint on the existence of the mu+-> e+ gamma decay*. 2013. eprint: arXiv:1303.0754.

[215] A. M. Baldini et al. *MEG Upgrade Proposal*. 2013. eprint: arXiv:1301.7225.

[216] U. Bellgardt et al. "Search for the decay + → e+e+e." In: *Nuclear Physics B* 299.1 (1988), pp. 1 –6. ISSN: 0550-3213. DOI: https://doi.org/10.1016/0550-3213(88)90462-2. URL: http://www.sciencedirect.com/science/article/pii/0550321388904622.

[217] A. Blondel et al. *Research Proposal for an Experiment to Search for the Decay -> eee*. 2013. eprint: arXiv:1301.6113.

[218] Wilhelm H. Bertl et al. "A Search for muon to electron conversion in muonic gold." In: *Eur. Phys. J.* C47 (2006), pp. 337–346. DOI: 10.1140/epjc/s2006-02582-x.

[219] L. Bartoszek et al. *Mu2e Technical Design Report*. 2015. eprint: arXiv:1501.05241.

[220] COMET Collaboration. *Experimental Proposal for Phase-I of the COMET Experiment at J-PARC*. URL: https://j-parc.jp/researcher/Hadron/en/pac_1207/pdf/E21_2012-10.pdf.

[221] DeeMe Collaboration. *, DeeMe KEK J-PARC Proposal*. URL: http://deeme.hep.sci.osaka-u.ac.jp/documents/deeme-proposal-r28.pdf.

[222] The BABAR Collaboration and B. Aubert. "Searches for Lepton Flavor Violation in the Decays tau -> e gamma and tau -> mu gamma." In: (2009). DOI: 10.1103/PhysRevLett.104.021802. eprint: arXiv:0908.2381.

[223] K. Hayasaka and for the Belle Collaboration. "Search for tau -> e gamma decay at Belle." In: (2005). DOI: 10.1016/j.physletb.2005.03.028. eprint: arXiv:hep-ex/0501068.

[224] A. M. Baldini et al. *MEG Upgrade Proposal*. 2013. eprint: arXiv:1301.7225.

[225] T. Aushev et al. *Physics at Super B Factory*. 2010. eprint: arXiv:1002.5012.

[226] C. Dohmen et al. "Test of lepton-flavour conservation in → e conversion on titanium." In: *Physics Letters B* 317.4 (1993), pp. 631 –636. ISSN: 0370-2693. DOI: https://doi.org/10.1016/0370-2693(93)91383-X. URL: http://www.sciencedirect.com/science/article/pii/037026939391383X.

[227] Akira Sato. "Muon Storage Ring PRISM - FFAG to Improve a Sensitivity of - e Conversion Experiment Below 10 17." In: 2008.

[228] R. P. Litchfield. *Muon to electron conversion: The COMET and Mu2e experiments*. 2014. eprint: arXiv:1412.1406.

[229] Diego Restrepo, Oscar Zapata, and Carlos E. Yaguna. "Models with radiative neutrino masses and viable dark matter candidates." In: *JHEP* 2013.11 (2013), p. 11. ISSN: 1029-8479. DOI: 10.1007/JHEP11(2013)011. URL: https://doi.org/10.1007/JHEP11(2013)011.

[230] Florian Bonnet et al. "Systematic study of the d=5 Weinberg operator at one-loop order." In: (2012). DOI: 10.1007/JHEP07(2012)153. eprint: arXiv:1204.5862.

[231] Ernest Ma. "Verifiable Radiative Seesaw Mechanism of Neutrino Mass and Dark Matter." In: (2006). DOI: 10.1103/PhysRevD.73.077301. eprint: arXiv:hep-ph/0601225.

[232] Michael Klasen et al. "Scalar dark matter and fermion coannihilations in the radiative seesaw model." In: (2013). DOI: 10.1088/1475-7516/2013/04/044. eprint: arXiv:1302.5298.

[233] Ernest Ma and Daijiro Suematsu. "Fermion Triplet Dark Matter and Radiative Neutrino Mass." In: (2008). DOI: 10.1142/S021773230903059X. eprint: arXiv:0809.0942.

[234] Yasaman Farzan, Silvia Pascoli, and Michael A. Schmidt. "AMEND: A Model Explaining Neutrino masses and Dark matter testable at the LHC and MEG." In: (2010). DOI: 10.1007/JHEP10(2010)111. eprint: arXiv:1005.5323.

[235] Mayumi Aoki, Shinya Kanemura, and Kei Yagyu. "Doubly-charged scalar bosons from the doublet." In: (2011). DOI: 10.1016/j.physletb.2011.07.017. eprint: arXiv:1105.2075.

[236] Sandy S. C. Law and Kristian L. McDonald. "A Class of Inert N-tuplet Models with Radiative Neutrino Mass and Dark Matter." In: (2013). DOI: 10.1007/JHEP09(2013)092. eprint: arXiv:1305.6467.

[237] Yasaman Farzan. "A minimal model linking two great mysteries: neutrino mass and dark matter." In: (2009). DOI: 10.1103/PhysRevD.80.073009. eprint: arXiv:0908.3729.

[238] Sean Fraser, Ernest Ma, and Oleg Popov. "Scotogenic Inverse Seesaw Model of Neutrino Mass." In: (2014). DOI: 10.1016/j.physletb.2014.08.069. eprint: arXiv:1408.4785.

[239] Diego Restrepo et al. "Radiative neutrino masses in the singlet-doublet fermion dark matter model with scalar singlets." In: (2015). DOI: 10.1103/PhysRevD.92.013005. eprint: arXiv:1504.07892.

[240] Amalia Betancur, Robinson Longas, and Oscar Zapata. "Doublet-triplet dark matter with neutrino masses." In: (2017). DOI: 10.1103/PhysRevD.96.035011. eprint: arXiv:1704.01162.

[241] Robinson Longas et al. "The Inert Zee Model." In: (2015). DOI: 10.1007/JHEP03(2016)162. eprint: arXiv:1511.01873.

[242] Timothy Cohen et al. "Singlet-doublet dark matter." In: *Phys. Rev. D* 85 (7 2012), p. 075003. DOI: 10.1103/PhysRevD.85.075003. URL: https://link.aps.org/doi/10.1103/PhysRevD.85.075003.

[243] Clifford Cheung and David Sanford. "Simplified models of mixed dark matter." In: *Journal of Cosmology and Astroparticle Physics* 2014.02 (2014), p. 011. URL: http://stacks.iop.org/1475-7516/2014/i=02/a=011.

[244] Amit Dutta Banik and Debasish Majumdar. "Inert Doublet Dark Matter with an additional scalar singlet and 125 GeV Higgs Boson." In: (2014). DOI: 10.1140/epjc/s10052-014-3142-6. eprint: arXiv:1404.5840.

[245] L. G. Cabral-Rosetti et al. "Scalar dark matter in inert doublet model with scalar singlet." In: *Journal of Physics: Conference Series* 912.1 (2017), p. 012047. URL: http://stacks.iop.org/1742-6596/912/i=1/a=012047.

[246] Lorenzo Calibbi, Alberto Mariotti, and Pantelis Tziveloglou. *Singlet-Doublet Model: Dark matter searches and LHC constraints*. 2015. eprint: arXiv:1505.03867.

[247] Shankha Banerjee et al. "WIMP Dark Matter in a Well-Tempered Regime: A case study on Singlet-Doublets Fermionic WIMP." In: (2016). DOI: 10.1007/JHEP11(2016)070. eprint: arXiv:1603.07387.

[248] Tomohiro Abe. "Effect of CP violation in the singlet-doublet dark matter model." In: *Physics Letters B* 771.Supplement C (2017), pp. 125 –130. ISSN: 0370-2693. DOI: https://doi.org/10.1016/j.physletb.2017.05.048. URL: http://www.sciencedirect.com/science/article/pii/S0370269317304112.

[249] G. Cardano. *Ars magna or The Rules of Algebra*, Dover, 1993.

[250] A. Semenov. *LanHEP - a package for automatic generation of Feynman rules from the Lagrangian. Updated version 3.2*. 2014. eprint: arXiv:1412.5016.

[251] Florian Staub. "SARAH 4: A tool for (not only SUSY) model builders." In: (2013). DOI: 10.1016/j.cpc.2014.02.018. eprint: arXiv:1309.7223.

[252] W. Porod and F. Staub. "SPheno 3.1: extensions including flavour, CP-phases and models beyond the MSSM." In: (2011). DOI: 10.1016/j.cpc.2012.05.021. eprint: arXiv:1104.1573.

[253] G. Belanger et al. "micrOMEGAs4.1: two dark matter candidates." In: (2014). DOI: 10.1016/j.cpc.2015.03.003. eprint: arXiv:1407.6129.

[254] J.A. Casas and A. Ibarra. "Oscillating neutrinos and →e," in: *Nuclear Physics B* 618.1 (2001), pp. 171 –204. ISSN: 0550-3213. DOI: https://doi.org/10.1016/S0550-3213(01)00475-8. URL: http://www.sciencedirect.com/science/article/pii/S0550321301004758.

[255] URL: https://www.wolfram.com/mathematica/.

[256] Adam Alloul et al. "FeynRules 2.0 - A complete toolbox for tree-level phenomenology." In: (2013). DOI: 10.1016/j.cpc.2014.04.012. eprint: arXiv:1310.1921.

[257] J. Kuipers et al. "FORM version 4.0." In: (2012). DOI: 10.1016/j.cpc.2012.12.028. eprint: arXiv:1203.6543.

[258] C. Patrignani et al. "Review of Particle Physics." In: *Chin. Phys.* C40.10 (2016), p. 100001. DOI: 10.1088/1674-1137/40/10/100001.

[259] M. C. Gonzalez-Garcia, Michele Maltoni, and Thomas Schwetz. "Updated fit to three neutrino mixing: status of leptonic CP violation." In: (2014). DOI: 10.1007/JHEP11(2014)052. eprint: arXiv:1409.5439.

[260] E. Aprile et al. "First Dark Matter Search Results from the XENON1T Experiment." In: (2017). DOI: 10.1103/PhysRevLett.119.181301. eprint: arXiv:1705.06655.

[261] Tomohiro Abe, Ryuichiro Kitano, and Ryosuke Sato. "Discrimination of dark matter models in future experiments." In: (2014). DOI: 10.1103/PhysRevD.91.095004. eprint: arXiv:1411.1335.

[262] Aaboud Morad et al. "Search for a scalar partner of the top quark in the jets plus missing transverse momentum final state at $\sqrt{s}$=13 TeV with the ATLAS detector." In: (2017). arXiv: 1709.04183 [hep-ex].

[263] CMS Collaboration. "Search for invisible decays of the Higgs boson produced through vector boson fusion at $\sqrt{s} = 13$ TeV." In: (2018).

[264] CMS Collaboration. *Search for new physics in events with two soft oppositely charged leptons and missing transverse momentum in proton-proton collisions at $\sqrt{s} = 13$ TeV*. 2018. eprint: arXiv:1801.01846.

[265] ATLAS Collaboration. "Search for dark matter and other new phenomena in events with an energetic jet and large missing transverse momentum using the ATLAS detector." In: (2017). DOI: 10.1007/JHEP01(2018)126. eprint: arXiv:1711.03301.

[266] CMS Collaboration. *Search for new physics in final states with an energetic jet or a hadronically decaying W or Z boson and transverse momentum imbalance at $\sqrt{s} = 13$ TeV*. 2017. eprint: arXiv:1712.02345.

[267] Ethan Dolle et al. "Dilepton Signals in the Inert Doublet Model." In: (2009). DOI: 10.1103/PhysRevD.81.035003. eprint: arXiv:0909.3094.

[268] The ATLAS collaboration. "Search for electroweak production of supersymmetric particles in the two and three lepton final state at $\sqrt{s} = 13$ TeV with the ATLAS detector." In: (2017).

[269] CMS Collaboration. "Search for selectrons and smuons at $\sqrt{s} =$ 13 TeV." In: (2017).

[270] ATLAS Collaboration. "Search for electroweak production of supersymmetric states in scenarios with compressed mass spectra at $\sqrt{s} = 13$ TeV with the ATLAS detector." In: (2017). DOI: 10.1103/PhysRevD.97.052010. eprint: arXiv:1712.08119.

[271] CMS Collaboration. *Search for new physics in events with two soft oppositely charged leptons and missing transverse momentum in proton-proton collisions at $\sqrt{s} = 13$ TeV*. 2018. eprint: arXiv:1801.01846.

[272] Federica Giacchino, Laura Lopez-Honorez, and Michel H. G. Tytgat. "Scalar Dark Matter Models with Significant Internal Bremsstrahlung." In: (2013). DOI: 10.1088/1475-7516/2013/10/025. eprint: arXiv:1307.6480.

[273] Michael Klasen et al. *Lepton flavor violation and scalar dark matter in a radiative model of neutrino masses*. 2016. eprint: arXiv:1602.05137.

[274] Giorgio Arcadi, Yann Mambrini, and Francois Richard. "Z-portal dark matter." In: (2014). DOI: 10.1088/1475-7516/2015/03/018. eprint: arXiv:1411.2985.

[275] Ansgar Denner et al. "Feynman rules for fermion number violating interactions." In: *Nucl. Phys.* B387 (1992), pp. 467–481. DOI: 10.1016/0550-3213(92)90169-C.

[276] Matthew D. Schwartz. *Quantum Field Theory and the Standard Model*. Cambridge University Press, 2014. ISBN: 1107034736, 9781107034730. URL: http://www.cambridge.org/us/academic/subjects/physics/theoretical-physics-and-mathematical-physics/quantum-field-theory-and-standard-model.

[277] K. A. Olive et al. "Review of Particle Physics." In: *Chin. Phys.* C38 (2014), p. 090001. DOI: 10.1088/1674-1137/38/9/090001.

[278] W. von Schlippe. *Relativistic Kinematics of Particle Interactions*. 2002. URL: http://www.helsinki.fi/~www_sefo/phenomenology/Schlippe_relativistic_kinematics.pdf.

[279] James D Bjorken and Sidney David Drell. *Relativistic quantum mechanics*. International series in pure and applied physics. New York, NY: McGraw-Hill, 1964. URL: https://cds.cern.ch/record/100769.

[280] Michael E. Peskin and Daniel V. Schroeder. *An Introduction to quantum field theory*. Reading, USA: Addison-Wesley, 1995. ISBN: 9780201503975, 0201503972. URL: http://www.slac.stanford.edu/~mpeskin/QFT.html.

[281] Warren Siegel. "Supersymmetric dimensional regularization via dimensional reduction." In: *Physics Letters B* 84.2 (1979), pp. 193 –196. ISSN: 0370-2693. DOI: https://doi.org/10.1016/0370-2693(79)90282-X. URL: http://www.sciencedirect.com/science/article/pii/037026937990282X.

[282] K.Kovařík. "HitchHiker's Guide to Renormalization." private communication.

[283] G. Passarino and M. Veltman. "One-loop corrections for e+e annihilation into + in the Weinberg model." In: *Nuclear Physics B* 160.1 (1979), pp. 151 –207. ISSN: 0550-3213. DOI: https://doi.org/10.1016/0550-3213(79)90234-7. URL: http://www.sciencedirect.com/science/article/pii/0550321379902347.

ACKNOWLEDGEMENTS

Here, I would like to express my thanks to all people who made this work possible.

I would like to express my great appreciation to Prof. Dr. Michael Klasen for giving me the opportunity to work on this topic and for the discussions and advice given to me. I am thankful for all the things I learned.
Further I would like to offer my special thanks to Prof. Dr. Christian Weinheimer for being my second supervisor and all the time and knowledge offered to me.
And I would like to thank the Graduate School 2149 in general for establishing an environment which allowed the pursuit of this work.
I am very grateful for all the discussion and helpful advice of Dr. Karol Kovařík and for always having an open ear.
I am thankful for Saskia Schmiemann for all the help and discussions.
I would like to thank Dr. Björn Hermman for the fruitful discussions, collaboration and the opportunity to stay at LATPh.
And I would like to express my gratitude to Dr. Kathrin Valerius and Dr. Marco Kleesiek for working with me in Karlsruhe.
Additionally I am thankful for all my colleagues at that time, especially Dr. David Lamprea for many useful discussions, Dr. Christoph Borschensky for all the help, Dr. Thomas Zub, Daniel Schwartländer, Dr. Marcel Rothering, Miguel Vargas and all the other for being good colleagues and making it a nice work place.
Further I would like thank my friends and family for the support they showed me all the time.

CURRICULUM VITAE

PERSÖNLICHE DATEN

Name	Sonja Esch
Geburtsdatum	7.11.1987
Geburtsort	Bonn
Staatsangehörigkeit	Deutsch
Eltern	Beatrix Wierlemann-Esch
	Thomas Karl Josef Esch

STUDIUM UND SCHULE

Seit 2014	Studium der Physik an der WWU mit angestrebter Promotion unter der Betreuung von Prof. Dr. M. Klasen und Prof. Dr. Chr. Weinheimer im Rahmen des Graduiertenkolleg 2149
2010 - 2014	Studium der Physik an der WWU mit dem Abschluss Master of Science, Nebenfach Mathematik
2007 - 2010	Studium der Physik und Mathematik an der WUU mit dem Abschluss Bachelor of Science
1998- 2007	Gymnasium Augustinianum in Greven
1996 - 1998	Martini Grundschule in Greven
1994 - 1006	Grundschule in Hohentengen am Hochrhein

PRAKTIKA & BERUFSERFAHRUNG

Seit 2011	Übungsgruppenleiter in Mathematik und Physik
2009	Studentische Aushilfe BKK vorOrt, Bochum
2008	Kassenaushilfe K&K, Greven
2007	Aushilfe Luhns GmbH, Reckenfeld
2006	Praktikum im Atelier für künstlerische Techniken der WWU, Münster
2002	Praktikum Druckhaus Cramer, Greven

COLOPHON

This document was typeset using the typographical look-and-feel `classicthesis` developed by André Miede.